ULYANA DUPLETSA

Cosmic Chirps

Extracting Cosmological and Astrophysical Information from Compact Binary Mergers

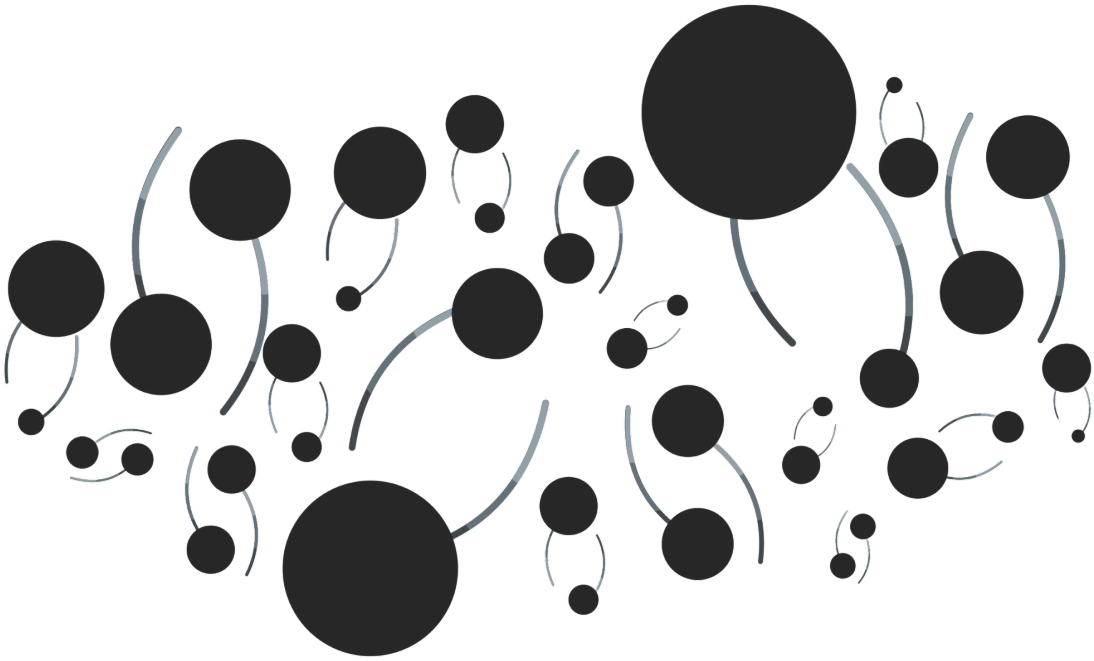

DOCTORAL THESIS

COVER ART IS ORIGINAL WORK BY THE AUTHOR

GRAN SASSO SCIENCE INSTITUTE
SCHOOL OF ADVANCED STUDIES
Scuola Universitaria Superiore

PhD Program in Astroparticle Physics - XXXVI Cycle

Cosmic Chirps

Extracting Cosmological and Astrophysical Information from Compact Binary Mergers

PhD Candidate: Ulyana Dupletsa

Supervisor: Prof. Jan Harms
Co-Supervisors: Prof. Marica Branchesi,
Dr. Riccardo Murgia

DOCTORAL THESIS

> *Everything must be taken into account.*
> *If the fact will not fit the theory*
> *- let the theory go*
>
> **— Agatha Christie**
> "The mysterious affair at Styles"

Preface

> *'It is completely unimportant', said Poirot.*
> *'That is why it is so interesting', he added softly.*
>
> **— Agatha Christie**
> "The Murder of Roger Ackroyd"

Explaining the Universe is a complex and highly intricate process. I like to think of it as a crime scene, with scientists acting as investigators.

It all begins with the right questions. Something has happened in the distant or recent past, somewhere in the Universe, and we have to understand what that was, why, and how the events took place. The information is out there but far from evident. The clues are in the data that we collect and analyze. It is not straightforward to distinguish between what is essential and what is circumstantial.

Next, we develop theories and models to connect all the pieces of evidence into a coherent narrative. What is more, we want our models and theories not just to explain but also to predict new information from data we have not yet observed. At its core, the pursuit of understanding is a structured investigation that follows logic, evidence, and inference.

I have always had an interest in crime stories, but it was during my PhD that I discovered Agatha Christie's wonderful works. Her adventurous life and immense production have paralleled my own everyday investigations. It felt natural to have her books open the chapters of my thesis. When I came across some of her sentences, I had the perfect fit for each.

L'Aquila, February 2025
Ulyana Dupletsa

Extended Abstract

This thesis explores the multi-faceted and promising science of gravitational waves (GWs) from compact binary coalescences (CBCs), focusing on the information they provide and how we can extract it. Central to our work is the question: What is the data content of the GW signals from CBCs, and how can we effectively analyze it to enhance our understanding of the Universe? This study addresses current detector networks and next-generation (XG) instruments, linking data analysis with multi-messenger (MM) applications and cosmology.

In the first part, the analysis centers on current detectors, using data from the LIGO-Virgo-KAGRA (LVK) network. We explore spectral siren cosmology by applying Hierarchical Bayesian Inference (HBI) to simulated and measured data. A significant focus is on quantifying the bias in the inferred Hubble constant value, H_0, that arises from mismodeling the black hole (BH) population—specifically, the effects of neglecting the redshift dependence of the BH mass spectrum. We report a bias at 2σ level, signaling the impact of the mass model. We also show preliminary results from the O4a observational run, presenting the latest estimate of H_0 and the impact of a new mass model that encompasses all the observed CBCs, without the need to distinguish between BHs or neutron stars (NSs). Being able to use all the available GW events gives us tighter constraints on H_0, although still far from the level of Planck or supernovae (SNe) results.

The second part shifts the focus to future GW observatories, with the Einstein Telescope (ET) exemplifying XG capabilities. We thoroughly discuss forecasting analysis techniques based on the Fisher matrix approximation, which is the current approach for assessing XG detectors performance. In this context, we present the software tool `GWFish`, which simulates GW detector networks and implements fast Fisher matrix parameter estimation (PE). Additionally, we integrate prior information into `GWFish` to study the interplay between Signal-to-Noise Ratio (SNR) and parameter correlations effectively, testing it

to be a reliable method for predicting detectors performance against measured data from the LVK Collaboration.

`GWFish` is employed for several different applications related to the rich ET science case. It is one of the two Fisher codes used for the design comparison (ET-Δ versus ET-2L) paper of ET. Specifically, one of the key aspects that we explore is MM astrophysics, evaluating the prospects for synergy between GW and electromagnetic (EM) observatories based on sky localization and pre-merger alerts analyses. This work highlights the performance of different ET designs, particularly stressing the role of the sensitivity at low frequencies.

Furthermore, we conduct an in-depth study of the joint GW and kilonova (KN) detections using future EM telescopes like the Vera Rubin Observatory, pinpointing which are the primary sources of uncertainties in MM studies, from the GW network to population models to the microphysics of NS systems.

Additionally, we investigate ET prospects for cosmological analysis using both bright siren -Binary Neutron Star (BNS) events with Gamma Ray Burst (GRB) counterparts- and dark siren -BBH events along with the large scale structure (LSS) data as mapped through the 21 cm emission from neutral hydrogen (HI)- approaches to infer cosmological parameters up to redshifts as high as $z \sim 3$ in the dark siren case. In both scenarios, we demonstrate the enormous potential of ET in constraining cosmological parameters, thanks to the enhanced PE and detection numbers.

This work builds a framework that links advanced data analysis techniques, predicts detector performance, and includes MM observations and cosmological inference. The findings improve our understanding of GW astronomy, paving the way for future studies with existing and XG observatories.

List of Publications

This thesis is based on the following publications:

1. *"GWFish: A simulation software to evaluate parameter-estimation capabilities of gravitational-wave detector networks"*
   U. Dupletsa, J. Harms, B. Banerjee, M. Branchesi, B. Goncharov, A. Maselli, A. C. S. Oliveira, S. Ronchini, J. Tissino; *Astronomy and Computing* (2023), DOI:10.1016/j.ascom.2022.100671, arXiv:2205.02499 [gr-qc], GitHub

2. *"Science with the Einstein Telescope: a comparison of different designs"*
   M. Branchesi, M. Maggiore et al. incl. **U. Dupletsa**; *JCAP* 07 (2023) 068, DOI:10.1088/1475-7516/2023/07/068, arXiv:2303.15923 [gr-qc] [astro-ph.CO] [astro-ph.HE]

3. *"Validating Prior-informed Fisher-matrix Analyses against GWTC Data"*
   U. Dupletsa, J. Harms, Ken K. Y. Ng, J. Tissino, F. Santoliquido, A. Cozzumbo; *Physical Review D*, 111 (2025), 2, 024036, DOI:10.1103/PhysRevD.111.024036, arXiv:2404.16103 [gr-qc], GitHub

4. *"Prospects for optical detections from binary neutron star mergers with the next-generation multi-messenger observatories"*
   E. Loffredo, N. Hazra, **U. Dupletsa**, M. Branchesi, S. Ronchini, F. Santoliquido, A. Perego, B. Banerjee, S. Bisero, G. Ricigliano, S. Vergani, I. Andreoni, M. Cantiello, J. Harms, M. Mapelli, G. Oganesyan; *Astronomy & Astrophysics*, 697 (2025), A36 arXiv:2411.02342 [astro-ph.HE]

5. *"Parameter estimation catalogs for binary neutron star mergers detected with next-generation gravitational wave detectors"*
   U. Dupletsa, F. Santoliquido, M. Branchesi, E. Loffredo; Sept. 2024, https://zenodo.org/records/13850416

6. *"Model-independent cosmology with joint observations of gravitational waves and γ-ray bursts"*
   A. Cozzumbo, **U. Dupletsa**, R. Caldèron, R. Murgia, G. Oganesyan, M. Branchesi; *accepted in JCAP*, arXiv:2411.02490 [gr-qc]

7. *"Blinded Mock Data Challenge for Gravitational-Wave Cosmology-I: Assessing the Robustness of Methods Using Binary Black Holes Mass Spectrum"*

A. Agarwal, **U. Dupletsa**, K. Leyde, S. Mukherjee, B. Revenu, J. E. Rivera, A. E. Romano, M. R. Sah, S. Vallejo-Pena, A. Avendano, F. Beirnaert, G. Dalya, M. C. Espitia, C. Karathanasis, S. Moreno-Gonzalez, L. Quiceno, F. Stachurski, J. Garcia-Bellido, R. Gray, N. Tamanini, C. Turski; *accepted in ApJ*, arXiv:2412.14244 [astro-ph.CO], GitHub

8. *"The Science of the Einstein Telescope"*
A. Abacet et al. incl. **U. Dupletsa**; *submitted to JCAP*, arXiv:2503.12263 [gr-cq]

The following are two works in preparation which partial results are discussed in this thesis:

9. *"Mapping the Universe's Expansion with Gravitational Waves and Neutral Hydrogen"*
U. Dupletsa, M. Spinelli, S. Mastrogiovanni, T. Ronconi, R. Murgia, M. Schulz, J. Harms; *in preparation*

10. *"GWTC-4.0: constraints on the cosmic expansion history and modified gravitational wave propagation"*
LIGO-Virgo-KAGRA Collaboration; *in preparation*

This is the list of publications related to side projects that did not directly enter the thesis:

11. *"On the single-event-based identification of primordial black hole mergers at cosmological distances"*,
K. K. Y. Ng, S. Chen, B. Goncharov, **U. Dupletsa**, S. Borhanian, M. Branchesi, J. Harms, M. Maggiore, B. S. Sathyaprakash, S. Vitale; ApJL 931 L12 (2022), DOI 10.3847/2041-8213/ac6bea, arXiv:2108.07276 [gr-qc], [hep-ph]

12. *"Perspectives for multi-messenger astronomy with the next generation of gravitational-wave detectors and high-energy satellites"*,
S. Ronchini, M. Branchesi, G. Oganesyan, B. Banerjee, **U. Dupletsa**, G. Ghirlanda, J. Harms, M. Mapelli, F. Santoliquido; *Astronomy & Astrophysics* (2022), Volume 665, A97, DOI:10.1051/0004-6361 /202243705, arXiv:2108.07276 [astro-ph.HE]

13. *"Measuring properties of primordial black hole mergers at cosmological distances: effect of higher order modes in gravitational waves"*,
K. K. Y. Ng, B. Goncharov, S. Chen, S. Borhanian, **U. Dupletsa**, G. Francicolini, M. Branchesi, J. Harms, M. Maggiore, A. Riotto, B. S. Sathyaprakash,

S. Vitale, *Physical Review D* 107, 024041, DOI:10.1103/PhysRevD.107.024041, arXiv:2210.03132 [astro-ph.HE] [gr-qc]

14. *"Pre-merger alert to detect the very-high-energy prompt emission from binary neutron-star mergers: Einstein Telescope and Cherenkov Telescope Array synergy"*,
B. Banerjee, G. Oganesyan, M. Branchesi, **U. Dupletsa**, F. Aharonian, F. Brighenti, B. Goncharov, J. Harms, M. Mapelli, S. Ronchini, F. Santoliquido *Astronomy & Astrophysics*, Vol. 678, DOI:10.1051/0004-6361/202345850, arXiv:2212.14007 [astro-ph.HE]

15. *"Phenomenological models of Cosmic Ray transport in Galaxies"*
C. Evoli and **U. Dupletsa**; 2023, in *Proceedings of the International School of Physics "Enrico Fermi"*, Volume 208: Foundations of Cosmic Ray Astrophysics, arXiv:2309.00298 [astro-ph.HE]

16. *"The Wide-field Spectroscopic Telescope (WST) Science White Paper"*
V. Mainieri et al. incl. **U. Dupletsa**; 2024, arXiv:2403:05398 [astro-ph.IM]

17. *"Classifying binary black holes from Population III stars with the Einstein Telescope: a machine-learning approach"*
F. Santoliquido, **U. Dupletsa**, J. Tissino, M. Branchesi, F. Iacovelli, G. Iorio, M. Mapelli, D. Gerosa, J. Harms and M. Pasquato ; *Astronomy & Astrophysics* 690 (2024), A362, DOI:10.1051/0004-6361/202450381, arXiv:2404.10048 [astro-ph.HE]

18. *"Fast and accurate parameter estimation of high-redshift sources with the Einstein Telescope"*
F. Santoliquido, J. Tissino, **U. Dupletsa**, M. Branchesi, J. Harms, M. Arca Sedda, M. Dax, A. Kofler, S. R. Green, N. Gupte, I. M. Romero-Shaw, E. Berti; *submitted to PRD*, arXiv:2504.21087 [astro-ph.HE] [astro-ph.IM] [gr-qc]

19. *25+ Collaboration Papers inside the LIGO-Virgo-KAGRA Collaboration*
[list here]

Contents

Ouverture

> *In all the world there is nothing so curious and so interesting and so beautiful as truth.*
>
> **— Agatha Christie**
> "Three Act Tragedy"

Light has been our primary source of knowledge ever since the first human-lit fire. Electromagnetic waves emitted by the Sun, distant stars, and even simple candlelight have provided valuable insights into the world around us. From ancient civilizations that gazed at the night sky to the invention of the first optical telescope to the observation of the cosmic microwave background, the very picture of the Universe's birth, our ability to perceive the cosmos has evolved alongside our technology and our mastery to harness the electromagnetic spectrum, far beyond the visible light, encompassing wavelengths from low-frequency radio waves to highly energetic gamma rays.

Despite its success, information coming from electromagnetic observation has intrinsic limitations. Electromagnetic waves traveling from distant sources to us might get absorbed, scattered, or completely blocked. On top of this, objects like black holes do not ordinarily emit light and might be bound to remain in the dark. We know there are supermassive black holes at the center of galaxies because they can bind and accelerate matter around them and cause electromagnetic emission. However, our theory of stellar evolution also predicts stellar mass black holes forming at the end of a massive star life cycle. Their existence has been just one of the predictions of General Relativity, our most successful theory of space and time. Until ten years ago.

September 14, 2015, unlocked an entirely new dimension. Another prediction of General Relativity has been proven: the existence of gravitational waves. These are ripples in the fabric of spacetime, generated by the most extreme cosmic events, such as the merger of black holes or neutron stars, that propagate to us at the speed of light, mostly undisturbed, and carry information about the sources that generated them in a way that electromagnetic waves never could. The first measurement of gravitational waves is also the first direct proof of the existence

of stellar-origin black holes. Until then, a strong indirect evidence for the existence of black holes has been the observation of X-ray binaries. Typically, these are light black holes, compared to the ones we observe through gravitational waves, accreting matter from a companion star.

The first gravitational-wave event, dubbed `GW150914`, comes from the merger of two black holes, of $36M_\odot$ and $29M_\odot$, at a distance of roughly 400 Mpc from us, which corresponds to a redshift of 0.09. The two LIGO interferometers, LIGO Hanford and LIGO Livingston, captured the signal. `GW150914` is a history marking event. Since then, we have observed tens of binary black hole systems, and our understanding of the black hole population is advancing as never before. Moreover, thanks to the joint effort of three gravitational wave detectors, the two LIGOs and Virgo, we were able to measure the first-ever binary neutron star event, accompanied by electromagnetic emission, both in the form of kilonova and the relativistic jet of a gamma-ray burst. Many fields, from astrophysics to fundamental and nuclear physics, are being revolutionized thanks to this one-only multi-messenger observation.

Gravitational waves have also revolutionized cosmology by providing a new way to observe the Universe. Unlike traditional standard candle methods, which rely on electromagnetic signals and complex calibration processes, gravitational waves are self-calibrated. This has opened the era of the standard siren cosmology. Gravitational wave detections can be used to map the entire expansion history of the Universe, shedding light on the nature of dark matter and dark energy.

Their potential extends far beyond what we can observe electromagnetically. Light started providing information as soon as the Universe became transparent, a moment captured by the cosmic microwave background. With gravitational waves, we can probe the earliest moments of the cosmos, potentially offering insights into the inflationary period that followed the Big Bang.

By analyzing the propagation of gravitational waves across cosmic distances, we can test fundamental physics on scales that were once purely theoretical. This provides new constraints on theories of quantum gravity and potential deviations from Einstein's theory of General Relativity.

Gravity and electromagnetism are the only two interactions that shape our everyday lives on the human scale. We see the world around us thanks to light; our touch experience is electromagnetic interaction among atoms. On the other hand, gravity, simply put, is what keeps our feet on the ground and makes objects fall. However, even though gravity dominates on astrophysical scales and is responsible for galaxies, clusters, and the whole large-scale structure of the Universe, it is

the most elusive of interactions. It is the geometry of spacetime itself, shaped by the masses of all the objects in the Universe. Unlike electromagnetic waves, emitted by a broad range of astrophysical phenomena, gravitational waves require cataclysmic events, the most extreme conditions where spacetime is heavily perturbed. Gravitational waves offer us insights into the most violent processes in the Universe.

Electromagnetic waves set the foundation of our understanding of the Universe. Gravitational waves provide us with a new and complementary observation window. The future lies in a synergy between electromagnetic and gravitational wave observations, combined to decipher what is still beyond our reach.

This thesis finds its place in times of discoveries and great expectations. The new field of gravitational waves is blossoming, and the research directions are many and rather promising. We have more and more observations from the existing gravitational wave detectors, and we are already planning for future interferometers. At the time of this thesis, we are in the fourth observing run of data taking. Both the LIGO detectors in the USA and Virgo in Europe are active and detecting more and more mergers. The number of compact binary coalescences has overcome the first hundred events. Most of them are binary black holes; a few are binary neutron star - black hole systems, and two binary neutron stars, of which one only has an identified electromagnetic counterpart, `GW170817`.

In this work, we focus on cosmology and multi-messenger astrophysics. We explore the information from current data and carry out multiple forecast studies for the planned gravitational wave observatories represented by the Einstein Telescope. From the cosmology side, gravitational waves constitute a new probe that could eventually disentangle the tension in measuring the expansion of the Universe. The future is also bright from the electromagnetic side, with many planned observatories that could join the Einstein Telescope in studying the cosmos. With their enlarged bandwidth and sensitivity, the future interferometers represent the potential for unique and great science.

1. Where do we stand?

> *The past is the father of the present.*
>
> **— Agatha Christie**
> "Hallowe'en Party"

The following chapter provides a broad overview of where we stand with our understanding of the Universe from the cosmological and gravitational points of view. Among the key questions are: Where does the information come from? What are data telling us? What role do our assumptions play? What can we learn?
Despite significant progress, many longstanding and emerging questions remain unanswered. A pivotal development in recent history, however, the beginning of the gravitational wave (GW) astronomy, has provided us with a whole new observation point. This exploration began only a decade ago and has already led to significant advancements across fields, from astrophysics to nuclear physics to cosmology. Beyond that, there is much more we can do and plan to do with increasingly advanced detectors, ready to listen to the faintest sounds of the Universe.
This chapter is a working summary of much more detailed information provided in numerous books [Ryden, 1970; Misner et al., 1973; Dodelson and Schmidt, 2020; Baumann, 2022; Maggiore, 2007; Creighton and Anderson, 2011; Maggiore, 2018], and major discovery research papers we refer to throughout the text.

1.1 An expanding Universe

Our address starts from Earth, the third planet from our only star, the Sun, in the Solar System, orbiting in one of the spiral arms of the Milky Way, a vast galaxy containing hundreds of billions of stars. Our galaxy, in turn, groups with tens of other galaxies in the Local Group, which, together with thousands of more galaxies, builds an even bigger cosmic structure out to the whole observable Universe. Everything we observe and somehow understand, the ordinary matter, as well as the mysterious dark matter, exists in an expanding Universe. And the expansion, which is accelerating, is driven by what we refer to as dark energy.

To describe our Universe, we start in Sec. 1.1.1 with its geometry focusing on distance measurements. We relate the geometry with the energy budget in Sec. 1.1.2. An overview of the standard cosmological model is provided in Sec. 1.1.3 along with its primary problem, the Hubble tension, described in the dedicated Sec. 1.1.4.

Contents

1.1.1 *Isotropy and homogeneity*

Complex and intricate interactions among various phenomena define our Universe. However, suppose we simplify our perspective by treating entire galaxies as particles, ignoring that these particles have internal structures or group together in clusters. In that case, we can reveal the Universe's highly symmetric structure and describe it with a few fundamental principles [Misner et al., 1973]. From this large-scale viewpoint, the *Cosmological Principle* applies: the Universe is isotropic and homogeneous, meaning there are no special points or directions. There is evidence of homogeneity in the distribution of galaxies in the sky, and the Cosmic Microwave Background (CMB) provides us with remarkable evidence for isotropy.

From the geometrical point of view, assuming homogeneity and isotropy means idealizing that the curvature is the same everywhere. As a consequence, we have three possibilities: a positive curvature for a spherical Universe, a negative curvature for a hyperbolic Universe, or no curvature for a perfectly flat Universe. The metric that describes such a Universe is the Friedmann-Lemaitre-Robertson-Walker (FLRW) metric [Friedman, 1922; Lemaitre, 1927]:

$$ds^2 = -c^2dt^2 + a^2(t)dl^2, \tag{1.1}$$

where

$$dl^2 = \frac{dr^2}{1 - k\frac{r^2}{R_0}} + r^2 d\Omega^2 \quad \text{with} \quad k = \begin{cases} +1 & \text{spherical} \\ -1 & \text{hyperbolic} \\ 0 & \text{flat} \end{cases} \tag{1.2}$$

where thanks to isotropy, we have the radial coordinate r and the sphere element $d\Omega^2$ to express a position in space. $a(t)$, the scale factor, describes the expansion of the Universe and R_0 represents the curvature scale at the present time.

In Eq. (1.1), we distinguish the temporal separation between events $-c^2dt^2$ and the spatial one $a^2(t)dl^2$, dependent on the three possible geometries. The scale factor $a(t)$ accounts for the expansion of the Universe and relates comoving coordinates to the physical ones:

$$\vec{r}_{\text{physical}} = a(t)\vec{r}_{\text{comoving}} \tag{1.3}$$

The comoving coordinates are defined to evolve together with the Universe so that objects' positions stay fixed. Conventionally, we set that at present time $a(t_0) = 1$. Starting from Eq. (1.3), we can evolve the position of objects, e.g. a galaxy, in time and obtain the following

relation:

$$\begin{aligned}\frac{\mathrm{d}\vec{r}_{\text{physical}}}{dt} &= \frac{\mathrm{d}a}{\mathrm{d}t}\vec{r}_{\text{comoving}} + a(t)\frac{\mathrm{d}\vec{r}_{\text{comoving}}}{\mathrm{d}t} \\ &= \frac{\dot{a}}{a}a\vec{r}_{\text{comoving}} + a(t)\frac{\mathrm{d}\vec{r}_{\text{comoving}}}{\mathrm{d}t} \\ &= H\vec{r}_{\text{physical}} + \vec{v}_{\text{peculiar}}\end{aligned} \tag{1.4}$$

where we have defined the Hubble parameter:

$$H \equiv \frac{\dot{a}}{a} \tag{1.5}$$

$H\vec{r}_{\text{physical}}$ is known as the *Hubble flow*, i.e. the velocity resulting from the expansion of space, and $\vec{v}_{\text{peculiar}}$ is the velocity measured by an observer who is comoving with the Hubble flow. The value of the Hubble parameter today $H(t_0) = H_0$ is known as the Hubble constant. It is customary to define its dimensionless version as:

$$h_0 = \frac{H_0}{100\,\text{km s}^{-1}\text{Mpc}^{-1}} \tag{1.6}$$

Equivalently, $h = H/100\,\text{km s}^{-1}\,\text{Mpc}^{-1}$.

Because of the expansion, any wavelength we receive is stretched by the scale factor with respect to the emitted one. Therefore, we can define the cosmological redshift z as:

$$1 + z = \frac{1}{a(t)} \tag{1.7}$$

with $a(t)$ the scale factor at the emission time. For very low values of $z \ll 1$, we can expand around $t = t_0$[1] and get the Hubble-Lemaitre law [Lemaitre, 1927; Hubble, 1929]:

$$z \sim \frac{d}{c}H_0 \implies v \sim cz \sim H_0 d, \tag{1.8}$$

where d is the physical distance (also called proper distance) from us to the observed object (see also Eq.(1.3)), and c is the speed of light. From now on, we will refer to distance quantities using the d notation. v is also known as recessional velocity, i.e. the velocity at which every object is moving away from an observer because of the expansion of the Universe. For small redshifts it holds that $v \sim cz$.

There are several definitions of distance in cosmology, and we use them depending on the problem we want to describe [Dodelson and Schmidt, 2020]. In what follows, we assume $k = 0$, as observations are consistent with a spatially flat Universe (see Sec. 1.1.3).

- *Comoving distance:* From the FLRW metric in Eq. (1.1), and as a function of redshift, we can write the comoving distance as:

$$d_{\text{comoving}} = \int_0^z \frac{cdz'}{H(z')} \tag{1.9}$$

[1] We start by expanding $a(t)$ around the present time t_0:

$$\begin{aligned}a(t) \sim& a(t_0) + (t - t_0)\frac{da}{dt}|_{t_0} \\ &= a(t_0) + (t - t_0)\frac{\dot{a}(t_0)}{a(t_0)} \\ &= 1 + (t - t_0)H_0,\end{aligned}$$

where we have used the fact that at present time $a(t_0) = 1$ and $\frac{\dot{a}(t_0)}{a(t_0)} = H_0$ as from Eq. (1.5). From Eq. (1.7), we can then write:

$$\begin{aligned}1 + z = \frac{1}{a(t)} &\sim \frac{1}{1 + (t - t_0)H_0} \\ &\sim 1 - (t - t_0)H_0 \\ &= 1 + (t_0 - t) \sim 1 + \frac{d}{c}H_0,\end{aligned}$$

where $(t_0 - t)$ is the difference between the present time and the time when the light was emitted (lookback time), and for $z \ll 1$, it can be approximated as $t_0 - t = \frac{d}{c}$.

It is useful when we are interested in the conformal time[2] required for radial propagation of light from the object to us.

- *Angular diameter distance:* When we know the transverse physical size L of an object on the sky, then we can write its angular size as:

$$\Delta\theta \sim \frac{L}{d_{\text{physical}}(z)} \tag{1.10}$$

assuming that $\Delta\theta \ll 1$. We have already shown the relation between comoving and physical distance in Eq. (1.3). Given its importance related to angular measurements, we also call it the angular diameter distance:

$$d_A(z) \equiv d_{\text{physical}}(z) = \frac{d_{\text{comoving}}}{1+z} \tag{1.11}$$

- *Luminosity distance:* When we know the intrinsic luminosity of an object, we can define its luminosity distance based on the observed luminosity:

$$d_L(z) = (1+z) d_{\text{comoving}} \tag{1.12}$$

In Fig. 1.1, we show the three distances as from Eq. (1.9), Eq. (1.11) and Eq. (1.12), as a function of redshift. We assume the standard Planck18 [Aghanim et al., 2020] cosmology (see next sections). We want to highlight how, at low z, the three functions coincide and agree with the Hubble law as in Eq. (1.8).

[2] Conformal time η is a definition of time rescaled by the scale factor as

$$d\eta = \frac{dt}{a(t)}$$

Integrated, it corresponds to the comoving distance divided by the speed of light.

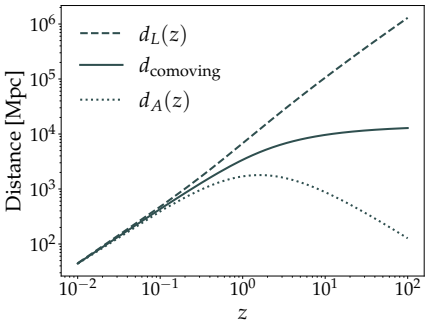

Figure 1.1: Different distance definitions, comoving, angular diameter, and luminosity distance, as a function of redshift, assuming Planck18 cosmology

1.1.2 *Universe's energy composition*

All the equations in Sec. 1.1.1 have been derived based on geometrical assumptions and under Einstein's theory of General Relativity (GR) [Einstein, 1916]. The FLRW metric in Eq. (1.1) is an exact solution of the Einstein's equations:

$$G_{\mu\nu} + \Lambda g_{\mu\nu} = \frac{8\pi G}{c^4} T_{\mu\nu}, \tag{1.13}$$

where $G_{\mu\nu}$ is the Einstein tensor, $g_{\mu\nu}$, the metric tensor, and $T_{\mu\nu}$ the stress-energy tensor. $T_{\mu\nu}$ describes the energy content that shapes the geometry of spacetime. G is the Newton's gravitational constant, and Λ the cosmological constant.

If in Sec. 1.1.1, we focus on $G_{\mu\nu}$, this section deals with the Universe's energy content, $T_{\mu\nu}$ and Λ, which governs the dynamics of the scale factor. When characterizing the large-scale behavior of matter and energy in the Universe, we idealize them as perfect fluids described only by their energy density and pressure. From the conservation of the stress-energy tensor, $\Delta_\mu T^\mu_\nu = 0$, we get the following continuity equation:

$$\dot{\rho} + 3\frac{\dot{a}}{a}\left(\rho + \frac{P}{c^2}\right) = 0 \tag{1.14}$$

where ρ identifies the different energy density components and P is the pressure term. Eq. (1.14), can be rewritten using the Equation of State (EoS) parametrization $\omega = P/\rho c^2$:

$$\frac{\dot{\rho}}{\rho} = -3(1+\omega)\frac{\dot{a}}{a}, \tag{1.15}$$

which solution can be written as:

$$\rho = a^{-3(1+\omega)} \tag{1.16}$$

From Eq. (1.13), we can derive the Friedmann equations [Friedman, 1922; Friedmann, 1924] linking the energy budget to the dynamics:

$$\begin{aligned} \left(\frac{\dot{a}}{a}\right)^2 &= \frac{8\pi G}{3}\rho - \frac{\Lambda c^2}{3} \\ \frac{\ddot{a}}{a} &= -\frac{4\pi G}{3}\left(\rho + \frac{3P}{c^2}\right) \end{aligned} \tag{1.17}$$

Eqs. (1.17), together with the continuity equation Eq. (1.16), describe how the scale factor evolves with time. The different energy density components entering the dynamics, according to the standard ΛCDM model (see Sec. 1.1.3) are:

- *Matter*: comprises baryonic matter, i.e., the ordinary matter, made up of electrons, protons, and neutrons; and dark matter (DM), all the matter that is not baryonic. It only interacts gravitationally, henceforth dark
- *Radiation*: the photon content
- *Dark energy*: energy content introduced to justify the Universe's accelerated expansion. It acts as a fluid with energy density $\rho_\Lambda = \Lambda/8\pi G$

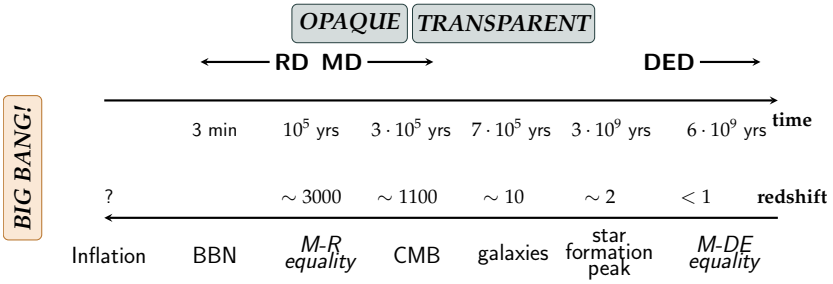

Figure 1.2: A schematic representation of the milestones in the Universe's history. Shortly after the Big Bang, the Universe is opaque and radiation-dominated. The Universe becomes transparent when the temperatures cool down for photons to move freely. A record of this is the CMB relic. After that, the matter domination (MD) era starts, until very recently, when the dark energy causing the accelerated expansion is prevailing. Freely adapted from Fig.1.1 in [Dodelson and Schmidt, 2020]

The different components affect the Universe's evolution differently at different moments of its history. In Fig. 1.2, we show a schematic representation of the milestones in the Universe's history. The origins

of our Universe are described by the hot Big Bang model, described as an energetic explosion that initiates the evolution of the Universe as we know it today. Shortly after the Big Bang, the temperatures are extremely high and the Universe is opaque. It is the radiation domination (RD) era. When the temperatures cool down, photons start moving freely, and the Universe becomes transparent. A record of this is the CMB relic. After that, it is the turn of the matter domination (MD) era, which lasts until very recently, when the dark energy causing the Universe's accelerated expansion takes over. Now we are in the dark energy domination (DED) era.

Usually, these components are expressed as a dimensionless ratio of their present value with respect to what is called the critical energy density, i.e. the energy density required to have a flat Universe:

$$\rho_{\text{crit},0} = \frac{3H_0^2}{8\pi G} \tag{1.18}$$

In this way, we can define the abundance parameters today as:

$$\Omega_i = \frac{\rho_{i,0}}{\rho_{\text{crit},0}} \tag{1.19}$$

In Fig. 1.3, we show the composition of the Universe's energy content today. According to the ΛCDM model, the baryonic matter accounts for the $\sim 5\%$ of the energy, the DM for the $\sim 27\%$, and the dark energy (DE) for the remaining 68%.

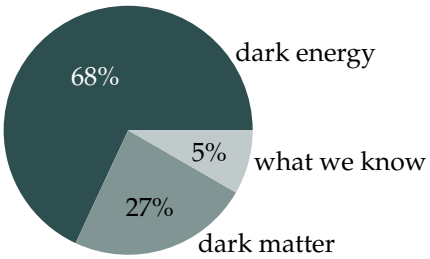

Figure 1.3: A diagram of the Universe's composition

Combining Eq. (1.19), together with Eq. (1.5) and Eq. (1.7), we can write Eq. (1.17) as:

$$H(z) = H_0\sqrt{\Omega_m(1+z)^3 + \Omega_r(1+z)^4 + \Omega_\Lambda}. \tag{1.20}$$

Given the subdominant role of radiation today, we can simply write:

$$H(z) = H_0\sqrt{\Omega_m(1+z)^3 + \Omega_\Lambda} \tag{1.21}$$

The flatness condition ensures that:

$$\Omega_m + \Omega_\Lambda = 1 \tag{1.22}$$

In the following sections and chapters, when we say we want to infer cosmological parameters, we refer to H_0 and Ω_m under the assumption of the basic ΛCDM model. It is noteworthy to mention that, a straightforward extension of the ΛCDM model, relaxes the assumption that ω, as introduced in Eq. (1.16), is a constant (equal to -1) and treats it as a free parameter:

$$H(z) = H_0\sqrt{\Omega_m(1+z)^3 + \Omega_\Lambda(1+z)^{3(1+w)}} \tag{1.23}$$

This is referred to as ωCDM model.

1.1.3 *The standard cosmological model*

Modern cosmology is based on the ΛCDM model. The standard cosmological model successfully explains many observed phenomena in our Universe, including its late-time accelerated expansion and the presence of the CMB. ΛCDM states that the present Universe is described by non-baryonic cold DM and a cosmological constant. All the structures we observe today are generated during an inflationary period at very early times (see Fig. 1.2). In the following, we review the principles on which ΛCDM is based:

- The *cold* part of the DM component is required for DM particles to manage to cluster efficiently in the early Universe. We have evidence of DM coming from observations of rotation curves of galaxies [Rubin, 1983], galaxy velocities within clusters [Zwicky, 1933], and lensing effects [Clowe et al., 2006]. Moreover, its presence is required to justify the structures in the Universe. Without DM, the Universe would have been much smoother. There are several candidates to describe DM [Lin, 2019]. The most popular idea is that DM consists of some kind of elementary particles produced at the early stages of the Big Bang.

- The *cosmological constant* Λ is introduced in accordance with the evidence suggesting that there must be some dark energy that causes the accelerated expansion of the Universe [Riess et al., 1998; Perlmutter et al., 1999]. At the quantum level, we can think of empty space itself as a source of energy for expansion. However, calculations done in quantum field theory on the expectation value of these quantum fluctuations disagree by ~ 120 orders of magnitude with what is required to explain cosmological observations.

- The *inflationary* period is required in the ΛCDM model to generate the initial perturbations that eventually evolve in the structures we observe today. Inflation occurs for a brief time in the very early Universe and causes the scale factor to grow exponentially.

The simplest version of the ΛCDM model has six parameters:

$$\{A_s, n_s, H_0, \omega_m, \omega_b, z_{re}\}, \tag{1.24}$$

where A_s is the amplitude of scalar perturbations, n_s the scalar spectral index, H_0 the Hubble constant, $\omega_m = \Omega_m h_0^2$ the cold DM density, $\omega_b = \Omega_b h_0^2$ the baryon density, and z_{re} the redshift at which the Universe is half reionized after the formation of the first generation of stars. Some simple extensions of ΛCDM include a non-vanishing curvature or neutrino masses.

ΛCDM is the standard cosmological model because it has shown remarkable agreement with complementary data sets. It is outstanding

that with just six parameters, we are able to fit exceptionally well the thousands of CMB multipoles, Baryonic Acoustic Oscillations (BAO) data[3], SNe observations, and structure formation data. As for the latter, the most straightforward description of the Universe starts very smoothly. The primordial perturbations are produced and expanded during inflation. These small perturbations grow during the MD era. In this period, DM simply clusters because of the nature of gravity. Eventually, in recent times, these perturbations stop being small and become the non-linear structures that we observe today. Moreover, ΛCDM successfully describes the relative abundances of light elements formed during the period of Big Bang Nucleosynthesis (BBN).

[3] BAO are the result of the coupled acoustic oscillations of baryons and photons before decoupling, leaving a distinct imprint on the observed matter power spectrum.

However, despite its success in describing our Universe's composition, structure, and evolution, the ΛCDM model faces significant challenges that could reshape our understanding of fundamental physics. The most striking one we will focus on in the next Sec. 1.1.4 is the so-called Hubble tension.

1.1.4 *The Hubble tension*

The discovery of the Universe's expansion by Hubble [Hubble, 1929] can be classified as one of the most significant breakthroughs in astrophysics. Since then, determining the Hubble constant has been one of the primary goals in cosmology. Several measurements have been carried out, using many different methods, to point to an unresolvable, at least yet, tension, dubbed the Hubble tension.

We can distinguish two categories of measurements: the indirect ones based on probes from the early Universe and the direct ones based on probes in our local Universe. The Hubble tension is a discrepancy between the locally measured and the cosmological inferred expansion rate.

In Fig. 1.4, we list some measurements diving into the local and early Universe probes. Many papers [Bernal et al., 2016; Verde et al., 2019; Knox and Millea, 2020; Di Valentino, 2021; Di Valentino et al., 2021; Shah et al., 2021; Kamionkowski and Riess, 2023] have been produced on the matter, and we refer to those for a thorough discussion. In a nutshell, as also from Fig. 1.4, we highlight two measurements that recently became so precise to manifest a $\sim 5\sigma$ tension:

- Measurements from CMB [Aghanim et al., 2020] report:

$$H_0 = 67.49 \pm 0.53 \,\mathrm{km\ s^{-1} Mpc^{-1}} \tag{1.25}$$

- Measurements from predominantly the local distance ladder [Riess et al., 2021], instead, read:

$$H_0 = 73.04 \pm 1.04 \,\mathrm{km\ s^{-1} Mpc^{-1}} \tag{1.26}$$

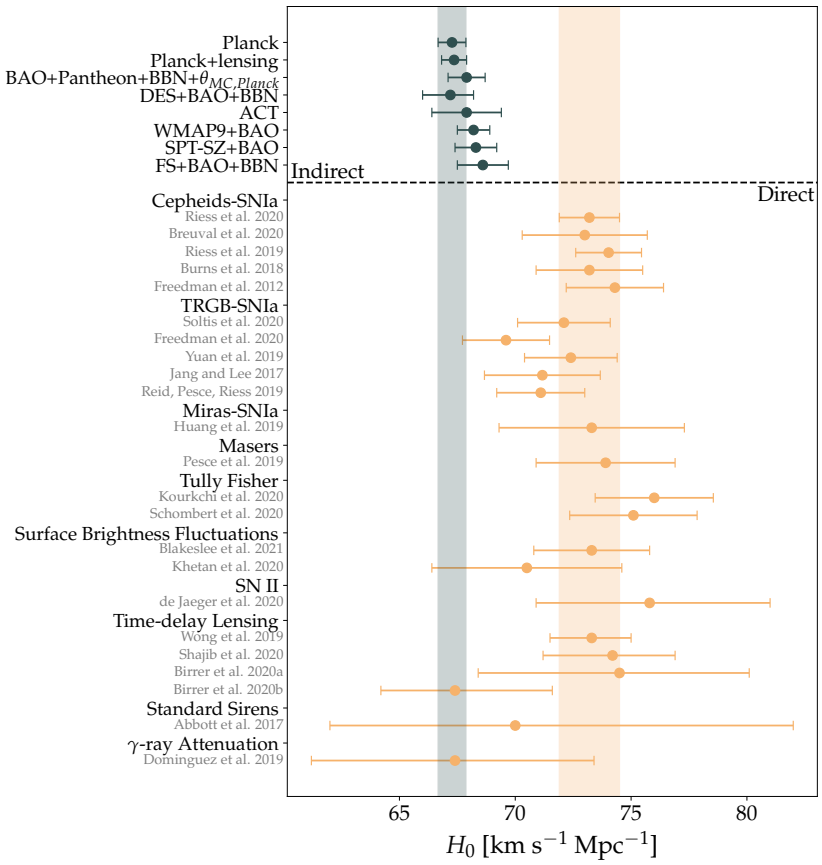

Figure 1.4: Tension in years from different methods. Figure adapted from Fig.1 in [Di Valentino, 2021]. A more extended plot can be found in a subsequent review by the same author [Di Valentino et al., 2021].

From a historical point of view, we show in Fig. 1.5 the time evolution, as a function of the year of publication, of the value of the Hubble constant and its uncertainty. The figure shows how the tension becomes evident very recently, thanks to the enhanced precision of the measurements.

The lower value of H_0 comes from the temperature and polarization fluctuations measurements in the CMB. Within the ΛCDM model, we try to fit the observed data to the model, and H_0 is one of the free parameters. Instead, the higher H_0 value is a direct measurement obtained using the recessional velocities, i.e. the distance to the standard candle and the redshift of the host galaxy. As already said, the biggest challenge is to measure distances. In the standard candle approach, the galaxy distance is inferred from the apparent brightness of a standard candle, the Type Ia SNe. Standard candles rely on a complex calibration process. Possible systematic errors have been carefully checked and ruled out. The discrepancy between the two approaches might be a hint to models beyond the standard cosmological ΛCDM model.

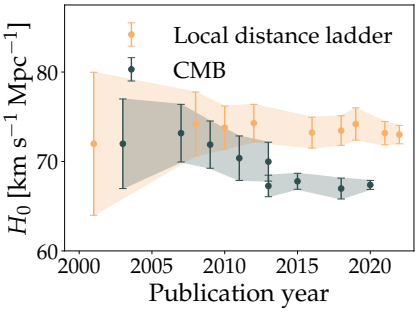

Figure 1.5: Time evolution of the H_0 tension: precision of the measurements as a function of the publication year. Adapted from Fig.1 in [Hu and Wang, 2023].

There have been, for example, proposals for modifications of the early Universe dynamics [Karwal and Kamionkowski, 2016; Poulin et al., 2018]. However, at the current status, CMB data are not precise enough to distinguish between ΛCDM and alternative models [Kamionkowski and Riess, 2023].

Among many promising research directions, the recent discovery of Gravitational waves (GWs) [Abbott et al., 2016b] might also shed some light on the Hubble tension question. This is discussed in Chapter 2. The thesis aims to explore this new probe and discuss the potential astrophysical and cosmological information in the GW data. In the remaining part of this chapter, we provide a broad introduction to the GW field, from theory to main sources to detection, with both current and future interferometers.

1.2 *The gravitational wave (GW) window*

September 14, 2015, marks the birth of gravitational wave (GW) astronomy. For the very first time, the gravitational signal coming from the merger of two black holes (BHs) has been detected by the two Laser Interferometer Gravitational-wave Observatory (LIGO) interferometers [Abbott et al., 2009]. `GW150914` [Abbott et al., 2016b] is the merger of two BHs, of $36M_\odot$ and $29M_\odot$, at a distance of roughly 400 Mpc from us, which corresponds to a redshift of 0.09.

GWs are a prediction of the theory of GR [Einstein, 1916]. These are disturbances of the spacetime geometry that propagate almost undisturbed at the speed of light. GR is a unified theory that encompasses the Newtonian law of gravitation and special relativity into a unique geometrical framework. Gravity is a geometrical description of spacetime, $G_{\mu\nu}$, in the presence of a distribution of matter, $T_{\mu\nu}$. Accelerating masses in a non-axisymmetric configuration emit GWs.

The first indirect evidence of GWs dates back to [Hulse and Taylor, 1975] and the observation of the binary system `PSR B1913+16`, composed of a neutron star (NS) and a pulsar orbiting around the common center of mass. Hulse and Taylor discovered that the observed orbital decay of the binary system is in precise agreement with the energy loss due to GWs.

However, given their extremely small amplitude, one century has passed between prediction and direct detection of GWs. Even the most violent processes, such as the merger of two BHs, produce a strain, i.e. a relative change in length due to the passage of the GW, of the order of 10^{-21}. Thanks to the advances in precision measurements, we are now able to measure GWs using laser interferometers. Currently, we have two GW interferometers in the USA, with two perpendicu-

lar arms of 4 km each, one located in Hanford and the other in Livingston. A third interferometer, Virgo, with arms of 3 km is operative in Cascina, Italy. A fourth 3 km arm detector, Kamioka Gravitational Wave Detector (KAGRA), is located in Japan but not always operative alongside the other three. Another LIGO detector will be built in India, LIGO-India, in the near future.

The birth of GW astronomy allows us to study and test a plethora of gravitational phenomena. On top of this, on August 17, 2017, the GW interferometers detected a new signal that set yet another milestone. The event `GW170817` [Abbott et al., 2017c] is the merger of two NSs, accompanied by the detection of both the kilonova (KN) and the short Gamma Ray Burst (GRB) signals. `GW170817` is the start of the multi-messenger (MM) astronomy era.

Since then, we have completed three observing runs [Abbott et al., 2019b, 2021a, 2023b] and are currently taking data for the fourth observing run. We now have more than one hundred events, mostly Binary Black Holes (BBHs), a couple of Neutron Star - Black holes (NSBHs), and two Binary Neutron Stars (BNSs), even though just `GW170817` with an electromagnetic (EM) counterpart. Given the increasing statistics, we are entering the era of population studies.

Current detectors have limited sensitivity. For more than a decade now, the scientific community has been planning the next-generation (XG) of GW ground-based interferometers, like the Einstein Telescope (ET) [Sathyaprakash et al., 2012; Maggiore et al., 2020] and the Cosmic Explorer (CE) [Evans et al., 2021, 2023; Kalogera et al., 2021]. XG detectors are one order of magnitude more sensitive, as shown in Fig. 1.6 where we compare the sensitivity[4] of the Hanford interferometer at the time of the first detection and the planned sensitivity for ET.

In what follows, we provide a brief derivation of the GW equations starting from the linearized GR theory in Sec. 1.2.1. In Sec. 1.2.2, we describe the main sources producing GWs, focusing in particular on compact binary coalescences (CBCs). Sec. 1.2.3 is dedicated to detecting GWs. Then, in Sec. 1.2.4, we focus on the current GW detectors, providing a summary of the observing runs and detected events. Last, Sec. 1.2.5 introduces the planned future ground-based GW interferometers.

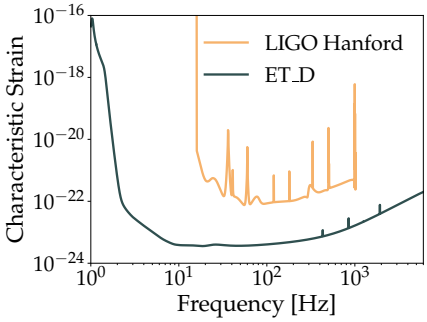

Figure 1.6: Comparison between the sensitivity curve of the LIGO Hanford interferometer at the time of the first detection, `GW150914`, and the planned sensitivity curve for the ET

[4] In Fig. 1.6, we plot on the y-axis a quantity called characteristic strain. For its definition, we refer to the explanation box in Sec. 3.4.2.

1.2.1 *GW theory in brief*

Starting from Einstein's equations as in Eq. (1.13), GWs are obtained as a solution to their linearized form [Maggiore, 2007]. Far away from dense objects, in fact, gravity is weak, and the metric tensor $g_{\mu\nu}$ can be viewed as a sum of a flat background metric $\eta_{\mu\nu}$ plus a small pertur-

bation $|h_{\mu\nu}| \ll 1$:

$$g_{\mu\nu} = \eta_{\mu\nu} + h_{\mu\nu}. \tag{1.27}$$

In order to simplify Einstein's equations, it is convenient to work in the so-called harmonic gauge[5], and with the trace-reversed metric perturbation:

$$\bar{h}_{\mu\nu} \equiv h_{\mu\nu} - \frac{1}{2}\eta_{\mu\nu}h, \tag{1.28}$$

where the trace is defined as:

$$h = \eta^{\mu\nu}h_{\mu\nu}. \tag{1.29}$$

Under these conditions, Eq. (1.13) and Eq. (1.27) reduce to a single wave equation combined with the harmonic gauge condition:

$$\begin{cases} \Box\bar{h}_{\mu\nu} = -\frac{16\pi G}{c^4}T_{\mu\nu} \\ \partial^\nu h_{\nu\alpha} = 0 \end{cases} \tag{1.30}$$

where $\Box$ is the d'Alembertian operator defined as:

$$\Box = -\frac{1}{c^2}\partial_t^2 + \nabla^2. \tag{1.31}$$

Outside the source, which is where the propagation of GWs happens, $T_{\mu\nu} = 0$, and we get the wave equation:

$$\Box\bar{h}_{\mu\nu} = 0 \tag{1.32}$$

We obtain that a perturbation of a flat spacetime propagates as a wave traveling at the speed of light. Therefore, we have shown that Einstein's theory predicts GWs. The simplest solution of the wave equation, Eq. (1.32), in vacuum is a monochromatic plane wave:

$$\bar{h}_{\mu\nu} = A_{\mu\nu}e^{ik_\alpha x^\alpha}, \tag{1.33}$$

where $A_{\mu\nu}$ is the polarization tensor, i.e., it contains information on the wave amplitude and polarizations, whereas k_α is the wave quadrivector, $k^\mu = (\omega/c, \vec{k})$.

Notice that we start with a symmetric 4×4 matrix $h_{\mu\nu}$. Imposing the gauge condition reduces the number of independent components to six. Furthermore, there is some residual symmetry, as the gauge condition holds under a further coordinate transformation, $x'^\mu = x^\mu + \xi^\mu$ as long as $\Box\xi^\mu = 0$. This allows us to impose four additional conditions on $h_{\mu\nu}$, which define the so-called Transverse-Traceless (TT) gauge.

In the TT gauge, and assuming that the propagation of the wave is along the z-axis, we can write the plane wave solution:

$$h^{TT}_{\mu\nu} = \begin{pmatrix} 0 & 0 & 0 & 0 \\ 0 & h_+ & h_\times & 0 \\ 0 & h_\times & -h_+ & 0 \\ 0 & 0 & 0 & 0 \end{pmatrix} \cos(\omega(t - \frac{z}{c})). \tag{1.34}$$

[5] In the harmonic gauge, the following condition holds:

$$\partial^\nu\bar{h}_{\nu\alpha} = 0$$

It is also called Lorentz gauge in analogy with the Lorentz gauge in electromagnetism.

A GW has only two physical degrees of freedom corresponding to the two possible polarization states. The gauge in which this is manifest is the TT gauge. Here, the components of $h_{\mu\nu}$ are different from zero only on the plane orthogonal to the direction of propagation; hence, transverse; and $h_{\mu\nu}$ is traceless. Fig. 1.7 illustrates the two independent polarizations of a GW. Between the two, there is a $\pi/2$ phase shift.

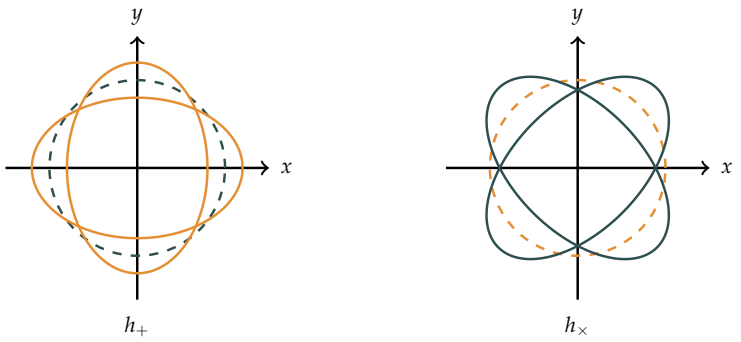

(a) Plus polarization (b) Cross polarization

Figure 1.7: Polarizations of a gravitational wave signal. Effect on a circle of test particles.

We can write a rather general form for Eq. (1.33), considering slowly moving, i.e. $v \ll c$, sources, and GWs propagating radially outward from the source:

$$h_{ij}(t,r) \sim \frac{2}{r}\frac{G}{c^4}\frac{\mathrm{d}^2}{\mathrm{d}t^2}\mathcal{Q}_{ij}(\omega(t-\frac{r}{c})), \tag{1.35}$$

where r is the distance between the source and the observer, the luminosity distance, as the one defined in Eq. (1.12), and $\mathcal{Q}_{ij}$ is the second mass moment, defined as:

$$\mathcal{Q}^{ij} = \int d^3\vec{x}\rho(t,\vec{x})x^i x^j, \tag{1.36}$$

with $\rho(t,\vec{x})$ the density. Notice the quadrupolar nature of GWs: if there is no second time-derivative variation of the quadrupole moment, there are no GWs[6]. The quadrupole moment is constant for a stationary and spherical axisymmetric distribution of matter. To produce GWs, we need a certain degree of asymmetry: non-radial pulsation of stars, non-spherical gravitational collapse, and coalescence of massive bodies.

In the box below, we provide a simple derivation of the GW strain from an equal-mass binary system. We provide further details working in the frequency domain in the next Sec. 1.2.3. Specifically, we will discuss the parameters entering in the description of a GW signals, both at the source and at the detector, along with the basics of GW data analysis.

[6] We can also define a dipole moment for a system of masses:

$$\vec{\mathcal{D}}_G = \sum_i m_i\vec{x}_i$$

which satisfies the conservation law of the total momentum of an isolated system:

$$\frac{\mathrm{d}^2}{\mathrm{d}t^2}\vec{\mathcal{D}}_G = 0$$

For this reason GWs do not have a dipolar contribution.

Example of GWs from a binary system

Suppose we have a binary system in the xy plane with orbital angular momentum along z, and $2a$ the orbital separation with a the semi-major axis. The binary describes the angle $\omega_{\rm orb}t$ during the motion. We can assume that both members have mass m and also assume zero eccentricity.
We need to take the second time derivative of the quadrupolar mass moment. The density of the system can be described by:

$$\rho(t,\vec{x}) = \sum_{i=1}^{2} c^2 m_i \delta(x-x_i)\delta(y-y_i)\delta(z), \tag{1.37}$$

since the masses are in the xy plane, and $m_1 = m_2 = m$. The components of the quadrupole are:

$$\begin{aligned} \mathcal{Q}^{xx} &= 2ma^2\cos^2(\omega_{\rm orb}t) = ma^2[1+\cos(2\omega_{\rm orb}t)] \\ \mathcal{Q}^{xy} &= 2ma^2\sin(\omega_{\rm orb}t)\cos(\omega t) = ma^2\sin(2\omega_{\rm orb}t) \\ \mathcal{Q}^{yy} &= 2ma^2\sin^2(\omega_{\rm orb}t) = ma^2[1-\cos(2\omega_{\rm orb}t)] \end{aligned} \tag{1.38}$$

The second time derivative is then:

$$\bar{h}^{ij} \sim -\frac{2}{r}\frac{G}{c^4}(2\omega_{\rm orb})^2 ma^2 \begin{pmatrix} \cos(2\omega_{\rm orb}(t-\frac{r}{c})) & \sin(2\omega_{\rm orb}(t-\frac{r}{c})) & 0 \\ \sin(2\omega_{\rm orb}(t-\frac{r}{c})) & -\cos(2\omega_{\rm orb}(t-\frac{r}{c})) & 0 \\ 0 & 0 & 0 \end{pmatrix} \tag{1.39}$$

Notice from Eq. (1.39), the frequency of GWs is twice the orbital frequency. Using the Kepler's third law, $\omega_{\rm orb}^2 = \frac{G2m}{a^3}$, we can write the two polarizations:

$$\begin{aligned} h_+ &\sim \frac{16G^2}{c^4}\frac{m^2}{ra}\cos(2\omega_{\rm orb}(t-\frac{r}{c})) \\ h_\times &\sim \frac{16G^2}{c^4}\frac{m^2}{ra}\sin(2\omega_{\rm orb}(t-\frac{r}{c})) \end{aligned} \tag{1.40}$$

We can also derive the amplitude of GWs:

$$h = \frac{1}{2}\left(h_+^2 + h_\times^2\right)^{1/2} \sim \frac{8G^2}{c^4}\frac{m^2}{ra} \sim 10^{-21}\left(\frac{m}{M_\odot}\right)^2\left(\frac{1\text{kpc}}{r}\right)\left(\frac{1R_\odot}{a}\right) \tag{1.41}$$

h is called the GW strain and in time domain it is dimensionless.
From Eq. (1.41), we can see that for typical values of a binary system, the GW amplitude is of the order of 10^{-21}.

1.2.2 *Sources of GWs: CBCs*

In the previous section, we have seen that to produce GWs, we need non-axisymmetric systems with a time-varying quadrupole moment. However, given the small amplitude of the GW strain, because of the G^2/c^4 suppression as from Eq. (1.41), only massive and quickly accelerating systems are able to produce a detectable GW signal.

We distinguish between four possible sources of GWs:

- *compact binary coalescences (CBCs)*: this type of source is the focus of this thesis. Compact binaries are pairs of compact objects, like

BHs or NSs. They can form three different compact binary systems: BBHs, BNSs, and NSBHs. The gravitational signal differs among them, with some common features. The GW emission is divided into three phases. The longest phase is the *inspiral* phase, where the two objects are orbiting each other. Because of the emission of GWs, they lose energy and shrink their orbit, with the gravitational emission increasing in amplitude and frequency, until the *merger* occurs. The result is a remnant compact object, either a BH or a NS, that, shortly after the merger, undergoes the *ringdown* phase of damped oscillations until settling into stability.

- *Continuous GWs*: these are expected to be produced by single spinning massive objects such as NSs with a certain degree of asymmetry

- *Burst GWs*: these come from short-duration sources, like hyperbolic encounters between a single BH and a binary [Codazzo et al., 2023, 2024].

- *Stochastic GWs*: these are produced by the incoherent superposition of signals emitted by different GW sources, either primordial or astrophysical, that we might detect but cannot singularly resolve.

This thesis focuses on GW signals from stellar mass CBCs. We outline the main formation channels for BHs and NSs in what follows. Depending on the formation history, the resulting systems have different properties. Conversely, these are precisely the properties we want to infer at the population level from GW data to reconstruct the formation channels.

Compact objects, either BHs or NSs, form at the end of the life cycle of massive enough stars [Prialnik, 2010]. One of the critical ingredients determining the final fate is the mass evolution of the progenitor. The mass evolution is an intricate play between metallicity, stellar winds, and binary mass transfer. As a rule of thumb, the lower the metallicity[7], the lower the mass lost due to the wind, and the more massive the remnant [Vink et al., 2001; Heger et al., 2003; Belczynski et al., 2010; Mapelli et al., 2011; Fryer et al., 2012; Mapelli and Bressan, 2013; Spera et al., 2015; Chen et al., 2015].

[7] In astrophysics, metals are all the elements heavier than Helium.

In a nutshell, stars born larger than $8M_\odot$ might end their life with an explosion, depending on the binding energy of the star's layers. If the explosion occurs, i.e., we have the core-collapse SN, then some material is lost, and the remnant, which could either be a BH or a NS, is less massive. Instead, if we have a failed SN, we expect to produce BHs more massive than $30M_\odot$. The mechanisms are not yet fully understood [Spera et al., 2015].

A very interesting point is when we have a core-collapse SN, but some ejected material has not reached the escape velocity and falls back. In this situation, we might be able to produce remnants of mass in the $3-7M_{\odot}$, which might be very light BHs. However, not all models produce remnants in this mass range. Also, from the observational point of view, as we will see in Sec. 1.2.3, we do not find many objects in this mass range, known as the lower mass gap.

When the initial star is extremely massive instead, its fate depends on the mass of the Helium core the star can produce. If the Helium core is above the $64M_{\odot}$, we have a pair-instability SN that explodes without leaving a remnant. We have a core-collapse SN or a direct collapse if it is less massive. Pair-instability SN is the reason why we have an upper mass gap, in the range $60-120M_{\odot}$, in our observed data. This is also the reason why systems like `GW190521` [Abbott et al., 2020c] with component masses falling in the gap, are likely to be a second-generation merger.

Most massive stars come in binary systems, and the merging of binary systems is what we see with GW detectors. We distinguish two main formation channels that produce compact binary systems [Mapelli, 2020]:

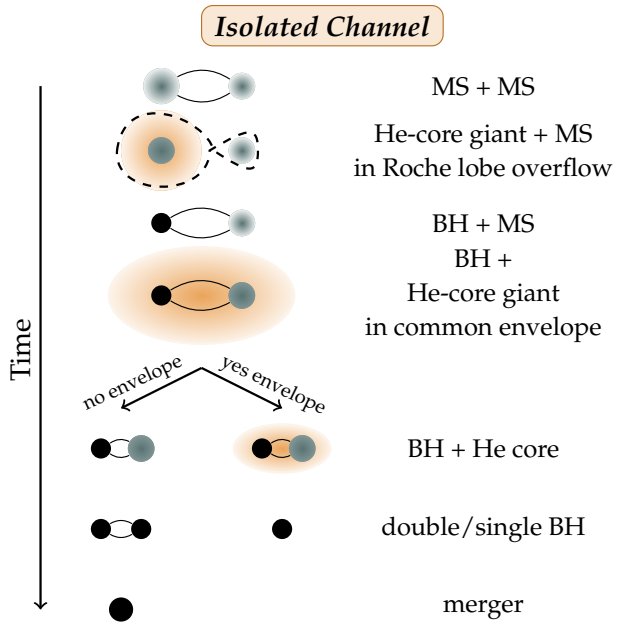

Figure 1.8: Isolated Channel: example of BBH formation through the isolated channel. Figure adapted from [Mapelli, 2020] (Figure 2, *left* panel).

- *Isolated channel*: as shown in Fig. 1.8, the evolution of a close binary star system is mainly influenced by mass transfer during the Roche lobe overflow and possibly the formation of a common envelope. The efficiency of the common envelope phase is what determines the successful formation of a compact binary. We will see its ap-

plication in Chapter 4. The compact binaries produced through the isolated channel have most likely similar masses and aligned spins. On the BBH side, the expected masses are in the $\sim 3 - 45 M_{\odot}$ range.

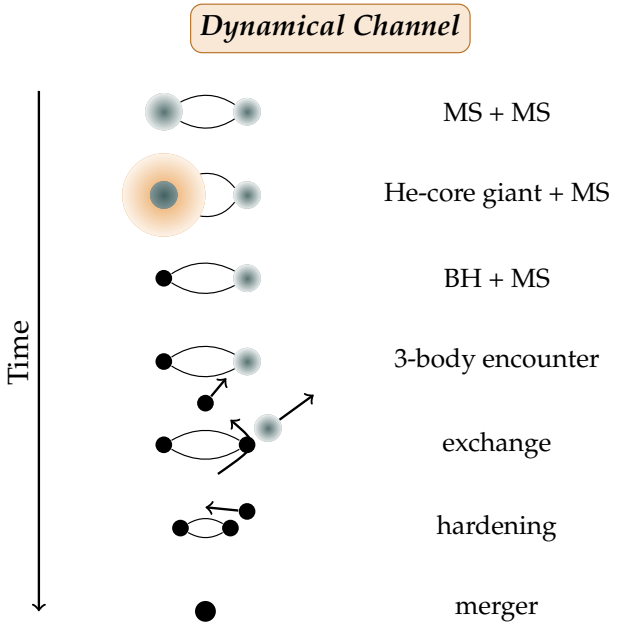

Figure 1.9: Dynamical Channel: example of BBH formation through the dynamical channel. Figure adapted from [Mapelli, 2020] (Figure 2, *right* panel)

- *Dynamic channel*: as shown in Fig. 1.9, a dynamical formation of a compact binary most likely happens in dense environments such as star clusters, where dynamical encounters with other objects in the cluster constantly perturb binary stars. BBHs formed through the dynamical channel are more massive than isolated BBHs and might even fall in the pair-instability mass gap as a result of hierarchical mergers. Additionally, the spins of dynamically formed compact binaries are randomized.

As we will see in Chapter 4 when modeling a population of compact binaries with population synthesis codes, like MOBSE [Mapelli et al., 2017; Giacobbo et al., 2018] or SEVN [Spera et al., 2019; Mapelli et al., 2020; Iorio et al., 2022], both channels are taken into consideration.

1.2.3 *GW detection*

This section restricts the detection and analysis methods of GW signals coming from CBCs. CBCs emit GWs at frequencies at which the current and the planned ground-based GW detectors are sensitive, i.e. from a few Hz to kHz (see box below).

The frequency of GWs

The link between the mass of a compact binary and the characteristic frequency at which it emits GWs is given by the dynamical frequency $f_{\rm dyn}$ of a self-gravitating system, and depends on its mean density [Schutz, 1997]:

$$f_{\rm dyn} = \sqrt{\frac{G\bar{\rho}}{4\pi}} \sim \left(\frac{GM}{16\pi R^3}\right)^{1/2}, \tag{1.42}$$

with M the total mass of the system and R its typical size. For a NS system, e.g., of a few $M_\odot$ and tens of km, $f_{\rm dyn}$ ∼kHz.
Notice that for a BBH, the typical size R is the Schwarzschild radius $R_S = \frac{2GM}{c^2}$. Therefore, the GW frequency scaling is inversely proportional to the system's mass:

$$f_{\rm dyn} \sim \frac{1}{M_{BBH}} \tag{1.43}$$

As a rule of thumb, the more massive the BH, the lower the frequency at which it emits GWs.
Different detectors are optimized for different frequency ranges. Terrestrial detectors, such as LIGO, Virgo, KAGRA, and the planned ET and CE, explore from Hz to kHz; proposals for lunar detectors as LGWA [Ajith et al., 2025] are thought for the dHz band, while space detectors as LISA [Karnesis et al., 2024] will go to the mHz regime.

The crucial problem in detecting GW signals is extracting them from the much larger detector noise in which they are buried. A GW detector is a Michelson-Morley interferometer, and what is being measured is the phase shift of the light recombined after traveling in the two arms.

We have seen in Sec. 1.2.1, that the GW signal is a tensor $h_{\mu\nu}$. At the input of the detector, it gets combined with the detector tensor D^{ij}, which depends on the detector's geometry, and generates a time-varying scalar quantity:

$$h(t) = D^{ij} h_{ij}(t) \tag{1.44}$$

The detector's output $s(t)$ is recorded as a time series and is a combination of the true signal $h(t)$ and noise $n(t)$:

$$d(t) = n(t) + h(t). \tag{1.45}$$

The noise generated inside a detector is characterized by a quantity called strain sensitivity, which we generally plot and refer to as the sensitivity curve. This is usually done in the frequency domain: under the assumption that noise is stationary so that the different Fourier components are uncorrelated, the detector's noise is defined as:

$$\langle \tilde{n}^*(f)\tilde{n}(f')\rangle = \delta(f - f')\frac{1}{2}S_n(f), \tag{1.46}$$

where $\tilde{n}(f)$ is the noise as a function of frequency, and $S_n(f)$ is the noise Power Spectral Density (PSD). Notice that the strain, either from

GWs or from noise, is dimensionless in the time domain and has the units of Hz^{-1} in the frequency domain. From Eq. (1.34), h_{ij} combines the two polarization modes. We can write them explicitly and characterize the detector geometry accordingly. Therefore, we can rewrite Eq. (1.44) in frequency domain as:

$$\tilde{h}(f) = \tilde{h}_+(f)F_+ + \tilde{h}_\times(f)F_\times, \tag{1.47}$$

where F_+ and $F_\times$ are the detectors' antenna pattern functions. These describe the detector's angular sensitivity; they depend on the detector geometry, the position of the source in the sky, the time of arrival of the event, and the polarization angle (see description below and in Tab. 1.1). Eq. (1.47) can be written in both the time and frequency domain. We will come back to this in Sec. 3.3.1.

In the following, given that in this thesis we work in the frequency domain, we provide the main equations describing the GW signal of a CBC in the frequency domain and the basics of its modeling.

The two polarizations of a GW signal, h_+ and $h_\times$ can be described in terms of spherical harmonics. We already stressed the quadrupolar nature of GWs, which correspond to the mode with $\ell = 2$ and $m = 2$. The other modes, generally called higher order modes, contribute at second order. Analytical expressions that describe the GW signal are called waveform approximants. The multipole expansion is equivalent to expanding Einstein's equation in the velocities of the components of the binary $[v/c]$, assuming that the sources are slowly moving. This is the Post-Newtonian (PN) approximation, and the order of the expansion is called the PN order, indicated as $[v/c]^{2\mathrm{PN}}$. At 1 PN order, the expansion stops at v^2/c^2. We refer to [Maggiore, 2007] for a comprehensive treatment. At the lowest PN order, and neglecting the contribution of spins, we can write the expressions for the two polarizations in the frequency domain:

$$\begin{aligned}\tilde{h}_+(f) &= \mathcal{A}(f, d_L, \mathcal{M}) \exp(i\psi(f, \mathcal{M})) \left[\frac{1+\cos^2(\iota)}{2}\right] \\ \tilde{h}_\times(f) &= \mathcal{A}(f, d_L, \mathcal{M}) \exp(\frac{\pi}{2} + i\psi(f, \mathcal{M})) \left[\cos(\iota)\right]\end{aligned} \tag{1.48}$$

where the amplitude $\mathcal{A}(f, d_L, \mathcal{M})$ is the same for the two polarizations. They are modified differently by the inclination angle ι dependence, and the corresponding phases $\psi(f, \mathcal{M})$ are shifted by $\pi/2$.

The GW amplitude, as a function of frequency, depends on the distance to the source and the detector-frame chirp mass $\mathcal{M}$:

$$\mathcal{A}(f, d_L, \mathcal{M}) \propto \frac{1}{d_L} \frac{(G\mathcal{M})^{5/6}}{f^{7/6}} \tag{1.49}$$

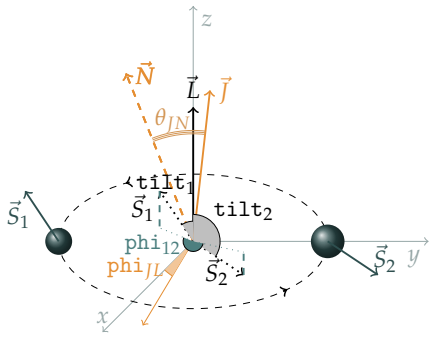

Figure 1.10: Schematic view of relevant angular parameters. $\vec{N}$ is the line of sight, connecting the center of Earth to the center of the elliptic orbit. $\vec{L}$ is the orbital angular momentum of the binary, perpendicular to the orbital plane. $\vec{S}_1$ and $\vec{S}_2$ are spin components, with dimensionless magnitude proportional to $a_1 \propto |\vec{S}_1|$ and $a_2 \propto |\vec{S}_2|$. $\mathtt{tilt}_1$ and $\mathtt{tilt}_2$ are the angles between $\vec{L}$ and single spin vectors, respectively. $\mathtt{phi}_{JL}$ is the angle between $\vec{L}$ and the total momentum $\vec{J}$ (sum of $\vec{L}$, individual spins $\vec{S}_1$, $\vec{S}_2$ and GR corrections). Last, $\mathtt{phi}_{12}$ is the angle between the projections of spin vectors on the orbital plane. θ_{JN} is the angle between the line of sight $\vec{N}$ and the total angular momentum $\vec{J}$. θ_{JN} reduces to the inclination angle ι, when the spins of the binary components are aligned to the orbital angular momentum. Figure from [Dupletsa et al., 2025] (Figure 7, ***authored by UD***)

The phase can be written as:

$$\psi(f,\mathcal{M}) = 2\pi f t_c - \frac{\pi}{4} + \frac{3}{128}\left(\frac{\pi G\mathcal{M}}{c^3}\right)^{-5/3}\frac{1}{f^{5/3}} \tag{1.50}$$

The GW signal depends on 15 parameters:

$$\{\mathcal{M}, q, d_L, \iota, \texttt{RA}, \texttt{DEC}, \phi, \Psi, t_c, a_1, a_2, \texttt{tilt}_1, \texttt{tilt}_2, \texttt{phi}_{12}, \texttt{phi}_{JL}\}, \tag{1.51}$$

with the addition of $\{\Lambda_1, \Lambda_2\}$ when NS systems are involved. We provide a detailed description in Tab. 1.1. The parameters entering in a GW signal can be classified into two categories:

- *intrinsic parameters*: masses, spins (these have six different components, we show a schematic representation of them in Fig. 1.10), tidal deformability parameters, Λ_i, for NSs (these are directly linked to the NS Equation of State (EoS))
- *extrinsic parameters*: location with respect to the detector, i.e. the sky position represented by the RA and DEC parameters (see Fig. 1.11 for an illustrative scheme), distance, merger time, orbital plane orientation. A complete list of GW parameters for a CBC is provided in Tab. 1.1.

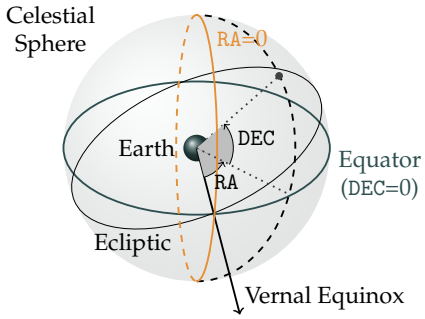

Figure 1.11: Schematic representation of angular parameters that describe the position of the source in the sky. RA and DEC correspond, respectively, to the longitude and latitude on Earth, but in reference to the celestial sphere. The zero reference for DEC is the Earth's equator projected onto the celestial sphere. Instead, the zero reference for RA is the meridian on the celestial sphere passing through the intersection of the equator line and the ecliptic (vernal equinox). Figure from [Dupletsa et al., 2025] (Figure 6, ***authored by UD***)

The primary effect of the Universe's expansion is to affect the masses we measure at the detector. The source-frame mass gets redshifted, and we can only directly measure the so-called detector-frame mass, which carries a $(1+z)$ factor multiplying the source masses, making the source-frame mass measurements degenerate with redshift. Massive systems at low z might mimic less massive ones at higher z. This is the working point of the spectral siren method, which we discuss in detail in Chapter 2.

Another relevant degeneracy is between the luminosity distance d_L and the inclination angle ι. As from Eq. (1.48), the observed amplitude depends on both d_L and ι. Sources that are *face-on*, meaning that $\iota = 0°$ or $180°$, have a larger amplitude and produce a stronger signal, compared to *edge-on* source, for which $\iota = 90°$. This means that a nearby but inclined system can mimic a more distant but *face-on* system, leading to uncertainty in distance estimation. We will come back to parameter degeneracies in Chapter 3.

Based on these parameters, we can build a template bank, a set of precomputed theoretical waveforms exploring different ranges. The templates are then compared to observations, considering the noise model of the detector. The analysis method we use to dig out the GW signal from the noise it is buried in, as from Eq. (1.45), is called matched-filtering. Matched-filtering works by computing the overlap

Parameter	Label	Description
chirp mass	$\mathcal{M}_c$	combination of detector-frame masses: $\mathcal{M}_c = \frac{(m_1 m_2)^{3/5}}{(m_1+m_2)^{1/5}}$
mass ratio	q	ratio between the secondary m_2 and the primary m_1 component masses, $0 < q \leq 1$
luminosity distance	d_L	luminosity distance to the source
theta_JN	θ_{JN}	angle between the line of sight $\vec{N}$ the total angular momentum of the binary $\vec{J}$
iota	ι	when $\vec{J} = 0$, θ_{JN} becomes the inclination angle
declination	DEC	coordinate on celestial sphere corresponding to latitude on Earth
right ascension	RA	coordinate on celestial sphere corresponding to longitude on Earth
phase	ϕ	phase of the gravitational wave at the coalescence
polarization angle	Ψ	rotation of GW polarizations reference frame with respect to detector's arms in Earth's frame
geocentric time	t_c	merger time, calculated as GPS time
a_1	a_1	dimensionless spin magnitude of primary component, defined as $a_1 = cS_1/Gm_1^2$ with S_1 the spin of the primary object
a_2	a_2	dimensionless spin magnitude of secondary component, defined as $a_2 = cS_2/Gm_2^2$ with S_2 the spin of the secondary object
tilt_1	$\texttt{tilt}_1$	angle between the spin vector of primary component and the orbital angular momentum $\vec{L}$
tilt_2	$\texttt{tilt}_2$	angle between the spin vector of secondary component and the orbital angular momentum $\vec{L}$
phi_12	$\texttt{phi}_{12}$	angle between the projections of the two spin vectors onto the orbital plane
phi_jl	$\texttt{phi}_{JL}$	azimuthal angle of the orbital angular momentum $\vec{L}$ around the total angular momentum $\vec{J}$
Lambda_1	Λ_1	tidal deformability of the first component in a BNS system
Lambda_2	Λ_2	tidal deformability of the second component in a BNS system
Sky localization	$\Delta\Omega$	the sky localization area, dependent on the constraints on RA and DEC

Table 1.1: List of GW parameters, entering in the description of a GW signal. The last two parameters, Λ_1 and Λ_2 apply to NSs only. For angular and spin parameters, see Fig. 1.11 and Fig. 1.10. Table from [Dupletsa et al., 2025] (Table 3, ***authored by UD***)

between the data, Eq. (1.45), and a template waveform so that the Signal-to-Noise Ratio (SNR) is maximized [Maggiore, 2007]. The detector output is filtered using a linear filter:

$$S = \int_{-\infty}^{+\infty} df \tilde{h}(f)\tilde{K}^*(f), \tag{1.52}$$

where $\tilde{K}^*(f)$ is the filter function. When a signal is not present, we

expect only noise:

$$N^2 = \int_{-\infty}^{+\infty} df \frac{1}{2} S_n(f) |\tilde{K}(f)|^2, \tag{1.53}$$

with $S_n(f)$ the detector sensitivity strain as defined in Eq. (1.46). For a given template $h(t)$, the optimal filter, or matched filter, is the one for which the SNR is maximized:

$$\frac{S}{N} = \frac{\langle u|h\rangle}{\langle u|u\rangle^{1/2}} \tag{1.54}$$

where $u(t)$ is a function whose Fourier transform is given by:

$$\tilde{u}(f) = \frac{1}{2} S_n(f) \tilde{K}(f) \tag{1.55}$$

The inner product $\langle \cdot | \cdot \rangle$ is defined as:

$$\langle a|b\rangle \equiv 4\,\mathrm{Re} \int_{f_{\min}}^{f_{\max}} df \frac{\tilde{a}(f)\tilde{b}^*(f)}{S_n(f)}, \tag{1.56}$$

where $f_{\min}$ and $f_{\max}$ define the frequency range over which the signal spans. The optimal filter is obtained when:

$$\tilde{K}(f) \propto \frac{\tilde{h}(f)}{S_n(f)} \tag{1.57}$$

This directly defines the optimal SNR:

$$\left(\frac{S}{N}\right)_{\mathrm{opt}} = \sqrt{\langle h|h\rangle}. \tag{1.58}$$

A signal is considered detected if its optimal SNR is above a certain detection threshold, which is usually set above the value of $SNR = 8$.

We extract the posterior distribution, $p(\vec{\theta}|d)$, of the signal parameters, i.e. those listed in Tab. 1.1, from the raw data d using a Bayesian parameter estimation (PE) approach [Thrane and Talbot, 2019; Christensen and Meyer, 2022]:

$$p(\vec{\theta}|d) = \frac{\pi(\vec{\theta})\mathcal{L}(d|\vec{\theta})}{\mathcal{Z}(d)}, \tag{1.59}$$

where $\mathcal{L}(d|\vec{\theta})$ represents the likelihood of the data given the source parameters $\vec{\theta}$, $\pi(\vec{\theta})$ is the parameters' prior, and $\mathcal{Z}(d)$ is the evidence. For CBC modeled sources, and assuming that noise is stationary and Gaussian, the likelihood function can be written as:

$$\mathcal{L}(d|\vec{\theta}) \propto \exp\left[-\frac{1}{2}\langle d - h(\vec{\theta})|d - h(\vec{\theta})\rangle\right], \tag{1.60}$$

where the inner product $\langle \cdot | \cdot \rangle$ is the one defined in Eq. (1.56), and $h(\vec{\theta})$ is the waveform approximant we use to model the signal. This introduction is the starting point of a more detailed discussion in the Fisher matrix analysis context in Chapter 3.

1.2.4 *Current detectors: the GWTC catalogs*

As introduced in Sec. 1.2, the currently operating GW detectors comprise the LIGO [Aasi et al., 2015] interferometers, Virgo [Acernese et al., 2015], and KAGRA [Somiya, 2012; Aso et al., 2013]. Instead, GEO600, located in Hannover, is used for technological developments [Grote et al., 2013].

At the time of this thesis, the LVK Collaboration has completed three observing runs, named O1, O2, O3a, and O3b, and are currently in the second part of the fourth observing run, O4:

- O1 happened from September 12th, 2015 to January 19th, 2016. The observed events have been published in [Abbott et al., 2016a].
- O2 took place from November 30th, 2016 to August 25th, 2017. Together with the events from O1, the first ever Gravitational-Wave Transient Catalogue (GWTC), namely GWTC-1 [Abbott et al., 2019b] has been officially released.
- O3a ran from April 1st, 2019, to October 1st, 2019; the data are presented in GWTC-2 [Abbott et al., 2021a], then updated in GWTC-2.1 [Abbott et al., 2024].
- O3b ran from November 1st, 2019, to March 27th, 2020; all the public data from the start of data taking to this date have been released as GWTC-3 [Abbott et al., 2023b].
- O4a lasted from May 24th, 2023, to January 16th, 2024
- O4b has started on April 10th, 2024, and transitioned to O4c on January 28th, 2025. A commissioning break is taking place from April 1st, 2025 till June 4th, 2025. O4 is foreseen to end on October 7th, 2025.

Data from O1, O2, and O3 have been publicly relesead in different catalogues, GWTC-1, GWTC-2, GWTC-2.1, and GWTC-3 [Abbott et al., 2019b, 2021a, 2024, 2023b]. Now, we are in the process of preparing the public release of data from O4a. Some insights from the upcoming catalogue applied to cosmology are provided in Chapter 2, Sec. 2.5.

The number of events presented in the catalogues may vary depending on the detection pipelines and the chosen detection thresholds. We report here the numbers as from the latest release of GWTC-3 [Abbott et al., 2023b]. From O1, we report three BBH events. With O2, we add the first-ever BNS event `GW170817`, and 7 additional BBH mergers. From O3a we have a total of 44 CBCs, among which a second BNS event `GW190425` with no identified EM counterpart and an asymmetric mass event `GW190814`. As mentioned earlier, another notable event from O3a is `GW190521` which produced a final BH of around $\sim 142 M_{\odot}$,

falling in the Intermediate Mass Black Hole (IMBH) region [Abbott et al., 2020c]. Finally, O3b has provided us with 36 more event, comprising three NSBH mergers, `GW191219`, `GW200105` and `GW200115`.

These events have been selected to have the probability of being of astrophysical origin greater than 50%, $p_{\text{astro}} > 0.5$ (except for `GW200105`, which has $p_{\text{astro}} < 0.5$ but it is still included as a candidate of interest). Other criteria are based on SNR detection threshold and the False Alarm Rate (FAR). FAR quantifies the probability that an event might occur by chance due to noise fluctuations. It is expressed as a number of events per unit of time, usually measured in years. A lower FAR value means that the event is more likely astrophysical. Typical values used in the LVK Collaboration are around $FAR < 1\,\text{yr}^{-1}$ for BBHs, meaning that noise could mimic a similar signal once per year, and $FAR < 0.25\,\text{yr}^{-1}$ for BNSs or NSBHs as they occur less frequently. We return to this when discussing the event's selection from O4a for cosmological analysis in Sec. 2.5.

The majority of observed events are BBHs. The numbers at play allow us to do population studies and infer some interesting properties [Abbott et al., 2021c], especially on masses and spins. The chirp mass is a well-measured parameter, as the evolution of the frequency scales as a power of $\mathcal{M}_c$. We find that the BH mass distribution shows features that can be explained with astrophysical processes, assuming that the merging BHs originate from the collapse of massive stars. The BH masses present clumps, most notably one around $10M_\odot$ and one around $35M_\odot$. We also observe a depletion of events roughly around $\sim 5M_\odot$ that we call lower mass gap. We discuss in detail the modeling of the BH mass spectrum throughout Chapter 2, and, in particular, in Sec. 2.2. On the other hand, spins are poorly constrained[8]. Almost all the events show $\chi_{\text{eff}} \sim 0$, meaning that either spins are usually small, or that we have an excess of spins lying in the plane, or a combination of both. This might also give us information on the formation channel (see Sec. 1.2.2).

The increased number of detections that we are experiencing with O4 will allow us to put increasingly better constraints. O4 is expected to end on October 7th, 2025. An additional observing run, O5, is planned to take place in 2028.

[8] What is usually measured is a combination of spins, called effective spin:

$$\chi_{\text{eff}} = \frac{m_1\vec{S}_1 + m_2\vec{S}_2}{m_1 + m_2} \cdot \vec{L}$$

where m_i are the masses, $\vec{S}_i$ the spins, and $\vec{L}$ the orbital angular momentum. χ_{eff} varies in $[-1, +1]$, with $|\chi_{\text{eff}}| = 1$ when the two objects are maximally spinning and aligned with $\vec{L}$, $\chi_{\text{eff}} = +1$, or anti-aligned $\chi_{\text{eff}} = -1$. $\chi_{\text{eff}} = 0$ means either zero spins or spins in the plane of the binary.

1.2.5 *Future ground-based detectors*

The number of CBC detections expected for the XG instruments is outstanding. Even though these numbers are highly uncertain, we are talking about an order of 10^5 events per year [Maggiore et al., 2020; Iacovelli et al., 2022a; Branchesi et al., 2023], both for BBH and BNS systems, and around 10^4 events for NSBH events. Plans in the

GW field include space-based, like Laser Interferometer Space Antenna (LISA) [Amaro-Seoane et al., 2017], Moon-based as Lunar Gravitational Wave Antenna (LGWA) [Ajith et al., 2025] and ground-based detectors. We focus on the ground-based future interferometers, which comprise the CE [Reitze et al., 2019; Evans et al., 2021] in the USA and the ET [Hild et al., 2008, 2011; Punturo et al., 2010] in Europe.

In Fig. 1.6, we have already shown the one order of magnitude improvement in sensitivity with respect to the current interferometers. In Fig. 1.12, we compare CE and ET reference sensitivities, highlighting the extended sensitivity of ET at low frequencies. The XG detectors provide an increasing number of detections, precision, and a wider frequency band. With ET and CE, we will be able to observe larger distances up to the dark age of the observable Universe. In redshift, this means going far beyond what we can currently reach, around $z \sim 1$, up to $z \sim 100$, and exploring CBC mergers along the cosmic history. The enormous increase of SNR for close events will enable accurate PE, allowing great precision in GW astronomy. In general, thanks to the enhanced precision of the source PE, among others, we expect to be able to provide early warnings for BNS events and to localize them well for MM studies [Banerjee et al., 2023; Branchesi et al., 2023]. The future of GW astronomy is full of exciting discoveries.

All the second part of this thesis is devoted to the XG detectors and their potential, from forecast analyses to assess detectors performance for different science cases in Chapter 3, to MM studies in Chapter 4, to cosmology in Chapter 5. Specifically, our primary focus is the ET. Therefore, we provide a brief introduction, leaving the details to Chapter 4.

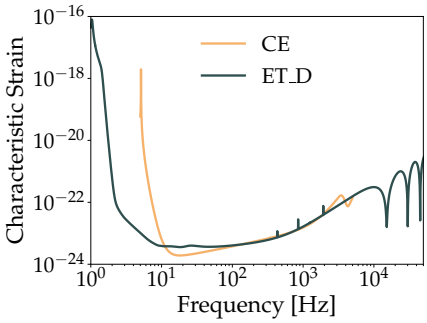

Figure 1.12: Comparing the sensitivity curves of CE and ET

The ET is a proposed European infrastructure. The frequency band of ET is planned to span from as low as 2 Hz on the lower end up to several kilohertz. The sensitivity at low frequencies is a key feature of ET. The observation is thus extended to much lower frequencies compared to current GW detectors, which leads to longer observation times of individual CBC signals, and it will also make it possible to observe larger-mass compact binaries well into the regime of IMBHs. Long observation times enable stand-alone sky-localization measurements by ET of NS binaries exploiting amplitude modulations due to Earth's rotation. Since the observed mass is the redshifted source-frame mass, the low-frequency sensitivity will make it possible to access BBH mergers in the early Universe where primordial BHs can be discriminated from BHs of stellar origin [Ng et al., 2022, 2023; De Luca et al., 2021].

The importance of low frequency is related to the design of ET. Since seismic and Newtonian noise set the limit at the low end, the infras-

tructure will be built underground to mitigate the noise contribution. Moreover, ET is designed in the so-called xylophone configuration, comprising two sets of interferometers, one for low and one for high frequencies. The idea of physically separating the two comes from the fact that the cryogenic temperatures of the low frequencies are incompatible with the high-power laser required to reduce quantum shot noise at high frequencies. Additionally, resolving to a xylophone configuration separates the technical challenges and risks.

Currently, two different configurations are being considered for ET:

- In its original configuration, ET has the geometry of an equilateral triangle and 10 km laser-interferometer arms launching from each of its vertices. It consists of 3 pairs of laser interferometers, each including a low-frequency interferometer and a high-frequency interferometer. This triangular configuration is expected to give it unique capabilities concerning the measurement of GW polarizations and parameters correlated with GW polarizations.

- The alternative proposal is to build two well-separated L-shaped detectors, most likely of 15 km arms. As for the triangular shape case, the L-shaped ET will feature the xylophone configuration.

The first thorough study of the different designs for ET has been carried out in [Branchesi et al., 2023], and a lot more work is in development. We will present some of the studies in [Branchesi et al., 2023] in Chapter 4, with a broader discussion on the design chosen for the study in Sec. 4.1.

One of the crucial points of the planning of ET is its location. We currently have three candidate sites: one in Sardinia, one in Saxony, and one in the Netherlands. We provide more details in Sec. 4.1.2. Nevertheless, the final decision has not yet been made and is out of the scope of this thesis.

It is fundamental to stress that the planning and the construction of an interferometer such as the ET is paramount for the scientific community and requires extremely careful and detailed considerations. In the coming years, all the details will be finalized.

1.3 *Thesis structure*

This thesis addresses a series of interconnected questions spanning the GW science with CBCs, covering aspects from data analysis to MM applications and cosmology. At its core, the central question is: What information do GW data from CBCs provide? Additionally, how can we effectively analyze this information? This leads directly to exploring the performance of both current and future detectors, evaluating

their ability to detect GW signals and the resulting implications for our understanding of the Universe.

This thesis aims to cover some aspects of interest of the extremely vast science case of the field of GW from CBCs. The primary goal is data analysis applied to cosmology and MM astrophysics, with a special focus on forecast analysis techniques for the XG GW instruments.

- On the side of the current detectors, in the first part of this thesis, we study spectral-siren cosmology using both simulated and measured data with the LVK network. This is the topic of Chapter 2, where we explore and apply the Hierarchical Bayesian Inference (HBI) analysis for the inference of cosmological parameters, especially H_0. In the first place, we quantify the bias on the Hubble constant coming from a mismodeling of the BH population, given a set of mock data. Specifically, we study the consequences of not assuming, at the analysis level, a redshift dependence of the mass spectrum even though the mock data has been generated assuming one. This is the scope of the `Mock Data Challenge` (MDC) [Agarwal et al., 2024]. Additionally, we present some preliminary results obtained with the recently measured data from O4a from the ongoing cosmology LVK Collaboration paper. In the latter, we do not provide a comprehensive description of the analyses and results of the paper, but only some hints focused on the spectral-siren topic, highlighting the advantages of a new mass model that describes both BHs and NSs under one framework.

- The future GW detectors, particularly the science case of the ET, is the main focus of the second part of this thesis. This comprises three chapters. The first is a detailed discussion of the analysis techniques employed to study the capabilities of the XG detectors. The other two are applications in the MM astrophysics and cosmology fields.

  - Chapter 3 is the core of the work, as it addresses the forecast analysis techniques [Dupletsa et al., 2023, 2025] developed in this thesis, which found several applications in multiple works [Ronchini et al., 2022; Banerjee et al., 2023; Branchesi et al., 2023; Santoliquido et al., 2024; Cozzumbo et al., 2025; Loffredo et al., 2025].

    Chapter 3 sets the analysis setup for the forecast studies for future detectors that we exploit in the subsequent two chapters and that is used in the ET community. As we will explain in detail, the Fisher analysis, based on Gaussian approximation, is a necessary step to assess future detectors performance, as the current Bayesian methods employed in the LVK Collaboration are not yet ready for the amount and computational load of data as expected from the XG observatories. Talking numbers, in an op-

timistic scenario, a full Bayesian analysis of one event requires some hours. Fisher analysis takes under one second per event. Given that forecast studies are population studies, which implies analyzing an order of $10^4 - 10^5$ signals at least, resolving to the Fisher analysis gives us the best trade-off.

We comprehensively discuss the Fisher matrix analysis and introduce the software `GWFish`, which implements it and simulates different GW detector networks. Additionally, we explore enhancing the Fisher matrix analysis by incorporating priors into the process. We address the interplay between SNR, parameter correlations, multi-modalities, and priors.

– Chapter 4 is a direct application of the `GWFish` software to study the capabilities of ET in the MM context. It features two works.

The first one [Branchesi et al., 2023] results from a considerable effort inside the ET Collaboration. It provides the first comprehensive study of the different designs of ET, primarily comparing the triangular and the 2L shapes and their impact on the scientific output. This thesis only focuses on the MM part of [Branchesi et al., 2023], which represents a milestone in the ET community, together with a companion paper, the Blue Book, which is the review process and which provides an even more detailed scientific analysis of ET focusing on the specific science cases from all the divisions of the ET Observational Science Board (OSB).

The second work is a short-author study [Loffredo et al., 2025], which, in turn, expands on the MM section of [Branchesi et al., 2023] by exploring the details of joint GW and kilonova (KN) detections, studying the synergy between ET and the Vera Rubin Observatory. In particular, we study the impact of different assumptions at the population level (population synthesis and mass modeling), at the microphysics level (the NS Equation of State (EoS), and at the detection level (different GW networks).

– In Chapter 5, we go back to cosmology, which has come to be one of the leitmotivs of this thesis. We focus on mock data with future GW detectors.

On one side, we tackle the bright sirens science case with BNS events, analyzing the hypothetical scenario of ET operating with the current Gamma Ray Burst (GRB) detectors, Fermi-GBM and Swift-BAT/XRT [Cozzumbo et al., 2025]. We quantify how the constraints on cosmological parameters would be tighter thanks to the technological advancements of ET. We also explore different cosmological models to assess the bias when the wrong model is assumed and investigate some model-independent approaches to reconstruct the evolution of the DE.

On the other side, we explore dark siren cosmology with BBH signals using the redshift information from the large scale structure (LSS) of the Universe, assuming that astrophysical BHs trace the same underlying DM distribution [Dupletsa et al., nd, *in preparation*]. In this work, we study the synergy between future GW detectors like the ET and future radio observatories like the SKA Observatory (SKAO). Specifically, we analyze the constraints on cosmological parameters using the 3-dimensional density fields of neutral hydrogen (HI) mapped thanks to the 21 cm line emission as a redshift prior for the BBHs events. Focusing on future detectors allows us to go to redshifts as high as $z \sim 3$ and trace the Hubble parameter as a function of redshift.

The diagram in Fig. 1.13 offers an overview of the structure of this thesis. This chapter has provided a broad introduction to the field, and each of the four chapters includes tailored introductory material. All the plots and figures presented in the thesis are reproducible thanks to a link to their `GitHub` script .

At the beginning of each chapter, the author's contributions are specified. The Figures and Tables of this thesis produced by the author in published papers report the specifics *authored by UD*. The ones from unpublished work, specifically in Sec. 2.5 and Sec. 5.3, represent preliminary work by the author. Some Figures do not refer to any paper and have been produced by the author for illustrative purposes specifically for this thesis.

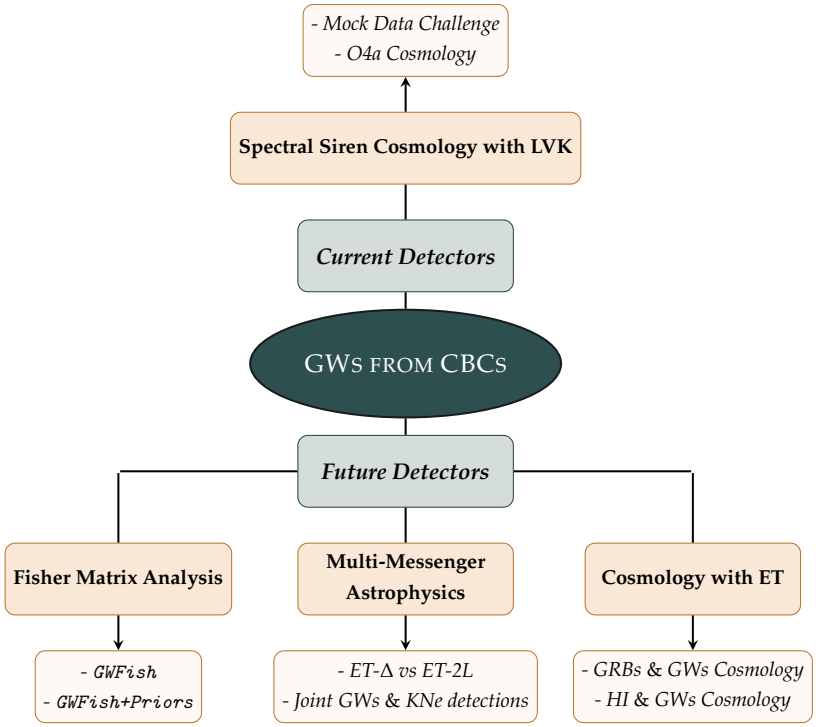

Figure 1.13: Outline of this thesis structure. It comprises two parts dedicated to current and future GW detectors. The chapters focus on specific science cases. In particular, for current LVK interferometers, we present the spectral siren method for cosmological inference. Whereas for the future ones, after a detailed analysis of the challenges of data analysis with the XG detectors, we present two wide science cases for the ET, that of MM astrophysics and back to cosmology

PART I

Current GW detectors

2. *Spectral siren cosmology, with LVK*

> *I do not follow you, M. Poirot. -*
> *Because you are deducing from things that you have seen.*
> *Nothing can be so misleading as observation.*
>
> **— Agatha Christie**
> "Death in the Clouds"

The following chapter is based on two papers, both of which are projects carried out inside the Cosmology division in the LIGO-Virgo-KAGRA (LVK) Collaboration. The field of cosmology with gravitational waves (GWs) is wide and covers different directions. I focus on the spectral-siren method in both the works presented here.
The first one is the `Mock Data Challenge` (MDC), set up to assess the robustness and quantify the systematics from population modeling in inferring the Hubble constant. Inside the MDC project, I was in charge of the analyses with the `icarogw` [Mastrogiovanni et al., 2024] pipeline to infer cosmological and population parameters from a set of mock GW events; I carried out the post-processing of the results, for both the cosmological scenarios addressed in the study, and I was a member of the paper writing team. The MDC paper [Agarwal et al., 2024] is a short-author paper inside the LVK Collaboration, and it is currently under review in ApJ.
The second work is only partially addressed in the last part of this chapter, as it is still in development. The project is the LVK Collaboration paper on the cosmological results with the data from the first part of the fourth observing run, namely the O4a data. The work is ongoing, and I am contributing both as a member of the analysis team, with the `icarogw` software, and as a member of the paper writing team. ***This second part contains still unpublished LVK Collaboration data from the O4a observing run and must be treated as sensitive material.***

2.1 Cosmic rulers: an overview

Measuring distances in cosmology is a centuries-long effort, starting from the ancient astronomers who used geometrical reasoning, as for the measurement of the Earth's circumference by Eratosthenes (around 240 BC), or the parallax method, and building, rung-by-rung, a cosmic distance ladder, up to the discovery of *Standard Candles* and Type Ia supernovae (SNe) [Leavitt and Pickering, 1912]. Each step of the ladder relies on carefully calibrating the previous ones. The suc-

Contents

cessive refinement of this process has allowed us to map the scale of the Universe and its expansion.

Gravitational waves (GWs) from compact binary coalescences (CBCs), being them Binary Black Holes (BBHs), Binary Neutron Stars (BNSs), or Neutron Star - Black holes (NSBHs), are the only astrophysical sources for which we can directly measure the luminosity distance, without the need to rely on any calibration or distance ladder. GW cosmology is a relatively recent field that dates back to a breakthrough idea of [Schutz, 1986]. For the first time, GWs can be used as *Standard Sirens* [Holz and Hughes, 2005], as opposed to the historical *Standard Candles* that rely on sources like Type Ia SNe and on a complex process of calibration [Tammann and Reindl, 2000]. GWs qualify as *cosmic rulers* as they give a self-calibrated measurement of the luminosity distance parameter. They do not provide us, though, with a direct redshift measurement. Since pinpointing cosmological parameters, and among them, H_0, boils down, as from Eq. (1.9), Eq. (1.12) and Eq. (1.21), to independent redshift-luminosity distance measurement, and since from the gravitational side, we get the distance, we need an independent measurement of the redshift to probe the expansion history of the Universe. By combining GW data with bright, when an electromagnetic (EM) counterpart has been identified, or dark, when there is no EM data to rely on, sirens, we can estimate cosmological parameters [Chernoff and Finn, 1993; Holz and Hughes, 2005; Dalal et al., 2006; Abbott et al., 2017a; Chen et al., 2019; Abbott et al., 2023a].

So far, we had one bright siren measurement only, `GW170817` [Abbott et al., 2017c], which led to an estimate of H_0 [Abbott et al., 2017a] compatible with other H_0 measurements, as shown in Fig. 2.1. On the other hand, the abundant observations of BBH systems provide us with increasing statistics for applying the dark sirens methods. These include the statistical host identification with galaxy surveys [Schutz, 1986; Fishbach et al., 2019; Soares-Santos et al., 2019; Gray et al., 2020; Palmese et al., 2021; Gray et al., 2023]; spectral sirens technique [Chernoff and Finn, 1993; Taylor et al., 2012; Farr et al., 2019; Mastrogiovanni et al., 2021; Mukherjee, 2021; Leyde et al., 2022; Ezquiaga and Holz, 2022; Mastrogiovanni et al., 2024; Leyde et al., 2024; Pierra et al., 2024; Magaña Hernandez and Ray, 2024; Farah et al., 2025; Mali and Essick, 2024]; cross-correlation techniques between GWs and galaxies [Mukherjee and Wandelt, 2018; Mukherjee et al., 2020, 2021; Bera et al., 2020; Ferri et al., 2024]. A recent review in [Palmese and Mastrogiovanni, 2025] gives an overall perspective on GW cosmology.

In the following chapter, we focus on the spectral sirens. The main idea behind this specific dark siren method is to model the mass distribution and the merger rate to break the degeneracy between mass and redshift. The chapter is organized as follows. We first give the

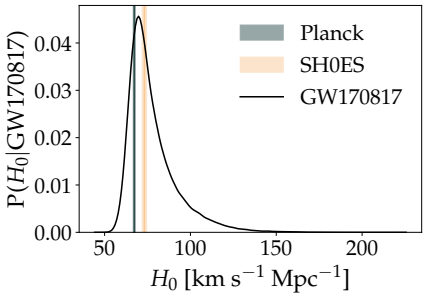

Figure 2.1: H_0 posterior as from the `GW170817` data. For comparison, we show the values obtained from the Cosmic Microwave Background (CMB) as in [Aghanim et al., 2020] and from SNe Type Ia [Riess et al., 2021]. Figure adapted from Fig.1 in [Abbott et al., 2017a]

details of the spectral sirens method in Sec. 2.2 and its mathematical framework, which involves Hierarchical Bayesian Inference (HBI), along with its numerical implementation in `icarogw` [Mastrogiovanni et al., 2024] in Sec. 2.3. Next, Sec. 2.4 is the main focus of this chapter. We report the setup and the results from the `Mock Data Challenge` (MDC) [Agarwal et al., 2024]. The main objective of the MDC is to test statistical and systematical uncertainties of the spectral siren method. In particular, we want to assess the resulting bias on the cosmological parameters if the underlying astrophysical black hole (BH) population has a redshift-evolving mass spectrum when such an assumption is not included in the analysis. Last, in Sec. 2.5, we briefly outline the latest updates on the Hubble constant measurements from the most recent data obtained in the LIGO-Virgo-KAGRA (LVK) Collaboration.

2.2 *Spectral sirens: modeling the mass spectra*

In spectral-siren cosmology, the redshift information comes from the mass spectrum of the CBCs [Taylor et al., 2012; Mastrogiovanni et al., 2021; Ezquiaga and Holz, 2022]. Spectral-siren cosmology needs the source-frame mass distribution, which is linked to the observed mass in the detector frame by the following relation:

$$(1+z) = \frac{m_i}{m_{i,\mathrm{src}}}, \tag{2.1}$$

where m_i and $m_{i,\mathrm{src}}$ are the two component masses in the detector and the source frame, respectively.

In Fig. 2.2, we show a few examples of possible mass spectra models. The presence of particular features helps infer redshift from the source mass distribution. These can either be mass regions accumulating more BBHs, called *peaks*, hence names like Power Law+Peak or Multi Peak; or points whose corresponding mass value is less likely to be observed. Points where the power law changes are called *breaks*. All these features might originate from astrophysical processes.

For the BBH population, for example, we expect a depletion of sources in the mass range between $\sim 50M_\odot$ and $\sim 120M_\odot$ [Farmer et al., 2019] due to the pulsational pair instability supernova (PISN) process. The first population model for BBHs was a simple Truncated model [Fishbach and Holz, 2017] (see subplot (a) in Fig. 2.2). In this model, the BBH mass distribution is a Power Law (PL) between a minimum, m_{min}, and a maximum, m_{max}, mass. The hard cut-off at m_{min} served to separate NSs from BHs, whereas the one at m_{max} is due to the PISN. After the first part of the third observing run [Abbott et al., 2021b], the Truncated model had to be modified to accommodate more complex features. At first order, to better model the high-

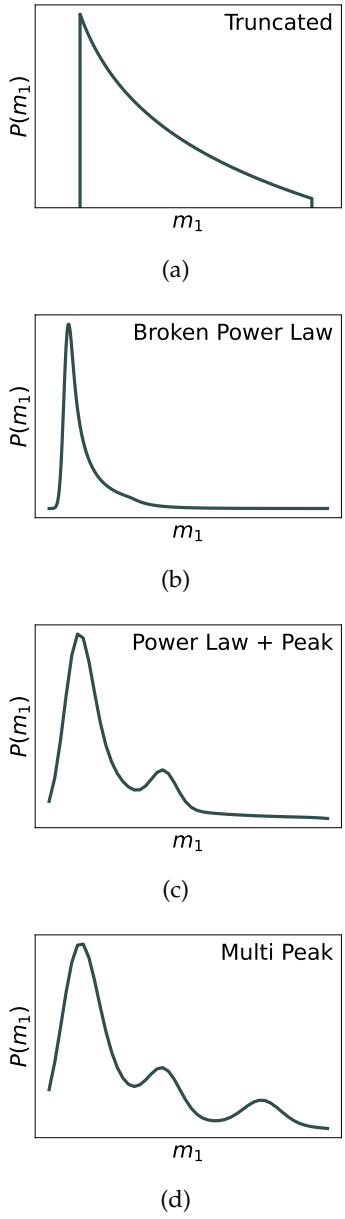

Figure 2.2: From *top* to *bottom*, we show the main features of the mass spectra models used in the LVK analyses, and, in order of complexity, the Truncated -in subplot (a)-, the Broken Power Law -in subplot (b)-, the Power Law+Peak -in subplot (c)- and the Multi Peak -in subplot (d) models. Figure adapted from [Abbott et al., 2021b] (Figure 1)

mass BBHs the BROKEN POWER LAW model has been introduced (see subplot (b) in Fig. 2.2). Furthermore, a better fit to data is provided by the POWER LAW+PEAK model (see subplot (c) in Fig. 2.2), in which a Gaussian peak around $\sim 30 - 40 M_\odot$ is present. The presence of this peak could be a smoking gun for the transition of BBHs produced in isolated binaries, and subject to the PISN, to the ones formed in hierarchical mergers [Mapelli, 2021]. We note that this transition is still speculative. In the MULTI PEAK (see subplot (d) in Fig. 2.2), we even allow for second-generation BBH mergers that create a second peak at higher masses. For the specifics of each population model, briefly described here, we refer to [Abbott et al., 2021b]. [Abbott et al., 2021c] shows that, given the data from the first three observing runs, namely GWTC-3, POWER LAW+PEAK seems the mass model preferred by data.

One of the crucial assumptions in all of these models is that the source-frame mass distribution is independent of redshift [Fishbach et al., 2021]. Even though we expect some evolution with redshift because of, e.g., the metallicity evolution [Belczynski et al., 2010], if the peak is due to PISN, we think that its location should not change much with redshift [Farmer et al., 2019]. Moreover, given the current detectors' sensitivities, we do not expect much evolution in any case, as the redshift range we are able to explore is limited. Indeed, the central part of this chapter will be dedicated to studying how biased our cosmological inference may be because of the redshift-independence assumption. This is, in fact, the scope of the MDC and will be thoroughly addressed in Sec. 2.4.

2.3 *Hierarchical Bayesian Inference (HBI)*

The statistical framework we need to work with is that of the Hierarchical Bayesian Inference (HBI) [Vitale et al., 2020; Mandel et al., 2019; Mastrogiovanni et al., 2024]. In layman's terms, we have two levels of inference: the first is the parameter estimation (PE) of the individual GW events, and the second is the population inference that describes the observed set of GW events in a unified model depending on mass spectrum, rate, and cosmological parameters. HBI allows us to infer the posterior distribution of the so-called *hyperparameters*[1] given a number of observed GW events.

The core of the analysis is Poisson statistics. We recap the basics in the box below and add the complexity levels needed to infer population and cosmological properties from GW observations. The number of GW events we can observe, at its essence, boils down to a counting problem and thus satisfies Poisson statistics. However, the event rate is not constant; it depends on several parameters. Therefore, the

[1] From now on, when using the term *hyperparameters*, we refer to the parameters entering at the population level of inference, in the mass spectrum, rate, and cosmological models. This distinction is essential to differentiate them from the parameters of individual GW events, such as masses, distance, and so on (the full list is provided in Tab. 1.1).

Poisson process is called *inhomogeneous* (as opposed to the standard *homogeneous* one). Moreover, we have to deal with *selection biases* since we do not observe all the sources, but the nearest and loudest ones are more likely to be detected, considering the limited sensitivity of our detectors. Therefore, when modeling the mass spectrum, we have to consider that the observed masses might not reflect the astrophysical population. This is the so-called Malmquist bias [Malmquist, 1922], and, if not accounted for, may lead to considerable discrepancies in our results [Mandel et al., 2019]. Therefore, we are dealing with an inhomogeneous Poisson process in the presence of selection biases. On top of this, our GW dataset is not measured precisely but is affected by noise.

Basics of Poisson statistics

A homogeneous Poisson process models the occurrence of discrete events over a finite interval, which can be temporal or spatial. The key features of this process are:

1. **Independence**: Events occur independently of one another
2. **Constant Rate**: The process is characterized by a constant rate λ (thus *homogeneous*), representing the average number of events per unit interval

Given an interval of length t (e.g., time or distance), the expected number of events is λt. The number of events within this interval, denoted as $N(t)$, follows a Poisson distribution:

$$p(N(t) = k|\lambda) = \frac{e^{-\lambda t}(\lambda t)^k}{k!}, \quad k = 0, 1, 2, \dots \tag{2.2}$$

We will now see how starting from Poisson and accounting for incomplete and noisy GW data, we build the hierarchical likelihood for the HBI analysis in Sec. 2.3.1, and how it is numerically implemented in the `icarogw` software in Sec 2.3.2.

2.3.1 *The hierarchical likelihood*

Given $N_{\rm obs}$ GW events, collectively specified as $\{x\}$, each of which is described by its own set of parameters θ, the hierarchical likelihood that describes the probability of observing the specific dataset in a given time $T_{\rm obs}$, and given the set of *hyperparameters* Λ, is [Mandel et al., 2019; Vitale et al., 2020; Mastrogiovanni et al., 2021, 2023, 2024]:

$$\begin{aligned}\mathcal{L}(\{x\}|\Lambda) &\propto \exp\left[-N_{\rm exp}(\Lambda)\right] \prod_{i=1}^{N_{\rm obs}} \int \mathcal{L}_{\rm GW}\left(x_i|\theta,\Lambda\right) \frac{{\rm d}N_{\rm CBC}}{{\rm d}t{\rm d}\theta}(\Lambda){\rm d}\theta{\rm d}t \\ &\propto \exp\left[-N_{\rm exp}(\Lambda)\right] \prod_{i=1}^{N_{\rm obs}} T_{\rm obs} \int \mathcal{L}_{\rm GW}\left(x_i|\theta,\Lambda\right) \frac{{\rm d}N_{\rm CBC}}{{\rm d}t{\rm d}\theta}(\Lambda){\rm d}\theta,\end{aligned} \tag{2.3}$$

where, passing from the first to the second line, we have integrated over the observing time, t, measured in the detector frame. First, notice the same structure as in Eq. (2.2), where we have the term dependent on the expected number of events $N_{\rm exp}$ in the observing time interval $T_{\rm obs}$, and the product over the observed number of events $N_{\rm obs}$. Then, we have two terms:

1. The individual GW event likelihood, $\mathcal{L}_{\rm GW}\left(x_i|\theta,\Lambda\right)$, which accounts for how precisely we can measure the binary parameters from GW observations;

2. The differential number of GW sources $\frac{{\rm d}N_{\rm CBC}}{{\rm d}t{\rm d}\theta}(\Lambda)$ modeling the probability of the single event parameters θ given the *hyperparameters* Λ. The set of *hyperparameters* Λ comprises parameters modeling the rate $\Lambda_{\rm rate}$, the source intrinsic parameters, as e.g. the masses, $\Lambda_{\rm pop}$, as well as cosmological parameters like H_0 and Ω_m, referred to as Λ_c.

The latter is the core term in HBI. It can be rewritten to emphasize the contributions from the rate and CBC population properties. We want to stress that the ${\rm d}t{\rm d}\theta$ term in the denominator refers to the measured quantities, i.e. the ones in the detector frame. Instead, the parameters entering the modeling of the CBC sources are the intrinsic ones, i.e. in the source frame. The relevant ones are the source-frame masses, m_1 and m_2, the spins χ_1 and χ_2[2], and redshift $z(d_L)$, which depends on the luminosity distance measurement:

$$\begin{aligned}\frac{{\rm d}N_{\rm CBC}}{{\rm d}t{\rm d}\theta}(\Lambda) &= \frac{{\rm d}N_{\rm CBC}}{{\rm d}t{\rm d}\vec{m}{\rm d}\vec{\chi}{\rm d}d_L}(\Lambda) \\ &= \frac{1}{1+z}\frac{{\rm d}N_{\rm CBC}}{{\rm d}t_{\rm src}{\rm d}\vec{m}_{\rm src}{\rm d}\vec{\chi}{\rm d}z}(\Lambda)\frac{1}{|J|}\end{aligned} \tag{2.4}$$

where $\frac{1}{1+z}$ accounts for time dilation, whereas the determinant of the Jacobian matrix, $|J|$, is needed to pass from the detector to the source frame quantities[3]. Distinguishing between the different contributions, we end up with:

$$\frac{{\rm d}N_{\rm CBC}}{{\rm d}t{\rm d}\theta}(\Lambda) = R_0\psi(z|\Lambda_{\rm rate})p_{\rm pop}(\vec{m}_{\rm src},\vec{\chi}|\Lambda_{\rm pop})\frac{p(z|\Lambda_c)}{1+z}\frac{1}{|J|} \tag{2.5}$$

R_0 is the local, at redshift $z=0$, CBC merger rate, expressed as the number density merger per comoving volume per time, [Gpc^{-3}yr^{-1}]. $\psi(z|\Lambda_{\rm rate})$ describes the redshift evolution of the merger rate and is customary to parametrize it following [Madau and Dickinson, 2014]:

$$\psi(z|\Lambda_{\rm rate}) = \psi(z|\gamma,\kappa,z_p) = \left[1+(1+z_p)^{-\gamma-\kappa}\right]\frac{(1+z)^{\gamma}}{1+\left[\frac{1+z}{1+z_p}\right]^{\gamma+\kappa}}, \tag{2.6}$$

[2] These parametrization refers to the dimensionless spin magnitudes, which can be derived from the spin parametrization as in Tab. 1.1 by:

$$\chi_i = a_1\cos(\texttt{tilt}_i)$$

We included spins here for completeness, even though we will neglect their contribution to the analyses presented in this thesis.

[3] We gathered in a single vectorial notation the two masses $\vec{m}_{\rm src}$, and the spins, $\vec{\chi}$

where we highlight the $\Lambda_{\rm rate}$ *hyperparameters*. $p_{\rm pop}(\vec{m}_{\rm src}, \vec{\chi}|\Lambda_{\rm pop})$ is the source-rame mass (and spin) distribution, and it depends on the modeling of the mass spectrum, e.g. the position and width of the Gaussian peak in the POWER LAW+PEAK model. All the relevant *hyperparameters* will be described in detail later on in the chapter. As an example, focusing on the generic source mass model (ignoring spins), we have:

$$p_{\rm pop}(\vec{m}_{\rm src}|\Lambda_{\rm pop}) = p(m_1|\Lambda_{\rm pop})p(m_2|m_1, \Lambda_{\rm pop}), \tag{2.7}$$

where we have to factorize between the two component masses and enhance that $m_2 < m_1$.

Last, $p(z|\Lambda_c)$ is the redshift prior, usually taken to be uniform in comoving volume, $p(z|\Lambda_c) = {\rm d}V_c/{\rm d}z$.

Selection effects enter in the evaluation of the expected number of events $N_{\rm exp}$:

$$N_{\rm exp}(\Lambda) = T_{\rm obs} \int p_{\rm det}(\theta) \frac{{\rm d}N_{\rm CBC}}{{\rm d}t{\rm d}\theta}(\Lambda){\rm d}\theta, \tag{2.8}$$

where $p_{\rm det}$ is the detection probability:

$$p_{\rm det}(\theta) = \int_{x\in{\rm detectable}} \mathcal{L}(x_i|\theta){\rm d}x, \tag{2.9}$$

where the integration is carried out over all the individual GW events likelihood in the set $\{x\}$.

Evaluating Eq.(2.9) is not straightforward. The customary approach is to use Monte Carlo simulations of injected and detected events, which are simulated based on the chosen *hyperparameters* Λ, as described in [Mastrogiovanni et al., 2024], or make some simplifying assumptions. In the latter, we may state that an event x is detectable if its distance is below a certain threshold, depending on the sensitivity of the GW detector [Gair et al., 2023]. $p_{\rm det}$ would be 1 if detectors were perfectly able to see all the GW events in the Universe. Instead, they are sensitive to a subset of the parameter space defined by Λ. This is why correcting for the selection bias [Abbott et al., 2021b] is paramount. The mock events used to evaluate selection effects are called *injections*. Recently, there have been efforts to model the detection probability analytically [Lorenzo-Medina and Dent, 2025].

Finally, the posterior on the *hyperparameters* Λ, which is the final goal of a HBI, is given by:

$$p(\Lambda|\{x\}) \propto \pi(\Lambda)\mathcal{L}(\{x\}|\Lambda), \tag{2.10}$$

where $\pi(\Lambda)$ denotes the prior assumptions on the *hyperparameters*.

2.3.2 *Numerical implementation in the* `icarogw` *software*

In `icarogw`, the two integrals in Eq. (2.3) for the hierarchical likelihood and in Eq. (2.9) for selection effects are evaluated numerically

using Monte Carlo methods, as throughoutly explained in [Mastrogiovanni et al., 2024]. The likelihood of a single GW event x_i, $\mathcal{L}_{\rm GW}\left(x_i|\theta,\Lambda\right)$, is not accessible, because we only have the posterior samples from a Bayesian PE software, such as `Bilby`. Since we know the prior, $\pi(\theta)$, used to generate the posterior samples, we can numerically evaluate the integral in Eq. (2.3) summing over the posterior samples where we have undone the prior used to generate the samples:

$$\begin{aligned}\int \mathcal{L}_{\rm GW}\left(x_i|\theta,\Lambda\right)\frac{{\rm d}N_{\rm CBC}}{{\rm d}t{\rm d}\theta}(\Lambda){\rm d}\theta &\sim \frac{1}{N_{s,i}}\sum_{j=1}^{N_{s,i}}\frac{1}{\pi(\theta_{i,j}|\Lambda)}\frac{{\rm d}N_{\rm CBC}}{{\rm d}\theta{\rm d}t}(\Lambda)|_{i,j}\\ &\equiv \frac{1}{N_{s,i}}\sum_{j=1}^{N_{s,i}} w_{i,j}\end{aligned} \tag{2.11}$$

where $N_{s,i}$ quantifies the number of posterior samples for the event x_i, and $\pi(\theta_{i,j}|\Lambda)$ is the prior used to obtain the posterior samples.

The integral in Eq. (2.9) is analogously computed via Monte Carlo:

$$\begin{aligned}N_{\rm exp} &= T_{\rm obs}\int p_{\rm det}(\theta)\frac{{\rm d}N_{\rm CBC}}{{\rm d}t{\rm d}\theta}(\Lambda){\rm d}\theta\\ &\sim \frac{T_{\rm obs}}{N_{\rm gen}}\sum_{j=1}^{N_{\rm det}}\frac{1}{\pi_{\rm inj}(\theta_j)}\frac{{\rm d}N_{\rm CBC}}{{\rm d}t{\rm d}\theta}|j\\ &\equiv \frac{T_{\rm obs}}{N_{\rm gen}}\sum_{j=1}^{N_{\rm det}} s_j\end{aligned} \tag{2.12}$$

where $N_{\rm gen}$ is the total number of *injections*, whereas $N_{\rm det}$ is the detected ones. $\pi_{\rm inj}(\theta_j)$ is the prior used to generate the *injections*.

The final numerical expression for Eq. (2.3), as computed in `icarogw`, is given by:

$$\ln\mathcal{L}(\{x\}|\Lambda) \sim -\frac{T_{\rm obs}}{N_{\rm gen}}\sum_{j=1}^{N_{\rm det}} s_j + \sum_{i=1}^{N_{\rm obs}}\ln\left[\frac{T_{\rm obs}}{N_{s,i}}\sum_{j=1}^{N_{s,i}} w_{i,j}\right] \tag{2.13}$$

Given the theoretical and mathematical framework of the spectral-siren method outlined in this section, we will now present and discuss the results from the MDC in Sec. 2.4 and will provide some hints from the recent development with data from the first part of the fourth observing run, in Sec. 2.5.

2.4 *Mock Data Challenge (MDC)*

One of the crucial questions to investigate when inferring cosmological parameters with a new probe, as it is with GWs, is to assess

both the impact of our assumptions and the robustness of our method. This motivates the MDC work in [Agarwal et al., 2024]. On the one hand, we study the possible sources of systematics in the spectral-siren method implementation in `icarogw`. On the other hand, the main focus is to understand what is the extent of the bias, if any, introduced by not considering the redshift evolution of the BH mass spectrum, using detectors' sensitivity as that of the LVK interferometers during the fourth observing run. Already [Pierra et al., 2024] considered a redshift-dependent mass spectrum. In [Agarwal et al., 2024], we systematically explore the problem and quantify the bias coming from the mismodeling of the astrophysical BH population.

Since the scope of the MDC is two-folded, we distinguish between two scenarios. The difference is at the data-generation level; the inference, instead, is done under the same conditions. We proceed as follows:

- The `Vanilla` scenario serves as our benchmark. We model the BH population using the Power Law+Peak mass model without any redshift evolution, and in recovering the *hyperparameters*' posteriors, we do not assume any redshift dependence either. We use the `Vanilla` scenario to calibrate the technical setup of the inference code and also to provide forecasts on the precision with which we will be able to measure cosmological parameters.

- The `Redshift-Dependent` scenario serves to quantify the bias coming from not assuming the redshift dependence when inferring the *hyperparameters*, after the model, still Power law+Peak, used to generate the data, is described by redshift-dependent parameters.

In what follows, we provide all the details of the MDC setup in Sec. 2.4.1. After some validation checks of the reconstructed *hyperparametrs*' posteriors in Sec. 2.4.2, we first discuss the statistical uncertainties thanks to the results from the `Vanilla` case in Sec. 2.4.3. In Sec. 2.4.4, we analyze the impact of the wrong assumptions about the possible redshift-evolution of the astrophysical BBH population. Some potential future directions are addressed in Sec. 2.4.5.

2.4.1 *MDC setup*

The setup of the MDC is summarized in the flowchart in Fig. 2.3. We distinguish two steps: the simulation setup, in which we generate the GW data; and the analysis setup, where the single event GW posteriors are used in the HBI framework, as explained in Sec. 2.3, to infer the cosmological, population and rate *hyperparameters* using `icarogw` [Mastrogiovanni et al., 2024].

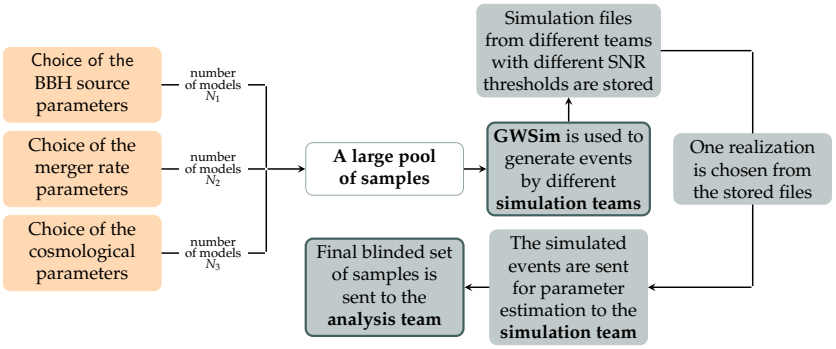

Figure 2.3: Schematic representation of the MDC setup. Figure adapted from [Agarwal et al., 2024] (Figure 1, ***authored by UD***)

In the generation of the mock GW data posterior samples, we simulate 3 years of observations with detectors' sensitivities as from the first four observing runs in the `Vanilla` case, and 1 year of observations with detectors' sensitivities as from the fourth observing run only in the `Redshift-Dependent` case. Tab. 2.1 reports the specifics of the simulation setup, the detectors' reference run sensitivities, and the corresponding duty cycles.

The mock data is generated with `GWSim` [Karathanasis et al., 2023]. All the *hyperparameters* entering in the rate, mass, and cosmological models are drawn randomly from a fixed prior range before being passed to `GWSim`. In the posteriors generation, with `Bilby` [Ashton et al., 2019], we assumed a threshold matched-filter SNR of $\rho_{\rm thr} = 10$ for the `Vanilla` case and $\rho_{\rm thr} = 12$ for the `Redshift-Dependent` case. A higher SNR threshold for the GW events in the `Redshift-Dependent` scenario is to reduce noise contamination and limit statistical fluctuations so that the effects of systematics coming from the population mismodeling can stand out more clearly.

We want to stress that the MDC is blinded, meaning that the *hyperparameters* used for the data generation are not revealed as long as the analysis with the HBI has not given the *hyperparameter* posteriors. Only at this point are the recovered and the injected values compared. This is meant to avoid any confirmation bias. In particular, ten different sets of *hyperparameters* are drawn from the same prior range, and ten sets of GW data are generated with `GWSim`. Only one of these data sets is randomly chosen and analyzed with `Bilby`. The posteriors are then used for the final analysis with `icarogw`. `Bilby` provides posterior distributions for [$\mathcal{M}_c$, q, d_L, `DEC`, `RA`, ι, Ψ, ϕ_c and t_c] for each of the analyzed GW events for both the scenarios, using the `IMPRhenomPv2` waveform approximant [Husa et al., 2016]. As of those in Tab. 1.1, all the other parameters are kept fixed by using a delta-prior. An example event for each case, `Vanilla` and `Redshift-Dependent`, is chosen to show the posterior distribution as obtained from `Bilby`. For the ana-

Table 2.1: List of detectors and relative duty cycle used in the analysis for both the `Vanilla` and the `Redshift-Dependent` scenarios. The sensitivities considered in the analysis correspond to the ones of the corresponding observing run. Adapted from [Agarwal et al., 2024] (Table 1)

`Vanilla` scenario: 286 **events** ($T_{\rm obs} = 3$ years)

Detector	Observation Run			
	O1	**O2**	**O3**	**O4**
LIGO Hanford	0.6	0.6	0.75	0.75
LIGO Livingston	0.5	0.6	0.75	0.75
Virgo	–	–	0.75	0.75

`Redshift-Dependent` scenario: 80 **events** ($T_{\rm obs} = 1$ year)

Detector	Observation Run			
	O1	**O2**	**O3**	**O4**
LIGO Hanford	–	–	–	0.75
LIGO Livingston	–	–	–	0.75
Virgo	–	–	–	0.75

lyzed parameters, instead, we used the standard priors used in LVK analyses [Abbott et al., 2019b, 2021a, 2023b]. Example corner plots are included in the Appendix A, and specifically, Fig. A.1 and Fig. A.2, for the `Vanilla` and `Redshift-Dependent` cases, respectively. The GW data posteriors serve for the single-event likelihood evaluation as described in Eq. (2.3).

The GW data differ between the two cases in the value of the *hyperparameters* used to generate them. In both scenarios, we assume BHs to have an astrophysical origin and model their population accordingly. In Tab. 2.2, we provide a list of all the used *hyperparameters*, distinguishing among the cosmological, mass, and rate ones. We describe each *hyperparameter* providing the injected values used for the `Vanilla` and `Redshift-Dependent` cases. For the `Vanilla` scenario we get 286 events over the three years of observation. For the `Redshift-Dependent` one, we simulate 80 events over one year of observation. In both cases, the simulated number of events represents the expected number of detections given the two rate models.

		Injected Value	
	Description	**Vanilla**	**Redshift-Dependent**
	ΛCDM Cosmological model		
H_0	Hubble constant in [km s^{-1}Mpc^{-1}]	67.8	173.28
Ω_m	Matter energy density today	0.3	0.3
	Madau-Dickinson rate model		
γ	PL exponent of rate ($z \lesssim z_p$)	2.7	0.03
κ	(Negative of) PL exponent of rate ($z \gtrsim z_p$)	2.9	2.92
z_p	Rate parameter (turnover point)	1.9	3.86
R_0	Local merger rate in [Gpc^{-3}yr^{-1}]	20	16.1
	Power Law + Peak mass model		
α	PL index of primary mass	3.4	$5.325 + 2.99z$
β	PL index of secondary mass	0.8	$3.05 - 1.063z$
$m_{\min}$	minimum source mass in $M_\odot$	5	$7.8 + 0.324z$
$m_{\max}$	maximum source mass in $M_\odot$	100	$87.58 + 17.16z$
δ_m	smoothing factor in $M_\odot$ at low-mass cut-off	4.8	3.19
μ_g	peak of the Gaussian in $M_\odot$	35	$40.9 + 2.84z$
σ_g	sigma of the Gaussian in $M_\odot$	3.9	$7.63 + 2.70z$
λ_{peak}	fraction of events in Gaussian, in $[0, 1]$	0.04	$0.04 + 0.43z$

Table 2.2: Summary of injected values used to model the GW events for the two scenarios: `Vanilla` and `Redshift-Dependent`. We provide a list of all the used *hyperparameters*, distinguish among the cosmological, mass, and rate ones. We describe each and give the injected values used for the `Vanilla` and `Redshift-Dependent` cases. Table adapted from [Agarwal et al., 2024] (Table 2, ***authored by UD***)

We assume the flat Λ Cold Dark Matter (ΛCDM) cosmological model.

The rate is described with a Madau-Dickinson model as in Eq. (2.6). Their *hyperparameters* are redshift-independent and different between the `Vanilla` and the `Redshift-Dependent` cases. For the mass model, instead, we use a POWER LAW+PEAK as shown in subplot (c) of Fig. 2.2, assuming a linear redshift dependence of the *hyperparameters* for the `Redshift- Dependent` case.

In the following, we provide the analytical expression for the POWER LAW+PEAK mass model [Abbott et al., 2019a, 2021b]:

$$p(m_{1,\mathrm{src}}|\Lambda_{\mathrm{pop}}) \propto [(1-\lambda_{\mathrm{peak}})\mathcal{P}(m_{1,\mathrm{src}}|-\alpha, m_{\mathrm{max}}) + \lambda_{\mathrm{peak}}\mathcal{G}(m_{1,\mathrm{src}}|\mu_g, \sigma_g)]S(m_{1,\mathrm{src}}|m_{\mathrm{min}}, \delta_m) \tag{2.14}$$

The *hyperparameters* it depends on, and specifically the PL indexes α and β, the mass range m_{min} and m_{max}, the Gaussian $\mathcal{G}$ peak parameters, μ_g, σ_g, the fraction of events in the peak λ_{peak}, and the smoothing parameter δ_m, are listed and described in Tab. 2.2.

What changes between the `Vanilla` and the `Redshift-Dependent` scenarios is that the mass model parameters in the latter case get a linear dependence on redshift [Karathanasis et al., 2023]. The redshift dependence of all the mass parameters is expressed as $x(z) = x_0 + z\epsilon_x$, where x_0 is the value at $z = 0$ (see Tab. 2.2 for the details of the chosen values).

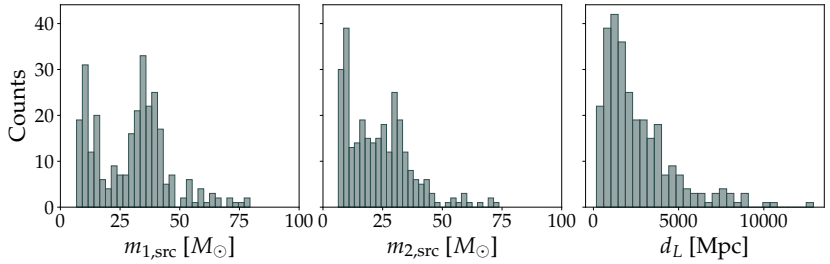

(a) `Vanilla` injections

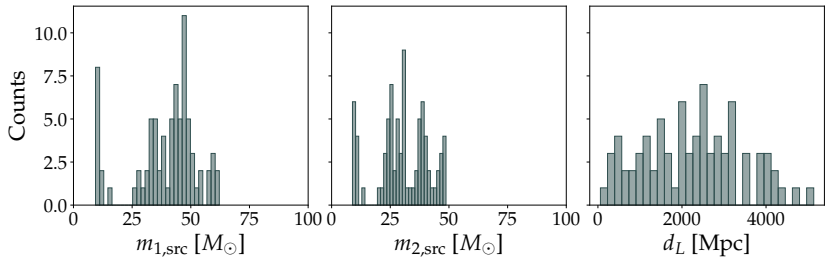

(b) `Redshift-Dependent` injections

Figure 2.4: Source parameters, the components masses and luminosity distance, distributions for the `Vanilla`, in the *top* panel, and the `Redshift-Dependent` scenario, in the *bottom* one. Figure adapted from [Agarwal et al., 2024] (Figure 2 and Figure 5)

We study a `Redshift-Dependent` scenario to take into account environmental effects on the stellar evolution. In fact, in [Dopcke et al., 2013] and [Li et al., 2023], it is shown that in low-metallicity environments, it is more likely to form more massive stars [Clarke and

Bromm, 2003; Dopcke et al., 2013]. Moreover, at higher metallicities, stellar winds are generally stronger resulting in lighter remnants [Vink et al., 2001; van Loon, 2005; Mokiem et al., 2007]. Therefore, we might expect more massive BHs at higher redshifts. Mass-dependent delay times should be also considered. Redshift-dependent BH mass distributions have been already addressed in [Mukherjee, 2021; Karathanasis et al., 2023].

In Fig. 2.4, we show both the masses and the luminosity distance distributions for the 286 events of the `Vanilla` model in the *top* panel, and the 80 events of the `Redhsift-Dependent` scenario, in the *bottom* panel. In both cases, the maximum injected redshift is $z_{\max} \sim 1.7$. Given the high H_0 value for the `Redshift-Dependent` scenario, the distance distribution ranges in relatively smaller values. Moreover, for the `Redshift-Dependent` scenario, there are fewer sources in the mass interval between $10M_\odot$ and $30M_\odot$ because of the steeper PL indexes for both the primary and the secondary BH masses.

In Fig. 2.5, we show the dependence of the primary BH mass spectrum on the redshift value: notice the shift towards heavier BHs for higher z values.

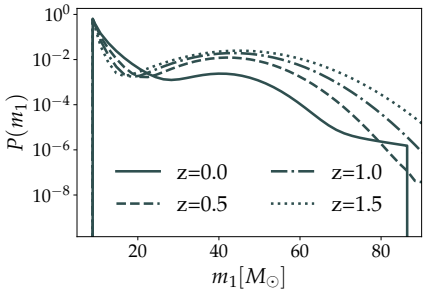

Figure 2.5: Evolution with redshift of m_1 as in the `Redshift-Dependent` scenario analyzed in the MDC. Figure adapted from [Agarwal et al., 2024] (Figure 3)

Table 2.3: List of priors used in the analysis for both the `Vanilla` and the `Redshift-Dependent` scenarios. Table from [Agarwal et al., 2024] (Table 3, ***authored by UD***)

	Priors	
	`Vanilla`	**`Redshift-Dependent`**
H_0	$\mathcal{U}(30,140)$	$\mathcal{U}(10,250)$
$\Omega_{m,0}$	$\mathcal{U}(0.1,0.9)$	$\mathcal{U}(0.1,0.9)$
α	$\mathcal{U}(1.5,12)$	$\mathcal{U}(1.5,12)$
β	$\mathcal{U}(-4,12)$	$\mathcal{U}(-4,12)$
$m_{\min}$	$\mathcal{U}(2,10)$	$\mathcal{U}(2,10)$
$m_{\max}$	$\mathcal{U}(50,200)$	$\mathcal{U}(50,200)$
δ_m	$\mathcal{U}(0,10)$	$\mathcal{U}(0,10)$
μ_g	$\mathcal{U}(20,50)$	$\mathcal{U}(10,80)$
σ_g	$\mathcal{U}(0.4,10)$	$\mathcal{U}(0.4,20)$
λ_{peak}	$\mathcal{U}(0,1)$	$\mathcal{U}(0,1)$
γ	$\mathcal{U}(0,12)$	$\mathcal{U}(0,12)$
κ	$\mathcal{U}(0,6)$	$\mathcal{U}(0,6)$
z_p	$\mathcal{U}(0,4)$	$\mathcal{U}(0,4)$
R_0	$\log\mathcal{U}(10^{-2},10^3)$	$\log\mathcal{U}(10^{-2},10^3)$

2.4.2 *Reconstructing the hyperparameters' posterior*

Starting from the posterior samples of the GW events, for each of the two scenarios, we reconstruct the posterior of the *hyperparameters* listed in Tab. 2.2, using the HBI scheme with the `icarogw` software [Mastrogiovanni et al., 2024]. Within `icarogw` the sampling is done with `Bilby` [Ashton et al., 2019] using `dynesty` [Speagle, 2020]. The priors we apply to the *hyperparameters* are listed in Tab. 2.3. In neither case, we assume a redshift dependence in the analysis, and the priors we use are broad and uninformative. Between the two cases, just three parameters, H_0, μ_g and σ_g, feature different prior ranges. These were changed from the reference `Vanilla` ones after preliminary results were obtained and showed railing on either side of the prior range for these three parameters. Therefore, H_0, μ_g, and σ_g are sampled from an enlarged prior interval with respect to the `Vanilla` case. This is justified given the blinded nature of the MDC.

In the following, we first present the reconstruction of the posterior distribution of the *hyperparameters* entering in the rate and mass model for both the analyzed scenarios, and compare them to the distributions from which the BBH populations have been sampled [4].

In Fig. 2.6, we show the rate reconstruction for the `Vanilla` scenario on the *left*, and the `Redshift-Dependent` one on the *right*. In each plot, the *dark green*-colored lines show the posterior samples from the 68% highest density interval (HDI). Instead, the *orange* lines represent

[4] All the scripts used for the analysis in the MDC are available on

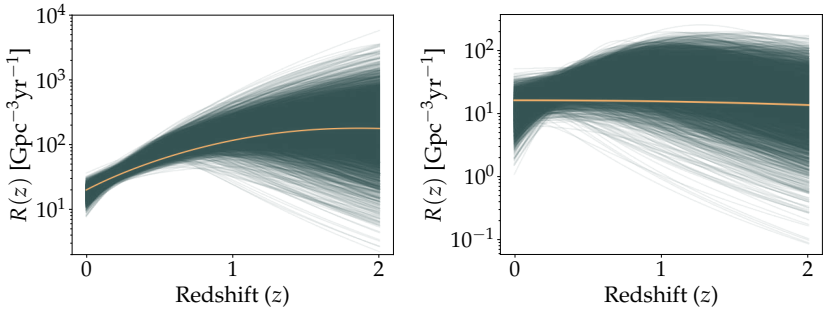

(a) `Vanilla` (b) `Redshift-Dependent`

Figure 2.6: Rate reconstruction for the `Vanilla` scenario, on the *left*, and the `Redshift-Dependent` scenario, on the *right*. The *orange* lines represent the two distributions from which the BBH populations were sampled. The *dark green*-colored lines, instead, are drawn from the 68% HDI of the parameter posterior distributions. Figure adapted from [Agarwal et al., 2024] (Figure 6 and Figure 17, ***authored by UD***)

the rate distributions from which the BBH events were drawn. The recovered distributions match well the injected ones.

The `Vanilla` mass distribution reconstruction is shown in Fig. 2.7-(a). The rationale behind the plot is the same as in Fig. 2.6, where the *orange* line represents the starting distribution and the *dark green* lines the ones reconstructed from the posterior samples at 68% HDI.

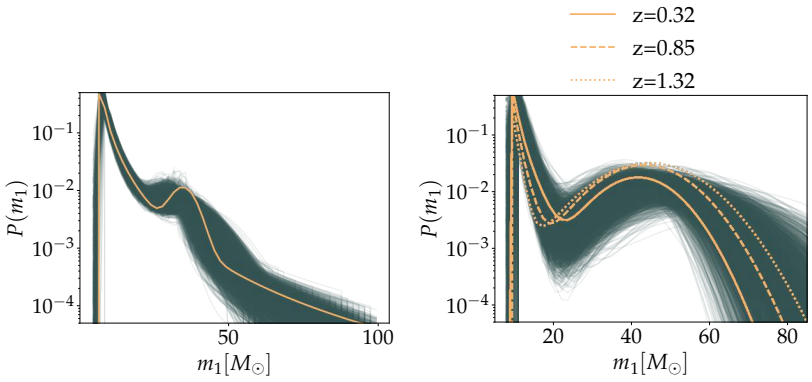

(a) `Vanilla` (b) `Redshift-Dependent`

Figure 2.7: Mass reconstruction for the `Vanilla` scenario, on the *left*, and the `Redshift-Dependent` scenario, on the *right*. In both subplots, the *dark green*-colored lines are drawn from the 68% HDI of the parameter posterior distributions. The *orange* line for the `Vanilla` case represents the distributions from which the BBH masses were sampled. The three *orange* lines (solid, dashed, and dotted), instead, represent the model at three example redshift values, as defined in Tab. 2.2. These redshift values have been selected to fall in the middle of the redshift ranges if we were to divide the events into three sets with a similar number of events each. Figures adapted from [Agarwal et al., 2024] (Figure 7 and Figure 16, ***authored by UD***)

For the `Redshift-Dependent` scenario, shown in Fig. 2.7-(b), the reconstructed posterior distribution features three *orange* lines (solid, dashed, and dotted) representing different examples of the model at three specific redshift values, as defined in Tab. 2.2. These redshifts were chosen to lie near the centers of redshift intervals that would result from dividing the events into three subsets containing approximately equal numbers of events (see discussion around Fig. 2.12 in Sec. 2.4.4).

The reconstructed rate and mass distributions for the `Vanilla` and the `Redshift-Dependent` cases agree with our starting assumptions. In what follows, the details of the reconstruction of single parameters are presented.

As for the cosmological parameters posterior reconstruction, and,

in particular, for the parameter of interest H_0, we have:

- For the `Vanilla` scenario, we obtain the following estimate of the Hubble constant at the 68% C.L.:

$$H_0 = 62^{+28}_{-21}\,\mathrm{km\ s^{-1}Mpc^{-1}}, \tag{2.15}$$

  which is within 1σ compared to the injected value of $67.8\,\mathrm{km\ s^{-1}Mpc^{-1}}$

- For the `Redshift-Dependent` scenario, we obtain, at the 68% C.L.:

$$H_0 = 103^{+38}_{-33}\,\mathrm{km\ s^{-1}Mpc^{-1}}, \tag{2.16}$$

  which falls in the 2σ region from the injected value of $173.28\,\mathrm{km\ s^{-1}Mpc^{-1}}$

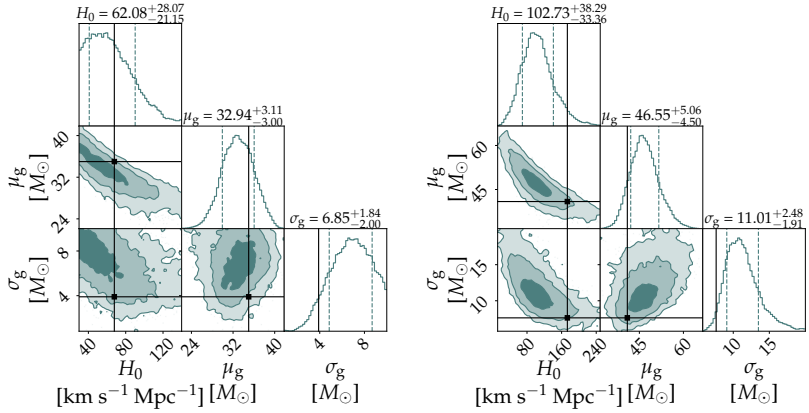

(a) `Vanilla` case (b) `Redshift-Dependent` case

Figure 2.8: Reduced corner plot for the `Vanilla` scenario, in subplot (a), and for the `Redshift-Dependent` case, in subplot (b), of H_0 and parameters that mostly correlate with H_0, namely μ_g and σ_g. The injected (true) values are plotted as black lines. Figure adapted from [Agarwal et al., 2024] (Figure 8 and Figure 13, ***authored by UD***)

In Fig. 2.8, we show the posterior distribution for the Hubble constant for both scenarios, the `Vanilla` one on the *left*, and the `Redshift-Dependent` one on the *right*. In the corner plot, we highlight the distributions of the two parameters that mostly correlate with H_0: the Gaussian peak parameters, μ_g, and σ_g. Both show a negative correlation with H_0. This is explained as follows: larger values of μ_g suggest that more massive, in the source frame, BBH systems are more likely. This implies the inferred redshifts are lower. Therefore, to accommodate such massive events at their observed luminosity distance, we need lower values of H_0[5]. We find that degeneracies between cosmological and mass model parameters might shift the H_0 value from the true one, even if the model to generate the astrophysical BBH population is the same used in the reconstruction analysis. The effect is minor and within 1σ.

In Appendix A, we show the full corner plots for all the 14 *hyperameters* analyzed in the HBI framework with `icarogw`, for the the `Vanilla`

[5] We have to keep in mind the luminosity distance, redshift, and H_0 interplay at low z (the Hubble law as in Eq. (1.4)):

$$d_L \sim \frac{cz}{H_0}$$

From here, it is straightforward to understand that if we measure a certain value for d_L, but the inferred redshift is lower because systems are generally more massive in the source frame, we need a lower value for H_0 as well.

case in Fig. A.1, and for the `Redshift-Dependent` case in Fig. A.2. What we can generally say is that, in both scenarios, leaving out H_0, which deserves a separate discussion, provided in Sec. 2.4.4, almost all the *hyperparameters* are recovered within the 1σ region from the injected values described in Tab. 2.2. Specifically, for the `Redshift-Dependent` scenario, we consider as for the injected values the ones at $z = 0$. A few parameters show a slight offset. These parameters are, in both cases, α, $m_{\rm min}$, σ_g, and γ. For the `Redshift-Dependent` case, we have to add β, $\lambda_{\rm peak}$, and $z_{\rm peak}$ to the list of *hyperparameters* recovered slightly outside the 1σ region. In the latter, the γ value is particularly off, as the injection itself is close to the border of the prior space. For the $z_{\rm peak}$ value, instead, another badly recovered *hyperparameter*, the reason lies in a low number of detected events at the injected value of high redshift (we inject $z_{\rm peak} = 3.86$).

2.4.3 *`Vanilla` scenario: statistical uncertainties*

The `Vanilla` scenario serves as our reference study. Since the models used to draw and recover the BBH population are the same, we can use the `Vanilla` setup to run some statistical tests and assess the robustness of the spectral-siren method, as it is implemented in `icarogw`.

As shown in Sec. 2.3, from Eq. (2.3), as well as from its numerical version Eq. (2.13), the two primary quantities governing the hierarchical likelihood are the number of observed GW events, and the number of detected GW in the calculation of the selection bias. In the following, we present a series of checks on the two Monte Carlo integrals.

- **Injection samples: number and realization**: to study the robustness of the HBI scheme, we examine the effects of both varying the number of injections, that is, the number of GW signals used to evaluate selection effects, and their sample realization. The precision of this estimation depends on the number of simulated injections relative to the number of observed GW events. Numerically, it comes down to a Monte-Carlo sum (see the first term of Eq. (2.13)); we expect to have more accurate results the larger the number of injections. We test this hypothesis using all the 286 events and varying the number of injections in $[10^4, 10^5, 10^6]$. We present the results for H_0 in subplot (a) of Fig. 2.9, and for all the *hyperparameters* in Appendix A.2 in Fig. A.3. We get very similar results with 10^5 and 10^6 injections. With 10^4 injections, the posteriors start to deviate from the injected values but still show good agreement. With 10^3 injections, instead, the integral is not able to converge. Usually, a rule of thumb to have good numerical stability in evaluating the integral for selection effects is that the effective number of injections, which depends on the total one, should be at least 4 times the number

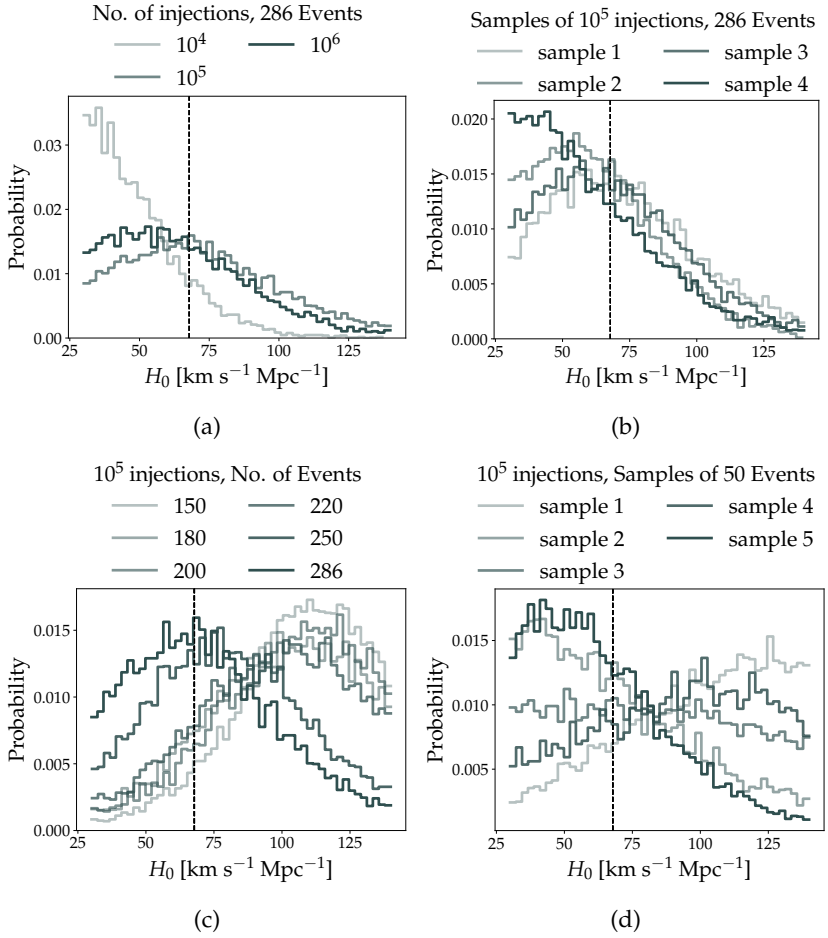

Figure 2.9: Posterior samples distribution for the H_0 parameter in a series of statistical tests within the `Vanilla` scenario. In the *top* two plots, we show the impact of the injections to account for the selection bias. The number of GW corresponds to the total of 286. In subplot (a), we vary the number of injections in $[10^4, 10^5, 10^6]$, while, in subplot (b), we use different sample realizations of 10^5 injections each. In the *bottom* two plots, instead, we fix the number of injections used for selection effects evaluation at 10^5, and vary, in subplot (c), the number of GW events used for the HBI, and in subplot (d), the GW events sample realization using batches of 50 events. Figure adapted from [Agarwal et al., 2024] (Figure 9, Figure 10, Figure 11, and Figure 12, ***authored by UD***)

of observed GW events (see [Farr, 2019; Talbot and Golomb, 2023; Mastrogiovanni et al., 2024] for a detailed discussion on numerical stability of the integrals in Eq. (2.13)). Since we use 286 observed GWs, 10^3 injections are indeed too few.

In Fig. 2.9, we show similar results for H_0 for different sample realizations of the 10^5 injections, while in Fig. A.4 the analysis is repeated for the whole set of *hyperparameters*. The results do not show any dependence on the realization of the injection sample.

- **GW events: number and sample realization**: we want to study the impact of the number of GW events on the *hyperparameter* posterior, and, given a fixed number of GW events, the presence of outliers by considering different event sample realization. In the first case, we compare the results using different numbers of GW events, specifically $[150, 180, 200, 220, 250, 286]$, with 10^5 injections. In the previous point, we assess that 10^5 and 10^6 injections produce the same outcome and are sufficient to ensure the integral's convergence. Anal-

ogously, we show the results for H_0 in subplot (c) of Fig. 2.9 and for all the *hyperparameters* in Fig. A.5. The results confirm that the larger the number of observed events, the better the constraints.

The last test studies the GW events sample realization. Due to the homogeneity principle, if no outliers are present, we expect results with random deviations that statistically average out. To this scope, we split the observed GW catalog into batches of 50 events and analyze the resulting sub-populations with 10^5 injections. We show the results for H_0 only in subplot (d) of Fig. 2.9, and full ones in Fig A.6. We find that there are no outliers in our sets of events.

2.4.4 `Redshift-Dependent` *scenario: the role of wrong assumptions*

With the `Vanilla` case analyses, we have shown that the inference pipeline is indeed robust. The statistical and sampling uncertainties presented in Sec. 2.4.2 are under control. The inference does not show biases when the model used to generate and recover the astrophysical population of BHs is the same.

The second part of our analysis, the `Redshift-Dependent` scenario, aims to quantify the bias from the mismodeling of the BBH population at the analysis level by assuming redshift independence when the data is generated under this assumption. Even though we use a specific mass model, the Power Law+Peak, the effects on the H_0 inference would happen with any other model, as there is a mismatch between the simulation and the analysis setups.

In the `Redshift-Dependent` case, we indeed find a value for the Hubble constant that lies in the 90th percentile, as shown in Fig. 2.8, at a distance of 2σ (if we approximate the posterior to a Gaussian) from the injected value (see also the discussion in Sec. 2.4.2). We tend to recover a lower value for H_0, and this is independent of the number of GW events we use in the analysis, as we can see from Fig. 2.10. Here, we vary the number of GW events with 10^5 injections for selection effects evaluation. The inferred value of H_0 is not closer than the 76th percentile. Therefore, the statistical uncertainty due to fewer events does not cause bias.

As we have already seen, a few other *hyperparameters*, α, β, $m_{\rm min}$, $\lambda_{\rm peak}$, $z_{\rm peak}$, μ_g, and σ_g show about 1σ discrepancy. Since, μ_g and σ_g are mostly correlating with H_0, in Fig. 2.11, we show in *black* their posterior distribution. There we compare the median of the recovered distribution, shown in *dotted black* line, to the values of the parameters at different redshifts, as in the colorbar, following the linear redshift dependence described in Tab. 2.2. Indeed, the recovered values fall in the range foreseen for the span in reshift of the analysis.

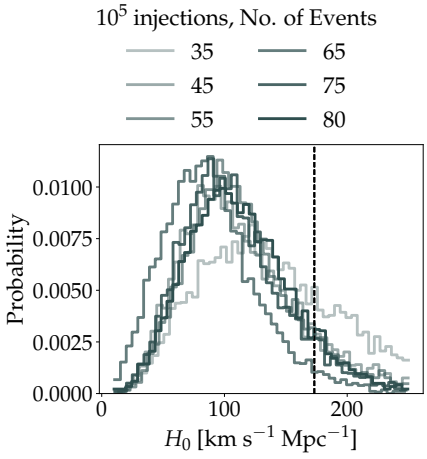

Figure 2.10: Posterior samples for H_0 in the `Redshift-Dependent` scenario, with varying number of GW events. The *dashed black* line represents the injected value. Figure adapted from [Agarwal et al., 2024] (Figure 18, ***authored by UD***)

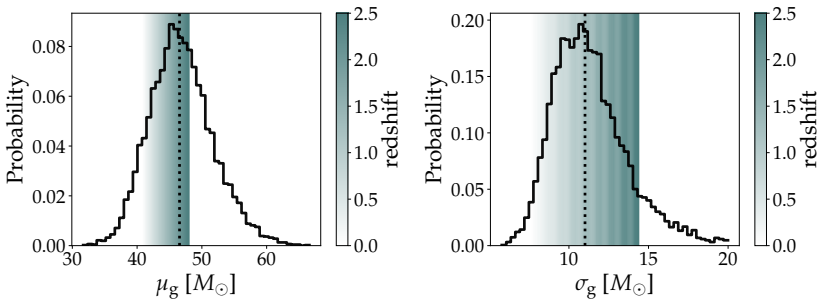

(a) `Redshift-Dependent` case: μ_g (b) `Redshift-Dependent` case: σ_g

Figure 2.11: Posterior samples for μ_g and σ_g from the `Redshift-Dependent` scenario are plotted in *black*. The *dotted black* vertical line represents the median of the distribution. The *dark green*-colored region represents the values of the injected μ_g, $40.9 + 2.84z$, and σ_g, $7.63 + 2.70z$, at different redshifts specified in the colorbars, shown on the *right* of each plot. Figure adapted from [Agarwal et al., 2024] (Figure 14 and Figure 15, ***authored by UD***)

The key point of our analysis is to explore the impact of mismodeling the mass on the inference of the Hubble constant. To better understand the origin of the measured discrepancy, as we did in Fig. 2.5, we divide our GW events into three redshift bins, with a nearly equal number of sources in each group. In this analysis, we split the events into three bins, redshift-wise, and evaluate the product over the observed events as in Eq. (2.13). The selection function of the analysis does not change, except for a reduction in T_{obs} by one-third for each group, since it does not depend on the index denoting individual GW events. The redshift bins are $z < 0.65$, $0.65 \leq z < 1.05$, and $z \geq 1.05$. However, it should be specified that to obtain physically correct results from the single bins, one should account for the selection bias properly. The binned analysis serves to look into the single partial contributions from the selected bins. It remains that multiplying the posteriors from the three bins leads to the overall correct results, as those reported in Fig. 2.8-(b).

In Fig. 2.12, we show the reduced corner plot for H_0, along with μ_g and σ_g for the three redshift ranges. We observe that for the lower redshift range, $z < 0.65$, the value of H_0 matches very well with the injected value of the Hubble constant as shown by the *solid black* line. This is also valid for the other parameters μ_g and σ_g, strongly correlated with H_0. However, as we move towards the two higher redshift bins, the posterior on H_0 moves towards lower values, and the posteriors on μ_g and σ_g move towards higher values, as a consequence of the negative correlation we explained in Sec. 2.4.2. Since higher redshift values correspond to intrinsically more massive mass distributions, an analysis model that fails to account for this effect tends to assign higher values to μ_g and σ_g. As a result, this leads to an inferred redshift that is lower than the actual redshift.

The sources from the lowest redshift bin have minimal impact on the redshift evolution of the mass model. Even though we are not assuming a redshift dependence in our analysis, the effects due to mis-

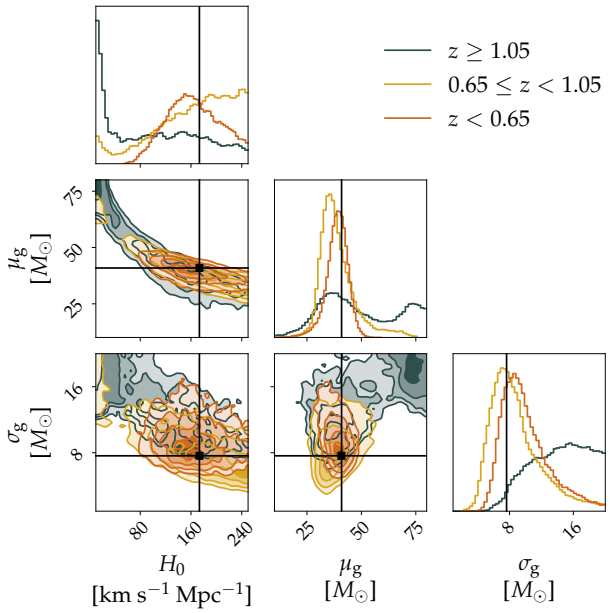

Figure 2.12: Reduced corner plot for H_0, μ_g and σ_g parameters for the `Redshift-Dependent` scenario. We show results obtained selecting events in three different redshift ranges: $z < 0.65$, $0.65 \leq z < 1.05$, and $z \geq 1.05$. The injected values are shown in *black*. For μ_g and σ_g they refer to the injected values at $z = 0$ as in Tab. 2.2. Figure adapted from [Agarwal et al., 2024] (Figure 19, ***authored by UD***)

modeling are minimal. On the other hand, for sources in the higher redshift bins, the redshift evolution of the μ_g and σ_g parameters moves the values by about 10% and 50% respectively towards a higher value in comparison to the lowest redshift bin case, resulting into larger mismodeling. The inferred value of the Hubble constant H_0 is shifted towards a lower value compared to the injected value, as demonstrated in Fig. 2.12. This decrease is largely due to a strong negative correlation between the mass parameters, μ_g and σ_g, and H_0. Consequently, the inferred H_0 is lower than the actual H_0 value used in the simulation. This effect becomes more pronounced for redshift bins above $z \sim 0.65$, where changes in μ_g and σ_g due to redshift are significant.

All our results, from both the `Vanilla` and the `Redshift-Dependent` cases, are summarized in Fig. 2.13. These refer to the two reference analyses involving 10^6 injections, using all 286 events for the `Vanilla` case (shown in *orange*) and 80 events for the `Redshift-Dependent` case (shown in *dark green*). The *x*-axis represents the inferred *hyperparameters*, while the *y*-axis displays all posterior samples normalized by the median value of each distribution to facilitate an easier comparison across a single plot. The boxplots are structured to show the 1σ range of the data around the median in a darker shade and the 2σ range in a lighter shade. The whiskers extend from the minimum to the maximum values, encapsulating all the data points. Additionally, the *black triangles* indicate the injected values normalized by the corresponding median of their distributions. The text provides the median values of the parameters along with their 68% confidence intervals. The same

information can be found in the two corner plots in Fig. A.1 for the `Vanilla` scenario and Fig. A.2 for the `Redshift-Dependent` one.

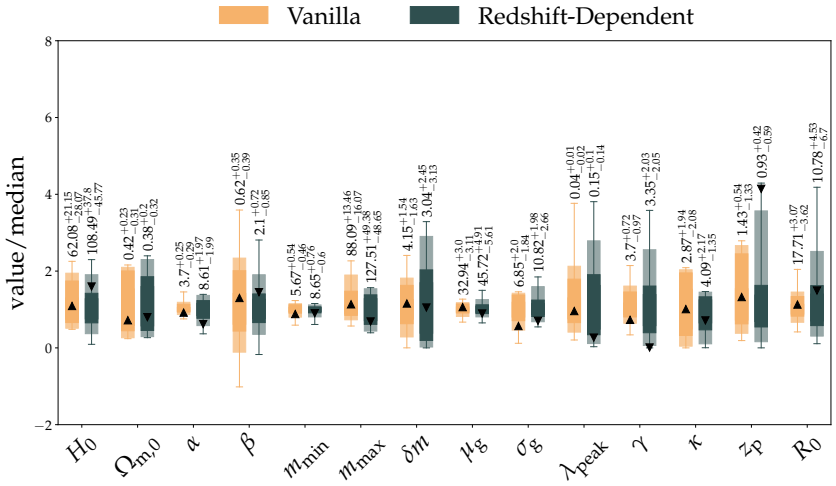

Figure 2.13: Summary of results for the `Vanilla` scenario (shown in *orange*) and the `Redshift-Dependent` scenario (shown in *dark green*). The findings are based on two reference analyses involving 10^6 injections, using all 286 events for the `Vanilla` case and 80 events for the `Redshift-Dependent` case. The x-axis represents the inferred *hyperparameters*, while the y-axis displays all posterior samples normalized by the median value of each distribution to facilitate an easier comparison across a single plot. The boxplots are structured to show the 1σ range of the data around the median in a darker shade and the 2σ range in a lighter shade. The whiskers extend from the minimum to the maximum values, encapsulating all the data points. Additionally, the *black triangles* indicate the injected values normalized by the corresponding median of their distributions. The text provides the median values of the parameters along with their 68% confidence intervals. Figure adapted from [Agarwal et al., 2024] (Figure 20, ***authored by UD***)

The plot in Fig. 2.13 also shows that the posteriors for μ_g and σ_g do not exhibit significant deviations. However, even a slight variation of 10% in μ_g can result in a deviation of more than 1.5σ for H_0 from the injected value, particularly due to sources located at greater distances.

The inferred parameters that describe the astrophysical mass distribution do not show any significant differences from the injected parameters even when the true underlying model is unknown. This means that even if the mass distribution changes slightly, the values of μ_g and σ_g align well with the inferred posterior distribution. Consequently, when analyzing different redshift bins of the GW sources, there is no significant deviation in the mass distribution within individual redshift bins mainly due to large error bars. However, the combined posterior estimate of the Hubble constant reveals a noticeable discrepancy from the true value.

The value of H_0 is influenced by sources located at various redshift ranges. Suppose there is a monotonic evolution in the mass distribution of BBHs. In that case, whether increasing or decreasing, the inferred redshift may start to deviate from the true redshift in a consistent manner. Consequently, the estimated value of the Hubble constant H_0 will also monotonically increase or decrease.

In reality, using an incorrect model for the inferred mass distribution might still provide a reasonable understanding of the mass distribution. However, this could lead to estimating H_0 as lower or higher than its true value, depending on whether the mass distribution is increasing or decreasing with redshift.

In this analysis, although the injected Hubble constant H_0 is set to a high value due to the blinded nature of the MDC, the essential finding regarding the impact of redshift evolution on mass distribution remains valid, indicating a discrepancy in the inferred value of H_0.

2.4.5 *Quantifying the bias: what's next?*

Exploring a `Redshift-Dependent` mass model aims to understand its effects on cosmological inference. This is crucial due to our limited knowledge of how mass evolves over time, which is influenced by complex BBH formation channels and their dependence on the metallicity of parent stars. The metallicity of the Universe varies significantly with redshift, exhibiting a decreasing trend at higher redshifts. Additionally, there is considerable variation in metallicity from one galaxy to another. Consequently, alongside a consistent redshift evolution, we can expect additional stochastic behavior in the masses of BHs over redshift. This variability can result in a broad mass distribution that diverges from any straightforward monotonic trend associated with redshift.

In this MDC, we have considered a simple scenario of linear evolution with redshift for the parameters controlling mass distribution. However, in reality, the evolution of mass distribution can be significantly more complex.

Quantifying the bias coming from the mismodeling of the astrophysical population of BBHs is a first step in investigating the possible sources of systematics. In the future, understanding the interplay between astrophysical assumptions and cosmological parameters will be crucial, requiring better sensitivity and a higher number of events.

The study conducted in the MDC provides a framework for assessing the reliability of a *Standard Siren* cosmology method and can be expanded in various directions. In [Agarwal et al., 2024], for example, we did not include the spins in our model. Generalizing the analysis to include both mass and spins in the BBH mass model is the natural continuation of [Agarwal et al., 2024]. There is, however, much more to explore, from studying the impact of inaccurate waveforms [Kunert et al., 2024], the systematics coming from the inclination angles estimates [Müller et al., 2024; Salvarese and Chen, 2024], from the peculiar velocity of galaxies [Mukherjee et al., 2021; Nimonkar and Mukherjee, 2023], or the photometric uncertainty of the galaxies' redshift [Turski et al., 2023], to extending to other *Standard Siren* techniques.

2.5 Cosmological constraints from O4a data

In the following section, we will give some hints from the cosmological analysis inside the LVK Collaboration considering the recently concluded first part of the fourth observing run, henceforth O4a. O4a data-taking occurred from May 2023 to January 2024 (see Sec. 1.2.4 for a detailed description of observing runs in LVK). Together with the data from the first three observing runs [Abbott et al., 2019b, 2021a, 2023b], we are now constructing the fourth catalogue of events, the GWTC-4 catalogue.

We are not going into the details of the ongoing LVK cosmological analysis as the work is still in development. The objective is to show some preliminary results, limiting ourselves to the spectral-siren method with the `icarogw` pipeline described in this chapter. We want to showcase how the constraints on H_0 are improving with the increased amount of observations. Additionally, we want to emphasize the crucial role of modeling the underlying population, which is the main focus of this chapter. To this scope, we present a new mass model that is being tested and used in LVK, which allows us to comprise all the CBCs in one mass distribution without the need to distinguish between NSs and BHs, which might be problematic in some cases, as for the `GW190814` event [Abbott et al., 2020d], an asymmetric binary case, where the heaviest component might either be a light BH, or a heavy NS.

In Sec. 2.5.1, we present the data from GWTC-4 that is used to infer cosmological parameters. In Sec. 2.5.2, we briefly address the new mass model that describes BHs and NSs masses in a unified framework. Additionally, we anticipate some H_0 estimates with the spectral-siren method. As stressed above, this section reflects the preliminary nature of the analysis conducted inside the LVK Cosmology group. On top of this, we report only a small subset of the results under study in the LVK Collaboration paper.

2.5.1 Data selection for O4a cosmology

To ensure the purity of the data used for cosmological inference, we filter the GWTC-4 catalogue by considering the events with a False Alarm Rate (FAR) less than $1\,\mathrm{yr}^{-1}$ (see Sec. 1.2.4). This leaves us with 155 events[6], of which 5 contain at least one neutron star. We are not considering the only bright siren, `GW170817`. This allows us to more than double the number of CBC events used in the previous cosmological analysis in [Abbott et al., 2023a], where 47 CBCs have been used. From now on, when referring to O4a data, we mean the ones that satisfy the selected FAR criterium.

[6] These numbers do not represent the final selection, which is ongoing.

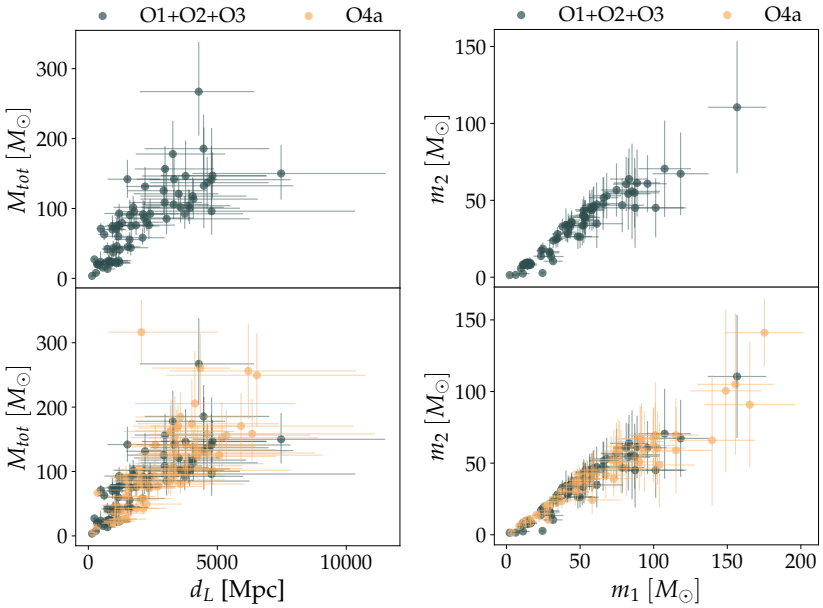

(a) $M_{tot} - d_L$ from GWTC-4

(b) m_1-m_2 from GWTC-4

Figure 2.14: GWTC-4 data in the $M_{tot} - d_L$ parameter space, on the *left*; and the m_1-m_2 parameter space, on the *right*. In the *top* panels, we show, in *dark green*, data from the first three observing runs, while, in the *bottom* panels, we highlight, in *orange*, the new events from O4a.

In Fig. 2.14, we show the mass and distance parameter space of the GWTC-4 catalogue, distinguishing, in *dark green*, the events from the previous three runs (these are also plotted separately in the upper panel of each figure), and, in *orange*, the new events from the first part of the fourth observing run. In the *left* panel, we plot the measured luminosity distances and the total mass of the binary in the detector frame. The error bars encompass the 90% C.L. In the *right* panel, we show the binary's masses in the detector frame. Comparing the new events with the ones from the first three runs, we see that the covered parameter space remains the same. We gain in statistics thanks to the improved sensitivities of the LVK detectors.

2.5.2 H_0 estimate with GWTC-4 data

In Sec. 2.2, we describe the mass models analyzed in LVK [Abbott et al., 2021b,c]. These refer to the status of our understanding as of the GWTC-3 catalogue. The preferred model was Power Law + Peak [Abbott et al., 2021c].

Currently, a new model is being used, encompassing both NSs at the low mass end and BHs. Since it allows us to consider all the CBCs observed so far in our spectral siren analysis, we manage to put tighter constraints on the H_0 value. We refer to it as the Multi Pop model.

In the analysis with GWTC-4, we use the new Multi Pop model, together with the Power Law + Peak and the Multi Peak mod-

els. The MULTI POP model takes inspiration from some previous works [Fishbach et al., 2020; Farah et al., 2022; Mali and Essick, 2024]. It features a BROKEN POWER LAW, $\mathcal{BPL}$, and two Gaussian Peaks. A smooth transition between NSs and BHs is guaranteed by a break located in a depletion region, called dip, which depth, representing how well separated the two populations are, is one of the model's *hyperparameters*. The analytical expression for the primary source mass distribution is given by:

$$\begin{aligned} p(m_{1,\mathrm{src}}|\Lambda_{\mathrm{pop}}) \propto & [(1-\lambda_{\mathrm{peak}})\mathcal{BPL}(m_{1,\mathrm{src}}|m_{\mathrm{min,NS}}, m_{\mathrm{max,BH}}, -\alpha_1, \alpha_2, b) \\ & + \lambda_{\mathrm{peak}}\lambda_{\mathrm{peak,low}}\mathcal{G}(m_{1,\mathrm{src}}|\mu_{g,\mathrm{low}}, \sigma_{\mathrm{low}}) \\ & + \lambda_{\mathrm{peak}}(1-\lambda_{\mathrm{peak,low}})\mathcal{G}(m_{1,\mathrm{src}}|\mu_{g,\mathrm{high}}, \sigma_{\mathrm{high}})] \\ & \times S(m_{1,\mathrm{src}}|\Lambda_{\mathrm{smooth}}), \end{aligned}$$

where the $\mathcal{BPL}$ models the transition between NSs and BHs. It depends on the maximum NS mass and the corresponding minimum mass for BHs. α_1 and α_2 are the two corresponding power law indexes, while b defines the position of the break. $S(m_{1,\mathrm{src}}|\Lambda_{\mathrm{smooth}})$ is the smoothing function.

With the MULTI POP model, we are able to include all the 155 events. Instead, with the other two mass models, we cannot include the events where at least one of the components might be a NS. For the rate model, we use the Madau-Dickinson one [Madau and Dickinson, 2014].

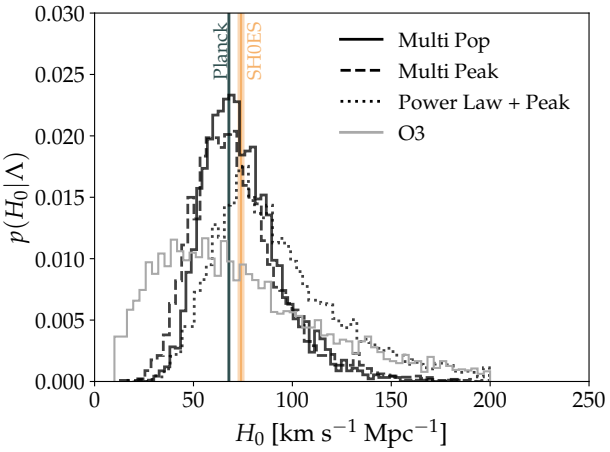

Figure 2.15: H_0 posterior from GWTC-4 data with `icarogw`. We consider three different mass models: MULTI POP, POWER LAW + PEAK, and MULTI PEAK. For comparison, we plot the constraints coming from both Planck and SH0ES measurements, as well as the H_0 posterior with the POWER LAW + PEAK mass model from the last LVK Cosmology paper [Abbott et al., 2023a].

For the HBI inference with `icarogw`, we use large and uninformative priors on all the *hyperparameters*. In Fig.2.15, we show the H_0 posterior from GWTC-4 data with the three different mass models. For comparison, we plot the constraints coming from both Planck [Aghanim et al., 2020] and SH0ES [Riess et al., 2021] measurements, as well as the H_0

posterior with the POWER LAW + PEAK mass model from the last LVK Cosmology paper [Abbott et al., 2023a].

We observe that with respect to the O3 results, we get tighter constraints, and even more so with the MULTI POP mass model, given that we can use a larger data set, comprising all the CBCs (although we are not including `GW170817`). In Tab. 2.4, we report the median of the posterior distributions for the three cases and the symmetric 68% C.L.

Table 2.4: Table of H_0 estimates (median value) from O4a data with the three different mass models.

Mass model	H_0 [km $s^{-1}Mpc^{-1}$] (68% C.L.)
MULTI POP	71^{+21}_{-15}
MULTI PEAK	69^{+24}_{-18}
POWER LAW + PEAK	85^{+37}_{-23}

The constraints we currently have are still insufficient to resolve the tension between the Planck and SH0ES results. However, the spectral sirens approach holds significant promise for transforming upcoming measurements into a valuable cosmological probe. The remaining part of the O4 run is expected to yield better-measured events, thanks also to the added contribution from Virgo. Several aspects are improving, including enhanced statistics, greater precision, more refined mass models, and more robust analysis methods. As a consequence, we are likely to see stronger constraints on key cosmological parameters, helping to bridge the gap between the Planck and SH0ES results. The potential of spectral sirens to play a pivotal role in this effort underscores the exciting prospects for cosmology in the coming years, driven by advancements in GW observations.

PART II

Next-generation GW detectors

3. Fisher Matrix Analysis

> *That would mean looking at the case from an entirely different angle, I said.*
> *One so often has to do that - about everything. Don't you think so?*
>
> **— Agatha Christie**
> "Murder at the Vicarage"

The following chapter primarily discusses the two `GWFish` *papers [Dupletsa et al., 2023, 2025].* `GWFish` *is a software developed for the simulation of detector networks and for forecasting purposes using Fisher matrices in the context of the next-generation (XG) gravitational wave (GW) detector science. I contributed significantly to the software. In particular, I took care of the waveform module, writing in* `Python` *the* `IMRPhenomD` *waveform approximant, and then integrating the module with* `LALSimulation`*. My responsibilities included debugging, testing, and validating the software, as well as creating guidelines and tutorials. For the first paper [Dupletsa et al., 2023], I was responsible for all comparisons with* `Bilby` *and the study case analyses. In the second paper [Dupletsa et al., 2025], I developed the priors module and tested it against real data from the GWTC-3 catalogue. Additionally, I took care of the testing and comparison of different Fisher matrix codes, on the* `GWFish` *side, participating in activities within Common Tools division of the Observational Science Board (OSB) in the Einstein Telescope (ET) Collaboration. This effort led to the corresponding chapter for the ET Blue Book [Abac et al., 2025], a detailed analysis of the ET science, for which I was part of the writing team.* `GWFish` *has been used in several scientific works in the ET community. Some of them are specifically addressed in the next two Chapters of this thesis.*

3.1 The challenge of the next-generation (XG)

Since the first detection of a gravitational wave (GW) signal [Abbott et al., 2016b], we have been collecting a considerable amount of interesting data [Abbott et al., 2019b, 2021a, 2024, 2023b], which has allowed us to make unprecedented breakthroughs in the GW field. The gravitational community, however, has already been planning for the future, both with potential upgrades of the current infrastructures and with proposals for new interferometers. The improvement of current GW observatories include the two LIGO interferometers [Abbott et al., 2016b], Virgo [Acernese et al., 2015], LIGO India [Souradeep, 2016], and KAGRA [Akutsu et al., 2019]. The next-generation (XG) de-

Contents

tectors include ground-based, like ET [Hild et al., 2008, 2011; Punturo et al., 2010] and CE [Reitze et al., 2019; Evans et al., 2021], space-borne, like LISA [Amaro-Seoane et al., 2017], and lunar proposals such as the LGWA [Ajith et al., 2025] detector.

The XG GW detectors are expected to observe an unprecedented amount of data [Maggiore et al., 2020; Branchesi et al., 2023], for which standard analysis techniques [Ashton et al., 2019; Romero-Shaw et al., 2020; Ashton and Talbot, 2021] are not a viable option, mainly due to their prohibitive computational costs. Currently, the Fisher matrix approximation [Cutler and Flanagan, 1994; Vallisneri, 2008] stands as an efficient and ready-to-use forecast tool, allowing us to target the science cases of future observatories at the population level. It is a crucial component in the development of the scientific case for future GW detectors.

In recent years, different Fisher matrix softwares have been developed. Starting from `GWFish` [Dupletsa et al., 2023], which we will extensively discuss in this chapter, we also have `gwbench` [Borhanian, 2021], `gwfast` [Iacovelli et al., 2022a,b], `TiDoFM` [Li et al., 2022; Chan et al., 2018]. The main differences between the codes are in their differentiation and matrix inversion methods, which, as will be discussed in the subsequent sections, are essential for the analysis. All the mentioned codes have undergone successful cross-checks within the *Common Tools* division in the Observational Science Board (OSB) of ET, and produce similar results [Branchesi et al., 2023].

In the following chapter, we will first give a brief review of the Fisher matrix analysis technique and its numerical implementation in the `GWFish` software, respectively in Sec. 3.2 and Sec. 3.3. Then, we will show the comparison between the Fisher results and the full Bayesian analysis from `Bilby`, alongside some reference study cases in Sec. 3.4. Then we will present an improvement of the Fisher analysis, thanks to the integration of a prior module within `GWFish` as well as its validation against measured data from the first three observing runs (the GWTC-3 catalogue) in Sec. 3.5.

3.2 *What is a Fisher matrix?*

Before exploring the Fisher matrix analysis details, we will give a working summary of the customary parameter estimation (PE) method, expanding on what has already been introduced in Sec. 1.2.3. When analyzing a GW signal, we want to reconstruct the source parameters. These divide into *intrinsic* parameters, like the component masses and spins (and tidal deformability if neutron star (NS) events are present), and *extrinsic* ones, dependent on the relative position of the source with respect to the observer. The last ones include the sky position

(RA and DEC), the time and phase at coalescence, the polarization and inclination angles, and the distance. A comprehensive list is provided in Tab. 1.1. As introduced in Sec. 1.2.3, according to standard Bayesian analysis, properties of astrophysical sources from observed GW signals [Thrane and Talbot, 2019; Christensen and Meyer, 2022] are inferred starting from the Bayes theorem:

$$p(\vec{\theta}|d) \propto \pi(\vec{\theta})\mathcal{L}(d|\vec{\theta}), \tag{3.1}$$

where the posterior distribution $p(\vec{\theta}|d)$ of a given set of parameters $\vec{\theta}$ is obtained by combining the prior information $\pi(\vec{\theta})$ on that parameter with the likelihood of observing the given data $\mathcal{L}(d|\vec{\theta})$. $\vec{\theta}$ denotes the parameters entering the modeling of the GW signal. The data d (see also Eq. (1.45)) is assumed to consist of both noise n and the true signal $h(\vec{\theta}_0)$, which depends on the unknown true parameters $\vec{\theta_0}$:

$$d = n + h(\vec{\theta}_0), \tag{3.2}$$

where h represents the waveform approximant chosen to model the data, the noise is assumed to be Gaussian and stationary. The likelihood $\mathcal{L}(d|\vec{\theta})$ is the one defined in Eq. (1.60) as the probability that the observed data are described by the model parameters $\vec{\theta}$. This is equivalent to the probability of a specific noise realization in the absence of biases.

The standard Bayesian analysis estimates the signal parameters employing algorithms like Markov Chain Monte Carlo (MCMC) or Nested Sampling [Speagle, 2020], to explore the parameter space and efficiently sample the posterior. However, as introduced in the previous Sec. 3.1 and in Sec. 1.3, its computational cost does not make it a suitable tool for XG forecasts.

The Fisher matrix analysis aims to quantify the information in the data, given a model [Fisher, 1920]. The concept is straightforward: the more peaked around the true parameter values a likelihood function is, the better a parameter can be estimated. Mathematically, it is defined as:

$$\Gamma_{ij} = -\mathbb{E}\left[\frac{\partial^2 \ln \mathcal{L}(\vec{\theta})}{\partial\theta_i \partial\theta_j}\right], \tag{3.3}$$

where $\mathcal{L}(\vec{\theta})$ is the likelihood function of the set $\vec{\theta}$ parameters, $\mathbb{E}[\dots]$ is the expectation value taken over all possible observations, and Γ_{ij} is the Fisher matrix representing the information content on parameters θ_i and θ_j, or, in other words, how sensitive the likelihood is to changes in the parameters θ_i and θ_j. Its inverse provides an approximation to the covariance matrix of the parameters.

Applying the definition Eq. (3.3) to the GW likelihood in Eq. (1.60), the expression simplifies to:

$$\Gamma_{ij} = \langle \frac{\partial h}{\partial \theta_i} | \frac{\partial h}{\partial \theta_j} \rangle. \tag{3.4}$$

The box below provides a step-by-step derivation of Eq. (3.4) from the mathematical definition in Eq. (3.3). From the general definition in Eq. (3.3), we expect the Fisher matrix to be a good guide to parameter measurement precision in the limit of many repeated measurements of the same parameter (the frequentist approach as explained in [Vallisneri, 2008]). We do not have such a luxury with GW observations. We address this in the next Sec. 3.2.1.

From the mathematical definition to the gravitational Fisher

Starting from the definition in Eq. (3.3) and applying it to Eq. (1.60), we get:

- for the logarithm of the likelihood:

$$\begin{aligned} \ln \mathcal{L} &= -\frac{1}{2}\langle d - h(\vec{\theta}) | d - h(\vec{\theta}) \rangle + cst. \\ &= -\frac{1}{2}\left[\langle d|d\rangle + \langle h(\vec{\theta})|h(\vec{\theta})\rangle \right] + \langle d|h(\vec{\theta})\rangle + cst. \\ &= \langle d|h(\vec{\theta})\rangle - \frac{1}{2}\langle h(\vec{\theta})|h(\vec{\theta})\rangle + cst. \end{aligned} \tag{3.5}$$

  where we absorbed the $\langle d|d\rangle$ term into the additive constant since it is independent of $\vec{\theta}$

- for the first partial derivative:

$$\frac{\partial \ln \mathcal{L}}{\partial \theta_i} = \langle d | \frac{\partial h(\vec{\theta})}{\partial \theta_i} \rangle - \langle h(\vec{\theta}) | \frac{\partial h(\vec{\theta})}{\partial \theta_i} \rangle \tag{3.6}$$

- for the second partial derivative:

$$\frac{\partial^2 \ln \mathcal{L}}{\partial \theta_i \partial \theta_j} = \langle d | \frac{\partial^2 h(\vec{\theta})}{\partial \theta_i \partial \theta_j} \rangle - \langle \frac{\partial h(\vec{\theta})}{\partial \theta_j} | \frac{\partial h(\vec{\theta})}{\partial \theta_i} \rangle - \langle h(\vec{\theta}) | \frac{\partial^2 h(\vec{\theta})}{\partial \theta_i \partial \theta_j} \rangle \tag{3.7}$$

When taking the expectation value of Eq. (3.7), we assume that the noise is Gaussian. Therefore, $\langle d \rangle = h$, and the first and last terms in Eq. (3.7) cancel out, leaving us with:

$$\Gamma_{ij} = -\mathbb{E}\left[\frac{\partial^2 \ln \mathcal{L}(\vec{\theta})}{\partial \theta_i \partial \theta_j} \right] = \langle \frac{\partial h}{\partial \theta_i} | \frac{\partial h}{\partial \theta_j} \rangle \tag{3.8}$$

3.2.1 *Fisher matrix and the linear signal approximation (LSA)*

The Fisher matrix in the GW field corresponds to a linear signal approximation (LSA) [Vallisneri, 2008]. Even with a single measurement, we can consider small perturbations of parameters around the true value, $\vec{\theta}_0$, and perform a first-order Taylor expansion of the waveform

approximant:

$$\begin{aligned} \vec{\theta} &\sim \vec{\theta}_0 + \Delta\vec{\theta} \\ h(\vec{\theta}) &\sim h(\vec{\theta}_0) + \frac{\partial h}{\partial \theta_i}\Delta\theta^i, \end{aligned} \tag{3.9}$$

where a sum is intended over repeated indexes, following the Einstein summation convention. This is known as LSA. Following [Vallisneri, 2008], the likelihood in Eq. (1.60) can be expanded, and we get:

$$\begin{aligned} \mathcal{L} \propto & \exp\left[-\frac{1}{2}\langle n|n\rangle + \langle n|\frac{\partial h}{\partial \theta_i}\rangle\Delta\theta^i - \frac{1}{2}\Delta\theta^i\langle\frac{\partial h}{\partial \theta_i}|\frac{\partial h}{\partial \theta_j}\rangle\Delta\theta^j\right] \\ =& \exp\left[-\frac{1}{2}\langle n|n\rangle\right]\exp\left[-\frac{1}{2}\left(\Delta\theta^i\Gamma_{ij}\Delta\theta^j - 2\langle n|\frac{\partial h}{\partial \theta_i}\rangle\Delta\theta^i\right)\right] \\ =& \exp\left[-\frac{1}{2}\langle n|n\rangle\right] \\ & \times \exp\left[-\frac{1}{2}\left(\Delta\theta^i - (\Gamma^{-1})_{ik}\langle n|\frac{\partial h}{\partial \theta_k}\rangle\right)\Gamma_{ij}\left(\Delta\theta^j - (\Gamma^{-1})_{jl}\langle n|\frac{\partial h}{\partial \theta_l}\rangle\right)\right] \\ & \times \exp\left[\frac{1}{2}\langle n|\frac{\partial h}{\partial \theta_i}\rangle(\Gamma^{-1})_{ij}\langle n|\frac{\partial h}{\partial \theta_j}\rangle\right] \end{aligned} \tag{3.10}$$

There are three terms[1]:

- **Noise term**: the first term depends only on the realization of detector noise. It does not affect parameter estimation; it just sets an overall normalization factor in the likelihood function.
- **Gaussian term**: the second one is a Gaussian centered[2] around $\Delta\theta^i = (\Gamma^{-1})_{ik}\langle n|\frac{\partial h}{\partial \theta_k}\rangle$, with the covariance matrix given by the inverse of the Fisher matrix. The Fisher matrix defines the width of the likelihood peak. Larger values in the Fisher matrix mean the likelihood is steeper; the derivatives are better resolved, so parameter uncertainties are better constrained. A smaller Γ_{ij} means the likelihood is broader, and parameters have larger uncertainties.
- **Noise-shifted term**: the last term encodes how noise affects parameter estimation. However, this term is $\mathcal{O}(1)$ in the signal amplitude, therefore subdominant with respect to the Gaussian term (see the discussion on SNR in the following Sec. 3.2.2).

[1] After rewriting the likelihood in Eq. (1.60) using Eq. (3.9), we have a quadratic and a linear term in $\Delta\theta$. Applying the square completion technique, one can rewrite it as a Gaussian centered in $\Delta\theta^i = (\Gamma^{-1})_{ik}\langle n|\frac{\partial h}{\partial \theta_k}\rangle$. The shift can be found by analogy with an example quadratic expression like $ax^2 - 2bx$, where $a \to \Gamma_{ij}$ and $b \to \langle n|\frac{\partial h}{\partial \theta_k}\rangle$. Completing the square sets $x \to x - \frac{b}{a}$, which is the new value around which the Gaussian is centered.

[2] The parameters' value is shifted from the true one because of noise.

Therefore, we can rewrite the likelihood in the LSA as:

$$\mathcal{L} \propto \exp\left[-\frac{1}{2}\left(\Delta\theta^i - (\Gamma^{-1})_{ik}\langle n|\frac{\partial h}{\partial \theta_k}\rangle\right)\Gamma_{ij}\left(\Delta\theta^j - (\Gamma^{-1})_{jl}\langle n|\frac{\partial h}{\partial \theta_l}\rangle\right)\right]. \tag{3.11}$$

This tells us that the Maximum Likelihood Estimator (MLE), $\Delta\theta^i$, has a mean given by:

$$\mathbb{E}\left[\Delta\theta_i\right] = (\Gamma^{-1})_{ik}\langle n|\frac{\partial h}{\partial \theta_k}\rangle, \tag{3.12}$$

which averages to zero over many noise realizations, $\langle n|\frac{\partial h}{\partial \theta_k}\rangle|_n = 0$, centering the Gaussian at the true parameters' value. The inverse of the Fisher matrix gives the covariance:

$$cov\left(\Delta\theta_i, \Delta\theta_j\right) = \Sigma_{ij} = \Gamma^{-1}_{ij} \tag{3.13}$$

Therefore, in the Fisher matrix approximation, we can write the likelihood as a multivariate Gaussian, centered around the true parameters' value, $\vec{\theta}_0$[3]:

$$\mathcal{L} \propto \exp\left[-\frac{1}{2}\left(\vec{\theta}-\vec{\theta}_0\right)^{\mathrm{T}}\Gamma\left(\vec{\theta}-\vec{\theta}_0\right)\right], \tag{3.14}$$

The square root of the diagonal elements of the Fisher matrix inverse then gives the parameters' uncertainties. The off-diagonal terms quantify correlations instead.

[3] In the Fisher matrix context, the true parameters' value θ_0 is referred to as injections. *These are not to be confused with the injections used to calculate selection effects throughout Chapter 2.*

3.2.2 *Fisher matrix and the high-SNR limit*

The Fisher matrix approximation is valid in the high-SNR limit. We can explain this going back to the likelihood in the LSA as in Eq. (3.10), and, term by term, discuss their dependence on the SNR. From the optimal SNR definition in Eq. (1.58), it is straightforward to see that it scales as the waveform amplitude A ($h \propto A$ and therefore $SNR \propto A$). Similarly, the derivatives of the waveform, $\frac{\partial h}{\partial \theta_i}$, scale linearly with A as well.

Therefore, we have that, for each contribution in Eq. (3.10):

- The **noise term** has no dependence on the signal strength, and so no dependence on the SNR; both at high and low SNR, this term remains unchanged.
- The **Gaussian term** scales as SNR^2, since $\Gamma_{ik} = \langle\frac{\partial h}{\partial \theta_i}|\frac{\partial h}{\partial \theta_j}\rangle \propto SNR^2$. The likelihood function becomes narrower the higher the SNR. This means that the covariance matrix scales as $\Sigma_{ij} = \Gamma^{-1}_{ij} \propto \frac{1}{SNR^2}$, and that parameters' uncertainties scale as $\sigma_i = \sqrt{\Sigma_{ii}} \propto \frac{1}{SNR}$. When SNR is high, the likelihood function is sharply peaked, and parameters estimation is precise. At low SNR, parameters uncertainties are large and the Gaussian approximation may break down. Moreover, the higher the SNR, the lower the contribution from the shift term, $(\Gamma^{-1})_{ik}\langle n|\frac{\partial h}{\partial \theta_k}\rangle \propto \frac{1}{SNR}$, meaning that the Gaussian is centered at the true parameters' value.
- The **noise-shifted term** does not depend on SNR in the LSA, as the waveform derivatives scaling with amplitude cancels out with the one coming from the inverse of the Fisher (see Sec. 3.2.1).

In conclusion, at high SNR, the likelihood is peaked and the Gaussian approximation holds; at low SNR, noise effects dominate, and

the Fisher approximation may be problematic. However, correlations among parameters, rather than low SNR, may limit the accuracy of parameters' errors under the Gaussian likelihood approximation (see the next Sec. 3.2.3 and then Sec. 3.5).

3.2.3 *Fisher matrix and priors*

In the standard Fisher matrix analysis, we assume the priors on the parameters to be uniform[4]. Since, in the high-SNR limit, the likelihood is expected to be a highly-peaked function around the injected values, no prior information is needed. In practice, correlations among parameters can broaden the likelihood, and underestimation and overestimations of PE errors may happen [Rodriguez et al., 2013], as well as overflows outside of the physical range of parameters[5]. Incorporating prior information within the Fisher matrix formalism might mitigate the problem. The multivariate Gaussian likelihood can be efficiently sampled and combined with arbitrary priors in the Fisher approximation. A detailed study is carried out in [Dupletsa et al., 2025] and discussed in 3.5.

[4] In this case, we see the Fisher analysis from the Bayesian point of view (see again [Vallisneri, 2008]).

[5] Sometimes, the Fisher estimates are seen as the lower limit of the covariance, the so-called *Cramer-Rao* bound. However, as [Rodriguez et al., 2013] and our results in [Dupletsa et al., 2025] show, Fisher forecasts are not necessarily tighter than full Bayesian PE results. This might be linked to the unrealistic assumption that the MLE is the true value. Degeneracies and multimodalities in the likelihood cannot be disentangled with a Fisher analysis and this might lead to underestimations of the true uncertainties, which are better captured by a more flexible Bayesian approach.

3.3 *The `GWFish` software*

`GWFish` is a Fisher-matrix code developed to investigate PE capabilities of future GW detectors. It is a robust and flexible detector simulation software:

- It combines frequency-domain GW models with time-domain simulations of GW detector networks[6], under the stationary phase approximation. Taking into account the detector motion is crucial when it comes to PE, especially for the sky localization [Grimm and Harms, 2020; Chan et al., 2018; Cutler, 1998; Nitz and Dal Canton, 2021];
- It can simulate from current ground-based detectors (LVKI) to future ones, including terrestrial (ET and CE), space-borne (LISA) and lunar (LGWA). A pictorial representation of the available detectors' types is shown in Fig. 3.2.
- It can use all LALSimulation approximants supporting precession as well as tidal deformation;
- It can simulate multi-band observations, combining the Fisher matrices of different detectors;
- It takes several measures to reduce the impact of numerical errors coming from the Fisher matrix PE errors.

Figure 3.1: Logo of `GWFish`.

[6] `GWFish` also provides time-domain GW approximants, even if the frequency-domain ones are the most used for forecast purposes.

In what follows, we first provide in Sec. 3.3.1 a brief description of how detectors and networks are implemented in `GWFish`, focusing on the ground-based ones. Then we look into the numerical implementation of the Fisher formalism in 3.3.2. Application of `GWFish` are examined in Sec. 3.4.

3.3.1 *Simulating (a network of) detectors in `GWFish`*

The simulation of a detector network must consider several aspects, which are sorted into different categories within `GWFish`.

- *Component*: single components of a detector, as laser interferometer for ground-based detectors, Time Delay Interferometry (TDI) channels for space LISA-like observatories, or accelerometers for lunar detectors as LGWA. At this level, one has to take into account the time-varying detector response to the GW signal, the noise modeling (the Power Spectral Density (PSD)), and the duty cycle[7]
- *Detector*: one or multiple components observing the same frequency band and added as a group to a detector network
- *Network*: one or multiple detectors observing together; which at the Fisher matrix level means a sum over the single detectors' Fisher matrices

The primary focus of detector simulation is the calculation of the detector's response. In this discussion, we will concentrate on ground-based detectors. A broader discussion, including space and lunar detectors, can be found in [Dupletsa et al., 2023] and references therein. By default, `GWFish` applies the long-wavelength approximation to all terrestrial GW observatories. This approximation assumes that the arm-length of a GW detector is much smaller than the wavelength of the GW signal. However, this assumption is not fully accurate above one kilohertz for a 40 km detector, such as CE [Schilling, 1997; Abbott et al., 2017b; Essick et al., 2017]. This feature is a detector property and can be disabled when needed. When this setting is disabled, the antenna pattern will vary at high frequency as well (the variation at low frequency is, in any case, given by the Earth's rotation).

The response of a detector also has to take into account the fact that the detector's orientation and position can change over time. The change in orientation is particularly important to simulate. Since signals are represented in the frequency domain in `GWFish`, we need to determine how to convolve the detector response with the signal. In `GWFish`, we assume that there is a function $t(f)$ that maps signal frequencies to times. To derive this function, we assume the stationary phase approximation, which is fundamental to most analytical models of compact binary signals and is known to provide very accurate

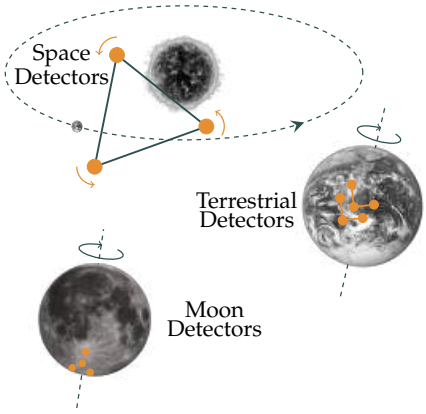

Figure 3.2: Detectors available in `GWFish`: terrestrial, lunar and space-borne. The arrows indicate the motion of the detectors, which is a fundamental feature simulated in `GWFish`. Figure adapted from [Dupletsa et al., 2023] (Figure 1)

[7] For a more realistic observing scenario, each component of a detector can be assigned a duty cycle. This is done by randomly sampling in $[0, 1]$ and checking whether the outcome is below (the component is *on*) or above (the component is *off*) the duty cycle threshold. The default one for most detectors is 0.85, meaning that each component is active 85% of the times.

approximations of the Fourier spectrum of these signals [Droz et al., 1999]. The time until merger as a function of frequency can be calculated from the lowest-order term of the phase $\phi(f)$ evolution [Marsat and Baker, 2018; Harms et al., 2013], and takes the following form (see an example in Fig. 3.3):

$$t(f) = -\frac{1}{2\pi}\frac{\mathrm{d}\phi(f)}{\mathrm{d}f} = t_c - \frac{5}{256\pi^{\frac{8}{3}}}\left(\frac{G\mathcal{M}}{c^3}\right)^{-5/3} f^{-\frac{8}{3}}. \tag{3.15}$$

This approximation is acceptable since only the early phase of the inspiral needs to be modeled accurately to account for the effects of detector motion on PE. Once $t(f)$ is calculated for a signal, it can be used as a time vector for the simulation of the motion of the detectors. The GW signal of a detector can then be written in terms of a response tensor $\mathcal{D}_{ij}(t(f))$ contracted with the GW strain tensor $h^{ij}(f)$ [Sathyaprakash and Schutz, 2009]:

$$h(f) = \mathcal{D}_{ij}(t(f))h^{ij}(f), \tag{3.16}$$

which is the equivalent in the frequency domain of Eq. (1.44). In the case of terrestrial detectors, the actual frequency-dependent response of a GW detector, e.g., any aspect going into detector calibration, is included in the instrument-noise spectrum referred to as GW strain.

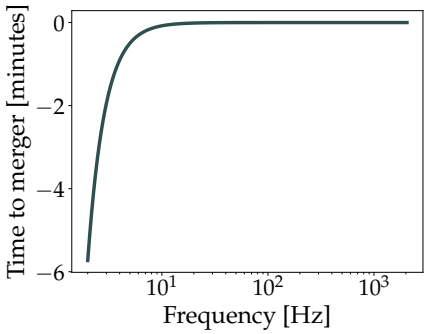

Figure 3.3: Example of the $t(f)$ function for `GW150914`-like signal, if observed with ET

3.3.2 *Numerical implementation*

`GWFish` simulates PE through the Fisher-matrix formalism, which is based on a Gaussian approximation of the likelihood function (see Sec. 3.2 for the theoretical framework about the Fisher analysis). The Fisher method is computationally efficient but numerically less stable than posterior sampling (see, for example, software like `Bilby`, to which we will compare `GWFish` in Sec. 3.4). The numerical challenges are related in the first place to the modeling of the waveform approxiamants, which we need to describe the signal analytically. The major issues are posed by derivative computation (see Fisher matrix definition in Eq. (3.4)) and Fisher matrix inversion (see the relation between covariance matrix, which gives us the PE errors and the Fisher matrix in Eq. (3.13)). We separately discuss each of these points below.

Waveform modeling `GWFish` is integrated with LALSimulation [LIGO Scientific Collaboration, 2020], and it can use all the waveform models available there. It also provides independent implementations of the `TaylorF2` [Isoyama et al., 2020] (until the 3.5 Post-Newtonian (PN) order) and `IMRPhenomD` [Husa et al., 2016; Khan et al., 2016] approximants. We will not get into much detail about the approximant usage with `GWFish`.

Generally, it is important to understand the physics that the waveform approximants incorporate and the enormous impact that they can have on PE. Current waveform models belong to either the Effective-One-Body (EOB) or the Phenomenological families. EOB models rely on semi-analytical resummations tuned to Numerical Relativity (NR) simulations, whereas phenomenological waveforms are much faster analytic fits to NR and Post-Newtonian (PN) data. In both cases, there might be biases induced either because in some parameter regions NR calibration points are sparse or because some physical effects are not modeled, such as precession effects, higher-order multiples, or tidal interactions. For example, a mismodeling of tidal effects can lead to a biased estimate of the NS Equation of State (EoS) [Gamba et al., 2021]. At the sensitivity level of current detectors, statistical errors are dominant. However, for XG interferometers systematic biases due to waveform modeling will become more and more relevant and need careful consideration [Pürrer and Haster, 2020; Owen et al., 2023; Read, 2023; Kapil et al., 2024].

Derivatives Waveform derivatives are carried out in a hybrid analytical-numerical scheme. In `GWFish`, derivatives with respect to waveform phase at merger ϕ_c, merger time t_c, and source luminosity distance d_L are calculated analytically. For all the other model parameters (masses, spins, tidal deformation, sky location, inclination angle, polarization angle), the derivatives need to be calculated numerically. This allows the code to be computationally efficient and compatible with arbitrary waveform models. Numerical derivatives are carried out at second-order precision[8], as shown in the following code snippet:

```
# shift target_parameter by a dp amount
# (of the order of 1e-5*target_parameter)
# roughly the cube root of numerical precision
self.pv_set1[target_parameter] = pv - dp / 2.
self.pv_set2[target_parameter] = pv + dp / 2
# Calculate signals at slightly shited target_parameter value
signal1 = det.projection(self.pv_set1, ...)
signal2 = det.projection(self.pv_set2, ...)
# output derivative
derivative = (signal2 - signal1) / dp
```

Numerical differentiation, however, suffers from limitations of numerical precision, e.g., some derivatives might be calculated from tiny variations of potentially very large numbers, which is the case for the waveform phase. Especially the component $2\pi f t_c$ can take very large numerical values. `GWFish` mitigates the impact of the large value of $2\pi f t_c$ by eliminating this term in calculations of numerical derivatives involving the phase of the waveform (all the parameters, except for `RA`,

[8] `GWFish` uses the *central-difference* numerical scheme for the derivative (see also the relative code snippet), which can be schematized as:

$$f'(x) = \frac{f(x+h/2) - f(x-h/2)}{h}.$$

If we Taylor expand the two term at the numerator and subtract them, we get:

$$f(x+h/2) - f(x-h/2) = hf'(x) + \frac{h^3}{24} f'''(x),$$

which shows us that the derivative is second-order accurate.

DEC, Ψ, which just influence the projection of the waveform onto the detector, and the ones for which analytical derivatives are straightforward). In other words, removing the global phase factor $2\pi f t_c$ ensures that the derivative reflects only the intrinsic shape change of the waveform. The t_c term, in fact, is numerically large, and even though it is the same for both the perturbed waveforms (see sidenote above), it can distort the finite difference due to numerical errors in subtracting nearly identical waveforms.

Fisher matrix inversion Another numerical challenge lies in the inversion of the Fisher matrix, necessary to obtain the PE errors as in Eq. (3.13). The main issue is that Fisher matrix might be close to singular. This happens when matrix eigenvalues vary over a huge range (even over 20 orders of magnitude). This is linked both to the fact that some model parameters can have a large range of numerical values, e.g., 10^{30} for masses in kg and values of order 1 for all angular variables. The situation can be mitigated by normalizing the Fisher matrix [Parida et al., 2016], before inverting it:

1. Collect the diagonal elements $d_i = \mathcal{F}_{ii}$ of the Fisher matrix.
2. Divide row k of the Fisher matrix by $\sqrt{d_k}$. Divide column k of the Fisher matrix by $\sqrt{d_k}$. This leaves a matrix with diagonal components around unity and all off-diagonal elements in the range $[-1, 1]$.
3. Invert the matrix, then undo the normalization by applying the second step to the inverted matrix using the same values for d_k.

The code-equivalent of this procedure is shown below:

```
def invertSVD(fisher_matrix):

  thresh = 1e-10 # to discard very small eigenvalues
  dm = np.sqrt(np.diag(matrix))
  normalizer = np.outer(dm, dm)
  matrix_norm = matrix / normalizer

  # SVD decomposition
  [U, S, Vh] = np.linalg.svd(matrix_norm)
  kVal = sum(S > thresh) # discard small eigenvalues
  inv_norm = U[:, 0:kVal] @ np.diag(1./S[0:kVal]) @ Vh[0:kVal, :]

  # undo the normalization
  inverse_fisher_matrix = inv_norm / normalizer

  return inverse_fisher_matrix
```

There is a remaining issue linked to signal-model degeneracies. To address this issue, `GWFish` excludes all singular values lying below a certain numeric precision threshold from the matrix before inverting it [Press et al., 2007]. The main outcome of this step is to make the matrix inversion robust with respect to all significant singular values containing physical information. In cases where components of small singular values need to be discarded, the waveform model is close to degenerate with respect to at least one parameter pair, e.g., distance and inclination angle can show strong correlations. The PE errors estimated for such strongly correlated parameters are typically substantially different from PE errors coming out of a full Bayesian analysis. For example, taking into account prior distributions in Bayesian analyses can substantially improve PE in these cases. We will specifically address the problem in Sec. 3.5, where we are discussing an enhancement of the Fisher analysis by including priors.

In Fig. 3.4 below, we provide a schematic representation of the rationale behind how `GWFish` operates. First, we need to create an input population file containing the GW injections. This involves generating mock GW events and supplying their parameter values as specified in Table 1.1.

Next, we must define the characteristics of the detector, including its position, arm length, PSD, and other relevant details. In the `main.py` file, these inputs are processed by relying on various modules within the code. For reference, the schematic indicates `detection.py`, which constructs the detector; `waveform.py`, which calculates the waveform approximant; and `fishermatrix.py`, which manages the calculation and inversion of the Fisher matrix.

The output consists of an `Errors.txt` file that provides the 1σ uncertainties for the parameters included in the Fisher matrix evaluation. Additionally, the Fisher matrices and their inverses can also be outputted.

3.4 *Comparison with `Bilby` and reference studies*

We put to test the `GWFish` code by comparing the Fisher matrix output to a Bayesian PE done with `Bilby` [Ashton et al., 2019]. This is done in Sec. 3.4.1. We also showcase a low-SNR example event comparing the performance of `Bilby` and the limitations of a Fisher approach. Then we present some reference studies using the ET detector to show the capabilities of `GWFish`. We compare PE outcomes using different waveform models with both BBH and BNS mock populations in Sec. 3.4.2. We then focus on sky-localization estimates for ET

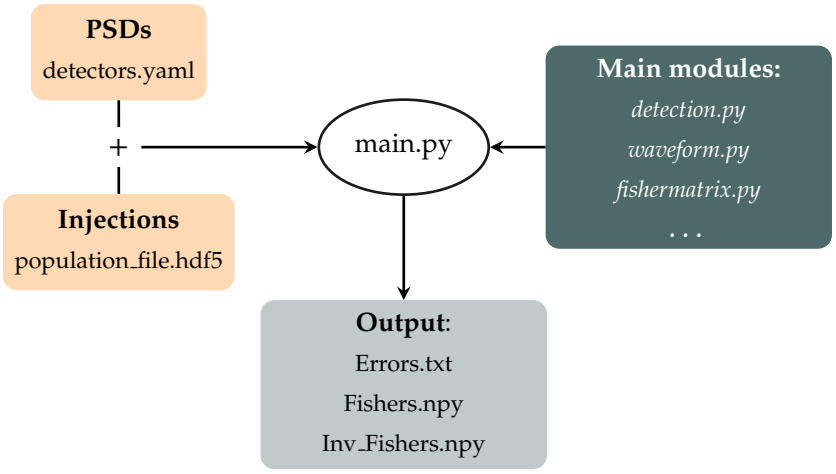

Figure 3.4: Basic structure of the `GWFish` code

using both the events observed in GWTC-3 and mock BNS events put at different distances, including a network with one or two CEs, in Sec. 3.4.3. Last, we present a potential multi-banding analysis with ET and LISA and the improvement in PE, especially for the sky localization, in Sec. 3.4.4. All these results have been published in [Dupletsa et al., 2023].

3.4.1 *`Bilby` vs `GWFish`*

We compare SNR and PE between `Bilby` and `GWFish` for four signals observed with ET (see Table 3.1). Due to current constraints imposed by `Bilby`, and by other state-of-the-art PE softwares, it is not possible to carry out accurate Bayesian analysis of BNS signals for ET. This is due to computational limitations. Standard representations of BNS waveforms for ET would require about 10^8 samples due to the day-long observation time of these signals with ET, and `Bilby` also does not consider Earth's rotation during the observation of GW signals for waveform modeling (an effect that does not play a role for analyses of compact binaries with current GW detectors). As a consequence, we carry out our comparison for BBHs, which, in some sense, is also more interesting since model degeneracies play a more important role. We do the comparison for each signal with a random realization of the detector noise in `Bilby` in order to compare the `GWFish` results with a more realistic simulation of the Bayesian analysis. However, while noise realizations can generally influence PE errors [Vallisneri, 2011], it turns out that it has a negligible effect here since the SNR of all signals is very high.

We compare four randomly sampled signals reported in Tab. 3.1. Signals 1 – 3 have randomly sampled angular parameters, while the

	Signal 1	**Signal** 2	**Signal** 3, 3∗
RA [rad]	0.375	3.026	4.154
DEC [rad]	−0.363	−0.282	−0.972
Ψ [rad]	1.738	4.552	2.071
ι [rad]	1.645	1.143	1.261
d_{L} [Mpc]	453	453	453
z	0.098	0.098	0.098
$m_{1,\mathrm{src}}[M_\odot]$	10.0	30.0	60.0, 10.0∗
$m_{2,\mathrm{src}}[M_\odot]$	5.0	15.0	30.0, 5.0∗
t_c [GPS]	1120381489.604	1124867056.193	1122192865.797
ϕ	3.472	1.098	3.441
a_1	0.729	0.729	0.729
a_2	0.620	0.620	0.620

Table 3.1: Parameters of the signals used for SNR and PE comparisons between Bilby and GWFish. The spin components, a_1 and a_2, are assumed to be aligned with the orbital angular momentum. The third column refers to two different signals, where only the mass parameters change, leaving all the others unchanged. Table from [Dupletsa et al., 2023] (Table 1, ***authored by UD***)

fourth signal (Signal 3*) has the same parameters as Signal 3 except for the two masses, which are the same as for Signal 1. The signals are at relatively low redshift to make sure that the SNR is high. In this case, the Gaussian approximation of the likelihood function is expected to hold, but we will see, not entirely surprisingly, that PE errors produced by GWFish and Bilby are still not identical. As for the detector, we employ ET alone with its three components. For both Bilby and GWFish, we are using the inspiral-merger-ringdown waveform IMRPhenomD from LALSimulation, setting the minimum frequency to 10 Hz and the maximum frequency to 1024 Hz. For GWFish, we include results with 2 Hz lower bound to show the impact of ET's low-frequency sensitivity on PE. The reason not to use a 2 Hz lower bound for waveforms in Bilby is that Bilby enforces a frequency resolution of about 1/(duration of signal), which means that the number of samples used for each waveform becomes very large even for BBHs with a 2 Hz lower bound compared to 10 Hz. Consequently, it would take a prohibitive amount of time to complete the posterior sampling. Our analysis uses a frequency resolution of 1/153 Hz for Signal 1, 2 and 3, and 1/108 Hz for Signal 3*. A simpler waveform model such as TaylorF2 would have been inappropriate here since model degeneracies would be higher, especially when simulating BBH observations involving only ET.

SNR results for these signals are summarized in Tab. 3.2. The SNR values match between GWFish and Bilby with expected minor deviations, for example, because GWFish simulates the effects of the rotation of Earth on the waveform while Bilby does not.

For the PE comparison between Bilby and GWFish, we use the same signals of Tab. 3.1. Posterior sampling requires to specify a prior on the parameters (at the very least a uniform prior to constrain the reasonable/physical range of parameter values). We used:

Table 3.2: The comparison between SNR for the four different signals (see Table 3.1) between Bilby and GWFish. The IMRPhenomD waveform model is used with $f_{\mathrm{min}} = 10$ Hz and $f_{\mathrm{max}} = 1024$ Hz. The SNR reported here is the sum (in quadrature) over ET's three components. Note that the SNR calculation with Bilby is done using the same waveform and the same instrument-noise spectrum as for GWFish. The main objective of the SNR comparison is to assess how well the two simulations match in terms of coordinate systems and detector models. Table from [Dupletsa et al., 2023] (Table 2, ***authored by UD***)

	SNR	
Signal	**Bilby**	**GWFish**
Signal 1	72.1	72.1
Signal 2	219	219
Signal 3	1038	1038
Signal 3*	236	236

- uniform in component masses priors for *mass ratio* and *chirp mass*
- uniform prior for the *polarization angle* Ψ
- uniform prior on the merger rate in comoving volume (fixing the prior on the *luminosity distance* $d_{\rm L}$)
- isotropic distribution in the sky (fixing the priors on `RA` and `DEC`)
- uniform prior for the cosine of the *inclination angle* ι

The other 8 parameters (6 spin components, phase and time) are given a delta prior and therefore are not taken into consideration for posterior sampling and are excluded also from the Fisher matrices. `Bilby` results are obtained using the `PEsummary` package [Hoy and Raymond, 2021]. In Tab. 3.3, we report the recovered median values for the parameters and the relative errors at the 90% C.L. for `Bilby`. The parameter values reported for `GWFish` are the true waveform parameters. `GWFish` outputs 1σ PE errors, which are converted to the 90% C.L. in Tab. 3.3, which can be done in Gaussian approximation by multiplying the errors by 1.645. Moreover, under the `GWFish` results column, for each signal, we have two results per parameter: the upper one is obtained using $f_{\rm min} = 10\,$Hz, the lower one with $f_{\rm min} = 2\,$Hz. Starting from 2 Hz yields smaller uncertainties on the parameters by about a factor 2.

Generally, there is good agreement between `GWFish` and `Bilby` PE errors when taking `GWFish` results with 10 Hz low-frequency cut-off. For example, mass errors match especially well. There are exceptions, which are all connected to multi-modal posterior distributions, e.g., several errors estimated with `Bilby` are significantly larger since they include the contribution of a second mode, which the Gaussian likelihood approximation cannot reproduce. Interesting to point out is that at least for these 4 signals, which all have very high SNR, ι, d_L are both well estimated. This tells us that ET, as suspected in the past due to its triangular configuration, is able to break the inclination-distance degeneracy. It needs to be noted, though, that our small and high-SNR sample of signals is not sufficient to draw general conclusions about ET PE capabilities, and errors might also increase when spins, merger phase, and time are included in the analysis. What we can conclude from this table is that correlations between model parameters do not necessarily invalidate the `GWFish` PE errors, which means that Fisher-matrix-based analyses can produce useful estimates of PE errors.

Corner plots of the posterior samples with `Bilby` are shown in the appendix in Figs. B.1 to B.4. These also report the contours from `GWFish` estimates. We would like to highlight problems with the `Bilby` PE for the low-mass system of Signal 1. This choice of parameters

Parameter	Signal 1		Signal 2		Signal 3		Signal 3*	
	GWFish	Bilby	GWFish	Bilby	GWFish	Bilby	GWFish	Bilby
RA [rad]	$0.37^{+0.3}_{-0.3}$ $0.37^{+0.18}_{-0.18}$	$2.2^{+3.5}_{-1.8}$	$3.0^{0.004}_{-0.004}$ $3.0^{+0.0031}_{-0.0031}$	$1.2^{+1.9}_{-0.009}$	$4.1^{+0.69}_{-0.69}$ $4.1^{+0.62}_{-0.62}$	$4.2^{+0.28}_{-0.11}$	$4.1^{+1.7}_{-1.7}$ $4.1^{+0.75}_{-0.75}$	$4.6^{+0.45}_{-0.47}$
DEC [rad]	$-0.36^{+0.19}_{-0.19}$ $-0.36^{+0.12}_{-0.12}$	$-0.3^{+1.1}_{-0.15}$	$-0.28^{+0.0037}_{-0.0037}$ $-0.28^{+0.0031}_{-0.0031}$	$0.82^{+0.54}_{-0.04}$	$-0.97^{+0.64}_{-0.64}$ $-0.97^{+0.58}_{-0.58}$	$-1.0^{+0.32}_{-0.087}$	$-0.97^{+1.6}_{-1.6}$ $-0.97^{+0.7}_{-0.7}$	$-0.8^{+0.37}_{-0.29}$
Ψ [rad]	$1.7^{+0.3}_{-0.3}$ $1.7^{+0.18}_{-0.18}$	$2.2^{+3.1}_{-1.8}$	$4.5^{+0.015}_{-0.015}$ $4.5^{+0.012}_{-0.012}$	$1.4^{+2.7}_{-0.44}$	$2.1^{+0.45}_{-0.45}$ $2.1^{+0.41}_{-0.41}$	$2.0^{+0.064}_{-0.21}$	2.1^{+1}_{-1} $2.1^{+0.49}_{-0.49}$	$4.8^{+0.46}_{-3.3}$
ι [rad]	$1.6^{+0.12}_{-0.12}$ $1.6^{+0.074}_{-0.074}$	$1.9^{+0.044}_{-0.045}$	$1.1^{+0.039}_{-0.039}$ $1.1^{+0.031}_{-0.031}$	$1.1^{+0.048}_{-0.06}$	$1.3^{+0.005}_{-0.005}$ $1.3^{+0.004}_{-0.004}$	$1.3^{+0.001}_{-0.002}$	$1.3^{+0.013}_{-0.013}$ $1.3^{+0.0071}_{-0.0071}$	$1.3^{+0.006}_{-0.007}$
d_L [Mpc]	453^{+390}_{-390} 453^{+241}_{-241}	576^{+70}_{-122}	453^{+37}_{-37} 453^{+29}_{-29}	477^{+53}_{-44}	453^{+6}_{-6} 453^{+5}_{-5}	$453^{+1.1}_{-1.2}$	453^{+14}_{-14} 453^{+6}_{-6}	$453^{+4.7}_{-4.6}$
$m_{1,src}[M_\odot]$	$10^{+0.35}_{-0.35}$ $10^{+0.19}_{-0.19}$	$9.8^{+0.33}_{-0.38}$	$30^{+0.46}_{-0.46}$ $30^{+0.26}_{-0.26}$	$30^{+0.62}_{-0.63}$	$60^{+0.13}_{-0.13}$ $60^{+0.12}_{-0.12}$	$60^{+0.095}_{-0.092}$	$10^{+0.11}_{-0.11}$ $10^{+0.061}_{-0.061}$	$10^{+0.11}_{-0.1}$
$m_{2,src}[M_\odot]$	$5.0^{+0.15}_{-0.15}$ $5.0^{+0.083}_{-0.083}$	$4.9^{+0.19}_{-0.16}$	$15^{+0.2}_{-0.2}$ $15^{+0.11}_{-0.11}$	$15^{+0.17}_{-0.17}$	$30^{+0.06}_{-0.06}$ $30^{+0.05}_{-0.05}$	$30^{+0.04}_{-0.04}$	$5.0^{+0.046}_{-0.046}$ $5.0^{+0.026}_{-0.026}$	$5.0^{+0.046}_{-0.045}$

Table 3.3: Comparing measurement uncertainties obtained with `Bilby` and `GWFish`. We use the signals outlined in Table 3.1 and `IMRPhenomD` as waveform model ($f_{\rm min} = 10\,$Hz and $f_{\rm max} = 1024\,$Hz). The errors are at 90% C.L.. The `GWFish` column presents two results for each parameter: the upper one is obtained starting from $f_{\rm min} = 10\,$Hz, the one below is obtained starting from a minimum frequency of 2 Hz. The parameter values reported for `GWFish` are the true waveform parameters, while the values reported for `Bilby` are the median values of the posterior distribution. Table from [Dupletsa et al., 2023] (Table 3, ***authored by UD***)

led to a multi-modal posterior distribution for the two masses. This happened with a rather broad prior on the mass values. We did not manage to tune the settings of the posterior sampling algorithm to correctly sample the posterior, e.g., by changing the number of sampling points or the correlation length. We then decided to reduce the width of the mass priors to a value just small enough to avoid a multi-modal distribution.

A Fisher matrix analysis is expected to break down when the signal SNR is low. Therefore, we show here a case for $SNR = 8$, where once again we compare `Bilby` to `GWFish` PE errors. We used the parameters from Signal 3 for this analysis, but we increased its distance to obtain $SNR = 8$. Since the observed masses now differ significantly from the intrinsic masses, we report the analysis for the two masses in the detector frame, instead of the source frame used in the previous analysis. We used a frequency range from 10 Hz to 1024 Hz, with a frequency resolution of 1/153.

Tab. 3.4 reports the results at 90% C.L. from both `Bilby` and `GWFish`. In contrast to the high-SNR signals, `GWFish` does not accurately estimate the errors for sky localization and polarization angles. The priors of the model parameters play a more important role in low-SNR observations. A comparison with the full posterior obtained from `Bilby` is shown in the corner plot of Figure B.5.

Table 3.4: Comparison between `Bilby` and `GWFish` for Signal 3 put at a distance such that $SNR = 8$. The reported errors are at 90% C.L. Table from [Dupletsa et al., 2023] (Table 4, ***authored by UD***)

	Bilby	GWFish
RA [rad]	$4.5^{+0.5}_{-0.5}$	4.1 ± 83
DEC [rad]	$-0.66^{+0.32}_{-0.39}$	-0.97 ± 81
Ψ [rad]	$1.8^{+0.35}_{-0.43}$	2.1 ± 54
ι [rad]	$1.2^{+0.19}_{-0.31}$	1.3 ± 0.6
d_L [Mpc]	68508^{+26173}_{-18288}	58115 ± 64040
m_1 $[M_\odot]$	$61.3^{+7.6}_{-7.2}$	65.9 ± 18
m_2 $[M_\odot]$	$35.2^{+4.3}_{-3.6}$	32.9 ± 8

3.4.2 *TaylorF2 vs IMRPhenomD vs IMRPhenomXPHM*

Next, we compare Fisher matrix results obtained with three different approximants: `TaylorF2` [Buonanno et al., 2009; Isoyama et al.,

2020], and two phenomenological waveforms, `IMRPhenomD` [Husa et al., 2016; Khan et al., 2016], and the `IMRPhenomXPHM` [Pratten et al., 2021] one. The `TaylorF2` model is the simplest frequency-domain approximant, which describes the inspiral phase and accurately only the early inspiral, which is sufficient for estimates, e.g., of the chirp mass and BNS localization through Earth's rotation. We apply a high-frequency cut-off at 4 times the frequency of the innermost stable circular orbit $f_{\rm isco} = 6^{-1.5}\pi^{-1}c^3/(GM)$[9] to approximately match the SNR obtained with other waveform models. The `IMRPhenomD` model extends over the full inspiral-merger-ringdown of a compact-binary signal, but there are still constraints on the physics described by this model. For example, it only models the fundamental mode of the GW signal and systems with aligned spins. The purpose of this comparison is to show how a waveform model affects PE, even at the simple level of Fisher-matrix-based error estimates.

[9] M denotes the total mass of the binary, $M = m_1 + m_2$

To highlight the model differences we display in Figure 3.5 the characteristic strain (see explanatory box below) for the three waveforms for Signal 2 (see Table 3.1) in comparison also with the ET sensitivity curve. It can be observed that the `IMRPhenomD` model shows the characteristic bump towards the merger frequency and provides a more natural cut-off at high frequency. The `IMRPehomXPHM` clearly shows the effects of including both precession and higher-order modes.

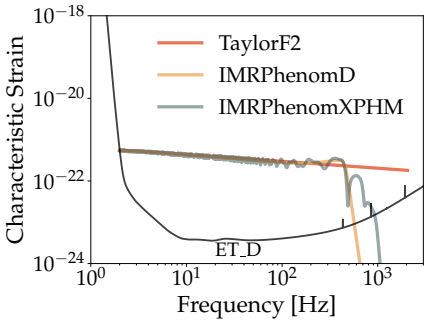

Figure 3.5: Example of the three different waveform models in frequency domain compared in the analysis, using the injection parameters of Signal 2

Characteristic strain

The characteristic strain, $h_c(f)$, is a key quantity in GW physics. Its advantage lies in being a dimensionless quantity that represents the effective amplitude of a GW signal at a given frequency f [Moore et al., 2015]. It incorporates both the strain amplitude and the frequency content. For the gravitational wave strain h, it means that:

$$h_c(f) = 2f|h|, \tag{3.17}$$

whereas for the detector's sensitivity curve we plot the quantity $\sqrt{f}\sqrt{PSD}$. It is then easy to interpret whether a signal is detectable or not: if the following condition is met:

$$h_c(f) > \sqrt{f}\sqrt{PSD} \tag{3.18}$$

for some frequency range, then the signal is detectable in that range. Additionally, the advantage is that the SNR is given by the area between the signal spectrum and the noise.

To compare the two approximants, we start with 1000 BBH signals and 1000 BNS signals. We constrain the BNS redshifts to a maximum of 0.4 so that the SNR distributions for BBHs and BNSs are similar. From these, 927 BBH and 966 BNS signals are seen with a minimum of $SNR = 8$ using `TaylorF2`, `IMRPhenomD`, or `IMRPhenomXPHM`

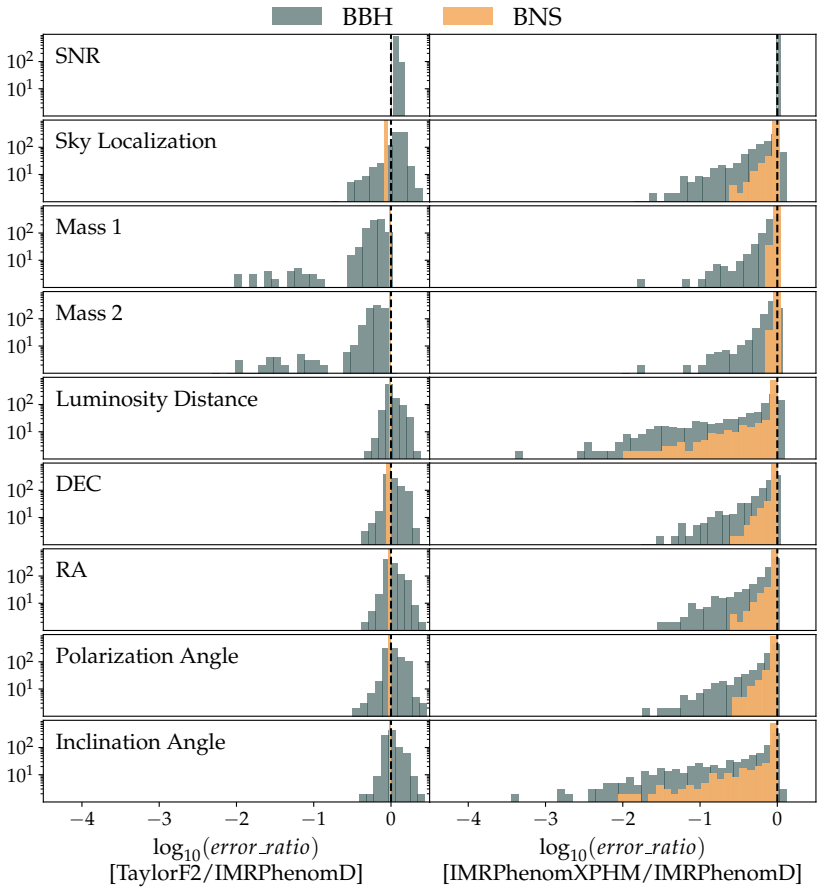

Figure 3.6: In the *left panel*, comparison between `TaylorF2` and `IMRPhenomD` approximants for BBH signals (in dark green) and for BNS signals (in orange). In the *right panel*, comparison between `IMRPhenomXPHM` and `IMRPhenomD` waveforms. We analyze 927 BBH signals and 966 BNS systems observed by ET with $SNR \geq 8$. The frequency range is from 2 Hz to 1024 Hz. The frequency resolution used is 1/32 Hz. We applied a cut at $4f_{\rm isco}$ for the `TaylorF2` waveform. The upper histogram shows the ratio between the SNR values. The histograms below show the ratio of the PE errors. The vertical dashed black line marks the equal ratio case. Figure adapted from [Dupletsa et al., 2023] (Figures 3 and 4, ***authored by UD***)

`LALSimulation` approximants. The distribution of SNR values of detected signals goes up to 200, peaking at 20. The signals are analyzed with a frequency resolution of 1/32 Hz. The analysis is carried out with ET alone over a frequency range from 2 Hz to 1024 Hz. The results are shown in Figure 3.6. We plot the ratios of the PE errors recovered for each of the parameters with `TaylorF2` and `IMRPhenomD` as histograms over the detected signals, in the *left* panel. We show a similar analysis for the `IMRPhenomXPHM` and `IMRPhenomD` approximants, and show it in the *right* panel. The BBH results are in *dark green*, while the BNS ones are plotted in *orange*. The upper plot in both panels shows the ratio of SNR values, while the other histograms show the ratio of the uncertainties on the other parameters.

`TaylorF2` vs `IMRPhenomD` For BBH systems, the PE errors of the individual masses are underestimated with `TaylorF2` (assuming that `IMRPhenomD` generally yields more accurate results), while all other parameters considered here are weakly biased towards larger errors

compared to IMRPhenomD. For BNS signals, there is no significant difference between the two considered approximants: the SNR values are consistent between the two analyses, and only the sky-localization errors are slightly underestimated with TaylorF2.

IMRPhenomXPHM vs IMRPhenomD The IMRPhenomXPHM approximant can describe precession (not considered in this study) and higher-order modes. The latter is well-known to have important consequences for BBH analyses [Van Den Broeck and Sengupta, 2007; Khan et al., 2020], and break the distance-inclination angle degeneracy [Usman et al., 2019; Chen et al., 2019]. Here, a significant improvement of PE can also be seen for a significant fraction of BNS signals. For about 5% of BNSs, the sky-localization error is significantly reduced by up to a factor 5 using IMRPhenomXPHM. For about 10% of BNSs, the distance error is significantly reduced by up to a few orders of magnitude. What this means is that some BNS signals show strong correlations in the likelihood between distance and inclination angle using IMRPhenomD, and the higher-order modes described with IMRPhenomXPHM lead to a suppression of these correlations.

All three approximants produce significantly different results for the BBH signals. For the BNS, considering SNR and sky localization, TaylorF2 vs IMRPhenomD produce almost identical results. However, for a significant fraction of BNS signals, PE errors with IMRPhenomXPHM are reduced compared to IMRPhenomD. The reduction is most substantial for distance errors (10% of signals significantly affected) because distance errors can be strongly correlated with errors of the inclination angle. The IMRPhenomXPHM approximant takes considerably longer to evaluate than TaylorF2 and IMRPhenomD (the latter two with similar evaluation times) when using the LALSimulation package. We conclude that the choice of approximant is generally more important for BBH analyses. For BNS signals, broad population studies can still be carried out with IMRPhenomD or TaylorF2, but results especially for distance and inclination errors are more reliable for a significant fraction of signals when using IMRPhenomXPHM.

3.4.3 *Sky localization studies with ET*

In the following, we present PE results obtained from GWFish focusing on sky localization with ET.

A single detector can accurately localize a GW source if the observation is long enough so that the motion of the detector leads to amplitude and phase modulations of GW signals, which depend on the direction of the source. This is the case for BNSs, which are observed

for several hours with ET. Even lighter NSBHs and BBHs can be localized this way by ET. For specific signals as well as for the average localization by Earth rotation, the localization errors depend on the latitude of the GW detector. Sky localization is greatly improved if additional detectors are present to form a network. In the latter case, the information comes from measurements of phase differences between signals observed in different detectors using the standard triangulation technique [Wen and Chen, 2010].

Sky Localization in Fisher Matrix analysis

In Fisher matrix analysis, the sky localization is computed from the `RA-DEC` covariance submatrix, which quantifies the uncertainty in the sky position. Taking into account that the position is on a sphere, the uncertainty area at 1σ is:

$$\Delta\Omega = \pi \cos(\texttt{DEC}) \sqrt{\sigma^2_{\texttt{RA}}\sigma^2_{\texttt{DEC}} - (\sigma^2_{\texttt{RA, DEC}})^2} \tag{3.19}$$

To obtain the X% level of sky localization, one should multiply the value obtained by `GWFish` by $2\ln(1 - X/100)$. This results in a multiplicative factor of ~ 4.6 when considering 90% confidence level.

	GW170817	GW190425	GW190707
Median SNR	710	190	230
Median sky-location error [deg^2] (90% C.L.)	4.0	67	34
Masses [$M_\odot$]	1.46, 1.27	2, 1.4	12, 8.4
Luminosity distance [Mpc]	40	160	800
Time until merger from 3 Hz [s]	$2.6 \cdot 10^4$	$1.8 \cdot 10^4$	930

Table 3.5: Median of the SNR values and sky localization errors for simulated observations of GWTC-3 signals with ET. Only masses, merger times, and distances are taken from GWTC-3. The sky-localization errors are evaluated for several random realizations, and only the signals with error $< 1000\,\text{deg}^2$ for all realizations are shown in the table. Table from [Dupletsa et al., 2023] (Table 5)

In Tab. 3.5, we present an analysis of 85 signals from GWTC-3 [Abbott et al., 2019b, 2021a, 2024, 2023b]. Only the merger time, masses and distance are taken from the catalogue. Angular parameters are drawn randomly, spins are set to zero. We simulate the observation of these signals with ET. The simulation is done for 10 realizations of the angular waveform parameters for each signal. Tab.3.5 summarizes the median of the SNR values and sky localization that would have been achieved with ET. The table only contains the signals whose sky localization is within $1000\,\text{deg}^2$ for all random realizations of the angular variables of the waveform. As expected, these signals are among the lowest-mass systems in GWTC-3, which means that ET would have observed them for a long time. Also, a low-mass BBH system like `GW190707` could potentially be detected before the merger occurs. We used the `IMRPhenomXPHM` approximant to include the potentially important higher-order modes, but for the signals reported in the table, the sky-localization results would have been the same using `TaylorF2` or `IMRPhenomD`. The localization even of larger BBHs can be $< 100\,\text{deg}^2$,

but it depends strongly on the values of angular parameters.

Next, we show in Fig. 3.7 the sky-localization results for BNSs at 90% C.L.. The results are presented as a fraction of signals localized within a specific area in the sky. Each curve corresponds to 1000 BNS signals located at fixed luminosity distances. The BNS masses are set to $1.4 + 1.4 M_\odot$ in the source frame. The plots confirm that ET has unique sky-localization capabilities for BNSs, enabling multi-messenger studies without other detectors. Still, it is also clear that the localization capabilities of a network are far superior even if only one other detector like CE is added. Nearer systems are better localized and the network of $ET + 2CE$ manages to localize almost all of the injected signals within $10\,\mathrm{deg}^2$. We find our results to be consistent with previously published results, e.g., [Chan et al., 2018; Li et al., 2022].

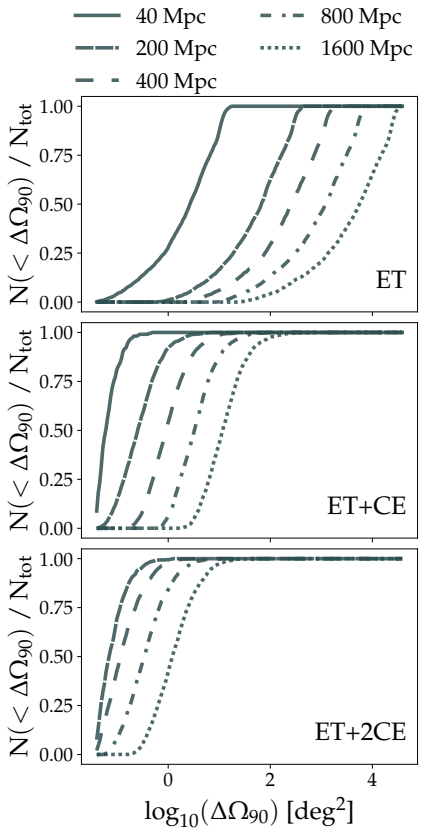

Figure 3.7: Sky-localization capabilities (90% C.L.) of future detector networks including ET and CE. We used the LIGO sites as locations for the two CE detectors. *Top*: ET alone, *middle*: ET and one CE detector at the LIGO Hanford site, *bottom*: ET with two CE detectors at the two LIGO sites. The sensitivity models used here is the ET sensitivity formerly known as ET-D [Hild et al., 2011], and the 40 km CE sensitivity [Evans et al., 2021]. Figure adapted from [Dupletsa et al., 2023] (Figure 5, ***authored by UD***)

3.4.4 *Multi-band study: ET and LISA*

In this section, we present a multi-band study of ET together with LISA, whose observation band extends from about 0.1 mHz to 0.1 Hz. We study an IMBH system of $4000 M_\odot$ and $2000 M_\odot$ in the source frame at a distance of 1.2 Gpc, which both detectors can observe. The masses are chosen large enough to move the signal across the full LISA band within a few years. The other parameter values are the same as for Signal 1. However, we add the remaining four spin parameters ($\texttt{tilt}_1 = 0.91$, $\texttt{tilt}_2 = 1.8$, $\texttt{phi}_{12} = 6.1$ and $\texttt{phi}_{jl} = 4.6$) and use the `IMRPhenomXPHM` waveform approximant, since higher-order modes and precession might play a role. All the 15 parameters are analyzed. Tab. 3.6 reports the results of the analysis with `GWFish`. We can see that LISA provides better information about the component masses, the source distance, and the sky localization, while the errors on the angular parameters are similar. Interestingly, when the two detectors are combined in a multi-band observation, then the sky-localization error and the errors on masses and luminosity distance are significantly reduced compared to the individual errors thanks to the dominating role of LISA. The opposite happens to the time parameter, which is much better estimated with ET alone. Most other errors are reduced more strongly (almost one order of magnitude) than expected from averaging independent errors.

Certain analyses are currently not possible with state-of-the-art detector simulation and Bayesian analysis software like `Bilby` due to the prohibitive computational resources that this would require. For example, if hundreds of thousands of GW signals need to be analyzed, sometimes repeatedly, to study the effect of changes in population or

	Injected Value	$\sigma_{\rm LISA}$	$\sigma_{\rm ET}$	$\sigma_{\rm ET+LISA}$
$m_{1,\rm src}$ [$M_\odot$]	4000	0.036	19	0.032
$m_{2,\rm src}$ [$M_\odot$]	2000	0.016	21	0.015
$d_{\rm L}$ [Mpc]	1200	21	218	19
RA [rad]	0.37	0.022	0.029	0.0072
DEC [rad]	-0.36	0.0082	0.046	0.0054
ι [rad]	1.6	0.010	0.040	0.0081
Ψ [rad]	1.7	0.015	0.040	0.0054
ϕ [rad]	3.5	0.72	0.11	0.028
t_c [s]	1120381489.6	0.59	0.0050	0.0020
$\Delta\Omega_{90\%}$ [deg^2]		7.2	56	1.1
SNR		70.5	250	260

Table 3.6: Multi-band observation with $ET + LISA$. We simulated an IMBH binary system of $4000M_\odot$ and $2000M_\odot$ at a distance of 1.2 Gpc. The errors are given at 1σ and the sky localization is at 90% C.L.. We used a frequency resolution of $1/16$ Hz for ET and 10^{-4} Hz for LISA. Table from [Dupletsa et al., 2023] (Table 6, ***authored by UD***)

waveform models, then Fisher-matrix codes are the best option.

`GWFish` has indeed been used for several detailed studies. These include the evaluation of the perspectives of multi-messenger (MM) observations for ET, both as a single observatory and in a network of other GW detectors, operating in synergy with γ and X-ray satellites using astrophysically-motivated populations of BNSs [Ronchini et al., 2022]. Among others, `GWfish` has been used to study the possibility of having a pre-merger alert and being able to detect the very high energy prompt emission from BNS mergers using a combination of ET and the Cherenkov Telescope Array (CTA) [Acharya et al., 2013].

`GWFish` is one of two codes, together with `gwfast`, that has been used for an extended and comprehensive study of the ET design [Branchesi et al., 2023]. Moreover, a detailed study of BNS populations, with different mass models and EoS, is performed with `GWFish` to assess the prospects of optical detections from BNS merger with ET in synergy with the Vera Rubin Observatory [Ivezić et al., 2019] in [Loffredo et al., 2025]. The results from these two works are extensively treated in Chap. 4.

The next part of this chapter is devoted to improving `GWFish` to include the implementation of a posterior-sampling algorithm starting from Gaussian likelihood, with priors. This will upgrade one of the strongest shortcomings of Fisher-matrix analyses while still avoiding the large computational cost of a full Bayesian analysis.

3.5 *Enhancing Fisher analysis with priors*

In Section 3.2.3, we stressed how the Fisher matrix analysis typically assumes flat, uninformative priors, considering them unnecessary given the information content of a sharply-peaked likelihood. However, we have also anticipated that parameter correlations can impact the accuracy of parameter error estimates from the Gaussian like-

lihood approximation without priors, leading to broader likelihood distributions.

Therefore, in this second part, we present a posterior sampling method to include prior information in the Fisher analysis so that posterior samples do not overestimate errors by orders of magnitude [Rodriguez et al., 2013] potentially going outside the physical range of parameters (see, e.g., in Fig. 3.8 the luminosity distance posterior extending to negative values with a Fisher-only analysis).

The influence of including priors into standard Fisher analysis is introduced in [Vallisneri, 2008], and implementation via a rejection sampling algorithm has been proposed in [Iacovelli et al., 2022a]. Some hints of the importance of priors implementation are already present in [Branchesi et al., 2023], mostly related to the inclination angle prior in MM studies with BNS systems. Furthermore, including priors is being exploited to ensure reliable distance errors, e.g., with a rejection sampling method in the work of [Santoliquido et al., 2024] for machine learning classification and with the method proposed in this work in [Cozzumbo et al., 2025] to reconstruct the expansion history of the universe in the bright sirens framework. This last work's results are discussed in Chapter 5

However, we recognize that if there are multimodalities as shown in Fig. 3.9, they are not generally suppressed by including priors. Multimodalities, which could arise from cyclic parameters, indeed pose a delicate issue in the analysis.

In what follows, we first provide in Sec. 3.5.1 an excursus on the motivation behind choosing specific priors for parameters entering in the description of a GW event. Then we describe in 3.5.2 a computationally efficient method we implemented in `GWFish` to incorporate priors into the standard Fisher analysis. We validate our method against the observed catalogue of GW events from the LVK Collaboration in Sec 3.5.3 and we discuss the results and effects of the combined `Fisher+Priors` analysis in Sec 3.5.4.

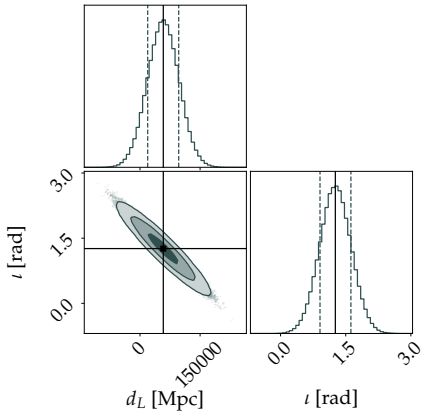

Figure 3.8: Example of a posterior distribution for a parameter, like the luminosity distance, that with a Fisher analysis only goes outside the physical range of the parameter (down to negative distance values). This figure is a zoom-in of Fig. B.5.

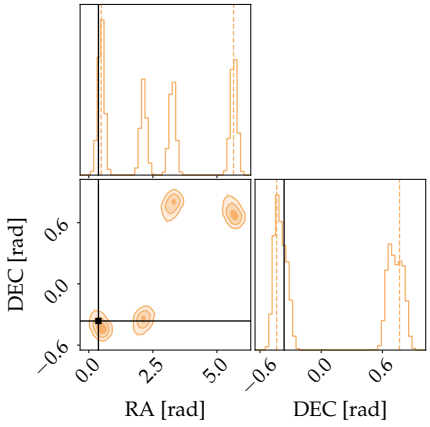

Figure 3.9: Example of multimodalities on angular parameter. Zoom-in from Fig. B.1 for the `Bilby` results, as multimodalities can only come out of a Bayesian analysis.

3.5.1 *Choosing priors in GW analysis*

In Tab. 3.7, we present an overview of the standard choice for GW parameters' priors in the LVK Collaboration [Abbott et al., 2019b, 2021a, 2024, 2023b]. These are the priors we will use throughout the analysis presented in this second part of the chapter.

The usual mass parametrization of a GW event uses the chirp mass $\mathcal{M}$ and mass ratio q as their behavior is more Gaussian and better suited for a Fisher analysis. Their distribution, though, is assumed to be uniform in the component masses, m_1 and m_2. The luminosity distance d_L parameter is uniformly distributed in an expanding Universe,

meaning that we have to consider a uniform in comoving volume distribution and account for time dilation between source and detector frame. The time of arrival t_c of the signal is usually well constrained, so that the uniform interval is tight. Angular parameters, instead, are either uniform or uniform on the sphere, in their ranges. In App. B, a detailed discussion and mathematical derivation of the different prior choices is provided.

parameter	units	prior	prior range
$\mathcal{M}_c$	$M_\odot$	$\mathcal{M}_c$	$[\min, \max]$
q	$M_\odot$	$q^{-6/5}(1+q)^{2/5}$	$[0.05, 1.0]$
d_L	[Mpc]	Uniform in source-frame	$[10, 10000]$
θ_{JN}	[rad]	Sine	$[0, \pi]$
DEC	[rad]	Cosine	$[-\frac{\pi}{2}, +\frac{\pi}{2}]$
RA	[rad]	Uniform	$[0, 2\pi]$
ϕ	[rad]	Uniform	$[0, 2\pi]$
Ψ	[rad]	Uniform	$[0, \pi]$
t_c	[s]	Uniform	$[t_c - 0.1, t_c + 0.1]$
a_1	-	Uniform	$[0, 0.99]$
a_2	-	Uniform	$[0, 0.99]$
$\texttt{tilt}_1$	[rad]	Sine	$[0, \pi]$
$\texttt{tilt}_2$	[rad]	Sine	$[0, \pi]$
$\texttt{phi}_{12}$	[rad]	Uniform	$[0, 2\pi]$
$\texttt{phi}_{JL}$	[rad]	Uniform	$[0, 2\pi]$

Table 3.7: List of analytic priors for each parameter entering the description of a GW event. For a more detailed description of the parameters refer to Tab. 1.1. Table from [Dupletsa et al., 2025] (Table 2, ***authored by UD***)

3.5.2 *An importance sampling algorithm to include priors*

In the following, we outline the procedure to get the prior-informed Fisher posteriors, starting from the Fisher likelihood as defined in Eq. (3.14). In a few words, this consists of drawing likelihood samples and weighting them by their prior probability.

- The Fisher matrix directly provides the multivariate Gaussian likelihood function, e.g., the covariance matrix which is one of the outputs of `GWFish`. In our Fisher analysis, we work in the zero-noise approximation and the likelihood is exactly centered on the injected values.
- Some parameters (especially angles and spins), even with high SNR, may still be poorly measured and show a largely-spread likelihood. Consequently, when drawing likelihood samples, most samples lie outside the physical range of parameters. Therefore, we sample directly from the truncated form of the Gaussian likelihood to prevent drawing a large number of samples with null prior, which would have to be discarded. In particular, we rely on the algorithm developed in [Botev, 2016][10]. This effectively accounts for the parameters'

[10] We slightly modified the `python` implementation of [Botev, 2016] publicly available on `github`

boundaries, ensuring the samples are in their physical range. When sampling from the truncated Gaussian we are not inverting again the covariance matrix. The algorithm, instead, uses the Cholesky decomposition.

- For each sample realization drawn from the likelihood, we evaluate the prior probability, according to what has been discussed in Sec. 3.5.1.

- In the final phase of the analysis, we construct the posterior distribution. We start by evaluating the prior probability of each likelihood realization. We use `numpy`'s `random.choice` [Harris et al., 2020] function to select the prior re-weighted samples. The re-weighting process favours samples with higher prior probabilities.

The outlined approach combines the information from the Fisher analysis (via the likelihood) as from Eq. 3.14 with the additional information provided by the priors following Eq. 3.1. Computationally speaking, including priors takes an overall time which is less than twice the one of the standard `GWFish` analysis to draw 10^4 samples. This assures the efficiency of the prior-informed Fisher matrix method presented here.[11]

[11] The code used to run the combined `Fisher+Priors` analyses is publicly available on GitHub. The *priors* modules have been also integrated in the standard `GWFish` code.

3.5.3 *Validation against GWTC data*

We conduct an extensive comparison with real data to validate our code and assess the impact of priors in standard Fisher analysis. To this scope, we recreate the same conditions used for the LVK data analysis and produced our Fisher matrix results. We use the updated version (*v2*) of the LVK publicly available GW event database present on `Zenodo` [Research and OpenAIRE, 2013] including all the BBH mergers from the first 3 observing runs [Abbott et al., 2019b, 2021a, 2024, 2023b]. Specifically, we use the cosmologically reweighted posterior samples labeled as *mixed_cosmo*. In Tab. 3.8, we report the comparison of the numbers between all the observed events and those we used in our analysis. In total, we have analyzed 78 events. For a comprehensive list of all the publicly available GW detections and why some of them were not included in our analysis, see Tab. B.1.

GWTC-2.1 for O1 + O2 + O3a and GWTC-3 for O3b

Table 3.8: List of detected events during the first 3 observing runs by the LVK Collaboration, compared to those used in our analysis (see Tab. B.1 in Supplements to Chapter 3 for further details). Table from [Dupletsa et al., 2025] (Table 1, ***authored by UD***)

	O1	**O2**	**O3a**	**O3b**	**tot**
observed	3	7	44	36	90
included	3	6	36	33	78

The Fisher analysis of each event is carried out under the same conditions the full Bayesian analysis is obtained. This means:

- Each event has its own detector network with specific sensitivity curves at the moment of detection.

- The waveform approximant is the same for all the events and is given by `IMRPhenomXPHM` [Pratten et al., 2021]. This is one of the

waveform approximants used in the LVK collaboration for BBH events, readily provided by `LALSimulation` [Husa et al., 2016].

- For each event, we take as injected values 30 different realizations[12] randomly sampled from the posterior distributions of the LVK analysis. This choice is motivated by the widely spread and often multimodal posteriors LVK provides. Averaging over different realizations provides a more robust comparison.

[12] The number of realizations is chosen to be at the same time computationally feasible and provide enough statistics.

- All the 15 parameters are included in the Fisher analysis: [$\mathcal{M}_c$, q, d_L, θ_{JN}, `DEC`, `RA`, ϕ, Ψ, t_c, a_1, a_2, $\texttt{tilt}_1$, $\texttt{tilt}_2$, $\texttt{phi}_{12}$, $\texttt{phi}_{jl}$]. The parameters represent the masses, in the form of chirp mass $\mathcal{M}_c$ (in detector frame) and mass ratio q, luminosity distance d_L, the inclination angle of the source with respect to the line of sight of the observer θ_{JN}, parameters describing the position of the source in the sky (`DEC` and `RA`), the phase ϕ and the time of arrival of the signal t_c, its polarization Ψ, and the six parameters (a_1, a_2, $\texttt{tilt}_1$, $\texttt{tilt}_2$, $\texttt{phi}_{12}$, $\texttt{phi}_{jl}$) describing the spins of the two compact objects. See Tab. 1.1 for details.

Starting from the Fisher results, we follow the outlined method to obtain the posterior samples. The Fisher posterior samples, with and without the addition of priors, are then compared to the ones obtained with the full Bayesian analysis. Therefore, we have adopted the same priors as the full Bayesian procedure to ensure consistent comparison. The specific priors are reported in Tab. 3.7. Since we have 30 different analyses for each event, the result of our comparison is a distribution.

In Fig. 3.10, we show an example event, the first ever detected GW event, `GW150914`. We plot for each of the 15 parameters 3 sample sets: in *black* the posterior samples provided by LVK, in *dashed black* the median value of the LVK distribution, which, in this example plot, we used as the injection for `GWFish`. We superimpose in *dark green* the samples obtained from the Fisher analysis alone (likelihood samples) as in Eq. 3.14 and, in *orange*, the samples we get after the inclusion of priors following Eq. 3.1. It is worth noting how including the prior information for some parameters, especially spins and angles, may play a crucial role and restrict the uncertainty estimates by a large amount.

Our main results are summarized in Fig. 3.11, Fig. 3.12 and in Fig. 3.13. In Fig. 3.11, for each of the 15 parameters, we plot the ratio distribution between the 90% C.L. we get from the Fisher analyses, without (in *orange*) and with priors (in *dark green*), and the 90% C.L. that was obtained with the full Bayesian approach. The events, placed along the $x-$axis are represented by boxplots. The distribution median for each event is highlighted as a horizontal line in a darker shade for both the analyses, with and without priors. In Fig. 3.12,

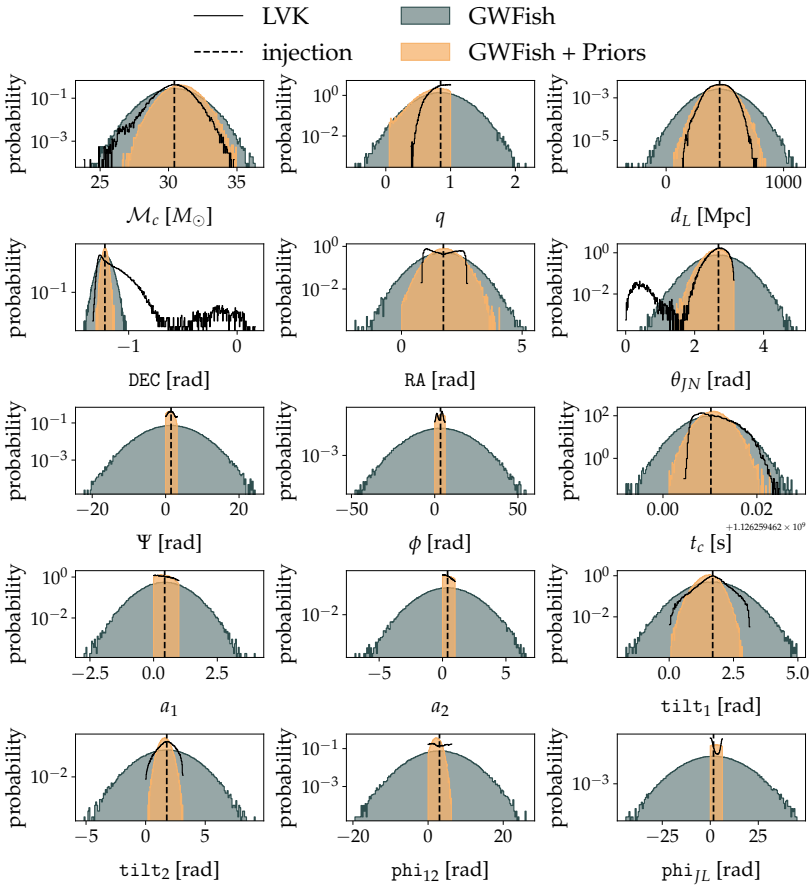

Figure 3.10: `GW150914` posterior distribution of all the 15 parameters. Full Bayesian parameter estimation results from LVK are shown in *black*, while `GWFish` results without (with) priors are shown in *dark green* (*orange*). The vertical *dashed black* line is the median of the LVK posterior distribution, also used as injection value for Fisher analysis. Figure adapted from [Dupletsa et al., 2025] (Figure 1, ***authored by UD***)

we plot the medians of the distributions as a function of the total mass of the binary (the median value in the detector frame). Furthermore, the size of the dots is proportional to the SNR of the signal (ranging in $[\sim 4, \sim 25]$), and the color shade indicates whether the event was seen by 2 (lighter shade) or 3 detectors (darker shade). The SNR obtained in each of the detectors and for the network are listed in detail in Tab. B.1. Fig. 3.13 shows the corresponding histograms of the medians of the 90% C.L. ratio distributions per event for each parameter, with (in *dark green*) and without (in *orange*) priors.

We are not evaluating the distance between our and the LVK results in a distributional sense using, for example, the Hellinger distance, as this leads to a case-by-case and, within one event, parameter-dependent results due to degeneracies and multimodality issues. Here are the observations:

- *mass parameters*: The Fisher analysis tends to overestimate chirp mass and mass ratio errors. The match with LVK results is better for

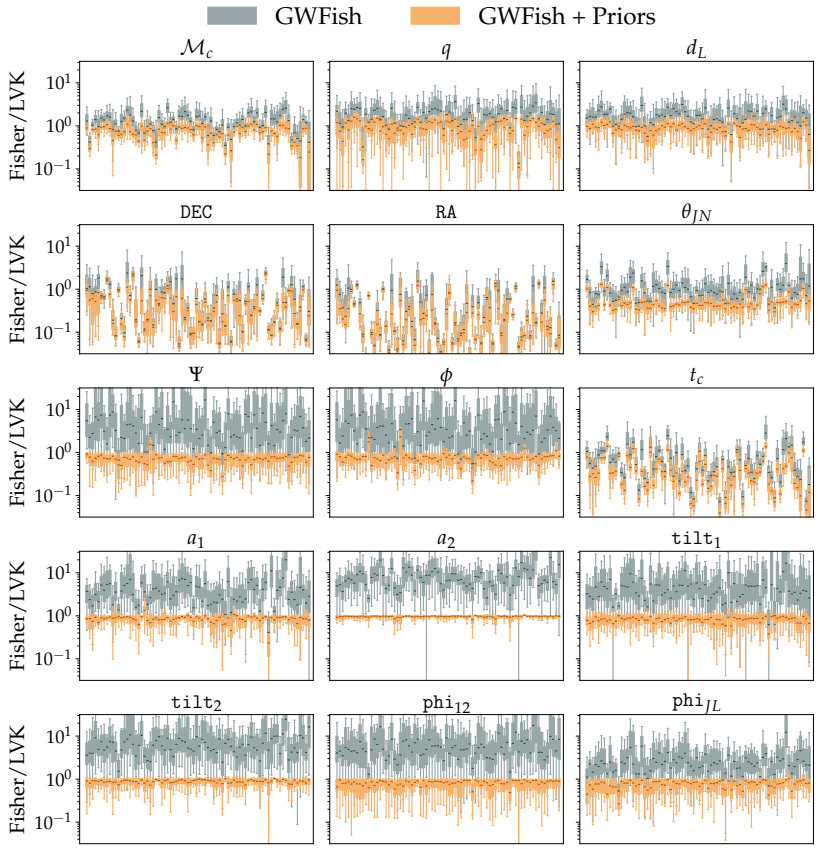

Figure 3.11: Distribution of ratios between the 90% C.L. obtained from `GWFish` results and the full Bayesian parameter estimation from LVK per each event and per each of the 15 parameters. Events are displayed along the $x-$axis, and each subplot refers to a different parameter. Results obtained without (with) priors are shown in *dark green* (*orange*). The median value of each distribution per event is indicated as a horizontal line of a darker shade. Figure adapted from [Dupletsa et al., 2025] (Figure 2, ***authored by UD***)

the chirp mass. When priors are included, the match becomes very good, and most of the bias of the error estimates (towards larger or smaller errors) is removed.

- *luminosity distance*: The Fisher analysis typically overestimates errors of the luminosity distance. The inclusion of priors leads to a good match with LVK results. When all three detectors are active (see Fig. 3.14), the constraint on the distance measurement is already done well by the Fisher analysis alone.

- *angular parameters*: The inclusion of priors does not generally improve the error estimates of `RA`, `DEC`, and the difference between LVK results and Fisher analysis spans over two orders of magnitude. θ_{JN}, Ψ and ϕ show a slight improvement from priors. We address this specifically in the related paragraph below.

- *time of coalescence*: The error on t_c is already well estimated with Fisher analysis alone. It is curious to observe that when priors are included in the `GWFish` analysis, the errors of the merger-time estimates can be significantly underestimated.

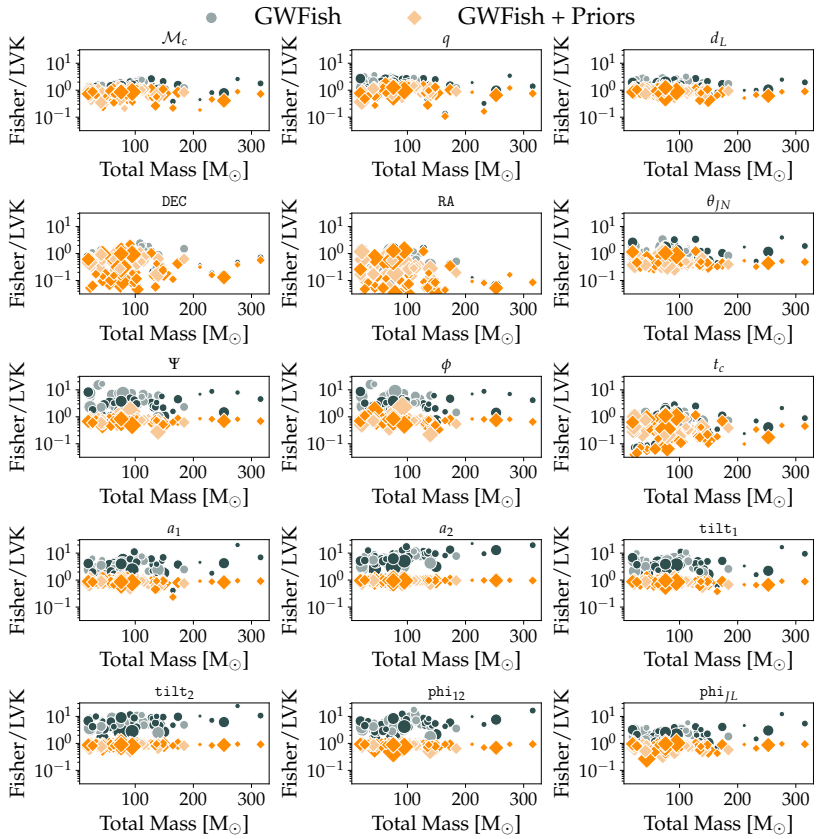

Figure 3.12: Median of the ratio between the 90% C.L. obtained from `GWFish` results and full Bayesian parameter estimation (LVK). Results obtained without (with) priors are shown in *dark green* (*orange*). The size of the markers is proportional to the median of the SNR of the network. Light (dark) shade refers to two (three) detectors observing the event. Figure adapted from [Dupletsa et al., 2025] (Figure 3, ***authored by UD***)

- *spin parameters*: All the spin parameters are poorly constrained with Fisher analysis alone. Including priors allows us to reproduce the LVK results. Still, it should be noted that even the LVK results are likely prior driven since the signals reported in GWTC carried very little information about spins (with some exceptions).

Angular parameters and multimodality A full Bayesian analysis might encounter multimodality issues. This happens especially when it comes to angular parameters (see, for example, the θ_{JN} parameter in Fig. 3.10). Moreover, it is more evident when fewer detectors are involved, and the SNR in each detector is low (below $4-5$). Multi-modality cannot, by definition, be a feature coming out of Fisher's analysis, as it provides a Gaussian likelihood centered around the injected value. This explains the ample range (up to two orders of magnitude) of the ratio between the 90% C.L. obtained with `GWFish` analyses and the LVK results from full Bayesian analysis as shown in Fig. 3.11, Fig. 3.12, and Fig. 3.13. Generally, the Fisher approximation tends to overestimate the uncertainties, as seen from parameters like the chirp mass, the

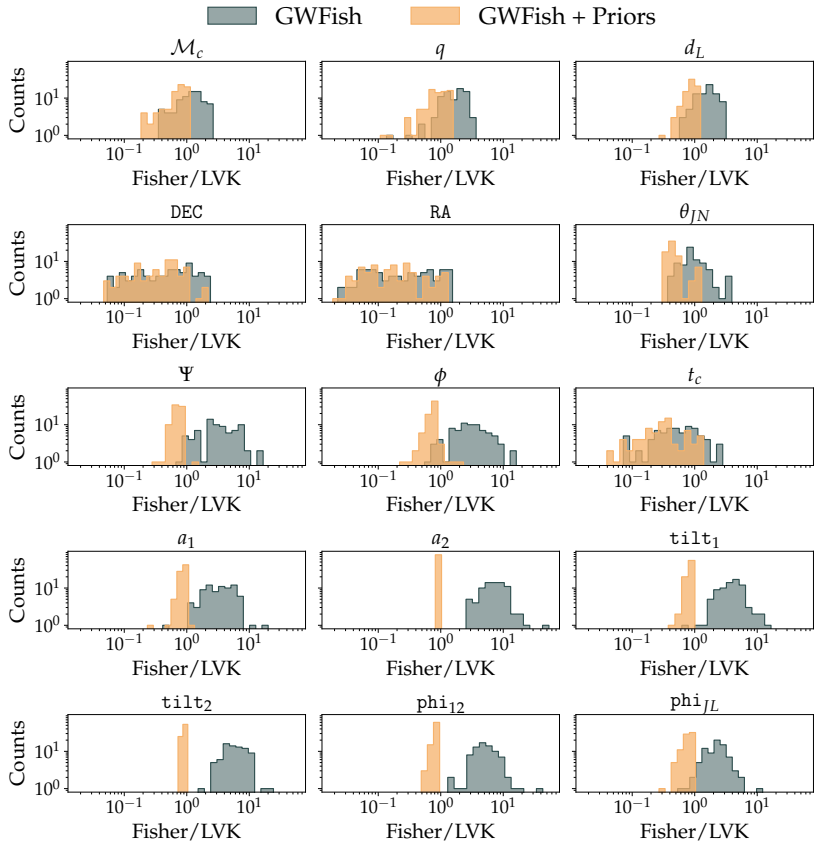

Figure 3.13: Histograms of the median of the ratio distribution between the 90% C.L. obtained from `GWFish` results and full Bayesian parameter estimation (LVK). Results obtained without (with) priors are shown in *dark green* (*orange*). Figure adapted from [Dupletsa et al., 2025] (Figure 4, ***authored by UD***)

mass ratio or the luminosity distance. However, when a parameter presents a multi-modal distribution in standard Bayesian analysis, the Fisher analysis provides poor error estimates as it represents a single mode. Therefore, the constraints from the Fisher analysis are likely to be tighter. To this scope, we selected a subsample of events, for which all 3 detectors were used and the SNR in each detector was around 4 or higher. This left us with 4 events, `GW190701`, `GW200202`, `GW200224` and `GW200311`. The results are shown in Fig. 3.14. They confirm the general trend discussed before: Fisher analysis alone gives broader or comparable estimates when multi-modality is broken by having more detectors in the analysis.

When it comes to sky localization with ET, multi-modality can also be suppressed by observing signals for long periods of time. For example, neutron-star binaries would be observed for hours up to a full day, and this would allow the use of the amplitude and phase modulations of the signal due to the rotation of the Earth to infer the source location.

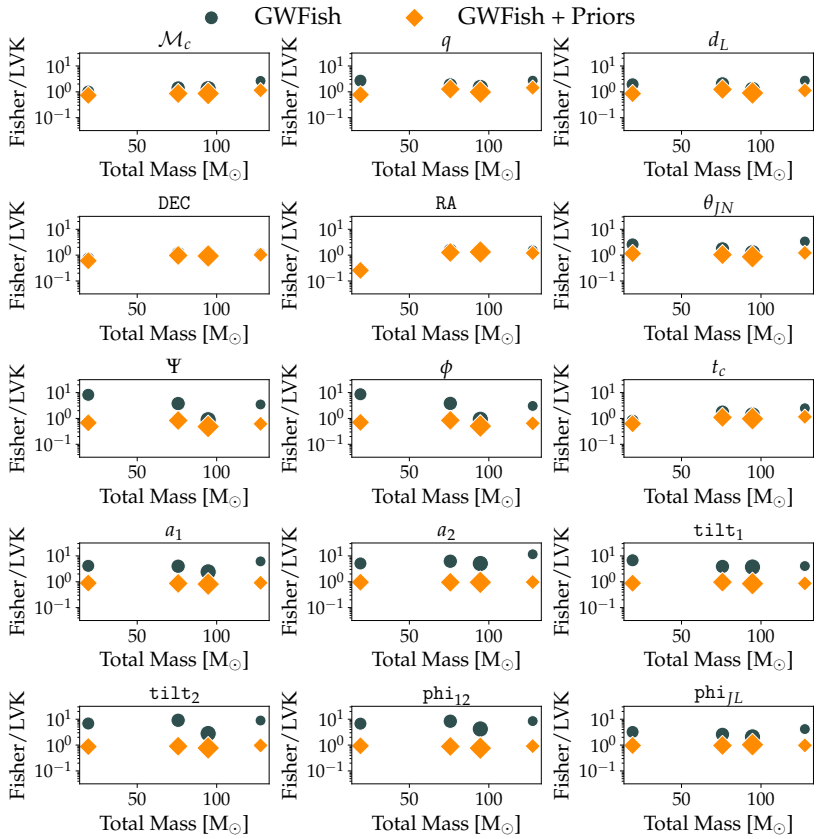

Figure 3.14: Same as in Fig. 3.12, but here we show only those events detected with all three interferometers and SNR in all three detectors is $\gtrsim 4$. The network SNR for these events varies in the range between 9 and 19. Figure adapted from [Dupletsa et al., 2025] (Figure 5, ***authored by UD***)

3.5.4 *The role of priors in Fisher analysis*

Our findings on the validity of Fisher's approximation center around two main themes. The first concerns the interaction between SNR and correlations, multimodality, and degeneracies, while the second focuses on the impact of prior information.

- Fisher-matrix analyses are always introduced as an approximation valid in the high-SNR limit [Vallisneri, 2008; Rodriguez et al., 2013]. Our results suggest, instead, that the accuracy of the Fisher analysis is mostly limited by model degeneracies and correlations among parameters, rather than the SNR. Specifically, degeneracies pose a major issue even if the SNR is high. It still holds that very low SNR Fisher matrix analyses provide less accurate estimates of parameter errors. We find that the Fisher analysis does well, with a trend to overestimate uncertainties, confirming the findings of [Rodriguez et al., 2013] (see Fig. 3.11, Fig. 3.12, Fig. 3.13). This is the case as long as the parameters are not degenerate and the Bayesian analysis does not output multi-modal posterior distributions. By con-

struction, in fact, the Fisher analysis cannot represent multimodal distributions. Therefore, when multimodality comes into play, the Fisher analysis represents one of the modes (centered around the injected parameter value), and this explains why the uncertainties are sometimes better estimated with Fisher approximation than with Bayesian analysis (see the angular parameters and hence sky localization). Multimodalities are not easy to deal with. Some insights on the issue are given in [Roulet et al., 2022] where ad-hoc reparametrizations are proposed.

- Adding priors improves the error estimates. Parameters like chirp mass, mass ratio, and luminosity distance benefit from including priors. Especially for luminosity distance, this assures that the posterior does not extend beyond the physical range to negative values. Priors' impact is even more evident for spin parameters, poorly constrained by Fisher analyses alone. This also happens in the full Bayesian analysis, where some parameters, like spins, are as well prior-driven.

  On the other hand, regarding sky localization and angular parameters in general, including prior, the error estimates might only slightly improve due to the inherent limitations of the Fisher analysis in handling multi-modal distributions.

- There is, in fact, an interplay among priors, correlations, and SNR, especially when few detectors are involved. In this case, the results for angular parameters are prone to degeneracies. When the sky localization suffers from multi-modality, the match between LVK results and `GWFish+Priors` is generally worse. Especially the sky-location errors produced by `GWFish+Priors` cannot be trusted in this case. As we have shown in Fig. 3.14, however, degeneracies can be effectively broken by having a network of 3 detectors, with a non-negligible SNR in each of them (at least around 4). This not only improves the match between LVK and `GWFish+Priors` results with respect to sky localization but, in fact, improves the match with respect to all parameters. This highlights the role of priors in taming degeneracies, and it indicates how well `Fisher+Priors` methods work in the absence of important multi-modality in the posterior distribution. In contrast, error estimates of mass parameters and distance match the LVK results very well, even when the observation is made with only two detectors of the LVK network.

We conclude that a Gaussian-likelihood approximation is a valid tool for providing estimates of parameter errors. However, it is crucial to note that this method has limitations. To corroborate the findings, more observations from 3-detectors need to be analyzed.

Our study in [Dupletsa et al., 2025] supports the results obtained in all the science case studies carried out so far with Fisher-matrix methods [Borhanian, 2021; Ronchini et al., 2022; Iacovelli et al., 2022a; Banerjee et al., 2023; Branchesi et al., 2023; Loffredo et al., 2025], with the exception of a few analyses that concern BBH localization with less than three detectors.

We have shown throughout this chapter that Fisher analysis tools are efficient for rapid PE and sensitivity forecasting. However, to face the challenge of data analysis with the future XG detectors, we need methods that go beyond the linear approximation and Gaussian likelihood. The ET community is managing the effort in the direction of machine learning [Cuoco et al., 2021; Razzano and Cuoco, 2018; Cuoco et al., 2024]. These comprise both tools for recognition and classification of signals at detector level like in [Razzano and Cuoco, 2018], and fast data analysis techniques [Cuoco et al., 2021, 2024]. A bridge between the Fisher approach and machine-learning-based algorithms is analyzed in the work of [Santoliquido et al., 2025] for BBH signals at high redshift. Looking ahead, improved forecasting tools will remain essential for validating analysis strategies and guiding detector design. At the same time, it is crucial to advance PE techniques in preparation for when the ET becomes operational and begins collecting data.

4. *Multi-messenger astrophysics in the ET era*

> *Any coincidence is always worth noticing. You can throw it away later if it is only a coincidence.*
>
> **— Agatha Christie**
> "Nemesis"

This chapter is based on two papers. The first one, [Branchesi et al., 2023], is a key paper in the Einstein Telescope (ET) Collaboration. It is a paramount study that compares different designs of ET and their scientific output. The study is a significant milestone in the planning process of the ET observatory. Within this major work, which involved the efforts of many people, I produced the parameter estimation (PE) of the Binary Neutron Star (BNS) population using `GWFish` *[Dupletsa et al., 2023], one of the two codes employed for this paper, along with* `gwfast` *[Iacovelli et al., 2022b]. The findings related to the BNSs constitute the majority of the second chapter of [Branchesi et al., 2023], which focuses on the multi-messenger (MM) capabilities of ET and which I discuss in the first part of this chapter of my thesis. Additionally, I analyzed the BBH population to compare and validate the results obtained with* `gwfast`*.*
The second work [Loffredo et al., 2025] is a more detailed and in-depth follow-up to the MM chapter of [Branchesi et al., 2023]. I am one of the three corresponding authors of this paper. I made a major contribution by producing all the PE of several astrophysically-motivated BNS merger populations, considering different observing networks and interpreting the gravitational results. The gravitational analyses, which I thoroughly present in the second part of this chapter, serve as the foundation of the electromagnetic (EM) studies connected to kilonova (KN) microphysics and observations studied in the paper [Loffredo et al., 2025]. Moreover, the catalogues with all the results of the gravitational analysis have been separately released on Zenodo [Dupletsa et al., 2024]. The release of these catalogues holds significant importance for the science community, as they provide valuable resources to enable studies evaluating next-generation (XG) detector achievements in astrophysics, nuclear physics, and cosmology.

4.1 *The Einstein Telescope (ET) design(s)*

As discussed in 1.2.5, the reference design of the Einstein Telescope (ET) [Hild et al., 2008; Punturo et al., 2010; Hild et al., 2011] has a triangular shape and includes three nested detectors, each with 10 km arms. Each detector features a 'xylophone' configuration comprising two interferometers: one tuned towards the High-Frequency (HF), and another tuned towards Low-Frequency (LF). This first conceptual design

Contents

goes back to 2011. Still, only recently, thanks to the work in [Branchesi et al., 2023], a detailed comparison of several different proposals for the design and their scientific achievements has been systematically carried out.

The main alternative to the triangle-shaped single ET detector is a configuration composed of two well-separated L-shaped interferometers (with arms oriented at 90°, instead of the 60° of the triangular design). In Fig. 4.1, we show a schematic representation of the two alternative designs. Throughout this chapter and in the literature, we will refer to the triangle-shaped detector as ET-Δ, while the 2L configuration will be referred to as ET-2L.

Both designs, ET-Δ and ET-2L, retain the key features proposed for ET: an underground observatory to reduce the seismic noise, with cryogenic technology for the LF instrument, and a xylophone configuration to benefit from both the LF and HF capabilities. In [Branchesi et al., 2023], we examine the performance of different configurations by varying both the length of the arms - between 10 and 15 km for ET-Δ, and between 15 and 20 km for ET-2L - as well as their orientation. The orientation aspect concerns the ET-2L case, where we consider both aligned and misaligned configurations, the latter at 45°.

Furthermore, we investigate the scientific implications should the cryogenic technologies not be available, at least in the initial phases of the detector, meaning that only the HF instrument would be operational.

The research conducted in [Branchesi et al., 2023] is thorough and extended and was carried out within the Observational Science Board (OSB) of the ET Collaboration. Building upon previous work referenced in [Maggiore et al., 2020; Sathyaprakash et al., 2012; Iacovelli et al., 2022a], it explores the impact of various choices in geometry and design, considering several scientific cases. The study covers detection and parameter estimation (PE) capabilities for compact binary coalescence (CBC)s, including Binary Black Hole (BBH), Binary Neutron Star (BNS), and Neutron Star - Black hole (NSBH) populations, which already provide a first reliable metric to compare different configurations. Additionally, [Branchesi et al., 2023] examines the possibility of detecting stochastic backgrounds, applications in astrophysics, fundamental physics, cosmology, and, nonetheless, the potential benefits of the null stream[1], a key feature of the triangular design.

In Sec. 4.1.1, we will give a brief description of the two sensitivity curves of ET: the HF only, and the full cryogenic one, the LF, since this will set the common ground for both the works presented in this chapter. Then, Sec. 4.2, will be devoted to the multi-messenger (MM) results from [Branchesi et al., 2023]. We will discuss, in particular, the sky-localization capabilities of the different configurations and the

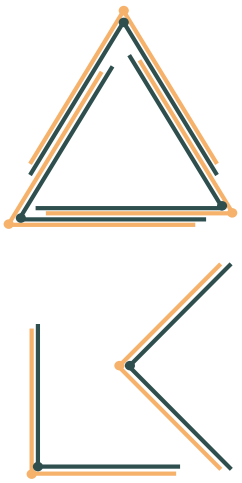

Figure 4.1: Schematic draft of the two main designs proposed for ET. A single triangle-shaped observatory or two L-shaped interferometers rotated by 45° to one another. Both alternatives use the xylophone configuration, visually represented in the figure using two distinct colors for each arm. The same color scheme is used for the corresponding sensitivity curves in Fig. 4.2.

[1] In the triangular design, there exists a combination of the outputs where the GW cancels out, allowing for a signal-free channel.

possibility of having pre-merger alerts in the context of ET operating in synergy with other electromagnetic (EM) observatories. In the second part of this chapter, instead, we will build upon the MM results of [Branchesi et al., 2023] and present the extensive work done in [Loffredo et al., 2025]. [Loffredo et al., 2025] expands the previous results implementing several networks of gravitational-wave detectors (ET operating with current and next-generation observatories), and state-of-the-art mass and Equation of State (EoS) models for two astrophysical populations of BNS mergers. In addition, we develop a refined modeling of kilonova (KN) emission and more realistic observational strategies. In Sec. 4.3, we focus on the gravitational results and how the PE of the BNS events is affected by the NS microphysics and population assumptions. In Sec. 4.3.4, we summarize the prospect for MM studies with ET.

4.1.1 *LF+HF sensitivity curves*

In the previous section, we introduced the concept of the xylophone design, which comprises two independent instruments operating under different conditions. In a nutshell, the HF instrument is specifically optimized for high frequencies and requires high laser power to reduce shot noise in that range. Notably, it operates at room temperature. In contrast, the LF instrument is optimized for low frequencies, requires cryogenic mirrors, and has the advantage of not needing high laser power. However, cryogenic technology is not straightforward and remains challenging in the current state of the art.

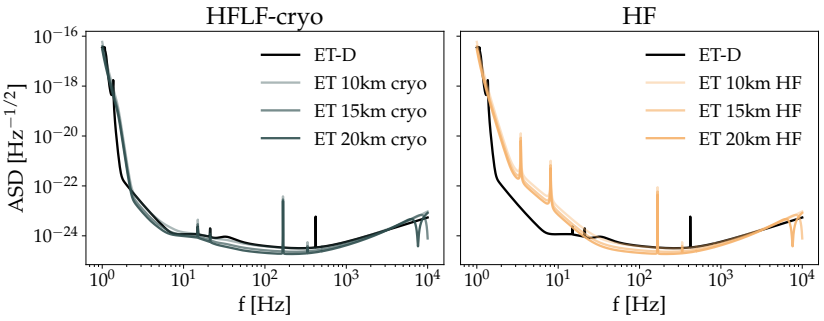

Figure 4.2: ASD plots for different ET scenarios and arm lengths. On the *left* we show the HFLF-cryo sensitivity curve, while on the *right* the HF one. In both cases, we present the three different arm lengths considered in [Branchesi et al., 2023], 10, 15, and 10 km, and we compare to the reference ET-D sensitivity curve, which describes a 10 km detector

Until recently, the reference sensitivity curve for ET has been the ET-D curve [Hild et al., 2011]. It is the basis for all ET studies, including those in [Dupletsa et al., 2023] referenced in Chapter 3. Thanks to the efforts of the Instrumental Science Board (ISB), two different sensitivity models have been developed to update the ET-D curve and highlight the challenges of achieving the cryogenic technology for the LF com-

ponent. All the research described in this chapter uses the updated sensitive curves.

The full cryogenic model, called HFLF-cryo, incorporates both the HF and LF instruments. The HF one includes only the HF part. In Fig. 4.2, we present the Amplitude Spectral Density (ASD) for the two sensitivity models considering the 3 different arm lengths analyzed in [Branchesi et al., 2023][2]. We also compare these curves to the reference ET-D sensitivity curve.

[2] The HFLF-cryo and HF sensitivity curves are available here.

4.1.2 *Where will ET be located?*

At the time of this thesis, there were two candidate sites: the Sos Enathos[3] site in Sardinia and the Mause-Rhine region, located at the border of three countries: Germany, Belgium, and the Netherlands.

[3] Usually it is written as Sos Enattos. However, in original Sardinian language, the double *t* is not used, *th* is used instead.

For the ET-Δ configuration, we consider the detector located in Sardinia. In the case of the ET-2L configuration, we place one detector in Sardinia and the other in the three-border region. The two observatories feature a $\sim 1165\,\mathrm{km}$ baseline. In Tab. C.1, among others, we provide the latitude and longitude coordinates for both sites.

Recently, a third candidate site has emerged in the Saxony region of Germany. The final location and design of ET are currently being discussed and investigated.

4.2 *BNS localization and pre-merger alerts*

ET has enormous potential in the context of MM observations. ET will bring BNS and NSBH merger detections from being rare and nearby events of today to approximately 10^5 per year, extending the detection distance beyond the star formation peak. For the closer events, ET will provide unprecedent accuracy in determining source parameters. Innovative EM observatories are planned to be operational in the ET era, and their synergy with ET will make the emerging field of MM a mainstream of the Universe exploration.

Among the many EM observatories, we include the Cherenkov Telescope Array (CTA) [Acharya et al., 2013], NewAthena [Cruise et al., 2025], the Vera Rubin Observatory [Ivezić et al., 2019], the James Webb Space Telescope (JWST) [Gardner et al., 2006], the Extremely Large Telescope (ELT) [Gilmozzi and Spyromilio, 2008], the Wide-field Spectroscopic Telescope (WST) [Mainieri et al., 2024], and the SKA Observatory (SKAO) [Weltman, 2020]. In particular, we explore in depth the synergy with the Vera Rubin Observatory. This is discussed in Sec. 4.3. Additionally, a synergy between ET and SKAO will be explored for cosmological inference in Sec. 5.3 of Chapter 5 of this thesis.

BNS mergers, on top of being sources of GW signals, are associated

with both GRB and KN emissions. Observations of ET together with EM observatories will probe the formation, evolution, and physical characteristics of BNS systems in connection with KNe and Gamma Ray Bursts (GRBs).

The GRB emission is produced by a relativistic jet and is beamed, making it typically observable only when the jet is directed towards the observer. Only a fraction of BNS mergers (the exact amount of which is still uncertain) are expected to produce a jet capable of successfully escaping the merger ejecta [Murguia-Berthier et al., 2014; Ronchini et al., 2022]. In contrast, the KN emission is isotropic and always present. During a BNS merger, neutron-rich matter from the stars is ejected and the conditions allow for the rapid neutron-capture nucleosynthesis [Eichler et al., 1989; Freiburghaus et al., 1999]. It is the radioactive decay of these heavy nuclei that powers the quasi-thermal emission known as the KN. With respect to a GRB, which can have luminosities as high as 10^{51} erg s^{-1} [Pescalli et al., 2016], the KN emission is intrinsically faint, with a peak luminosity in the interval $10^{39} - 10^{42}$ erg s^{-1}. The KN emission evolves rapidly, on the scale of days, and undergoes a characteristic color evolution, from UV/blue to red/near-infrared [Li and Paczynski, 1998; Metzger et al., 2010; Kasen et al., 2013; Barnes and Kasen, 2013; Grossman et al., 2014; Metzger, 2019]

Given the nature of the EM counterparts we are considering in this work, namely KNe and GRBs, we need to distinguish redshift regimes. KNe are intrinsically fainter than GRBs, meaning that we will be able to do MM astronomy only in the local Universe up to redshifts $z \sim 0.3 - 0.4$. The distant Universe, instead, will be accessible only thanks to the beamed emission of GRBs.

Likewise, we will benefit differently from the two EM transients. Observing GWs and KNe will allow us to study the nucleosynthesis process and the chemical enrichment of the Universe, not to mention the internal composition of NSs, e.g., their Equation of State (EoS). With joint GW/GRB detections, instead, we will be able to probe the structure and composition of the GRB relativistic jet, and notably, given the high redshift till which we can detect GRBs, we will be able to infer cosmological parameters across the cosmic history. In [Cozzumbo et al., 2025], we address the possibility to constrain cosmological parameters using joint GW/GRB detections. This is the topic of discussion in Sec. 5.2 of the next chapter, Chapter 5, devoted to cosmology with ET.

The primary metrics used to assess MM capabilities of ET comprise BNS detection and sky localization. Detection boils down to SNR evaluation, and when the event's SNR is larger than a threshold, it is considered detected, while sky localization requires PE. More details are

provided in the following Sec. 4.2.1.

In what follows, we first present in Sec. 4.2.2 the sky localization results as a function of redshift, and then, in Sec. 4.2.3, the pre-merger alert possibility, which would allow detecting BNSs a non-negligible amount of time before the merger occurs. Identifying the GW signal before the merger is crucial to timely prepare the EM instruments to detect prompt/early counterparts.

4.2.1 *BNS population modeling and PE analysis setup*

The catalogue of BNSs used in [Branchesi et al., 2023] has been generated with the population synthesis code MOBSE [Mapelli et al., 2017; Giacobbo et al., 2018]. We refer to [Branchesi et al., 2023] for the population modeling details, and here we report the most relevant information. We use a number of events corresponding to one year of observations. The NS mass is uniformly distributed in $[1.1M_\odot, 2.5M_\odot]$ in the source frame. The common envelope efficiency is set to $\alpha = 3$, which, given the adopted evolution with redshift [Santoliquido et al., 2021], yields to a local merger rate value of $R_0 \sim 250\,\mathrm{Gpc^{-3}yr^{-1}}$ consistent with the LIGO-Virgo-KAGRA (LVK) findings [Abbott et al., 2021c].

For PE with `GWFish` we use the `IMRPhenomD_NRTidalv2` [Khan et al., 2016; Dietrich et al., 2019] waveform approximant. We estimate the uncertainties on the following parameters [m_1, m_2, d_L, θ_{JN}, `DEC`, `RA`, ϕ, Ψ, t_c, a_1, a_2, Λ_1, Λ_2][4] (refer to Tab. 1.1 for parameters description). We use $SNR = 8$ as the threshold for detection. We also assume a duty cycle of 85% for each of the ET components (see discussion about duty cycle and how it is implemented in `GWFish` in Chapter 3).

[4] We considered the two aligned spin components only, as we expect NSs to have small spin magnitudes [Burgay et al., 2003]

We take into consideration both the sensitivity curves described in Sec. 4.1.1, HFLF-cryo and HF, with 4 different networks: ET-Δ with either 10 or 15 km arms; and two 2L configurations, with 15 and 20 km arms, and 45° misalignement. We did not consider the 2L aligned configurations because aligned detectors give worse sky localizations.

We present the sky localization results in Sec. 4.2.2 and the analysis of pre-merger alerts in Sec. 4.2.3.

4.2.2 *Sky localization capability*

The ability of GW detectors to localize sources in the sky significantly impacts the efficiency of searching for their EM counterparts. This capability determines how many observations are needed to cover the area where the GW signal originated, the amount of observational time required, the sensitivity of the search, and the effectiveness of selecting and removing contaminating transients. Therefore, good sky

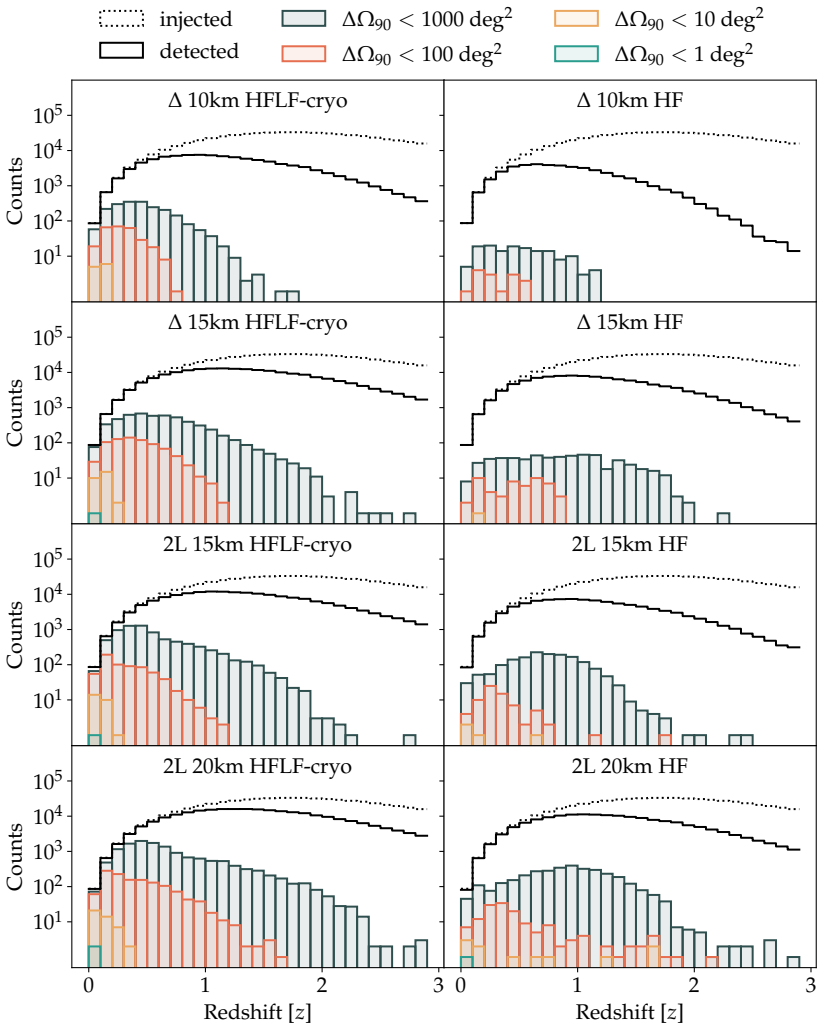

Figure 4.3: Redshift distribution of the sky localization uncertainty (given at the 90% C.L.) of the analyzed BNS population. We present the results for all the simulated networks, respectively, the ET-Δ 10 km, the ET-Δ 15 km, the 2L with 15 km misaligned arms, and the 2L with 20 km misaligned arms. The plots on *left* refer to the full HFLF-cryo sensitivity curve, whereas the ones on the *right* show the results with the HF curve only. Figure adapted from [Branchesi et al., 2023] (Figure 22, ***authored by UD***)

localization is crucial.

Fig. 4.3 shows the redshift distribution of the sky localization uncertainty at 90% C.L. for all the detected BNS events. Different colors represent the corresponding upper thresholds for the sky localization errors, respectively, less than 1000, 100, 10, and 1 deg^2. The dotted and solid *black* lines show the injected and detected events (at $SNR \geq 8$), regardless of their sky localization. The plots on the *left* have been produced with the HFLF-cryo sensitivity curve, while the ones on the *right* with the HF only one. For both sensitivity curves, we have simulated all the 4 networks: the ET-Δ 10 km, the ET-Δ 15 km, the 2L with 15 km misaligned arms, and the 2L with 20 km misaligned arms.

- Comparing the different geometries, we see that the ET-Δ of 15 km and ET-2L of 15 km give similar results and have a better perfor-

mance than the reference ET-Δ of 10 km. The 2L with 20 km arms design has a performance that is almost 4 times better than the baseline ET, managing to localize well at higher redshifts. These observations hold for both sensitivities.

- Comparing the plots *left/right*-wise, which means having or not the cryogenic instrument, we see how without the LF part, we lose a significant number of well-localized events, even at low redshifts. This loss occurs because we can no longer use at its fullest the Earth's rotation to help localize the events. The decrease is more important for the ET-Δ configurations with respect to the misaligned 2L ones.

$\Delta\Omega_{90\%}(\mathrm{deg}^2)$	HFLF-cryo							
	All orientation BNSs				BNSs with $\theta_v < 15°$			
	Δ10	Δ15	2L 15	2L 20	Δ10	Δ15	2L 15	2L 20
10	11	27	24	45	0	1	2	5
40	78	215	162	350	8	22	20	33
100	280	764	644	1282	26	74	68	133
1000	2112	5441	7478	13482	272	632	1045	1725

Table 4.1: Expected number of detections per year with a sky localization uncertainty $\Delta\Omega_{90\%}(\mathrm{deg}^2)$ smaller than a certain threshold specified in the first column. Results for the 4 detector networks and the HFLF-cryo sensitivity curve. In the *left* part of the table, we consider all randomly oriented BNS systems, whereas, in the *right* part, face-on systems only (see description in the main text). Table from [Branchesi et al., 2023] (Table 1, ***authored by UD***)

In Tab. 4.1, we again show the expected number of detections per year with a sky localization uncertainty $\Delta\Omega_{90\%}\,\mathrm{deg}^2$ smaller than a certain threshold (this time using 10, 40, 100 and 1000 deg^2)[5], with all the 4 different ET configurations with the HFLF-cryo sensitivity, but comparing the results from all the randomly oriented BNS systems, and selecting the face-on only. The face-on systems are the ones for which the viewing angle[6], θ_v is smaller than 15°. We make this selection because since we expect a fraction of the face-on systems to be able to produce GRBs, which relativistic jet we assume to be perpendicular to the orbital plane of the binary.

The corresponding results, obtained with the HF sensitivity curve only, are presented in Tab. 4.2.

$\Delta\Omega_{90\%}(\mathrm{deg}^2)$	HF							
	All orientation BNSs				BNSs with $\theta_v < 15°$			
	Δ10	Δ15	2L 15	2L 20	Δ10	Δ15	2L 15	2L 20
10	0	1	5	5	0	0	2	2
40	4	10	20	47	0	5	6	17
100	14	53	76	144	7	33	35	64
1000	145	548	1662	3378	80	336	672	1302

Table 4.2: Same as Tab. 4.1 but considering the detectors operating with only the HF interferometers. Table from [Branchesi et al., 2023] (Table 2, ***authored by UD***)

Distinguishing between randomly oriented and face-on systems allows us to make the following observations:

[5] The thresholds are connected to the FoV of the EM instruments working in synergy with ET.

[6] Since the inclination angle ι spans in $[0°, 180°]$, the viewing angle is directly ι if ι is in $[0°, 90°]$, or it is $|\iota - 180°|$ if ι is in $[90°, 180°]$

- We confirm that also for face-on events, ET-Δ of 15 km and ET-2L of 15 km give similar results and have a better performance than the reference ET-Δ of 10 km.
- When the LF instrument is not considered, we lose the well-localized events, again with ET-Δ design being more penalized than the 2L one. Still, when restricting our analysis to the face-on events, the percentage by which well-localized events are lost is smaller. Additionally, for the on-axis events, the ET-Δ design at full HFLF-cryo sensitivity is comparable to 2L of 15 km operating with the HF instrument, and outdone by the 2L of 20 km HF only. The results with HF only sensitivity stress the importance of having the LF part.

4.2.3 *Pre-merger alerts*

Detecting and localizing BNS system during the inspiral phase, before the merger, enables the identification of potential EM emission precursors. This allows telescopes to point to the GW source to capture the prompt/early EM emission. The first EM emission is crucial for probing the central engine of GRBs. Doing so would significantly enhance our understanding of various aspects, including jet composition, particle acceleration mechanisms, radiation, and energy dissipation processes. On the KNe side, instead, detecting early emission from KN events would provide valuable insights into the structure of the outer sub-relativistic ejecta [Banerjee et al., 2020].

Having stated the advantages of pre-merger alerts for MM astronomy, we analyze the capabilities of ET to detect BNSs and provide a good enough sky localization before the merger.

Table 4.3 presents the annual number of detected BNS mergers (under the condition of SNR $\geq$ 8), before merging, within a redshift of $z = 1.5$, for the HFLF-cryo sensitivity curve. We examine three pre-merger timeframes: 30 minutes, 10 minutes, and 1 minute before the merger.

For each ET configuration, we give the number of detection below 10, 100, 1000 deg^2. The sky localization is reported at 90% C.L. The results include randomly oriented BNSs, and BNSs with a viewing angle less than 15° (face-on). Detecting on-axis sources is crucial for identifying the prompt or early beamed emissions linked to relativistic jets. In [Banerjee et al., 2023], we extensively analyzed the prospects for detecting the very high-energy prompt emissions from GRBs, which have yet to be observed, by exploiting the synergy between ET and the CTA [Acharya et al., 2013].

Focusing on well-localized events detected pre-merger with a sky localization smaller than 100 deg^2, we find that the ET-Δ of 15 km outperforms the ET-Δ of 10 km and the 2L misaligned configuration with

Configuration	HFLF-cryo						
	$\Delta\Omega_{90\%}$ [deg^2]	All orientation BNSs			BNSs with $\theta_v < 15^\circ$		
		30 min	10 min	1 min	30 min	10 min	1 min
ET-Δ-10 km	10	0	1	5	0	0	0
	100	10	39	113	2	8	20
	1000	85	293	819	10	34	132
	All detected	905	4343	23597	81	393	2312
ET-Δ-15 km	10	1	5	11	0	1	1
	100	41	109	281	6	14	36
	1000	279	806	2007	33	102	295
	All detected	2489	11303	48127	221	1009	4024
ET-2L-15 km	10	0	1	8	0	0	0
	100	20	54	169	2	7	26
	1000	194	565	1399	23	73	199
	All detected	2172	9598	39499	198	863	3432
ET-2L-20 km	10	2	4	15	1	1	2
	100	39	118	288	7	19	47
	1000	403	1040	2427	47	128	346
	All detected	4125	17294	56611	363	1588	4377

Table 4.3: Number of BNS mergers per year detected (SNR $\geq$ 8) before the merger within $z = 1.5$ for the different ET configurations with the HFLF-cryo sensitivity curve. We show the number of detected events for 30, 10, and 1 minute(s) before the merger. For each detector configuration, we consider different sky localization thresholds, within 10, 100, 1000 deg^2, at 90% C.L. Table from [Branchesi et al., 2023] (Table 3, ***authored by UD***)

15 km arms. Its performance is comparable to the 2L configuration with 20 km misaligned arms. Additionally, the 2L configuration with 15 km misaligned arms performs better than the ET-Δ configuration of 10 km. Notably, the results are consistent for on-axis events as well.

Tab. 4.4 illustrates the significant reduction in pre-merger alerts without the LF interferometers. For all configurations of the ET, there are no localized pre-merger detections, with only a few events having sky localizations smaller than 1000 deg^2 per year occurring one minute before the merger. Specifically, a handful of events show localizations less than 100 deg^2 for the 2L of 20 km configuration.

In the context of multi-messenger astrophysics, the 2L misaligned configuration with 15 km arms offers significant improvements over the already impressive performance of the baseline ET-Δ design, and it is comparable to the ET-Δ of 15 km. This advancement enables the observation of many well-localized events, even at higher redshifts. Specifically, the incidence of KNe associated with GW signals increases significantly.

The enhanced localization of the 2L 15 km configuration compared to the baseline ET-Δ makes searching for EM counterparts easier. This improvement allows for implementing a galaxy-targeting strategy and facilitates the efficient removal of contaminants.

For pre-merger alerts with sky localizations, the ET-Δ of 15 km performs better than both the baseline triangle and the 2L 15 km configu-

Configuration	HF						
	$\Delta\Omega_{90\%}$ [deg^2]	All orientation BNSs			BNSs with $\theta_v < 15°$		
		30 min	10 min	1 min	30 min	10 min	1 min
ET-Δ-10 km	100	0	0	0	0	0	0
	1000	0	0	4	0	0	1
	All detected	0	3	317	0	0	26
ET-Δ-15 km	100	0	0	2	0	0	0
	1000	0	0	10	0	0	4
	All detected	2	8	891	0	1	84
ET-2L-15 km	100	0	0	0	0	0	0
	1000	0	0	7	0	0	3
	All detected	0	7	743	0	1	69
ET-2L-20 km	100	0	0	3	0	0	0
	1000	0	0	13	0	0	6
	All detected	2	11	1535	0	1	146

Table 4.4: Same as Tab. 4.3 but for the HF sensitivity ET. Table from [Branchesi et al., 2023] (Table 4, ***authored by UD***)

ration, approaching the capabilities of the 2L configuration with 20 km arms.

In a nutshell, the work in [Branchesi et al., 2023] shows us that:

- With respect to the current infrastructure of LVK, any ET design would improve the current performance by orders of magnitude
- The misaligned 2L configuration of 15 km seems to give the best scientific return
- The LF part is crucial for several science cases

4.3 *How EoS and mass model impact BNS PE*

In the first part of this chapter, we focus on the evaluation of the optimal ET design for MM studies. We focused on the sky localization capabilities and the related possibility to send pre-merger alerts for BNS sources, but we have not considered the impact of different EoS and mass models on GW detection when modeling the BNS population.

In this second part of the chapter, we examine in depth how uncertainties in NS population properties and microphysics may influence detection rates. In particular, we investigate the potential for detecting optical emissions from BNS mergers using XG detectors. The results are detailed in [Loffredo et al., 2025]. The EoS of the dense matter inside a NS has a direct impact both on the GW signal and on the ejected matter, which is then responsible for the KN emission. Therefore, joint

KN/GW observations constitute a powerful tool to investigate the inside of NS sources.

So far, we had two relevant BNS detections. The first one, `GW170817` was accompanied by an unequivocal EM counterpart, `AT2017gfo` [Abbott et al., 2017c,d], which gave us the first evidence that BNSs produce KN emission and are responsible for the formation of the heavy elements in the Universe. The extended observational campaign allowed us to follow the distinct color evolution of the KN, and the absorption features proved consistent with the presence of neutron-capture elements. The second observation, `GW190425` [Abbott et al., 2020a], is again a BNS candidate, but without an observed EM counterpart. The peculiarity of this system is its unusually high total mass, around $3.3 M_{\odot}$, with respect to the BNS systems in the Milky Way, observed electromagnetically. This triggered the community to hypothesize the higher-mass component of the system to be either a heavy NS or a light BH [Kyutoku et al., 2020; Raaijmakers et al., 2021; Barbieri et al., 2021; Camilletti et al., 2022; Dudi et al., 2022; Radice et al., 2024]. These are two events on which we calibrate the KN modeling in [Loffredo et al., 2025].

Besides these two isolated detections, no significant BNS candidates have been detected during the fourth run of LVK. At the current status, we expect LVK detectors to be able to observe eventual BNS events up to $z \sim 0.2$ [Abbott et al., 2020b; Petrov et al., 2022].

Observatories like ET and CE from the XG GW network, instead, will observe BNS mergers throughout cosmic history, allowing for precise parameter estimates for the nearest events. ET and CE will be able to probe BNS mergers up till $z \sim 4$ with ET [Branchesi et al., 2023], and $z \sim 10$ with CE [Evans et al., 2021, 2023; Gupta et al., 2024], respectively. Innovative wide-field observatories, such as the Vera Rubin Observatory [Ivezić et al., 2019], will rapidly cover large sky areas with unprecedented sensitivity, enabling the detection of faint transients. Furthermore, spectroscopic telescopes, such as the ELT [Gilmozzi and Spyromilio, 2008] and the Wide-field Spectroscopic Telescope (WST) [Mainieri et al., 2024], will provide us with a precise characterization of EM counterparts.

We carry out a three-step study. We start by examining BNS merger populations with varying NS mass distributions and EoS. We model the GW signals based on the properties of the sources. In the second step, we analyze both the KN and the GRB emissions. To do this, we simulate the KN ejecta using numerical relativity-informed fits, taking into account the potential prompt collapse of the remnant into a black hole and introducing new fitting formulas that are suitable for more massive BNS systems, such as the aforementioned `GW190425` system. We also ensure the optical afterglow emission from relativistic

jets aligns with the observed characteristics of short GRBs. In the last step, we estimate the number of detected optical signals by simulating realistic observational strategies employed by the Rubin Observatory.

In what follows, we present all the GW signal modeling and PE. To analyze the detection potential of the GW signals emitted by BNS mergers, we consider various detector networks, including both current and XG GW detectors. We describe the employed BNS population in Sec. 4.3.1 and the GW analysis setup in Sec. 4.3.2. We discuss the GW results in Sec. 4.3.3 and present an overview of what has been discussed in [Loffredo et al., 2025] on joint GW/KN and/or GW/GRB observations in Sec. 4.3.4.

4.3.1 *BNS population and EoS modeling*

The population of BNSs is obtained using the population-synthesis code SEVN [Spera et al., 2019; Mapelli et al., 2020; Iorio et al., 2022], which takes into account both isolated and binary star systems. With respect to the MOBSE code used in [Branchesi et al., 2023] (see Section 4.2.1), SEVN is a more recent code that improves over the simplifying fitting formulas used in MOBSE. SEVN implements single-star evolution tracks to interpolate the status of the two stars in the binary evolution.

The merger rate density, on the other hand, is derived using the code of [Santoliquido et al., 2020], COSMO$\mathcal{R}$ATE, which follows the metallicity evolution outlined in [Madau and Fragos, 2017]. The dominant source of uncertainty in compact binary coalescence (CBC) rate modeling arises from the α parameter, which determines the efficiency of the common envelope [Santoliquido et al., 2021]. To assess the impact of varying common envelope efficiencies, we consider two values for α: $\alpha = 0.5$ for a pessimistic scenario and $\alpha = 1.0$ for a fiducial scenario. Based on these assumptions, we generate two populations corresponding to 71338 events for $\alpha = 0.5$ and 363560 events for $\alpha = 1.0$, considering a redshift cut of $z < 1$. This results in a local merger rate of $23\,\mathrm{Gpc\,yr^{-1}}$ for $\alpha = 0.5$, and $107\,\mathrm{Gpc\,yr^{-1}}$ for $\alpha = 1.0$, both of which are consistent with what is measured with LVK [Abbott et al., 2021c] and current LVK observations. This mass distribution is currently supported by GW observations, including `GW190425`.

We determine the component masses of the NS binaries, $m_{1,\mathrm{src}}$ and $m_{2,\mathrm{src}}$, using two distinct mass distributions: Gaussian and uniform, illustrated in Fig. 4.4. The Gaussian distribution is characterized by a peak value at $1.33\,M_\odot$ and a standard deviation of $0.09\,M_\odot$. This model is derived from a fit to the masses of NSs in binary systems in the Milky Way [Ozel et al., 2012; Kiziltan et al., 2013; Özel and Freire, 2016]. In contrast, the uniform mass distribution spans values from

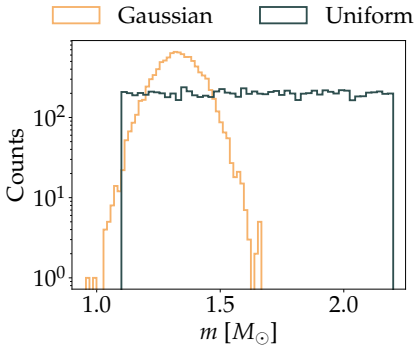

Figure 4.4: Comparison between Gaussian and uniform mass distribution

$1.1 M_\odot$,up to a maximum mass, denoted as $m_{\rm max}$, where $m_{\rm src,max}$ depends on the selected EoS. We do not directly use the masses predicted by the population synthesis code, as these are not compatible neither with the galactic SN spectrum, which is Gaussian, nor the poorly reconstructed one from the very few LVK observations, which is broadly unconstrained but uniform. The reason lies in the poor prescription for SN explosion mechanisms in the available population synthesis codes [Giacobbo and Mapelli, 2018].

We consider two different EoS: `APR4` [Akmal et al., 1998; Baym et al., 1971; Douchin and Haensel, 2001] and `BLh` [Bombaci and Logoteta, 2018; Logoteta et al., 2021]. Both the EoSs used in our study are obtained from first-principles calculations and are fully compatible with the most recent astrophysical constraints on the NS mass, radius, and tidal deformability. `APR4` predicts $m_{\rm src,max} = 2.2 M_\odot$, and for `BLh` we have $m_{\rm src,max} = 2.1 M_\odot$, for the maximum mass $m_{\rm src,max}$ of a cold non-rotating NS[7]. These values are used to set the maximum mass for our populations.

The tidal deformabilities, Λ_1 and Λ_2, for each component of the BNS, are determined based on the selected EoS and binary masses. While the maximum masses values are similar, `APR4` produces significantly more compact NS, with larger compactness and smaller tidal deformability. These differences affect the amount of the ejected material, typically larger for `BLh` than for `APR4`, and, as a consequence, the properties of the KN emission.

Between the two EoSs, the mass distributions are identical in the Gaussian case, while we have some higher masses for the `APR4` EoS in the case of the uniform one. When comparing `APR4` and `BLh`, the most significant difference is the tidal deformability, as shown in Fig. 4.5.

The BNS mergers are distributed isotropically in the sky, meaning they occur uniformly in all directions. In other words, the inclination of the orbital plane with respect to the line of sight is randomly distributed. This is obtained by uniformly sampling `RA` in the interval $[0, 2\pi]$ and `DEC` uniform in cosine in $[-\pi/2, +\pi/2]$. The inclination angle, ι, follows a uniform in sine distribution in $[0, \pi]$. The polarization, Ψ, and phase ϕ angles are both uniformly distributed in the range $[0, 2\pi]$ (see the discussion in Appendix B).

To effectively sample the parameter space of BNS mergers properties and their GW and EM signals, we analyze catalogues of BNSs observed in 10 years by an ideal instrument from Earth.

[7] We assume non-spinning NSs, since NSs in binary systems are expected to have negligible spins [Burgay et al., 2003]

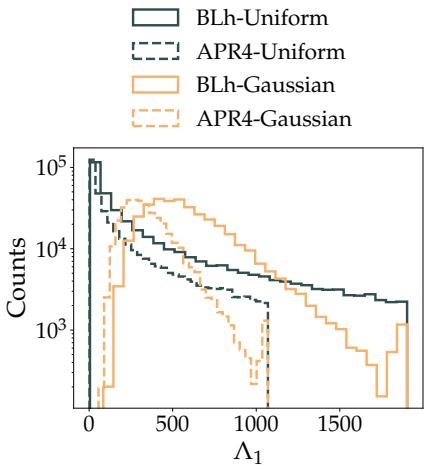

Figure 4.5: Tidal deformability for the primary component of the BNS population, with $\alpha = 1.0$. Figure adapted from [Loffredo et al., 2025] (Figure A.1+A.2)

4.3.2 *GW simulation setup*

Starting from the populations of 10 years of BNS mergers as described in the previous Sec. 4.3.1, we analyze all the mergers up to

$z = 1$, and we associate to each merger a coalescence time, t_c, uniformly sampled between the year 2035 and the year 2045, which is roughly the period when the XG ground-based observatories as ET are expected to be operative. For each BNS merger, we inject a GW signal described by `IMRPhenomD_NRTidalv2` [Khan et al., 2016; Dietrich et al., 2019], a state-of-the-art waveform approximant including tidal effects.

NETWORKS	INJECTION SETS			
	α	# events	EOS	Mass distr.
ET-Δ-10 km	0.5	71338	APR4	Gaussian
ET-Δ-10 km + LVKI				Uniform
ET-Δ-10 km + 1CE			BLh	Gaussian
ET-Δ-10 km + 2CE				Uniform
ET-2L-15 km	1.0	363560	APR4	Gaussian
ET-2L-15 km + LVKI				Uniform
ET-2L-15 km + 1CE			BLh	Gaussian
ET-2L-15 km + 2CE				Uniform

Table 4.5: List of detector networks and injections data sets used in the analysis. Table from [Loffredo et al., 2025] (Table 2, ***authored by UD***)

We consider different detector networks, including the current generation and the XG one. In Tab. 4.5, we describe the networks and a summary of the properties of the populations we have used. From Tab. 4.5, we have two common envelope efficiency values, two different EoS and two different mass models. Together with the eight different detector networks, this adds up to 64 simulations. We can distinguish two groups of detector networks:

- ET-Δ with 10 km arms, located in Sardinia: alone and in a network with, respectively, 1CE, and the upgraded version (O5) [Abbott et al., 2020b] of the LVKI network. When using the network of 2CEs, we locate one at the LIGO Hanford site and the second in Australia (see Tab. C.1).

- ET-2L, misaligned at 45°, with 15 km arms, one detector in Sardinia and the second in the Netherlands, as in [Branchesi et al., 2023]: as a single observatory and in the same network configurations as the ET-Δ detector

For further details about the detector networks simulation, we refer to Tab. C.1, where we have provided the precise location (latitude and longitude), the sensitivity range, and curves. Here, in Fig. 4.6, we show the plot of the ASDs for the different detectors used in the analysis. For both the ET configurations, we used as the starting frequency 2 Hz, while using 8 Hz, for all the other detectors. This does not mean,

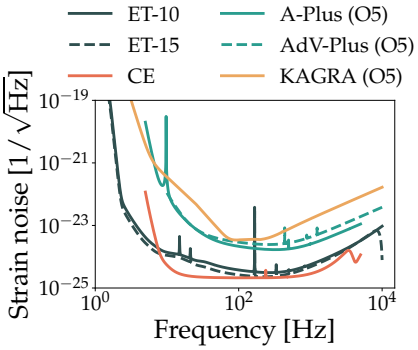

Figure 4.6: Sensitivity curves used in the analysis. The ET strain noise is the HFLF-cryo one (see Sec. 4.1.1). ET-10 and ET-15 refer, respectively, to a 10 km and a 15 km detectors. The used sensitivity curves are available here. Figure adapted from [Loffredo et al., 2025] (Figure B.1, ***authored by UD***)

however, that these detectors will be sensitive down to such low frequencies, as it is also evident from Fig. 4.6, where at low frequencies, even the XG observatories show a rapid decline.

The parameter estimation of the injected GW signals by the various detector networks is obtained through the Fisher matrix software `GWFish` [Dupletsa et al., 2023]. We refer to Chapter 3 for a detailed presentation and discussion of the Fisher matrix code.

A detection SNR threshold of 8 is applied for our analysis. All the parameters [$\mathcal{M}$, q, d_L, ι, `RA`, `DEC`, Ψ, ϕ, t_c, Λ_1, Λ_2] are considered for the Fisher matrix derivation. The uncertainties on parameters coming from the covariance matrix are given at 1σ. The sky-localisation uncertainty, Ω_{90}, is given as 90% credible region.

We implement a duty cycle of 85% independently for each of the L-shaped detectors, and in each of the three nested detectors composing the triangle, so that we take into consideration a more realistic scenario, where detectors are not operative all the time as occurs with current GW detectors.

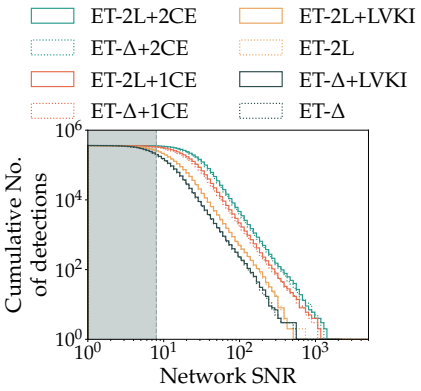

Figure 4.7: SNR distribution for the detector networks analyzed in our study as in Tab. 4.5. The reported results consider the fiducial population, uniform mass distribution, and `BLh` EoS. The colored region excludes the events with $SNR < 8$. Adapted from [Loffredo et al., 2025] (Figure 13, ***authored by UD***)

4.3.3 *The role of EoS and mass model on GW detection*

The different choices we make at the BNS population level, from microphysics, e.g. the EoS, to mass distribution, have an imprint on the GW signal that we might observe. In turn, this depends on the network we use for the detection.

In Fig. 4.7, we show the SNR results for all the detector networks considered in our analysis, fixing the results to the fiducial population with the `BLh` EoS and uniform mass distribution. We show in the same color the networks containing one of the two ET configurations, ET-Δ or 2L, but distinguishing them by the style of line, *solid* for the 2L, and *dotted* for the ET-Δ. The best network performance for both ET configurations is when also 2CEs are operative, and, then, in descending order, 1CE, LVKI, and the standalone ET. Between the two ET geometries, the 2L gives a better outcome, confirming the findings of [Branchesi et al., 2023]. If we instead fix the network, as shown for ET-Δ in Fig 4.8, and compare the two mass distributions, we find that the uniform distribution yields higher SNR values. This occurs because sampling masses from a uniform distribution generally results in a greater number of more massive systems compared to sampling from a Gaussian distribution centered at $1.33M_\odot$, as is clear from Fig. 4.4.

In Fig. 4.8, we fixed the EoS to `BLh`, but same holds for `APR4`. We have even higher SNRs with the uniform `APR4` case, since `APR4` allows for even larger masses. At the SNR level, the comparison boils down to privilege the model that accommodates more massive binaries. This happens for the `APR4` EoS, which predicts $m_{\rm src,max} = 2.2M_\odot$, and uni-

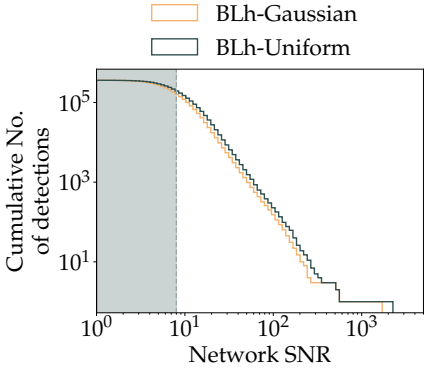

Figure 4.8: SNR distribution ET-Δ comparing uniform and Gaussian mass distributions. The reported results consider the fiducial population and the `BLh` EoS. The colored region excludes the events with $SNR < 8$

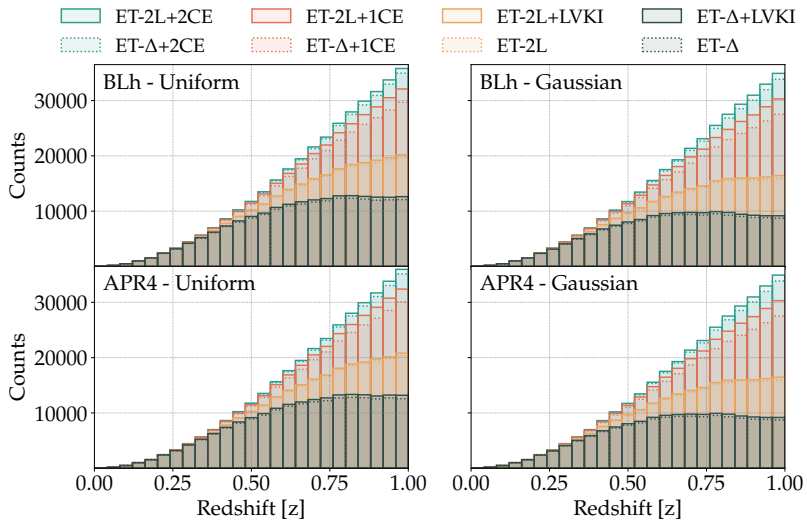

(a) $\alpha = 1.0$

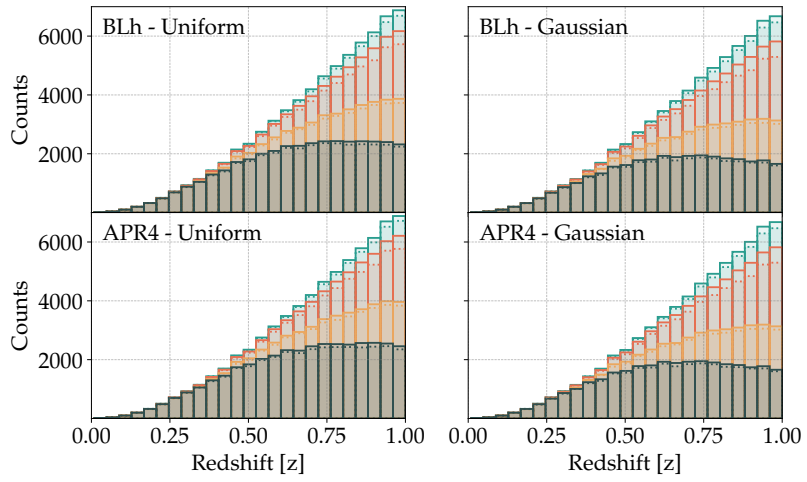

(b) $\alpha = 0.5$

Figure 4.9: Ten-year detection distribution as a function of redshift for the 8 different networks using the fiducial population ($\alpha = 1$) in the *top* panel and the pessimistic one in the *bottom* ($\alpha = 0.5$), showing all the 4 combinations of EoS and mass distributions. For a given α value, all the axes have the same scale. Figure adapted from [Loffredo et al., 2025] (Figures. 10 and D.1, ***authored by UD***)

form mass distribution.

Fig. 4.9 shows the number of detections over ten years up to redshift $z = 1$ for all the 64 cases analyzed in [Loffredo et al., 2025]. The *top* panel reports the results for the fiducial population. Each subplot in the panel shows the results for each one of the 4 mass distribution-EoS combinations. Different colors represent different networks of ET, with the *solid* linestyle for ET-2L networks, and the alike color but *dotted* linestyle for the corresponding ET-Δ network. Tab. 4.6 report the corresponding absolute numbers for the fiducial population, and adding the two networks composed of LVKI only and 3 LIGO-like[8] detectors with A# sensitivity [Fritschel et al., 2022].

Similar to the findings in [Branchesi et al., 2023], the ET-2L net-

[8] We put the 3 LIGOs at the Hanford, Livingston and LIGO-India sites.

NETWORKS	APR4		BLh	
	Uniform	Gaussian	Uniform	Gaussian
ET-Δ	191949	153726	186543	153632
ET-Δ + LVKI	198168	159203	192384	159087
ET-Δ + 1CE	316884	300098	314644	300043
ET-Δ + 2CE	348424	341191	347575	341164
ET-2L	251997	219780	247494	219676
ET-2L + LVKI	255215	223361	250869	223266
ET-2L + 1CE	332262	319490	330526	319446
ET-2L + 2CE	353506	348098	352836	348076
LVKI	1529	884	1403	883
A#	8349	4936	7645	4930

Table 4.6: Number of BNS mergers detected in ten years by several networks of current and next generation detectors for the fiducial populations (α =1.0). We added two more detector networks with respect to 4.5. Table from [Loffredo et al., 2025] (Table D.1, ***authored by UD***)

work outperforms the ET-triangle, which supports our observations regarding the SNR. In various configurations, the total number of detections up to a redshift $z = 1$ increases by approximately 30%, when moving from ET-Δ to ET-2L. The detection capabilities of both the 2L and triangle configurations of ET are significantly enhanced when they operate within a network of detectors. Specifically, the number of detections increases by around 3% when ET operates alongside existing detectors, e.g. with LVKI at O5 sensitivities. When ET-Δ is part of a network with XG detectors, including either one CE (or two CEs), the number of detections can rise by approximately 70% (90%). For ET-2L configuration, the increase in detections is about 30% (40%).

Fig. 4.10 compares detection numbers for ET-Δ up to $z = 1$ across different choices for the NS mass distribution and the EoS. For the uniform mass distribution, the number of detections increases by about $20 - 25\%$ compared to the Gaussian mass distribution, regardless of the EoS. This is expected due to the larger masses achieved by binary systems with a uniform NS mass distribution.

When comparing the two EoSs, the differences in detection numbers are negligible. However, we do observe that `APR4` yields a slightly higher detection rate (by 3%) than `BLh` for the uniform mass distribution. This detail is emphasized in the zoomed-in region of Fig. 4.10. The increased detection rate is primarily driven by the larger maximum NS mass supported by `APR4`, which results in louder GW signals.

These findings align with the analysis conducted by [Iacovelli et al., 2023], which noted an increased detection rate for EoSs with a higher maximum mass, particularly under a uniform NS mass distribution.

The sky localization capabilities of ET, whether operating independently or within a network of detectors, are summarized in Tab. 4.7 and Tab. 4.8 for ET-Δ and ET-2L, respectively. These tables present

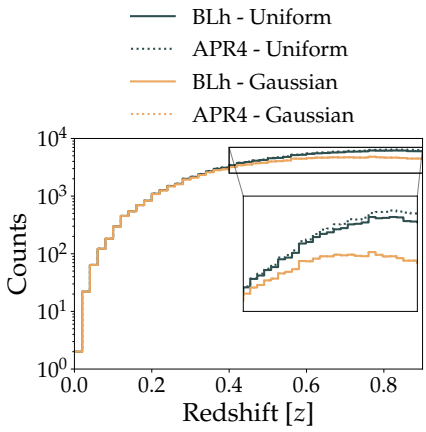

Figure 4.10: Ten-year detection distribution as a function of redshift for the reference ET-Δ using the fiducial population ($\alpha = 1$) and comparing different NS mass distributions and EoS models. Figure adapted from [Loffredo et al., 2025] (Figure 11, ***authored by UD***)

the number of detections made by various detector networks over ten years, focusing on sky-localization accuracy, Ω_{90}, that is smaller than specific thresholds. This is evaluated for both the pessimistic population ($\alpha = 0.5$) and the fiducial one ($\alpha = 1$), for the analyzed NS EoSs (APR4 and BLh) and NS mass distributions (uniform and Gaussian).

The results in the tables, Tab. 4.7 and Tab. 4.8, indicate significant uncertainties in the absolute detection numbers stemming from variations in the common envelope efficiency. Compared to the pessimistic one, the fiducial population results in five times more detections with sky localization less than $100\,\mathrm{deg}^2$. As previously noted, this aligns with the limited observational constraints on the local BNS merger rate.

By comparing Tab. 4.7 and Tab. 4.8, we observe that the ET-2L, when operating as a single observatory, achieves better localization than ET-Δ. Specifically, it detects 2.4 times more events within a sky localization area of $100\,\mathrm{deg}^2$. This trend also holds when ET operates together with current detectors, where ET-2L allows for $40-50\%$ more detections within 100 deg^2 compared to ET-Δ. The enhanced performance of ET-2L in source localization is also evident when ET operates in a network with one CE; in this case, ET-2L localizes better than $10\,\mathrm{deg}^2$ about $30-40\%$ more events compared to ET-Δ. When ET is operating with two CEs, the difference between 2L and triangle is negligible, except for the events localized better than $1\,\mathrm{deg}^2$. These results are fully consistent with the findings of [Branchesi et al., 2023].

The number of well-localized events significantly increases when ET operates within a network of detectors, as demonstrated in Tab. 4.7 and Tab. 4.8. For the fiducial population, the number of events localized better than 100 deg^2 increases from a few hundred per year to several thousand per year when ET operates with current detectors LVKI rather than alone. ET will significantly benefit from the presence of current detectors (mainly from the distant ones, while Virgo gives a negligible contribution due to its vicinity), and the number of events detected better than 10 deg^2 will increase from a few tens to a few hundreds per year.

Fig. 4.11 illustrates the advantages of detector networks in achieving larger redshifts for well-localized events. With the addition of a network of the XG detectors, the number of events localized better than 10 deg^2 amounts to 10^3 (10^4) per year for $ET + 1CE$ ($ET + 2CE$) up to $z \sim 0.9 - 1.0$.

The higher number of GW detections for the uniform mass distribution compared to the Gaussian one results in a systematically larger number of well-localized events in the case of uniform mass distribution. Moreover, for a given luminosity distance, the accuracy of sky localization tends to be higher in the uniform distribution scenario due

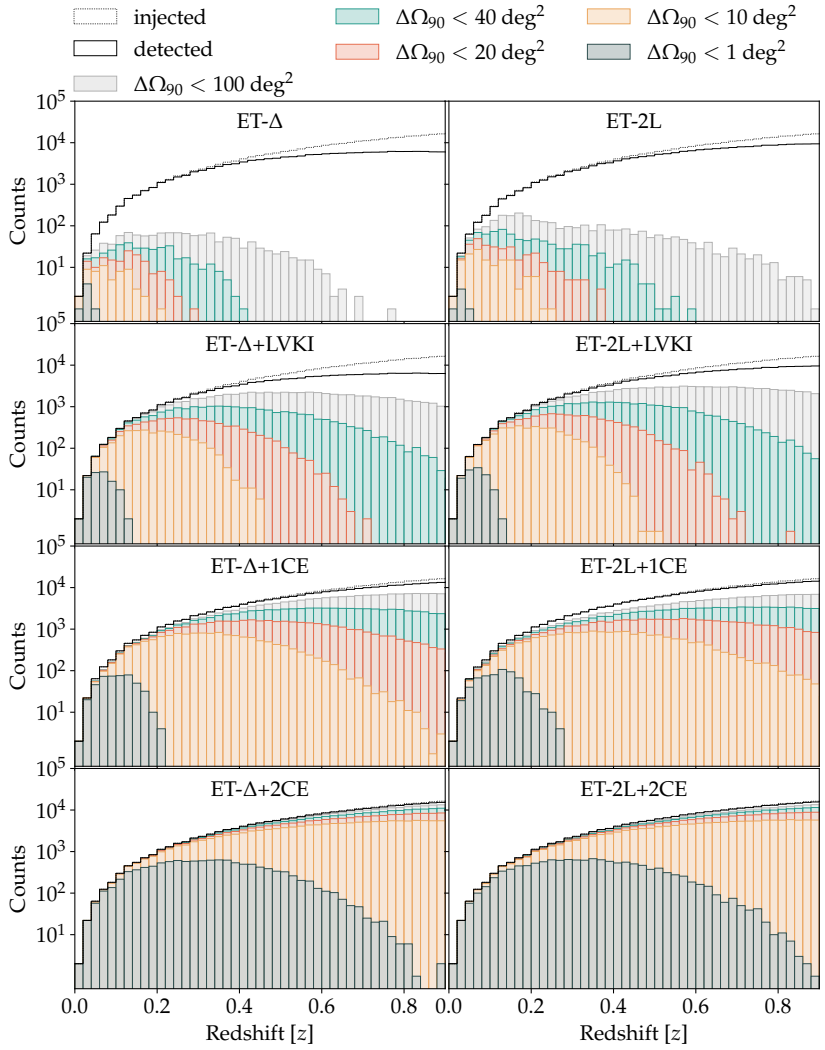

Figure 4.11: Number of injected events and events localized better than $100\,\mathrm{deg}^2$, $40\,\mathrm{deg}^2$, $20\,\mathrm{deg}^2$, $10\,\mathrm{deg}^2$, and $1\,\mathrm{deg}^2$ by the different detector networks considered in this work for the fiducial population obtained assuming the `BLh` EoS and uniform NS mass distribution. The left plots show ET-Δ, and the right plots ET-2L. In App. C, we show the same plots for `BLh` Gaussian NS mass distribution, and `APR4` uniform and Gaussian NS mass distribution. Figure adapted from [Loffredo et al., 2025] (Figure 12, ***authored by UD***)

to the presence of more massive systems, which generate higher SNRs.

Finally, also the NS EoS affects the number of GW detections at a given sky localization. A comparison between the number of detected events for `APR4` and `BLh` at $\Omega_{90} < 100,\ 40,\ 20,\ 10\,\mathrm{deg}^2$ shows that typically the number of detections increases for `APR4` up to 4%, in the case of Gaussian mass distribution, and 10%, in the case of uniform mass distribution. This is because `APR4` is more compact, therefore it has smaller tidal deformability compared to `BLh4`, so the inspiral of the GW signal lasts more time in the detector. Moreover, as mentioned above, in the case of uniform mass distribution, `APR4` supports a larger maximum NS mass with respect to `BLh` providing systems with larger mass, and thus larger SNR which can improve the sky localization.

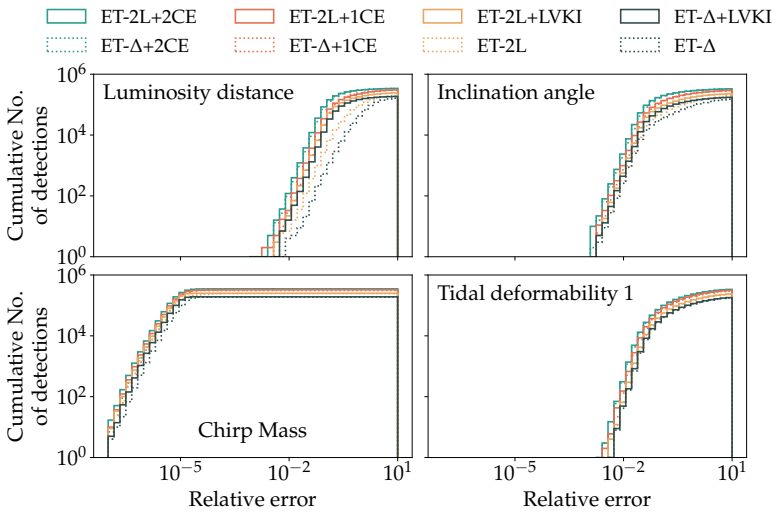

(a) BLh Uniform, $\alpha = 1.0$

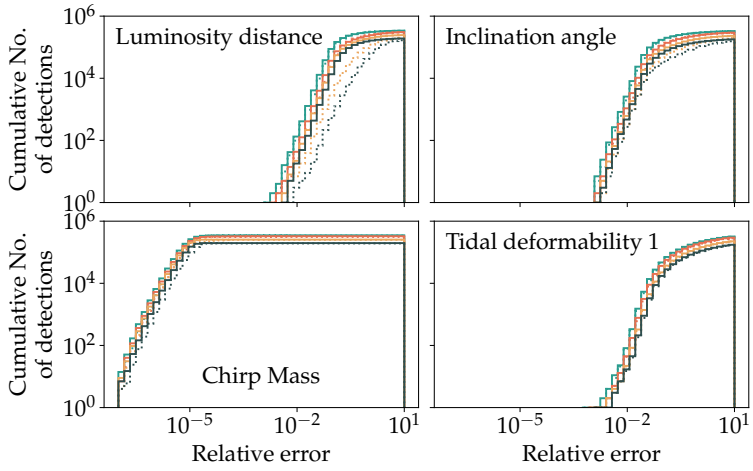

(b) APR4 Uniform, $\alpha = 1.0$

Figure 4.12: PE for a subset of parameters, namely luminosity distance, inclination angle, primary component mass, and tidal deformability of the primary component, for the uniform mass distribution of the fiducial population with `BLh` EoS in the *top* panel, and `APR4` EoS in the *bottom* one. We show the relative errors on the parameters on the x-axis and the cumulative number of detections on the y-axis. Different colors indicate different networks. The same color and lifestyle schemes as in Fig. 4.9 apply. Figure from [Loffredo et al., 2025] (Figures 13 and D6, ***authored by UD***)

Fig. 4.12 presents PE for a subset of parameters, namely luminosity distance, inclination angle, chirp mass, and tidal deformability of the primary component, based on the uniform mass distribution of the fiducial population. The *top* panel presents results using the `BLh` EoS, while the *bottom* panel corresponds to the `APR4` EoS. The x-axis represents the relative errors on these parameters, whereas the y-axis denotes the cumulative number of detections. Notably, PE accuracy is significantly improved with ET-2L compared to the triangular configuration when each functions as an independent detector. Although the improvement is less pronounced, it remains evident when ET is integrated into a network of detectors. Moreover, it is worth emphasizing that substantial enhancement in parameter estimation is already

achieved when ET operates in synergy with current detectors. This is particularly important for the luminosity distance, a key parameter in cosmological studies. This finding is pertinent to the redshift range $[0, 1]$ considered in this study, as extending the analysis to higher redshifts would render the presence of current detectors ineffective in improving PE. The parameter estimation accuracy further increases with the inclusion of next-generation detectors, as reflected in the distribution of well-localized events across different redshift values.

In App. C, we show a plot analogous to 4.12, but for the Gaussian mass distribution. The network of GW detectors plays a major role in PE precision, whereas mass model and EoS are subdominant.

4.3.4 *Summary of prospects for KN MM astrophysics*

We investigate the potential of MM astronomy with XG detectors by assessing the detectability of KNe and GRB afterglows associated with BNS mergers. We explore scenarios where ET operates alone or within a network of current and XG GW detectors and in synergy with the Vera Rubin Observatory. Besides the impact of the choice of the GW detector network, we explore different sources of uncertainty, starting from the BNS merger rate quantified by the common envelope efficiency parameter α, the NS mass model (Gaussian or uniform in our analysis), and, at the microphysics level, the NS EoS, exemplified by ours more compact `APR4` or the less compact one, `BLh`.

We aim to quantify the impact of these sources of uncertainties as they affect the KNe MM predictions and, consequently, observational strategies. Our key findings are summarized as follows:

- ET (as single observatory in either of its configurations, ET-Δ or ET-2L) operating with the Rubin Observatory will be able to detect large numbers of KNe, up to $10 - 100$ per year. The number of MM detections significantly increases when ET is considered in a network with current or XG observatories.

- The key parameter is the sky localization capability. It gives us a criterion for events to follow up with the Vera Rubin Observatory. The larger the number of detectors in the network, the better the sky localization. The network of ET and LVKI increases the number of optical counterparts detected by Rubin by an order of magnitude with respect to ET alone. However, even if the ET+2CE network gives better sky localization at higher redshifts, on the EM detection part, we are limited by Rubin's sensitivity, which drops significantly for redshifts above ~ 0.3. This means that an upgrade of the current detectors operating in a network with ET and working in synergy with the Rubin Observatory delivers results similar to ET observing

in a network with XG observatories.

- The uncertainty on the number of KN detections is largely dominated by the poor knowledge of the local BNS merger rate, while factors such as the mass model and EoS influence the results to a lesser extent. However, we do observe some detectable differences between the models we analyzed. In the Gaussian mass model case, we detect more KNe with `BLh` EoS. In the uniform mass model, instead, the situation is reversed. We can provide a preliminary explanation for these observations, even though the interactions are complex. In the first case, `BLh` predicts a higher ejected mass that, in turn, produces brighter KNe. In the second case, the `APR4` EoS predicts larger masses, resulting in a greater number of well-localized events.

- The addition of the afterglow emission typical of short GRBs increases the number of MM detections. The ET+2CE network shows the best performance. It localizes well and at higher redshifts when the afterglow emission, being intrinsically brighter than the KN one, is still detectable.

Schematic outline of the observational strategy with Vera Rubin

As mentioned above, the sky localization capability plays a crucial role in the follow-up observations with the Vera Rubin Observatory. In [Loffredo et al., 2025] we plan to use target-of-opportunity (ToO) observations as the most effective follow-up strategy. We, therefore, select among the detected GW events those that are well-localized and accessible within Rubin's sky coverage. The localization threshold depends on the specific GW detector network and is set to ensure that the number of follow-up targets remains manageable, and in any case not exceeding 100 $\deg^2$ for the sky localization at 90% C.L.
In brief, the observational strategy uses a mosaic approach, tiling the localization region according to Rubin's FoV of 9.6,$\deg^2$. Each GW source is randomly assigned to one of the tiles, assuming a uniform distribution within the localization area. Observations are carried out in two filters: g (probing the blue part of the spectrum) and i (red), over two epochs within 2–3 nights after the merger, starting no earlier than 1.5,hours post-merger due to limitations in early-time KN modeling. Each pointing uses a 600,s exposure, with additional time budgeted for slewing and filter changes.
Two detection criteria are used: a one-epoch (1ep) criterion requiring detections at least once in both filters in a single epoch, and a more stringent two-epoch (2ep) criterion which requires the source to be detected in the two filters in the first epoch and at least in the i filter in the second epoch. The latter enables tracking color evolution to reduce contaminants.
The outlined strategy balances depth and efficiency, aiming to maximize the number of GW events followed up with Rubin's limited ToO time in the era of XG GW detectors.

In summary, the theoretical framework and simulations on the ET capabilities to detect and estimate the parameters of BNS mergers developed in this thesis made it possible to evaluate the optimal design of ET operating together with EM observatories and to evaluate in depth the prospects of KN detection for ET operating with the Vera Rubin Observatory. Our work makes a significant step forward in quantifying theoretical uncertainties (merger rate, NS mass distribution, EoS) affecting predictions for GW and MM detections and source characterization.

ET, especially in networks with XG GW observatories, will generate an extremely large number of alerts, making it prohibitive to follow up every one of them. In our work, we explore selection based on the sky localization. However, the prioritization of alerts to be followed can be optimized and tuned to specific scientific cases by incorporating additional information on source parameters. To explore science-dependent observational strategies and prospects, we made available to the community the catalogues containing all our injected BNS populations and the source parameters estimates for the 64 performed simulations. All the catalogues are publicly available on Zenodo.

			APR4		BLh	
		Ω_{90} [deg^2]	Uniform	Gaussian	Uniform	Gaussian
$\alpha = 0.5$	ET-Δ	< 100	266	233	272	233
		< 40	79	62	75	62
		< 20	29	23	25	23
		< 10	8	6	8	6
	ET-Δ + LVKI	< 100	14946	10031	13873	9797
		< 40	5105	3159	4659	3074
		< 20	1808	1149	1673	1131
		< 10	671	403	592	391
		< 1	15	9	19	9
	ET-Δ + 1CE	< 100	41229	35355	40086	34950
		< 40	21881	15848	20685	15490
		< 20	9505	5874	8741	5747
		< 10	3370	2012	3086	1985
		< 1	99	58	85	58
	ET-Δ + 2CE	< 100	62252	59712	61865	59525
		< 40	54122	50462	53407	50088
		< 20	44976	40266	43896	39742
		< 10	33336	27980	32070	27341
		< 1	2620	1587	2413	1548
$\alpha = 1.0$	ET-Δ	< 100	1295	1085	1261	1084
		< 40	400	315	387	315
		< 20	147	135	154	135
		< 10	59	49	58	49
	ET-Δ + LVKI	< 100	74095	49000	69098	47662
		< 40	25246	15499	23009	15075
		< 20	8904	5615	8205	5506
		< 10	3221	2027	3007	1989
		< 1	105	71	103	71
	ET-Δ + 1CE	< 100	207029	176325	201449	174112
		< 40	109116	77348	103009	75578
		< 20	46537	28731	42915	28127
		< 10	16231	9759	14893	9639
		< 1	514	309	466	307
	ET-Δ + 2CE	< 100	316613	303242	314298	302312
		< 40	275354	256334	271701	254435
		< 20	228395	204945	223353	202064
		< 10	169922	142069	163892	138734
		< 1	12829	7849	11713	7659

Table 4.7: Number of BNS mergers detected by ET-Δ with 10 km arms in ten years with a sky localization better than 100 deg^2, 40 deg^2, 20 deg^2, 10 deg^2, and 1 deg^2. Table from [Loffredo et al., 2025] (Table 4, ***authored by UD***)

			APR4		BLh	
		Ω_{90} [deg^2]	Uniform	Gaussian	Uniform	Gaussian
$\alpha = 0.5$	ET-2L	< 100	636	543	623	539
		< 40	173	144	164	144
		< 20	64	50	63	50
		< 10	26	22	26	22
	ET-2L + LVKI	< 100	21049	15144	19709	14604
		< 40	6581	4112	6071	3993
		< 20	2300	1469	2151	1429
		< 10	819	524	774	516
		< 1	24	15	26	15
	ET-2L + 1CE	< 100	36935	33298	36258	32974
		< 40	22655	17904	21781	17574
		< 20	11699	7795	10952	7593
		< 10	4437	2731	4062	2678
		< 1	128	74	112	73
	ET-2L + 2CE	< 100	61800	60175	61527	60058
		< 40	55474	52339	54783	51981
		< 20	46874	42275	45786	41708
		< 10	35058	29499	33707	28931
		< 1	2911	1810	2681	1753
$\alpha = 1.0$	ET-2L	< 100	3065	2595	2977	2584
		< 40	895	760	863	759
		< 20	336	285	331	284
		< 10	140	123	138	123
	ET-2L + LVKI	< 100	105210	75008	98629	72230
		< 40	32600	20315	29938	19712
		< 20	11400	7266	10577	7092
		< 10	4103	2628	3802	2591
		< 1	134	87	120	85
	ET-2L + 1CE	< 100	187619	168206	184000	166575
		< 40	114328	89433	109393	87665
		< 20	57718	37996	53790	37095
		< 10	21782	13429	20114	13166
		< 1	682	435	636	435
	ET-2L + 2CE	< 100	312610	304213	311070	303455
		< 40	280242	264039	277022	262179
		< 20	235691	211974	230760	209108
		< 10	175625	147446	169663	144339
		< 1	13958	8619	12886	8400

Table 4.8: Number of BNS mergers detected by the ET-2L with 15 km arms in ten years with a sky localization better than 100 deg^2, 40 deg^2, 20 deg^2, 10 deg^2, and 1 deg^2 respectively. Table from [Lofredo et al., 2025] (Table 5, ***authored by UD***)

5. Back to Cosmology, with ET

> *To be sure means that when the right solution is reached, everything falls into place. You perceive that in no other way could things have happened.*
>
> **— Agatha Christie**
> "The Clocks"

The next-generation (XG) gravitational wave (GW) detectors present exceptional opportunities in the field of cosmology. This chapter explores the prospects for cosmology with the Einstein Telescope (ET).
In the first part, we examine potential scenarios involving the ET operating alongside the Fermi and Swift telescopes in the observation of short Gamma Ray Bursts (GRBs), jointly with Binary Neutron Star (BNS) mergers. This work is published in JCAP [Cozzumbo et al., 2025]. I contributed to gravitational data analysis and overall discussions.
The second part of this chapter focuses on ongoing research regarding the joint observations of ET and SKA Observatory (SKAO). The project aims to constrain cosmological parameters by inferring the redshift of Binary Black Hole (BBH) mergers, observed with ET, thanks to the spatial distribution of hydrogen overdensities, measured with SKAO, under the assumption that BBHs trace the hydrogen density field. I am leading the ongoing forecast effort [Dupletsa et al., nd, in preparation] to investigate the synergy between ET and future intensity mapping (IM) surveys with SKAO. The list of collaborators is included in the List of Publications, provided at the beginning of this thesis.

5.1 Probing the Universe's expansion with the XG GW observatories

The next-generation (XG) gravitational wave (GW) interferometers will be able to probe the Universe up to very high redshifts. Focusing on the Einstein Telescope (ET) observatory, we will be able to observe mergers from compact binary coalescences (CBCs) up to $z \sim 100$ [Ng et al., 2022, 2023; Branchesi et al., 2023]. The expected unprecedented sensitivity makes an instrument like ET ideal to probe the expansion history of the Universe and trace $H(z)$ as in Eq. (1.20) well beyond the local Universe explored with current detectors. Moreover, this can give us insights into the Hubble tension problem (see Sec. 1.1.4).

For a general introduction to cosmology with GWs, refer to Sec. 2.1 of Chapter 2. In the following chapter, we consider two scenarios, focusing on bright sirens in the first part and dark sirens in the second.

Contents

Regarding the observation of bright sirens with ET, we present the work in [Cozzumbo et al., 2025], where we analyze the hypothetic scenario of what constraints we could have put on cosmological parameters if ET were operating together with Fermi-GBM [Meegan et al., 2009] and Swift-BAT/XRT [Gehrels et al., 2004] instruments, for the last 20 years, specifically from 2005 to 2023, and observed the corresponding GW signals from the merging Binary Neutron Star (BNS) events. Since ET is planned to be operative for ~ 50 years, the amount of GRBs observed over a 20-year time span looks like a plausible scenario. In the work, we explore different cosmological models and GW detector networks, and a model-independent approach based on Gaussian Process (GP) methods. This is addressed in Sec. 5.2.

The second part explores the dark siren sector. Specifically, we investigate the synergy between GWs and the large scale structure (LSS) of the Universe, exploring the potential of a detector like ET for the Binary Black Hole (BBH) detection on the gravitational side and SKA Observatory (SKAO) [Weltman, 2020] on the electromagnetic (EM) side. SKA-Mid[1], in fact, is expected to carry out intensity mapping (IM) surveys of the LSS distribution up to redshift $z \sim 3$ [Bacon et al., 2020], through the measurement of the 21 cm line emission from neutral hydrogen (HI). This is thoroughly discussed in Sec. 5.3.

[1] All the useful information is available on the website.

5.2 *Cosmology with joint BNS and GRB observations*

The only so far bright siren event `GW170817` [Abbott et al., 2017c,a] has already shown us the great opportunity represented by the ability to detect EM counterparts, despite the large uncertainties on the Hubble parameter estimates. Moreover, `GW170817` also provides us with the first direct evidence of the link between BNS mergers and production of short Gamma Ray Bursts (GRBs) [Ascenzi et al., 2021][2]. This is why we decided to explore how these constraints would shrink if the catalog of GRBs associated with a BNS merger had a gravitational counterpart. In other words, what if we had observed the corresponding GW signals with a combination of different detectors, including ET. This allows us to consider all the detected GRBs, roughly up to $z \sim 3$, and simulate the corresponding GW data.

[2] The link between BNS mergers and short GRBs production is not straightforward. We briefly discuss the recent developments in the dedicated box.

The scope of [Cozzumbo et al., 2025] is twofold. First, we compare two different cosmological models, both in good agreement with the observations. These are the standard Λ Cold Dark Matter (ΛCDM) and the Phenomenological Emergent Dark Energy (PEDE) models [Li and Shafieloo, 2019, 2020]. The latter is based on the same model parameters as ΛCDM but assumes an emergent component of dark

energy (DE) in the late Universe. In practice, in the ΛCDM cosmology, the DE is assumed to be constant, whereas in the PEDE model, it follows a redshift-dependent Equation of State (EoS), according to which the DE component phenomenologically emerges at late times, after $z < 2$[3]. Recent results from Dark Energy Spectroscopic Instrument (DESI) [Adame et al., 2024; Calderon et al., 2024; Lodha et al., 2024] have revived the interest in this model. Second, since we must recognize that alternative models to ΛCDM cannot deviate significantly without compromising the fit to the Cosmic Microwave Background (CMB) data, we opt for a model-independent, non-parametric, and data-driven approach, based on machine learning (ML), and specifically on GP methods. This is done to reconstruct the DE phenomenology. In what follows, we briefly discuss the mock data setup in Sec. 5.2.1, and, in Sec. 5.2.2, some results from [Cozzumbo et al., 2025].

[3] In the PEDE model, the redshift evolution of the DE EoS is given by [Cozzumbo et al., 2025]:

$$w(z) = -\frac{1}{3\ln(10)}\left(1+\tanh\left[\log_{10}(1+z)\right]\right) - 1$$

BNSs and GRBs: what's the link?

The historical classification of GRB progenitors is based on their duration, defined by a parameter called T_{90}. This parameter represents the time span during which 90% of the prompt emission is detected. Specifically, we observe a bimodal distribution: short GRBs ($T_{90} < 2\,\mathrm{s}$) and long GRBs ($T_{90} > 2\,\mathrm{s}$) [Kouveliotou et al., 1993]. The two classes are associated with two different progenitors. Short GRBs are linked to BNS mergers [Eichler et al., 1989], while the long ones are associated with the collapse of massive stars [Woosley, 1993; MacFadyen and Woosley, 1999], core-collapse supernovae (SNe). The progenitor association is supported by the type of galaxies GRBs are observed in: the long ones are mostly found in young galaxies and accompanied by supernova transients, while the short ones are observed in older galaxies, so compact objects had enough time to form, and are associated to kilonova (KN) emission.
Nevertheless, the distinction based on duration is not quite accurate since we have evidence of long GRBs, which are likely originated from BNS mergers [Rastinejad et al., 2022; Troja et al., 2022; Levan et al., 2024]. The current approach is to categorize GRBs based on their progenitor, classified in *collapsars* and *non-collapsars*. *Non-collapsars* are the ones associated with BNS or Neutron Star - Black hole (NSBH) mergers, regardless of their duration. One of the conditions to have a successful GRB launch [Murguia-Berthier et al., 2014] is related to the creation of an accretion disk around the central engine, which can happen if at least one of the components in the binary is a neutron star (NS), namely BNS or NSBH mergers.

5.2.1 *Mock data reconstruction*

The mock data is reconstructed starting from the catalogue of the observed GRBs that are most likely associated with a BNS merger (see box above) and for which we have a precise, with less than 10% of relative uncertainty, redshift measurement of the corresponding host galaxy. Moreover, based on the probability that the associated host

galaxy is the correct one, we have three different catalogues, the *fiducial* (with 38 events), the *extended* (with 54 events), and the *very extended* (with 61 events), with a decreasing probability of correct host galaxy identification.

We then associate to each of the observed GRBs a GW event. To this scope, we sample the source-frame BNS masses uniformly in the interval $[1.1, 2.1]M_\odot$. The sky position, `RA` and `DEC`, as well as the time of arrival t_c are fixed by the GRB data. Phase and polarization angles are sampled from their prior range as from Tab. 3.7. The inclination angle ι is constrained to be uniform in cosine in the two possible intervals, i.e. $[0°, 5°]$ and $[185°, 190°]$, since we can observe the GRB emission only if the jet is pointing towards us. The six spin parameters and tidal deformability are not considered and are kept fixed at zero. Last, the luminosity distance is set from the measured redshift of the GRBs, once we establish a cosmology (see Eq. (1.12)). The gravitational analysis is done with the Fisher matrix code `GWFish` with the addition of priors [Dupletsa et al., 2023, 2025], and considering a duty cycle of 85% (see Sec. 3.3.1). We do not use a full parameter estimation (PE) software like `Bilby` for both prohibitive computational costs and lack of Earth rotation modeling (impactful in the case of long-lasting BNS mergers), as discussed at length in Chapter 3.

The parameter we are most interested in is the posterior distribution of the luminosity distance. The samples obtained from `GWFish+Priors` analysis are interpolated with a kernel density estimator (KDE), after the inclusion of uncertainties coming from peculiar velocity corrections [Mukherjee et al., 2021; Nimonkar and Mukherjee, 2023] for the nearby events for which this correction matters.

Starting from the luminosity distance posteriors, we perform a Markov Chain Monte Carlo (MCMC) analysis with a likelihood that generalizes the χ^2 function [Cozzumbo et al., 2025], to reconstruct the distribution on cosmological parameters.

Network	*Fiducial*		*Extended*		*Very Extended*	
	$z_{\max}$	# events	$z_{\max}$	# events	$z_{\max}$	# events
LVK	0.248	8	0.248	10	0.248	10
LVKI	0.46	16	0.46	20	0.46	21
ET-Δ, HF	1.37	30	1.465	40	1.465	43
ET-Δ	1.754	36	2.58	48	2.58	55
ET-Δ + CE	2.609	38	2.609	53	2.609	60
ET-2L, HF	1.754	36	2.58	48	2.58	54
ET-2L	1.754	37	2.58	50	2.58	57
ET-2L + CE	2.609	38	2.609	53	2.609	60

Table 5.1: List of detections for the three mock BNS catalogues, *fiducial*, *extended*, and *very extended*, observed with different GW networks. We indicate the number of detected events ($SNR \geq 8$) and the maximum redshift achieved. Table adapted from [Cozzumbo et al., 2025] (Table 1).

In Tab. 5.1, we report the number of joint GRB/GW detections for the three catalogues of events, *fiducial*, *extended*, and *very extended*, and

for the considered list of GW detector networks. For each case, we highlight the largest achieved redshift. We consider an SNR threshold of $SNR \geq 8$ for detection. We refer to the broad discussion in Chapter 4 for the network configuration and sensitivity curves. Briefly, when considering the LVK networks, we adopt the O5 sensitivities [Abbott et al., 2020b]. In the LVKI network, the three LIGOs are upgraded to A# sensitivity [Fritschel et al., 2022]. If not else specified, the reference sensitivity for ET is the HFLF-cryo one, both for ET-Δ and ET-2L (the 45° misaligned configuration). Otherwise, it is the HF one (see Sec. 4.1.1). The location of the ET detectors is the same as in [Branchesi et al., 2023] described in Chapter 4. The CE interferometer, instead, is placed in the LIGO Hanford site. The reported detections are the same with both the cosmological models, ΛCDM and PEDE.

From the results of Tab. 5.1, when a network of two XG detectors is used, almost all the events are accessible and help us to put tighter constraints on the cosmological parameters. This is addressed in the next section.

5.2.2 H_0 and dark energy constraints

The findings in [Cozzumbo et al., 2025] highlight the importance of joint GRB/GW observations and, in particular, of measuring the distant GRB sources along with their gravitational counterpart.

Network	*Fiducial*		*Extended*		*Very Extended*	
	$\Delta H_0/H_0$	$\Delta\Omega_m/\Omega_m$	$\Delta H_0/H_0$	$\Delta\Omega_m/\Omega_m$	$\Delta H_0/H_0$	$\Delta\Omega_m/\Omega_m$
LVK	0.055	1.8	0.055	1.8	0.055	1.8
LVKI	0.044	1.1	0.043	1.1	0.043	1
ET-Δ, HF	0.017	0.33	0.015	0.29	0.015	0.28
ET-Δ	0.013	0.22	0.011	0.19	0.011	0.18
ET-Δ + CE	0.0096	0.14	0.0081	0.11	0.0079	0.11
ET-2L, HF	0.014	0.25	0.012	0.22	0.012	0.2
ET-2L	0.012	0.19	0.0098	0.17	0.0096	0.15
ET-2L + CE	0.0088	0.13	0.0075	0.11	0.0073	0.1

Table 5.2: Relative uncertainty on H_0 and Ω_m parameters with the ΛCDM model for the three mock BNS catalogues, *fiducial*, *extended*, and *very extebnded*, observed with different GW networks. Table adapted from [Cozzumbo et al., 2025] (Table 3).

In Tab. 5.2, we report the cosmological constraints for the ΛCDM model, showing the relative uncertainties on H_0 and Ω_m for the three BNS catalogues considered in the work and for the GW detector networks listed in Tab. 5.1. Starting from the current GW detectors in either their O5 or A# configurations, we find that due to the small number of detections, the constraints on H_0 are rather loose if compared to either Planck [Aghanim et al., 2020] or SH0ES [Riess et al., 2021] results. At the same time, Ω_m is practically unconstrained, given the limited redshift coverage. With ET, we manage to achieve the high

redshift events and any configuration of XG detectors spans the whole redshift range of the GRB data and allows us to reach sub-percent precision on H_0. As expected, the constraints get tighter the more events we consider in our analysis, going from the *fiducial* to the *very extended* catalogue.

Tab. 5.2 is an illustrative example of the results presented in [Cozzumbo et al., 2025]. The observations for the constraints within the ΛCDM model also hold for the PEDE one. The results are even more promising if we combine GRB/GW data with the independent sets of observations coming from SNe, like the Pantheon+ [Brout et al., 2022] or the SH0ES dataset [Riess et al., 2019], or the Baryonic Acoustic Oscillations (BAO) measurements [Beutler et al., 2011; Ross et al., 2015; Alam et al., 2017; de Sainte Agathe et al., 2019; Blomqvist et al., 2019].

In [Cozzumbo et al., 2025], it is also shown that if the model used to reconstruct cosmological parameters is different from the one used to generate the data, e.g., using the PEDE cosmology to analyze the data generated within the ΛCDM model, or vice-versa, we get biased results. This is a hint to the importance of considering a model-independent and data-driven approach, which is indeed the second main focus of [Cozzumbo et al., 2025]. GP methods based on non-parametric analyses allow us always to retrieve the injected cosmology and give us robust, less susceptible to bias results, not only in inferring the cosmological parameters but also, and more importantly, in reconstructing the DE evolution over redshift. Additionally, a model-independent approach would help us to assess departures from the ΛCDM model at more than 2σ level in an entirely data-driven fashion.

In brief, the thorough analyses carried out in [Cozzumbo et al., 2025] point to the relevance of a multi-probe and model-independent approach in cosmology and showcase the significance of precise and statistically relevant multi-messenger (MM) observations.

5.3 *Cosmology with BBHs and HI IM*

A new synergy is emerging between GWs and the LSS of the Universe. Along this line of research, we combine mock observations of stellar-origin BBH mergers and HI IM to constrain the expansion history of the Universe. GW signals from BBHs provide direct distance information, while HI's 21 cm line intensity maps offer a tomographic view of the LSS of the Universe. Using 3-dimensional density fields of hydrogen as a prior for GW events, we explore a novel dark siren-like approach that allows us to trace the Hubble parameter as a function of redshift [Dupletsa et al., nd, *in preparation*].

On the gravitational side, we focus on the upcoming XG GW detectors, and specifically the ET, to ensure enough statistics, precise PE,

and access to high redshift events [Branchesi et al., 2023].

On the EM side, near-future single-dish IM surveys with the SKA-Mid telescope will be capable of tracing the underlying dark matter (DM) distribution at large scales up to redshift $z \sim 3$, strongly improving over similar surveys conducted with MeerKAT [Santos et al., 2017; Wang et al., 2021] in terms of SNR and redshift coverage. IM measures the 21 cm line emission from HI, to map the distribution of the underlying LSS. The measurements integrate the emission from unresolved galaxies and the intergalactic medium [Kovetz et al., 2017; Scelfo et al., 2022].

In the following sections, we present the preliminary results of our work [Dupletsa et al., nd, *in preparation*]. In Sec. 5.3.1, we broadly discuss the LSS of the Universe and introduce the mathematical tools necessary for its description. Sec. 5.3.2, outlines the simulated maps of HI used in our analysis, highlighting two approaches: the linear regime and the N-body simulations. We dedicate Sec. 5.3.3 to describe the shot noise, which occurs when we sample a continuous distribution through discrete realizations. Finally, Sec. 5.3.4 and Sec. 5.3.5 illustrate the settings of the analysis and present some partial results from our ongoing work. In Sec. 5.3.6 we outline the next steps in our analysis.

5.3.1 *The large scale structure of the Universe*

The cosmological principle (see Sec. 1.1.1), i.e. isotropy and homogeneity of the Universe, holds above a certain scale. However, we do observe structures, like galaxies, clusters of galaxies, and so on. To understand the LSS of the Universe, we have to deal with primordial inhomogeneities and their evolution. The LSS we observe today results from the growth of the primordial quantum fluctuations of the DM density field under the effect of gravity. The process is hierarchical, meaning structures start from small and evolve into larger and larger ones. The DM field forms the so-called *cosmic web*, with dense nodes and filaments, and the baryonic matter falls in its gravitational potential.

On large scales, structures can be described analytically using the linear theory since the fluctuations with respect to the background density are small. On small scales, the process is highly non-linear and can only be captured by numerical simulations.

The basic tools we use to characterize the statistical properties of the LSS are the 2-point correlation function, the power spectrum, and the angular power spectrum. In the rest of this section, we outline each of them, highlighting the reciprocal relations.

We aim to describe the statistical properties of the DM density field.

We start with the density fluctuation about the mean value:

$$\delta(\vec{x}) = \frac{\rho(\vec{x}) - \bar{\rho}}{\bar{\rho}}, \tag{5.1}$$

with $\vec{x}$ being a generic point in space, $\rho(\vec{x})$ the density at that point, and $\bar{\rho}$ the average density. For a homogeneous density distribution, the 2-point correlation function is defined as:

$$\xi(\vec{r}) = \langle \delta(\vec{x} + \vec{r}) \delta(\vec{x}) \rangle \tag{5.2}$$

It quantifies the excess probability of finding another overdensity at a distance $\vec{r}$ from what we have in $\vec{x}$ with respect to what is expected for a random Poisson distribution. We can also write $\xi(\vec{r}) = \xi(r)$ under the assumption of isotropy.

If we decompose Eq. (5.1) in Fourier modes, we get:

$$\delta(k) = \int d^3x e^{-i\vec{k}\cdot\vec{x}} \delta(\vec{x}), \tag{5.3}$$

where k is related to the spatial scale as $2\pi/\lambda$, with λ setting the scale. The 2-point correlation function in Fourier space then becomes:

$$\begin{aligned} \langle \delta(k) \delta^*(k') \rangle &= \langle \int d^3x e^{-i\vec{k}\cdot\vec{x}} \delta(\vec{x}) \int d^3r e^{i\vec{k'}\cdot(\vec{x}+\vec{r})} \delta(\vec{x}+\vec{r}) \rangle \\ &= \int d^3x e^{-i\vec{x}\cdot(\vec{k}-\vec{k'})} \int d^3r e^{i\vec{k'}\cdot\vec{r}} \langle \delta(\vec{x}) \delta(\vec{x}+\vec{r}) \rangle \\ &= \int d^3x e^{-i\vec{x}\cdot(\vec{k}-\vec{k'})} \int d^3r e^{i\vec{k'}\cdot\vec{r}} \xi(r) \\ &= (2\pi)^3 \delta_D(\vec{k} - \vec{k'}) P(k), \end{aligned} \tag{5.4}$$

where δ_D is the Dirac delta-function, and where in passing from the second to the third line, we used Eq. (5.2). In the last passage, we set the DM[4] power spectrum $P(k)$ as the Fourier transform of the 2-point correlation function. As for Eq. 5.2, the power spectrum depends only on the magnitude of the wavenumber. Eq. (5.4) describes the link between the power spectrum and the 2-point correlation function.

$P(k)$ describes the variance of density fluctuations of DM. It is easy to visualize it as a way of measuring how smooth or bumpy the Universe is at different scales. The wavenumber k sets the scale. Low k means large scales and large k corresponds to small scales. The power spectrum $P(k)$ quantifies the variance at each scale. A high value of $P(k)$ at a specific scale indicates that structures of that size are strongly present in the Universe.

In Fig. 5.1, we show the DM power spectrum today as a function of k. We use `CLASS` [Lesgourgues, 2011; Blas et al., 2011], which simulates the evolution of linear perturbations in the Universe, to compute $P(k)$ for the DM field at redshift $z = 0$. In *dark green*, we show the

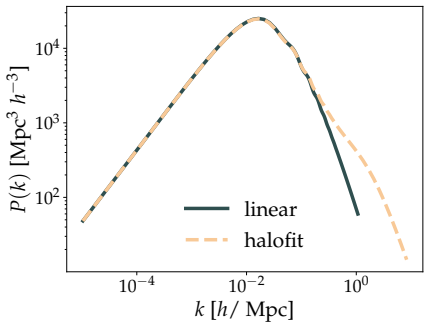

Figure 5.1: DM power spectrum at redshift $z = 0$: linear vs halofit

[4] Usually, the power spectrum is referred to as the matter power spectrum comprising both baryonic and cold dark matter. In our analysis, we only study the DM field and use the DM power spectrum term. Nevertheless, the tools outlined in this section apply to any field.

linear power spectrum. We see that at low k (large scales), the spectrum resembles the primordial scale invariant one predicted by inflation, which follows a simple power law, $P(k) \sim k^n$, with n close to unity. At the turnover point, around $k \sim 0.02\,h\,\mathrm{Mpc}^{-1}$, we have the passage between the scale-invariant form to a suppressed form. This corresponds to the epoch of matter-radiation equality, where the radiation pressure suppresses the small scales that re-enter the horizon earlier. Then we have a series of wiggles. This is the effect of Baryonic Acoustic Oscillations (BAO). The BAO manifest as a small preference of matter to be separated by a typical scale, which creates a distintive peak in the 2-point correlation function. In the Fourier space, the corresponding signatures is the series of wiggles in the power spectrum. Last, at very high k, linear theory breaks: non-linearities kick in, and the power spectrum is steeper than the linear one. Non-linearities are addressed thanks to halofit models [Smith et al., 2003], as the one represented in *orange* in Fig. 5.1, or N-body simulations, as we will discuss in Sec. 5.3.2.

The same properties of $P(k)$ can be expressed as a function of angular separation between points[5]. This leads to the angular power spectrum. Similarly to how the Fourier transform breaks down spatial distributions into sinusoidal components, spherical harmonics break down angular distributions into components on a sphere. Each spherical harmonic corresponds to a particular angular frequency. The index ℓ is the analogue of the wavenumber k: low ℓs corresponds to large angular scales (big features on the sky); large ℓs correspond to small angular scales (small features). The C_ℓs coefficients represent the power at each angular scale, i.e. they tell us how much fluctuation exists at different angular scales. The angular power spectrum can be obtained integrating the power spectrum through Bessel functions.

[5] In the box below, we provide a useful approximations to pass between k and angular scales set by ℓ.

The fluctuations in Eq. (5.1) can be projected onto the sky surface and written as a function of angular coordinates on a sphere. We refer to RA and DEC altogether as $\Omega = \Omega(\mathtt{RA}, \mathtt{DEC})$:

$$\delta(\Omega) = \frac{\rho(\Omega) - \bar{\rho}}{\bar{\rho}} \tag{5.5}$$

These can be expanded in spherical harmonics:

$$\delta(\Omega) = \sum_{\ell,m} a_{\ell m} Y_{\ell m}(\Omega), \tag{5.6}$$

where the $a_{\ell m}$ coefficients encode the contribution to fluctuations at each angular scale ℓ. The angular power spectrum is defined as the variance of $a_{\ell m}$ coefficients[6]:

$$C_\ell = \frac{1}{2\ell + 1} \sum_m \langle |a_{\ell m}|^2 \rangle. \tag{5.7}$$

[6] Note that the mean $\langle a_{lm} \rangle = 0$ by definition, since fluctuations have been rescaled by the mean.

From now on, we will work with angular power spectra. We must specify that all the equations discussed so far, from Eq. (5.1) to Eq.(5.7), are valid at each redshift bin if we imagine dividing the Universe in shells redshift-wise.

Shell by shell, the angular power spectrum of the DM distribution gives us all the necessary statistical information to reconstruct spatial maps of $\delta(\Omega)$.

As we will explain in Sec. 5.3.3, measuring the angular power spectrum boils down to discrete counts, e.g. we measure the positions and corresponding masses of DM haloes. This means that when reconstructing the angular power spectrum of the underlying DM continuous field, we need to consider the Poisson noise due to the discreteness of our tracer. The following relation holds:

$$C_\ell^{\rm obs} = C_\ell^{\rm true} + C_\ell^{\rm shot} \tag{5.8}$$

Consequently, when comparing the theoretical angular power spectrum, as the one we can easily get from `CLASS`, with the angular power spectrum coming from, e.g., N-body simulations, we need to subtract the effects of shot noise correctly.

Link between k and ℓ

We already said that the wavenumber k is related to the physical scale λ of fluctuations:

$$k = \frac{2\pi}{\lambda} \tag{5.9}$$

It is usually measured as a comoving wavenumber in $h\,\mathrm{Mpc}^{-1}$.
When fluctuations are projected onto the sky, and we are dealing with the angular power spectrum, then the multipole moment ℓ describes the angular scale of these fluctuations, and roughly the following holds:

$$\theta \sim \frac{180^\circ}{\ell}, \tag{5.10}$$

with θ being the angular scale.
The connection between the 3D power spectrum and the 2D angular power spectrum is given by:

$$k \sim \frac{\ell}{d_{\rm comoving}(z)}, \tag{5.11}$$

where $d_{\rm comoving}(z)$ is the comoving distance to the redshift z defined in Eq. (1.9).
The relation in Eq. (5.11) is known as the Limber approximation and is good for small angular scales. It is used to project the 3D power spectrum $P(k)$ into the 2D angular power spectrum C_ℓ, assuming that only transverse modes as of Eq. (5.11) contribute significantly. Nevertheless, it provides good intuition at large scales as well.
For example, the peak we see in Fig. 5.1 at $k \sim 0.02$ corresponds to $\ell \sim 200$, which is the corresponding acoustic peak in the Cosmic Microwave Background (CMB) angular power spectrum.

5.3.2 *DM map reconstruction*

Our work in [Dupletsa et al., nd, *in preparation*] aims at exploring the synergy between GWs and the IM of HI. As a first approximation, we assume that both GW sources and the HI field follow the underlying DM field without any bias. Therefore, if BHs, for which, on the gravitational side, we can measure the luminosity distance, e.g. with ET, are more likely to be found where there are HI overdensities, we can use this information to pinpoint their redshift, which can be precisely measured with the upcoming radio surveys as SKA-Mid. This gives us the luminosity distance - redshift pair for cosmological inference.

Our starting point is the simulation of the DM distribution at different redshift bins. Given that SKA-Mid frequency coverage will allow tomography of the 21 cm line of HI up to $z \sim 3$ and ET can trace BBHs up to even $z \sim 100$, we set our analysis for $z \in [0, 3]$. We compare two simulated maps of DM distribution. Using `CLASS`, we work in the linear regime and thanks to the functions in `healpy` [Górski et al., 2005; Zonca et al., 2019], we can simulate a realization of the DM maps from the angular power spectrum output of `CLASS`. This can be done at each redshift shell. Conversely, we use DM maps coming from an N-body simulation since, where more realistic features, e.g. non Gaussianities, are included.

As for the N-body DM maps, we use the Dark Energy and Massive Neutrino Universe (DEMNUni) set of simulations [Castorina et al., 2015; Carbone et al., 2016; Parimbelli et al., 2021] in their new high-resolution configuration of HR-DEMNUni [Hernández-Molinero et al., 2024]. These simulations have been produced using the code Gadget-3 [Springel, 2005]. They are characterized by a Planck 2013 [Ade et al., 2014] baseline flat ΛCDM cosmology with different values of the total neutrino mass and of the parameters characterizing the DE EoS. Concerning the maps used in [Dupletsa et al., nd, *in preparation*], the model considers only the massless neutrino flat ΛCDM case and a box with side length of $500\,\mathrm{Mpc}\,h^{-1}$ in comoving coordinates, with 2048^3 DM particles and no neutrino particles. A full-sky lightcone from redshift $z = 0$ to redshift $z \approx 8$ is then built, corresponding to a total comoving volume of approximately $3 \times 10^3\,\mathrm{Gpc}^3\,h^{-3}$. Around 39 billion haloes are identified through the Friends-of-Friends (FoF) algorithm. We use the DM haloes as a biased tracer of the underlying continuous DM distribution.

In Fig. 5.2, we show three example maps of the distribution of the DM haloes. From the simulation data, which provides us with the `RA` and `DEC` positions of each DM halo, we choose a pixelization corresponding to `nside` value of 128, and count how many objects fall into each pixel. Numerically, we reconstruct the maps at each redshift by

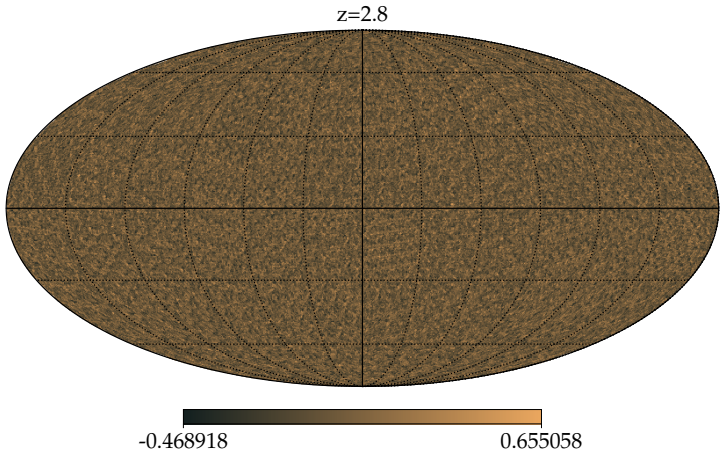

(a)

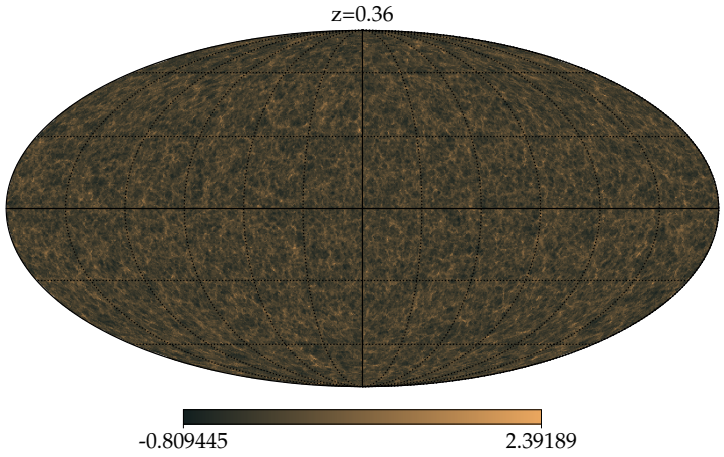

(b)

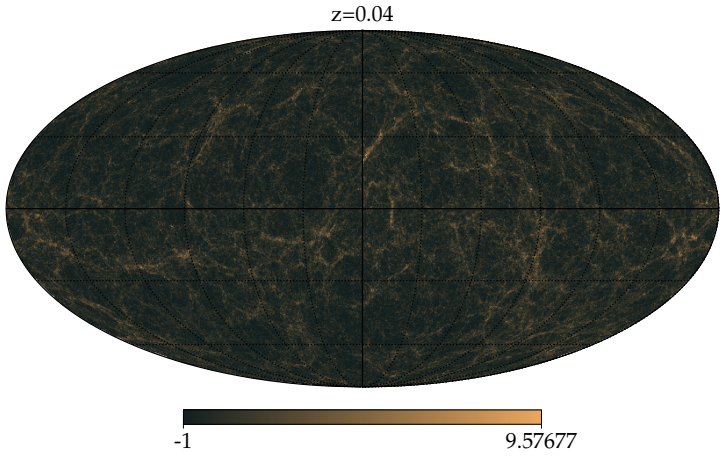

(c)

Figure 5.2: N-body maps at different, progressively -from subplot (a) to (c)- lower, redshifts, indicated above each map. These maps describe the spatial distribution of DM haloes with a pixelization choice of `nside` = 128. The colorbars at the bottom of each map indicate the density contrast quantity $\delta(\Omega)$ as in Eq. (5.5). The values get larger for lower redshifts, as bigger structures have had time to collapse, with respect to the more uniform distribution at higher redshift values

calculating the over or underdensities of the number counts in each pixel with respect to the mean value of objects per pixel[7]:

$$\mathrm{map}(z, \mathrm{pix}) = \frac{\mathrm{N}(\mathrm{z}, \mathrm{pix}) - \bar{\mathrm{N}}_{\mathrm{pix}}(\mathrm{z})}{\bar{\mathrm{N}}_{\mathrm{pix}}(\mathrm{z})}, \tag{5.12}$$

with

$$\bar{N}_{\mathrm{pix}}(z) = \frac{\sum_i^{\mathrm{npix}} N(z, \mathrm{pix}_i)}{\mathrm{npix}}, \tag{5.13}$$

where pix represents a single pixel, while npix the total number of pixels. Eq. (5.12) is the discretized version of Eq. (5.5).

Thanks to `healpy`, we generate the maps corresponding to the count fluctuations as shown in Fig. 5.2. From Fig. 5.2, we observe large-scale structures at low redshift. As we go at higher redshifts, the distribution of structures becomes increasingly uniform.

Notably, beyond a certain redshift, we begin to observe what are known as box replication effects. These effects occur because in N-body simulations as DEMNUni it is customary to model the evolution of a finite-sized box at different redshifts. When constructing the lightcone, a cut is done at a comoving distance that corresponds to the analyzed redshift bin. When the redshift is sufficiently high, the corresponding radius of the spherical shell may exceed the size of the box. At this point, the boxes are tiled together using periodic boundary conditions, which also guarantee the continuity of the structures. This replication effect becomes more pronounced as more and more boxes are needed to cover the sky at such large comoving distances. In Fig. 5.3, we can observe the relationship between redshift and comoving distance, in relation to the box size of the simulation. As we will soon see, the replication effect creates large-scale fictitious structures visible from the angular power spectrum.

In Fig. 5.4, we compare the theoretical angular power spectrum obtained with `CLASS` under linear conditions and the one we compute from the N-body maps from the DEMNUni simulation. We report the results for each redshift bin in which we divided our simulation.

The *dark green* line shows the `CLASS` result for the linear angular power spectrum. In *orange*, we present the angular power spectrum reconstructed from the maps generated with DEMNUni, from which we subtract the shot noise. Therefore, from `CLASS`, we directly have the C_ℓ^{true} quantities. From our N-body simulation, we plot the $C_\ell^{\mathrm{true}} = C_\ell^{\mathrm{obs}} - C_\ell^{\mathrm{shot}}$ quantity. We specifically address the shot noise calculation in Sec. 5.3.3.

From the comparison shown in Fig. 5.4, we see good agreement at all redshift bins. The first bin only shows a significant shot noise contribution at small scales. This is explained with the finite-size box N-body simulation. Looking at the plot in Fig. 5.3, we see that the cov-

[7] The `nside` parameter in `healpy` is related to how many pixels are used to divide the sky. When `nside` = 128, we have a total of 196608 pixels. Given that the whole sky has an area of 4π sr, this pixelization choice allows each pixel to cover approximately an area of less than one square degree. A detailed description of how the `healpy` package works is provided here.

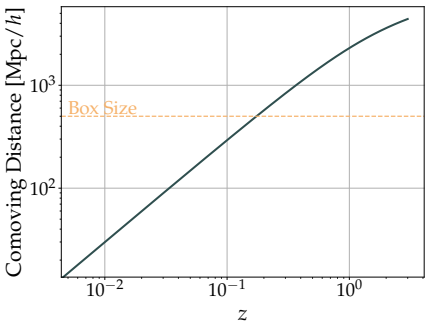

Figure 5.3: Comoving distance as a function of redshift. The *orange* line shows the size of the box in the N-body DEMNUni simulation

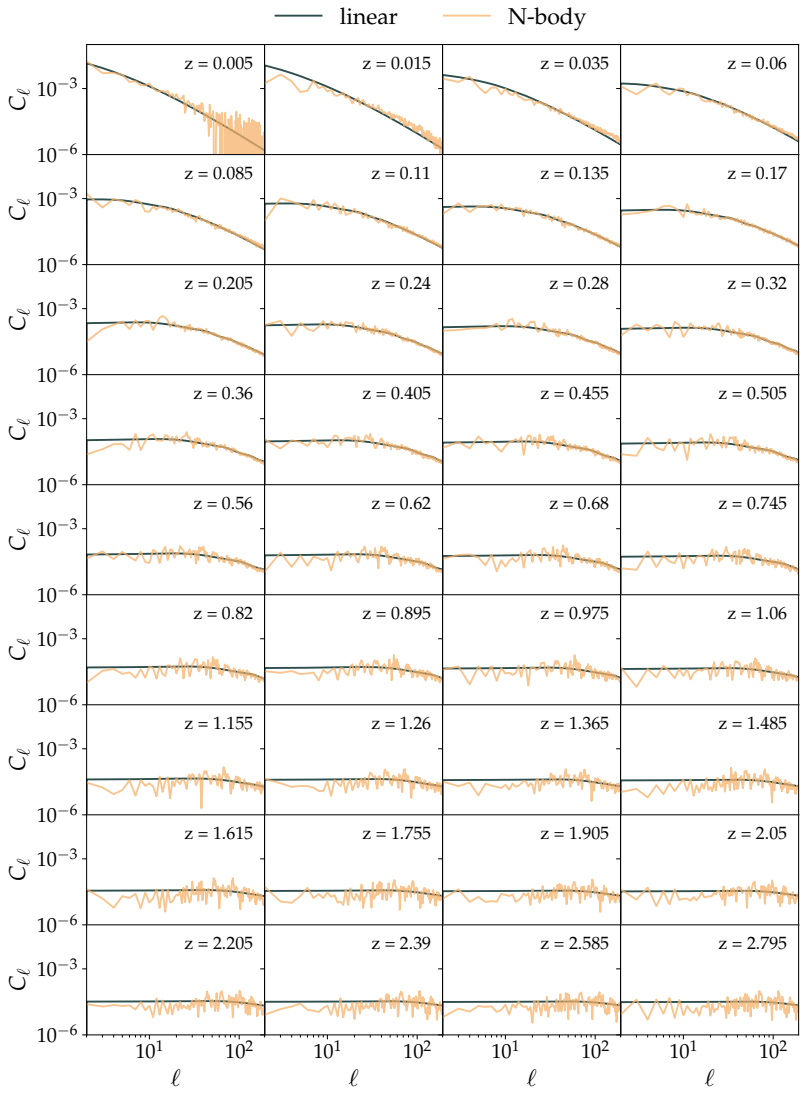

Figure 5.4: Angular power spectrum: comparing linear results from `CLASS` and the reconstructed angular power spectrum from N-body maps of the `DEMNUni` simulation. We report the results for each redshift bin in which we divided our simulation. The *dark green* line shows the `CLASS` result for the linear angular power spectrum. In *orange*, instead, we present the angular power spectrum reconstructed from the mass maps from DEMNUni, from which we subtracted the shot noise. Therefore, from `CLASS`, we directly have the $C_\ell^{\rm true}$ quantities. From our N-body simulation, we plot the $C_\ell^{\rm true} = C_\ell^{\rm obs} - C_\ell^{\rm shot}$ quantity

ered distance is just a few tens of comoving Mpc at such low redshift. As a result, in this volume, there are not enough objects with which we can resolve the small structures. For reference, in Fig. 5.5, we show the corresponding map, from which we see a few objects present, and we can only resolve the large scales.

At high redshifts, the box replication plays a role, and we still see some large-scale structures that are artificial due to the box replication itself, as we have already observed from the map in Fig. 5.2.

From this result, we can say there is good agreement between the linear and N-body angular power spectra if we account for the limitations coming from the finite size of the box at very low redshifts. This allows us to generate DM maps with `CLASS`, studying different cosmo-

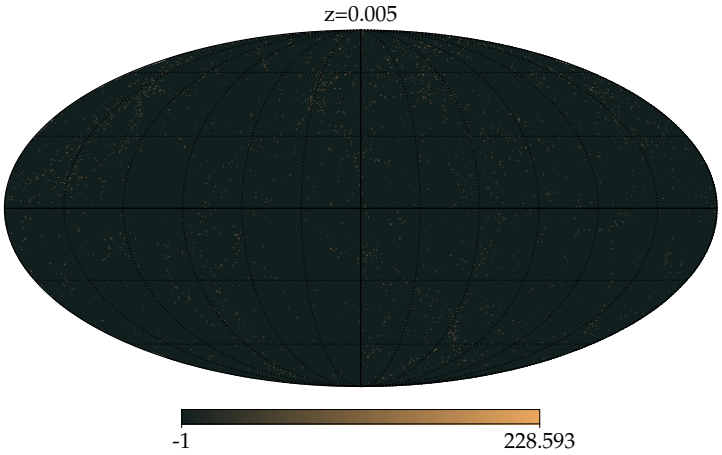

Figure 5.5: Map at the lowest redshift bin $z \sim 0.005$. The colorbar at the bottom indicates the density contrast quantity $\delta(\Omega)$ as in Eq. (5.5)

logical scenarios without the need to run complex and time-consuming N-body simulations. However, resolving to linear approximation, we lose all the non-Gaussianities that N-body maps provide.

5.3.3 *Shot noise*

Shot noise arises because of the discreteness of sources when modeling a continuous distribution. Both DM halos and GWs represent discrete tracers of the underlying continuous DM density field. The shot noise is related to the variance in the number count because of its Poisson nature: counts of halos or galaxies or GWs fluctuate about a mean value.

In what follows, we will refer to the DM halos to pinpoint a tracer, but a similar reasoning applies to any other discrete tracer. Observations or simulations of DM involve counting the number of halos in small sky regions dependent on the chosen pixelization. Since we are working with the angular power spectrum, we will fix the redshift bin and focus on the distribution over the sky.

Evaluating the shot noise means linking the statistical properties of the tracers to their discrete nature. The number of halos in a pixel can vary for two reasons:

1. The underlying dark matter density field $\rho(\Omega)$, where Ω, as before, depends on the two angular parameters `RA` and `DEC`

2. Random fluctuations due to the discreteness of the tracer

The angular distribution of halos in the sky can be expressed as a fluctuation of the number density, which we can think of as the discrete approximation to $\delta(\Omega)$, and rewrite Eq. (5.5) to express the expected

number of objects at a given position in the sky:

$$n(\Omega) = \bar{n}_{\rm sky}\left[1 + \delta n(\Omega)\right], \tag{5.14}$$

where $\bar{n}_{\rm sky}$ is the mean number density of objects over the sky:

$$\bar{n}_{\rm sky} = \frac{N}{4\pi} \tag{5.15}$$

If we measure the number of halos in a certain direction, then we expect:

$$n_{\rm obs}(\Omega) = n_{\rm true}(\Omega) + \text{Poisson noise} \tag{5.16}$$

These fluctuations are reflected in the a_{lm} coefficients when expanding in spherical harmonics:

$$a_{\ell m}^{\rm obs} = a_{\ell m}^{\rm true} + a_{\ell m}^{\rm shot} \tag{5.17}$$

In a process governed by Poisson statistics[8], the variance in the number count is equal to the mean, i.e., $\bar{n}_{\rm sky}$. At the angular power spectrum level, the C_ℓs computation translates into summing over the independent contributions of each halo. Therefore, the variance of the $a_{\ell m}$ coefficients due to shot noise is given by:

$$\langle |a_{\ell m}^{\rm shot}|^2 \rangle = C_\ell^{\rm shot} = \frac{1}{\bar{n}_{\rm sky}}. \tag{5.18}$$

This scaling reflects the fact that the more objects we observe, the less significant the discreteness fluctuations, i.e., shot noise, become. In other words, if $\bar{n}_{\rm sky}$ is large, the random sampling better approximates the true continuous field. The result is also independent of ℓ as shot noise is flat (scale-independent): it introduces uncorrelated fluctuations at all angular scales equally. For a full derivation of Eq. (5.18) see Appendix D.

[8] See also the summary box on Poisson distribution given at the beginning of Chapter 2.

5.3.4 *Simulating the GW distribution*

The maps of DM, either linear or from N-body simulations, are used both as a probability distribution to simulate the spatial location of GW sources and as a redshift prior in the final analysis phase to pinpoint the BBHs redshift and infer cosmological parameters. The rationale is the following:

- First, we distribute GW events on the sky at each redshift shell, according to the probability given by the distribution of HI, which we said is in a one-to-one correspondence with DM maps. In Fig. 5.6, we show an example of the distribution of illustrative 500 GW events following the probability given by the map.

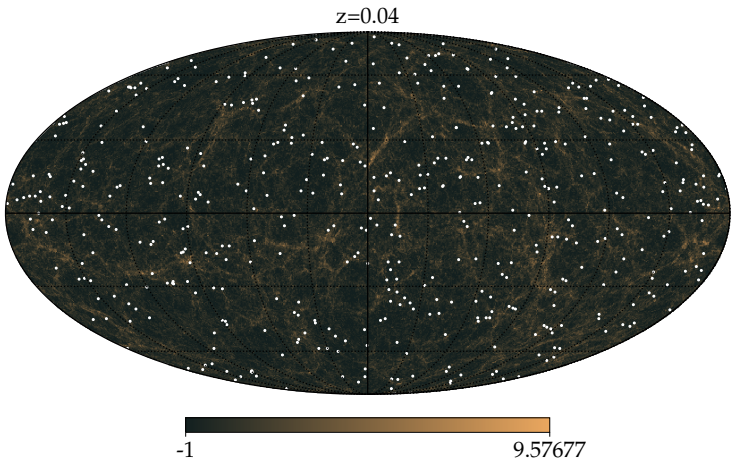

Figure 5.6: Illustrative example of the distribution of 500 GW events on the HI map, at redshift $z \sim 0.035$. The colorbar indicates the density contrast quantity $\delta(\Omega)$ as in Eq. (5.5)

- Second, we simulate the measured GW signals, by a parameter estimation (PE) of the parameters characterizing each event, namely the ones described in Tab. 1.1. Since we are using a population of BBHs as expected to be observed with ET, our parameter estimation is performed under the Fisher matrix approximation with `GWFish`, enhanced with priors [Dupletsa et al., 2023, 2025].
- We use the Hierarchical Bayesian Inference (HBI) scheme described in Chapter 2, Sec. 2.3, to reconstruct the posterior on the cosmological parameters. We use the `icarogw` [Mastrogiovanni et al., 2024] pipeline. The HI maps enters in the rate modeling as explained in the next Sec. 5.3.5.

In the remaining part of this section, we present a test on the distribution of GW events when it follows the probability set by HI density maps. We compare once again the angular power spectrum of the hydrogen maps to the angular power spectrum we reconstruct from the GW distribution. We expect the two to match, since we distribute BBHs according the density of HI. We pick three example redshift bins, and simulate five different numbers of GWs, namely 10^3, 10^4, 10^5, 10^6, and 10^7, at each redshift[9]. We present the results in Fig. 5.7. In the *top* panel, we separately present the C_ℓs from GWs and the corresponding shot noise, in the same color but different linestyles: solid for $C_\ell^{\rm obs}$ and dashed for $C_\ell^{\rm noise}$. In the *bottom* panel, instead, we directly show the $C_\ell^{\rm true}$, where we have subtracted the shot noise. In both panels, the solid *black* line represents the angular power spectrum of the HI field, which, as we stated above, we assume to be in a one-to-one correspondence with the DM field.

From Fig. 5.7, we see that we manage to reconstruct from the discrete GW distribution an angular power spectrum that matches the HI one, as expected. However, we are dominated by shot noise until a

[9] These numbers of GWs serve as an example to study the impact of shot noise. Based on a realistic rate, we would see $\sim 10^5$ BBHs per year in all the redshift range

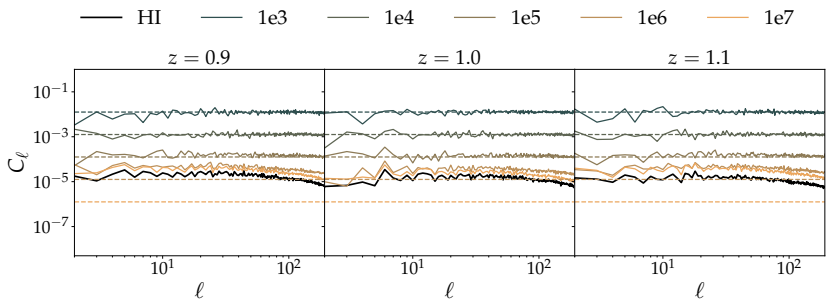

(a) $C_\ell^{\rm obs}$ in solid line and $C_\ell^{\rm shot}$ in dashed line

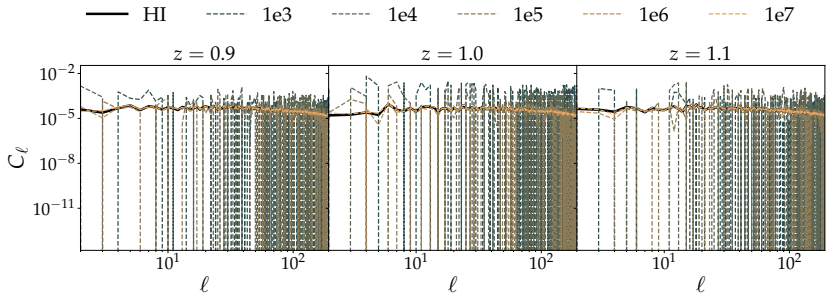

(b) $C_\ell^{\rm true} = C_\ell^{\rm obs} - C_\ell^{\rm shot}$

Figure 5.7: Comparing the angular power spectrum from the discrete distribution of different number of GWs to the power spectrum used to realize a DM distribution according to which the GW sources have been distributed. In the *top* panel, we separately present the C_ℓs from GWs and the corresponding shot noise, in the same color but different linestyles: solid for $C_\ell^{\rm obs}$ and dashed for $C_\ell^{\rm noise}$. In the *bottom* panel, instead, we directly show the $C_\ell^{\rm true}$, where we have subtracted the shot noise. In both panels, the solid *black* line represents the angular power spectrum of the HI field, which we assumed to be in a one-to-one correspondence with the DM field. The results are shown for three redshift bins as an illustrative example

number of GWs of 10^5.

5.3.5 *Tracing $H(z)$: preliminary results*

In the following section, we present preliminary results on estimating the cosmological parameters with the machinery we presented in the previous sections. For the time being, we focus on the Hubble constant only and use 500 perfectly measured GW signals.

We work within the HBI framework outlined in Sec. 2.3 with the `icarogw` pipeline. We set distance and position, i.e. the `RA` and `DEC` parameters, to the injected values without considering any measurement errors. To inform the likelihood of the redshift of the gravitational events, we use a modified Madau-Dickinson rate model [Madau and Dickinson, 2014] to account for the HI distribution:

$$\frac{{\rm d}N_{\rm CBC}}{{\rm d}z{\rm d}t} = \frac{{\rm d}N_{\rm CBC}}{{\rm d}M_H{\rm d}t_{\rm src}}\frac{1}{1+z}\frac{{\rm d}M_H}{{\rm d}z{\rm d}\Omega}, \tag{5.19}$$

where $\frac{{\rm d}N_{\rm CBC}}{{\rm d}z{\rm d}t}$ defines the number of CBC mergers per redshift and detector time. We can rewrite the first term as:

$$\frac{{\rm d}N_{\rm CBC}}{{\rm d}M_H{\rm d}t_{\rm src}} = \mathcal{R}_H\psi(z|\gamma,\kappa,z_p), \tag{5.20}$$

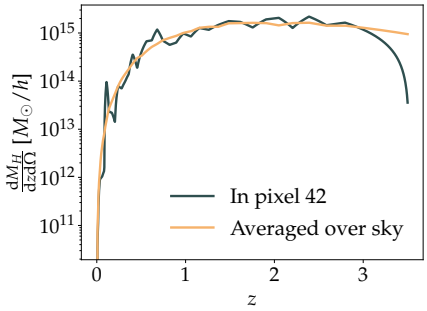

Figure 5.8: Line of sight, fixing a random pixel in the sky, distribution of the HI mass as from the N-body simulations in *dark green*. In *orange*, we compare it to the averaged over sky distribution of the HI mass

where $\psi(z|\gamma,\kappa,z_p)$ has been introduced in Eq. (2.6) and $\mathcal{R}_H$ depends on the HI distribution. The second term can be written as:

$$\frac{\mathrm{d}M_H}{\mathrm{d}z\mathrm{d}\Omega} = \frac{\mathrm{d}M_H}{\mathrm{d}V_c}\frac{\mathrm{d}V_c}{\mathrm{d}z\mathrm{d}\Omega} = \rho_H(z,\Omega)\frac{\mathrm{d}V_c}{\mathrm{d}z\mathrm{d}\Omega}, \tag{5.21}$$

where $\rho_H(z,\Omega)$ is given by the mass maps of HI. In Fig. 5.8, we compare, in *dark green*, the impact of the $\frac{\mathrm{d}M_H}{\mathrm{d}z\mathrm{d}\Omega}$ term as from the N-body maps with what we would expect if the HI distribution was averaged over the sky at each redshift, in *orange*. The spiky features of the $\frac{\mathrm{d}M_H}{\mathrm{d}z\mathrm{d}\Omega}$ distribution help us constrain the redshift of GW events.

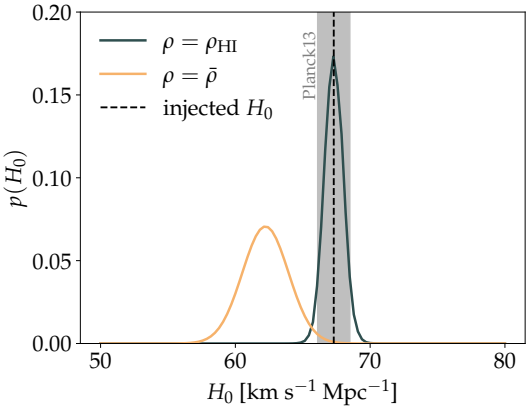

Figure 5.9: Preliminary reconstruction of the H_0 posterior using `icarogw` with 500 perfectly measured GW events. In *dark green*, we show the results using the N-body HI maps from the DEMNUni simulation to model the GW rate. In *orange*, instead, we compare it to posterior we get assuming an averaged-over-sky distribution of the HI mass across at each redshift bin

In Fig. 5.9, we show our preliminary H_0 posterior obtained with the 500 GW events, within the two scenarios for the redshift prior depicted in Fig. 5.8, i.e., the HI distribution as from the N-body mass maps, in *dark green*, and the averaged smoothed distribution, in *orange*. We fix all the parameters except for H_0. We can see that under the simplified analysis, using the HI maps, not only do we manage to recover the injected H_0 value (the one from Planck 2013 [Ade et al., 2014] used for the N-body maps simulations), but we also recover it with great precision. For comparison, we report the measurement from Planck 2013, which estimate of H_0 is at the percent level. The posterior we get using the average HI mass distribution is biased and mainly driven by fixing the rate parameters.

5.3.6 *Next steps*

With our preliminary work, we have set up a framework for further developments in the direction of synergies between GWs and HI IM.

We have showed the limits and advantages of linear approach with `CLASS` and N-body simulations as with DEMNUni. As expected, we have found that the maps obtained from `CLASS` under the linear approximation match well the ones from the N-body simulation DEMNUni. These two approaches go in two different directions:

- Using `CLASS`, either in linear theory or in the halofit approximation, we can explore and test different cosmologies, since the simulations are fast computationally. For example, we can build maps under different cosmological assumptions to test what bias we get when distributing the GW events on maps obtained with one cosmology and use maps constructed under a different cosmology as a prior for redshift.
- On the other side, the computationally expensive N-body simulations, such as the DEMNUni one, allow us to explore cosmic structures beyond the information contained in the power spectrum. This provides us more realistic maps of the LSS, including also the non-Gaussian features and higher order correlations, which are not present in `CLASS`.

Moreover, all our assumptions so far are highly simplified. In the first place, we are not accounting, for the time being, for proper PE of GW events. We plan to do so and perform a HBI analysis varying all the *hyperparameters*[10] at play. Then, we are not assuming any bias between the DM haloes and HI. Neither are we considering instrumental effects, e.g., the dish response. Including the latter would prevent us from resolving small scales. However, given the resolution on the gravitational side, we still expect the synergy between GWs and HI to help in the estimation of the redshift of the GW events. Furthermore, we can explore different biases, meaning that we can relax the assumption that HI and GWs (even though affected by measurement errors) follow one-to-one the DM distribution, which would also be more realistic. Additionally, we can take the direction of C_ℓs and cross-correlate GWs and the HI field to infer cosmological parameters.

[10] See Sec. 2.3 in Chapter 2 for the definition of *hyperparameters*

The point to stress is that the synergy between GWs and HI is setting a new field, and the paths of investigation are many and promising. The potential lies in the possibility to do tomographic studies, redshift bin per redshift bin, of the 21 cm HI line and explore all the related advantaged with respect to what is currently feasible with galaxy surveys.

6. Conclusions

> *Sometimes one sees things clearly years afterwards than one could possibly at the time.*
>
> **— Agatha Christie**
> "The Mysterious Mr. Quin"

This thesis explores the information content of the gravitational wave (GW) signals from compact binary coalescences (CBCs), addressing current and next-generation (XG) ground-based detectors. Specifically, the research focuses on analyzing GW events, applied, in particular, to cosmology and multi-messenger (MM) astrophysics.
In the following, we highlight the main questions the thesis is answering and its key findings, stressing the impact of the research alongside its limitations. We also explore some of the open questions and future perspectives of the presented work.

The findings of this thesis contribute to several key areas of the gravitational wave (GW) astronomy. Following the thesis structure, we can group the main results distinguishing between current and future GW ground-based detectors.

In the first part, we analyze mock and measured data from the LIGO-Virgo-KAGRA (LVK) network, applying spectral-siren cosmology techniques through Hierarchical Bayesian Inference (HBI). The results from the `Mock Data Challenge` (MDC) [Agarwal et al., 2024] show us the importance of refining the models that describe the compact binary coalescence (CBC) population. In particular, we investigate the open question about the dependence or not of the black hole (BH) mass spectrum on redshift. We find that, if it is not correctly accounted for, we get a bias in the inference of cosmological parameters, and H_0 in particular, which is currently the major focus, given the Hubble tension status. The work is the basis for further studies on the possible sources of systematics we can get in cosmological inference with GWs. The population model is based on simplifying assumptions that may not fully capture the complexity of the underlying astrophysical processes. The study can be developed into multiple directions for further investigation, including much-refined details, e.g., spins, and exploring the effects of additional astrophysical uncertainties.

Along this line, we show how the estimate of the Hubble constant

improves because of more advanced modeling of the mass spectrum using measured data up to the currently ongoing fourth observing run, O4a[1]. In this case, a mass spectrum like the presented MULTI POP one, that does not have to distinguish between neutron stars (NSs) or BHs, manages to describe CBCs as a whole, avoiding leaving ambiguous events, like `GW190814` out of the analysis. Furthermore, it allows to exploit all the observed CBCs in a common analysis.

[1] I am part of both the analysis and the paper writing teams for the official Collaboration Cosmology paper for O4a data.

We are gathering an increasing number of detections, and as we collect more data, we can obtain more precise constraints, particularly on cosmological parameters. Thanks to the GW events we are collecting, we are making extraordinary advances in many fields, cosmology, population studies, and fundamental physics, just to mention some of interest to this thesis.

The second part of this work focuses on the next-generation (XG) observatories, exemplified by the Einstein Telescope (ET). The potential for precision and discovery expected from a detector such as ET is enormous. Given the extraordinary impact of a XG detector and the need to assess its capabilities, the forecast studies require an analysis framework of their own. We need data analysis tools capable of dealing with the toll of computational power required for a XG detectors. This is why the core of this thesis is the development of a fast and reliable analysis software, `GWFish` [Dupletsa et al., 2023, 2025]. `GWFish` is a Fisher matrix parameter estimation (PE) software that simulates all the different GW detector networks. It implements the Earth's rotation and goes beyond the long wavelength approximation. Additionally, it can be used at its full capability, including the prior module, to take into account the physical range and prior knowledge of the signal's parameters. We have exhaustively shown that there is a non-trivial relation between the Signal-to-Noise Ratio (SNR) of a signal, the correlations among parameters, and possible multi-modalities that might create issues when analyzing GW events. `GWFish` has passed several tests and stands as a reliable and fast method for forecast purposes. The theoretical framework and data analysis developed in this thesis, namely `GWFish`, have been applied in several works [Ronchini et al., 2022; Banerjee et al., 2023; Branchesi et al., 2023; Cozzumbo et al., 2025; Loffredo et al., 2025], where we explore multi-messenger (MM) and cosmology perspectives for XG observatories.

`GWFish` has provided many interesting results. It is one of the two Fisher matrix codes employed for the paramount work in the ET Collaboration that led to the first systematic study of the ET design and its scientific implications [Branchesi et al., 2023]. `GWFish` provided the PE for the Binary Neutron Star (BNS) population, and has been used to cross-check all the Binary Black Hole (BBH) results. The impact of this

work on the scientific community is vast. Moreover, we have currently under review the follow-up work of the Blue Book, where `GWFish` has been used to produce results for both the *Common Tools* and *Multi-Messenger Observations* divisions[2]. Furthermore, it is now fundamental to analyze the detector's layouts within the ETO task force[3], within which we want to highlight the importance of considering all possible outcomes and balancing the corresponding risks and opportunities.

Furthermore, investigating MM synergies emphasizes the need to combine GW and electromagnetic observations to amplify the scientific yield of the XG experiments. This thesis shows many of the MM opportunities. From [Branchesi et al., 2023], we highlight the potential of using the precise sky localization and pre-merger detections provided by ET to study joint observations of GWs and Gamma Ray Bursts (GRBs) and kilonovae (KNe). In [Loffredo et al., 2025], we discuss the different sources of uncertainty entering the joint GW/KN detection. Starting from the GW detector network, we outline the impact of uncertainties coming from population synthesis, mass modeling, and the microphysics governing the neutron star (NS) Equation of State (EoS). This work will be used as the starting point for cosmology with the joint GW/KN observations. Going back to cosmology, we have also shown the constraining potential of combining ET with GRB observations in [Cozzumbo et al., 2025], and the great opportunity represented by the synergy between the GW field and the study of the large scale structure (LSS). Combining the potential of ET with that of a radio survey instrument like SKA Observatory (SKAO) would give us a unique chance to trace the Universe's expansion history up to high redshift.

The upcoming years will rapidly evolve in the GW astronomy, transitioning from current detector networks to XG observatories. The methods and results presented in this thesis provide a solid foundation for future studies to maximize these facilities' scientific output.

As we have seen, several promising directions for future research emerge from this work. Improved population synthesis models will enable more accurate cosmological measurements with spectral sirens. Integrating machine learning into the PE pipelines could be the direction of future analysis techniques. Finally, the synergies between GW observatories and future EM surveys such as the Vera Rubin Observatory will open new prospects for MM cosmology, offering unprecedented insights into the nature of the Universe.

In conclusion, this thesis advances our understanding of GW signals from CBCs, linking data analysis techniques, detector performance predictions, and MM applications.

[2] I am part of the editorial and writing team for the *Common Tools* division chapter; and part of the writing team of the *Multi-Messenger Observations* division chapter.

[3] I have recently been requested to be part of the OSB liaisons to coordinate and analyze the scientific risks connected to the different proposed sensitivity curves related to changes in the detector's optical layout. `GWFish` will be one of the two softwares - together with `gwfast`- employed for the analyses.

A. Supplements to Chapter 2

A.1 `Vanilla` and the `Redshift-Dependent` cases corner plots

We report here the full corner plots showing the posterior distributions and the correlations among the 14 *hyperparameters*, from the cosmological, population, and rate models, obtained with `icarogw`.

- In Fig. A.1, we show the results for the `Vanilla` scenario. We use all the 286 GW events and the 10^6 injections. Almost all recovered values fall in the 1σ region around the injected *hyperparameters* values. α, $m_{\rm min}$, σ_g, and γ, are slightly outside the 1σ region, but still well reconstructed.
- In Fig. A.2, we show the the `Redshift-Dependent` case results, obtained with 80 GW events and 10^6 injections. In this case, besides H_0, which is recovered at the 90% C.L. from the injected value, and besides the parameters that also in the `Vanilla` case were slightly off the 1σ region, in this second scenario, there are two more parameters, β and $\lambda_{\rm peak}$, that are not recovered within 1σ. γ is particularly off, but this might be because the injected value is very close to the border of the prior range.

A.2 Statistical tests for the `Vanilla` case: all parameters

We report the posterior distribution for all the 14 *hyperparameters* from the statistical tests done with the `Vanilla` case. In summary, Fig. A.3 tests the impact of the number of injections, Fig. A.4 tests the impact of injection sample realization, Fig. A.5 tests the impact of the number of GW events, and Fig. A.6 tests the impact of the GW event sample realization.

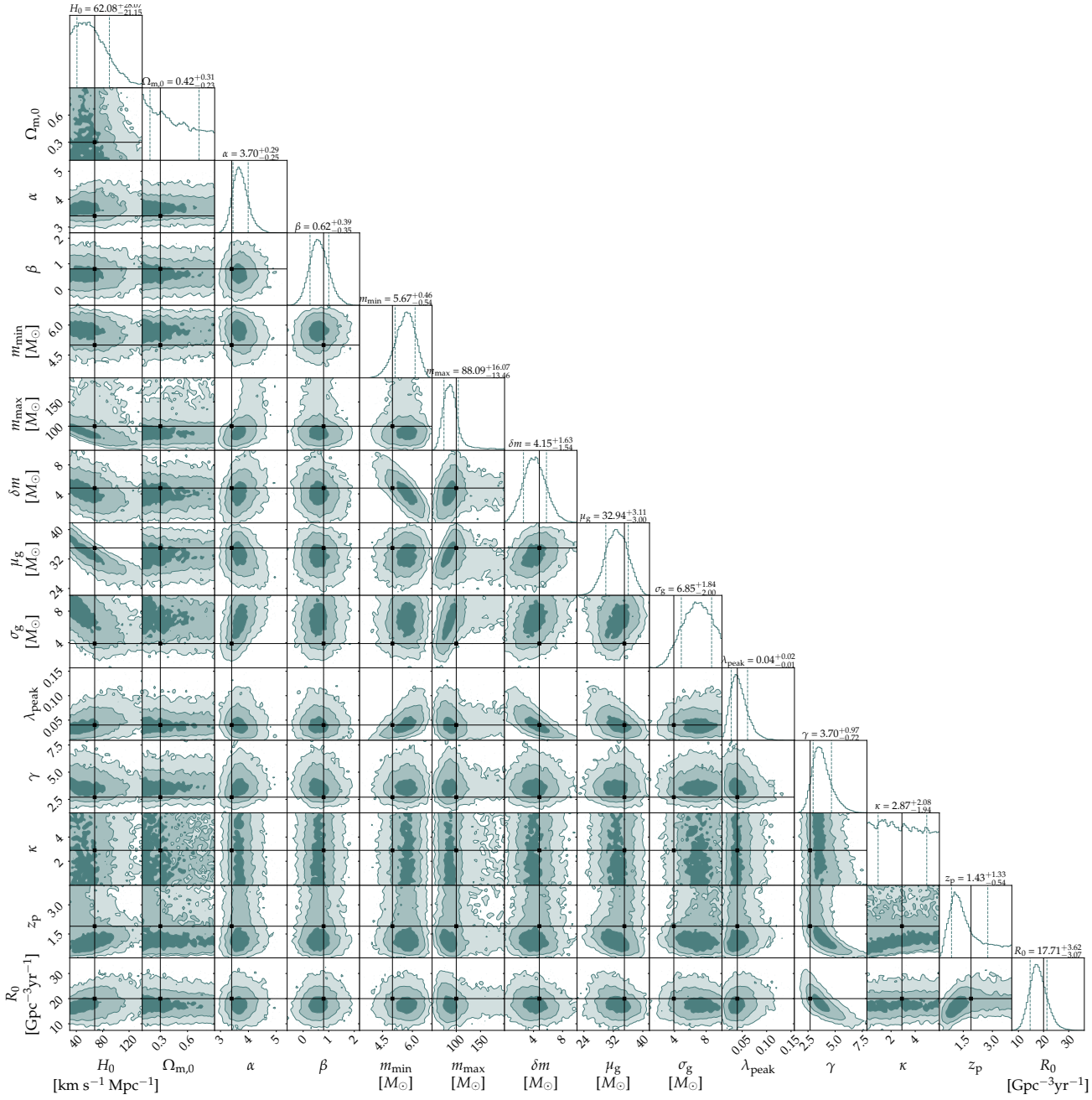

Figure A.1: Full corner plot for the 14 *hyperparamters* in the `Vanilla` case. The analysis was done with 286 events and 10^6 injections. Figure adapted from [Agarwal et al., 2024] (Figure 23, ***authored by UD***)

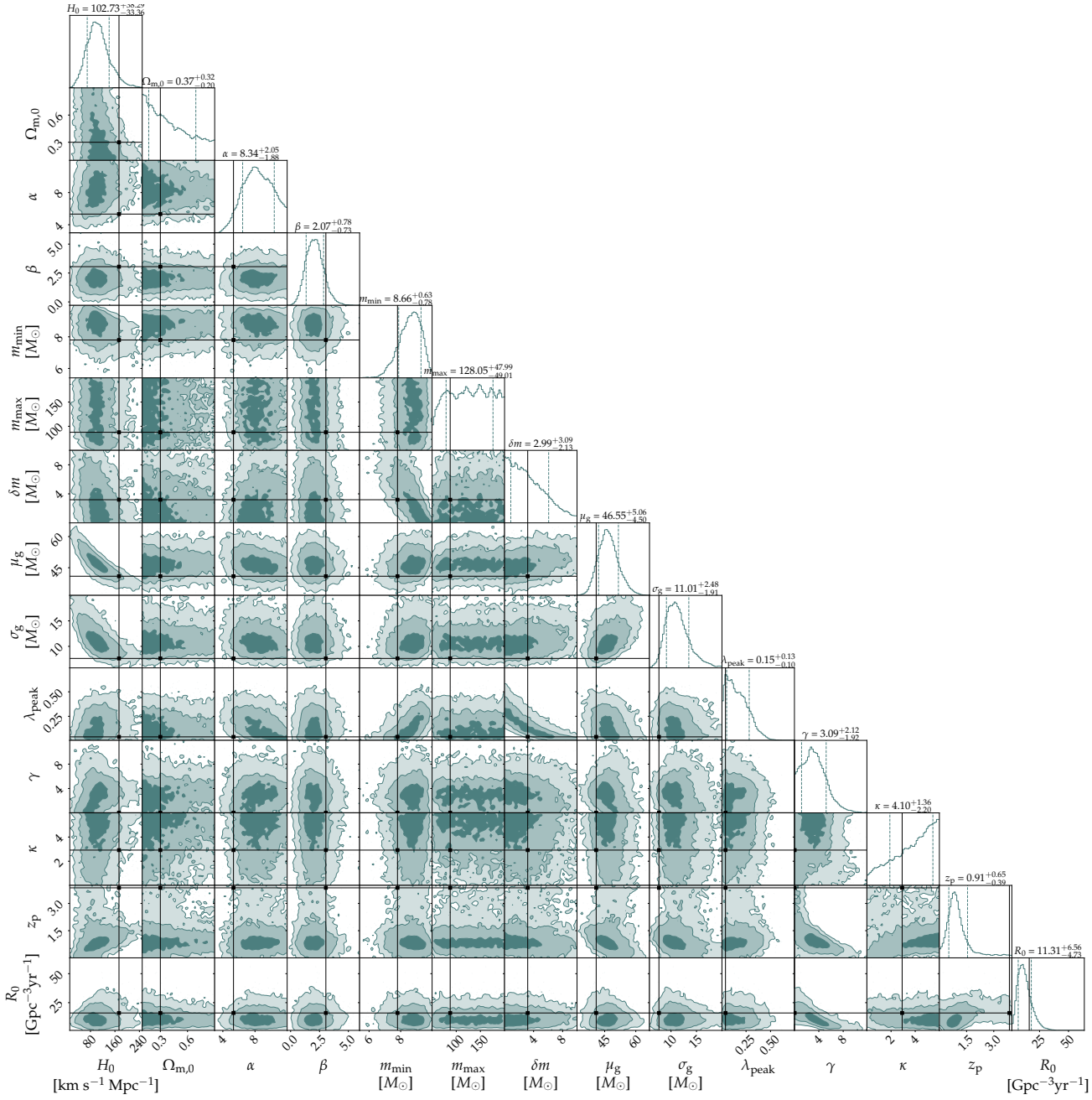

Figure A.2: Full corner plot for the 14 *hyperparamters* in the `Redshift-Dependent` case. The analysis was done with 80 events and 10^6 injections. Figure adapted from [Agarwal et al., 2024] (Figure 24, ***authored by UD***)

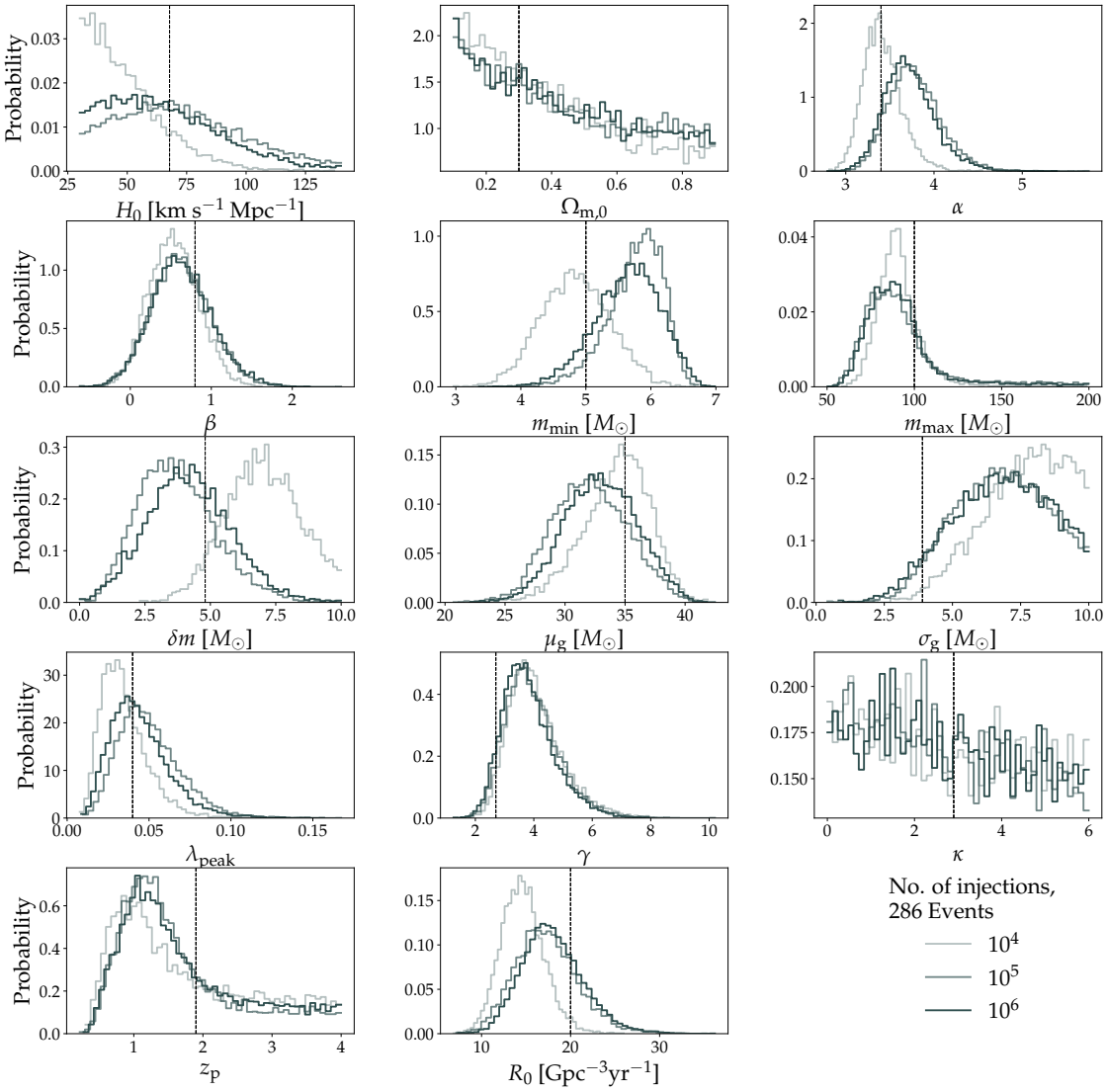

Figure A.3: Posterior distributions of the 14 *hyperparameters* in the `Vanilla` scenario. We vary the number of injections used to evaluate selection effects in the set $[10^4, 10^5, 10^6]$ to assess the impact of injection number. Figure adapted from [Agarwal et al., 2024] (Figure 25, ***authored by UD***)

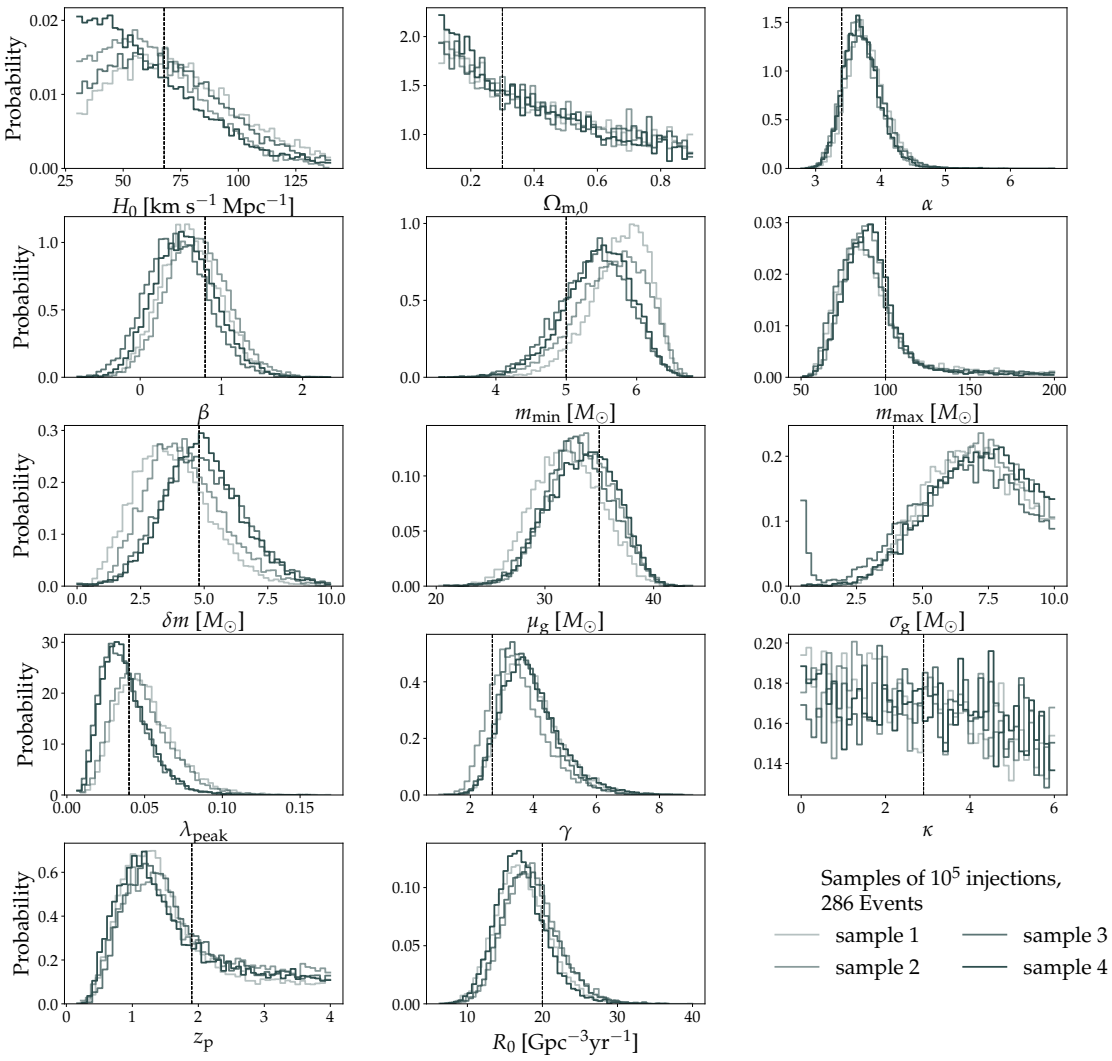

Figure A.4: Posterior distributions of the 14 *hyperparameters* in the `Vanilla` scenario. We vary the sample of injections used to evaluate selection effects, keeping the number of injections fixed at 10^5 to assess the impact of injection sample realization. Figure adapted from [Agarwal et al., 2024] (Figure 26, ***authored by UD***)

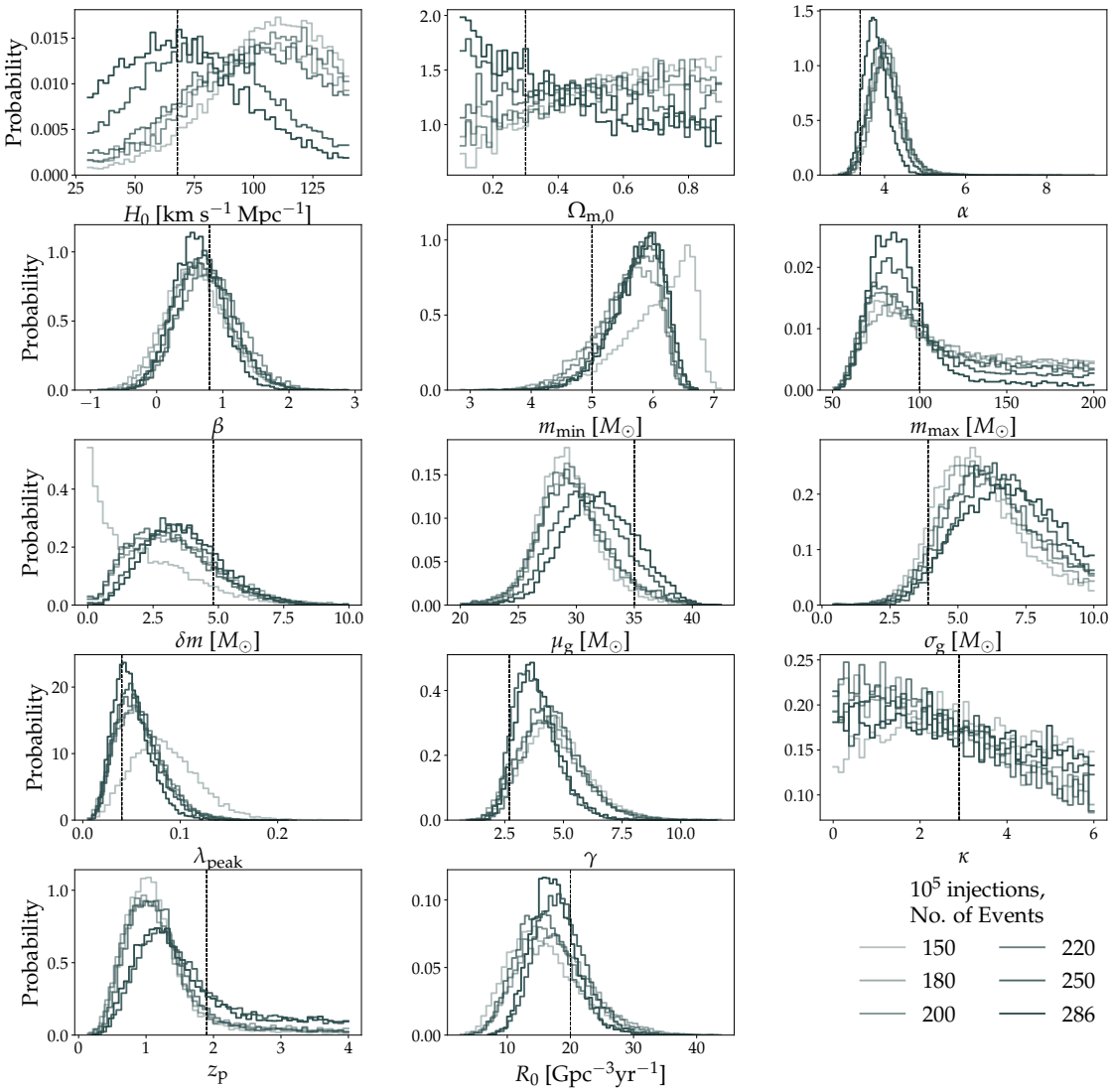

Figure A.5: Posterior distributions of the 14 *hyperparameters* in the `Vanilla` scenario. We vary the number of GW events, keeping the number of injections fixed at 10^5 to assess the impact of an increasing number of GWs. Figure adapted from [Agarwal et al., 2024] (Figure 27, ***authored by UD***)

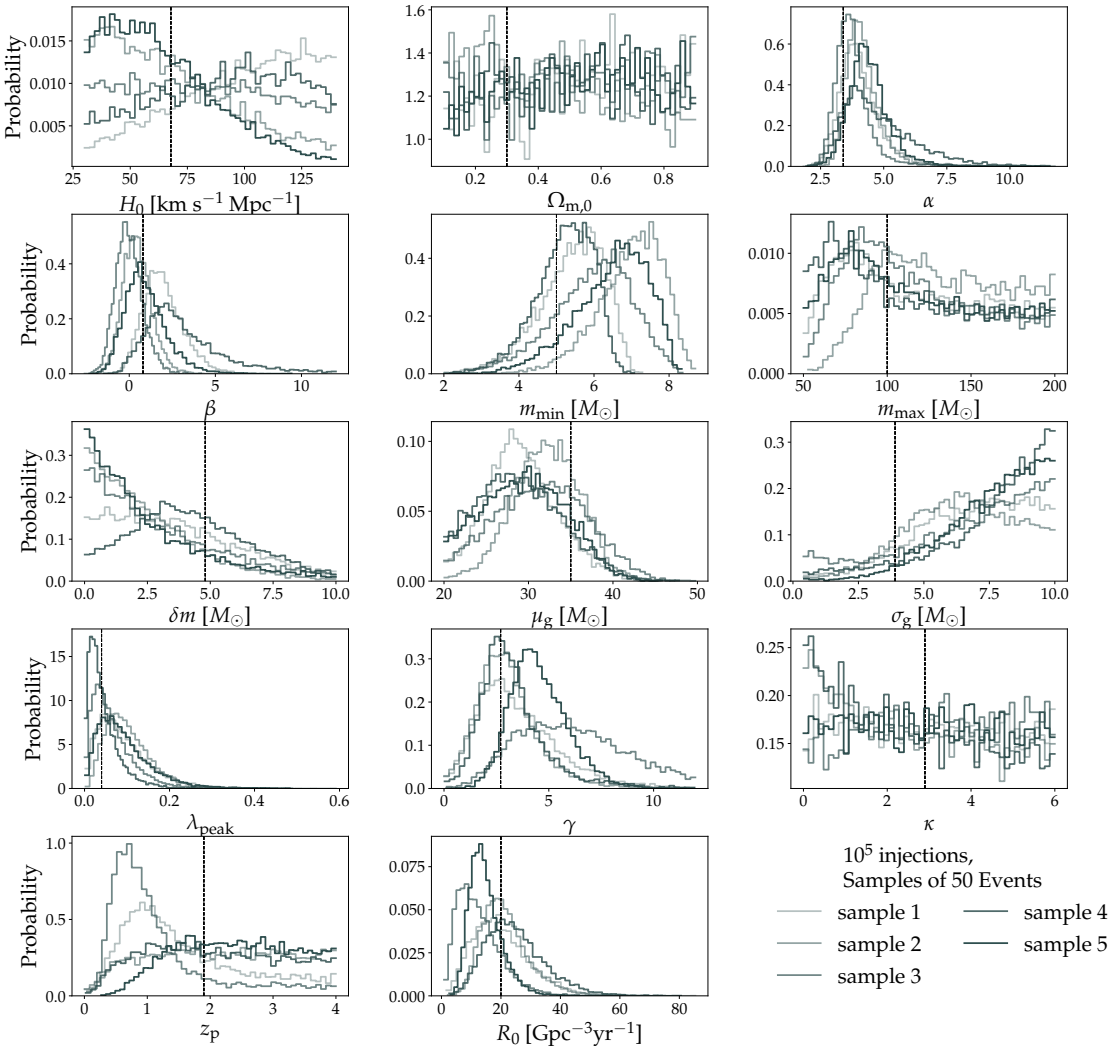

Figure A.6: Posterior distributions of the 14 *hyperparameters* in the `Vanilla` scenario. We vary the sample of GW events, keeping the total number equal to 50, and using a number of injections fixed at 10^5 to assess the impact of event sample realization. Figure adapted from [Agarwal et al., 2024] (Figure 28, ***authored by UD***)

B. Supplements to Chapter 3

B.1 `Bilby` vs `GWFish`: corner plots

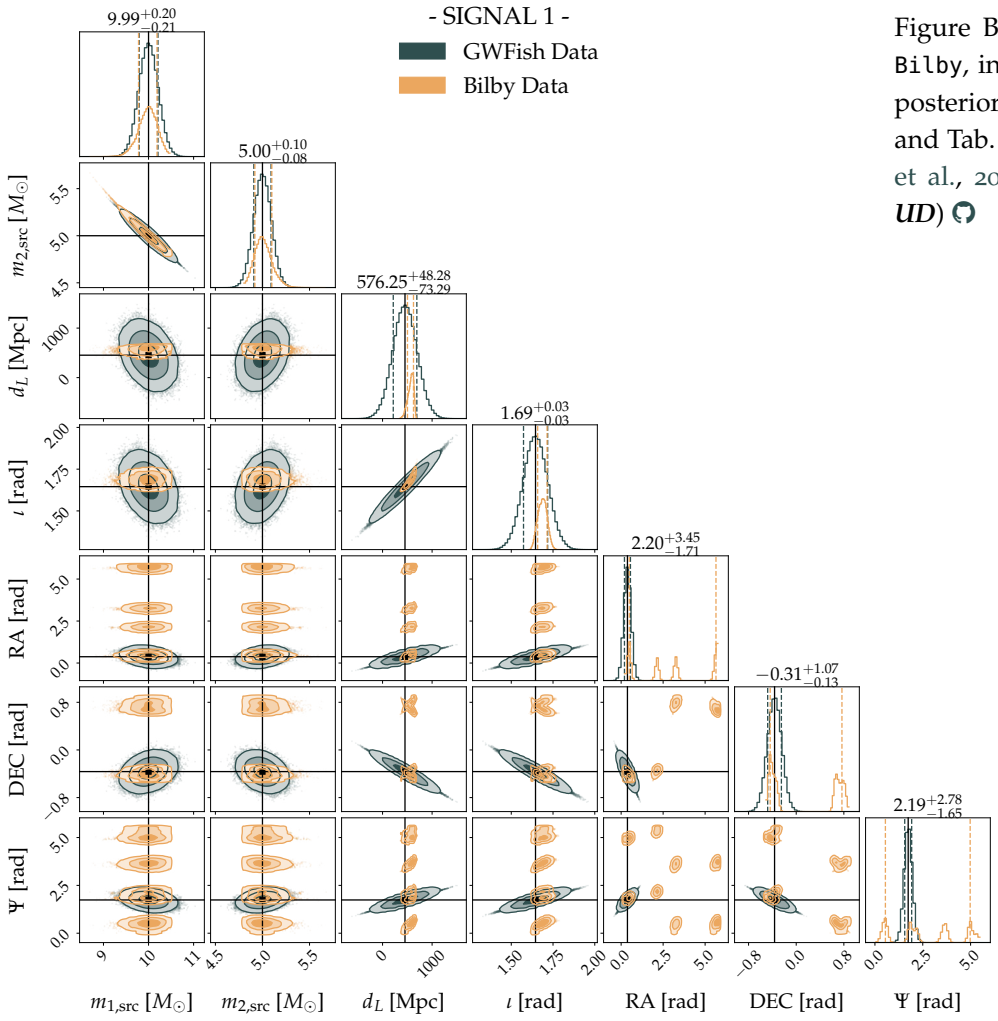

Figure B.1: Corner plot comparing `Bilby`, in *orange*, and `GWFish`, in *teal*, posteriors for Signal 1 (see Tab. 3.1 and Tab. 3.3). Figure from [Dupletsa et al., 2023] (Figure 6, ***authored by UD***)

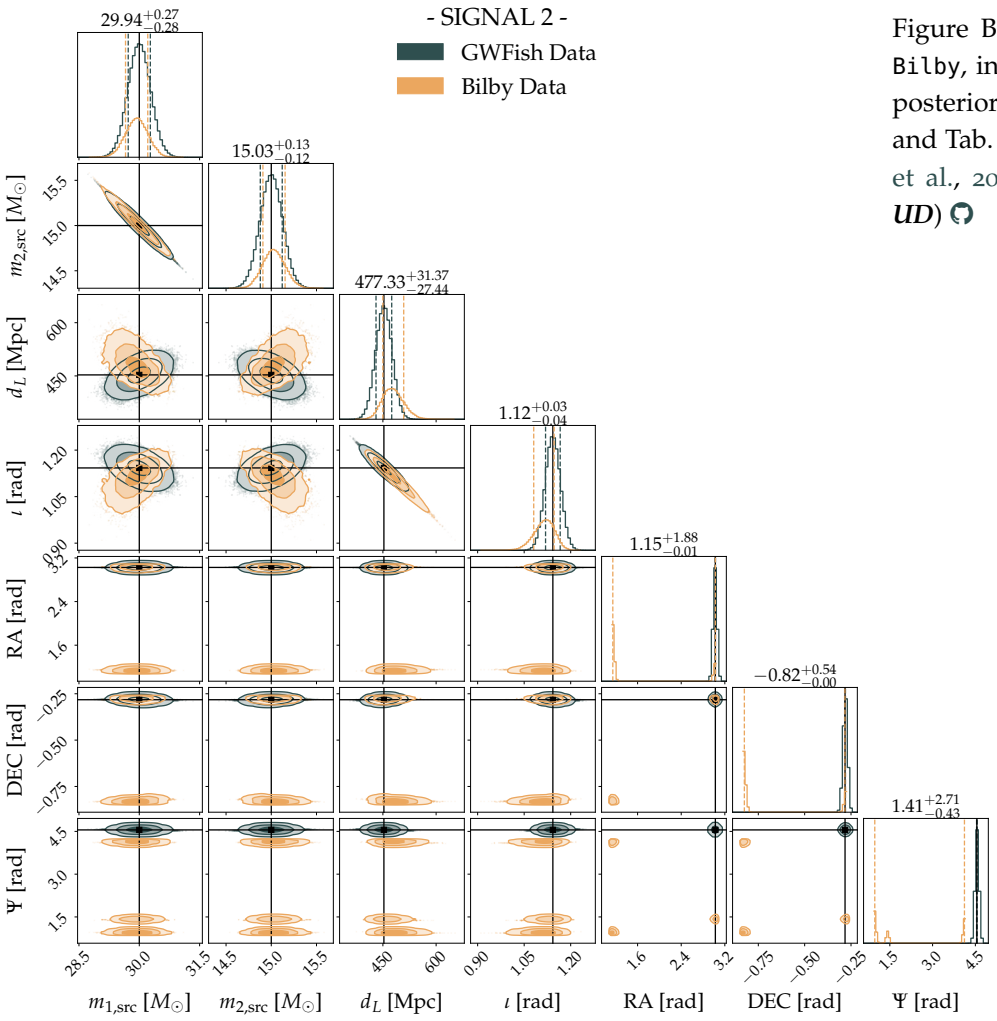

Figure B.2: Corner plot comparing `Bilby`, in *orange*, and `GWFish`, in *teal*, posteriors for Signal 2 (see Tab. 3.1 and Tab. 3.3). Figure from [Dupletsa et al., 2023] (Figure 7, ***authored by UD***)

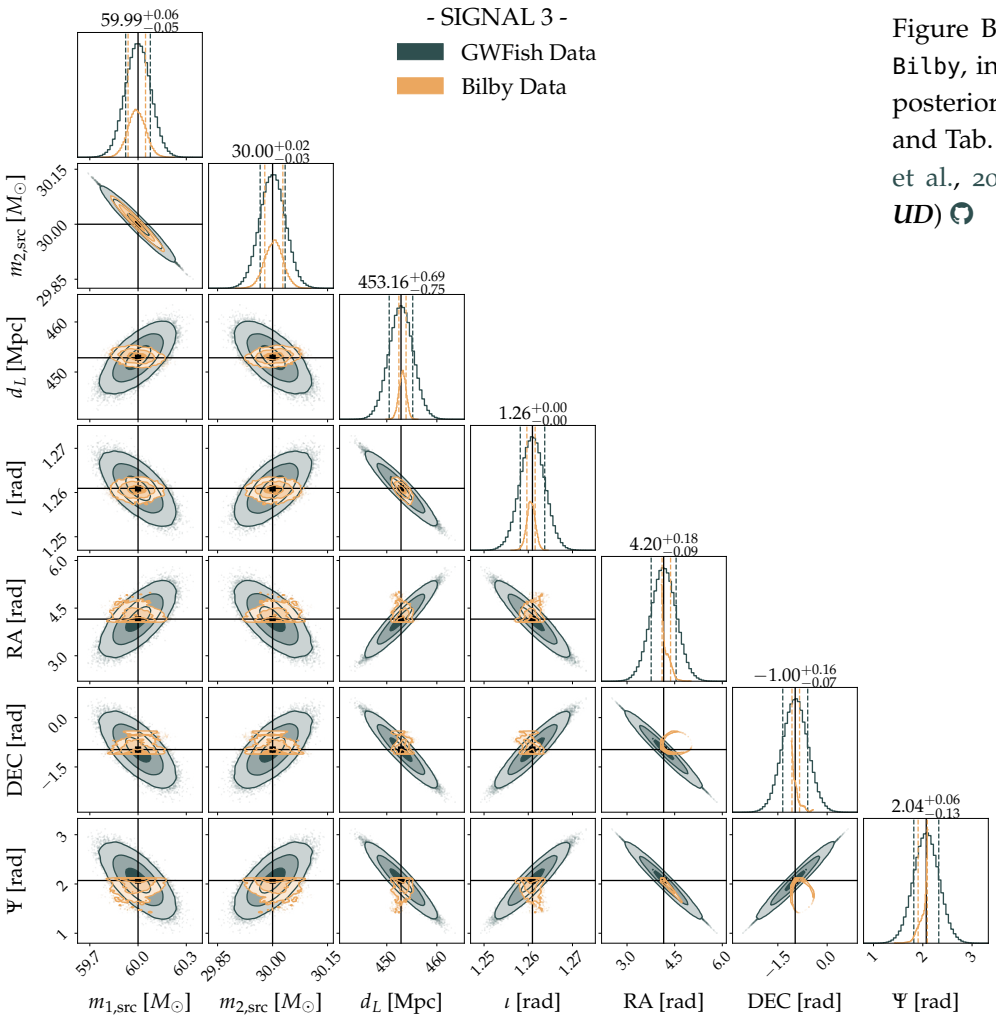

Figure B.3: Corner plot comparing `Bilby`, in *orange*, and `GWFish`, in *teal*, posteriors for Signal 3 (see Tab. 3.1 and Tab. 3.3). Figure from [Dupletsa et al., 2023] (Figure 8, ***authored by UD***)

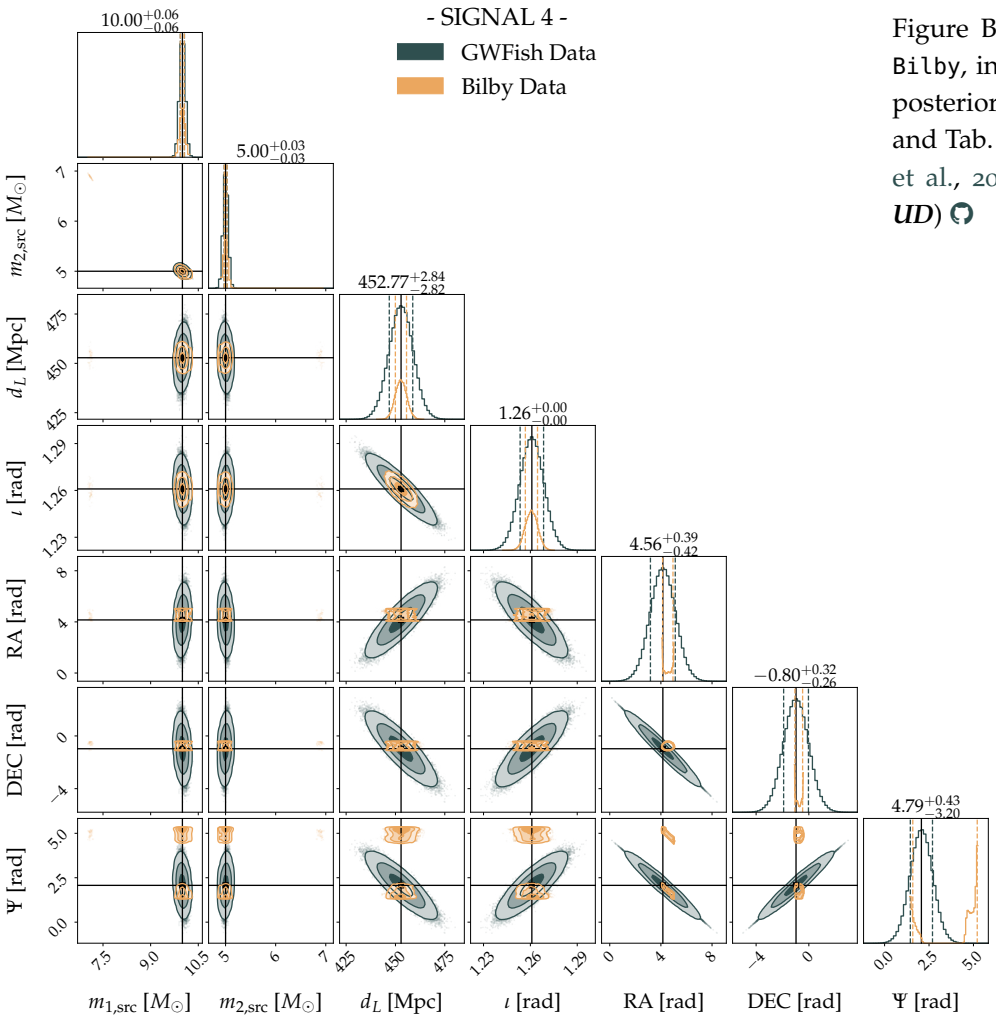

Figure B.4: Corner plot comparing `Bilby`, in *orange*, and `GWFish`, in *teal*, posteriors for Signal 3* (see Tab. 3.1 and Tab. 3.3). Figure from [Dupletsa et al., 2023] (Figure 9, ***authored by UD***)

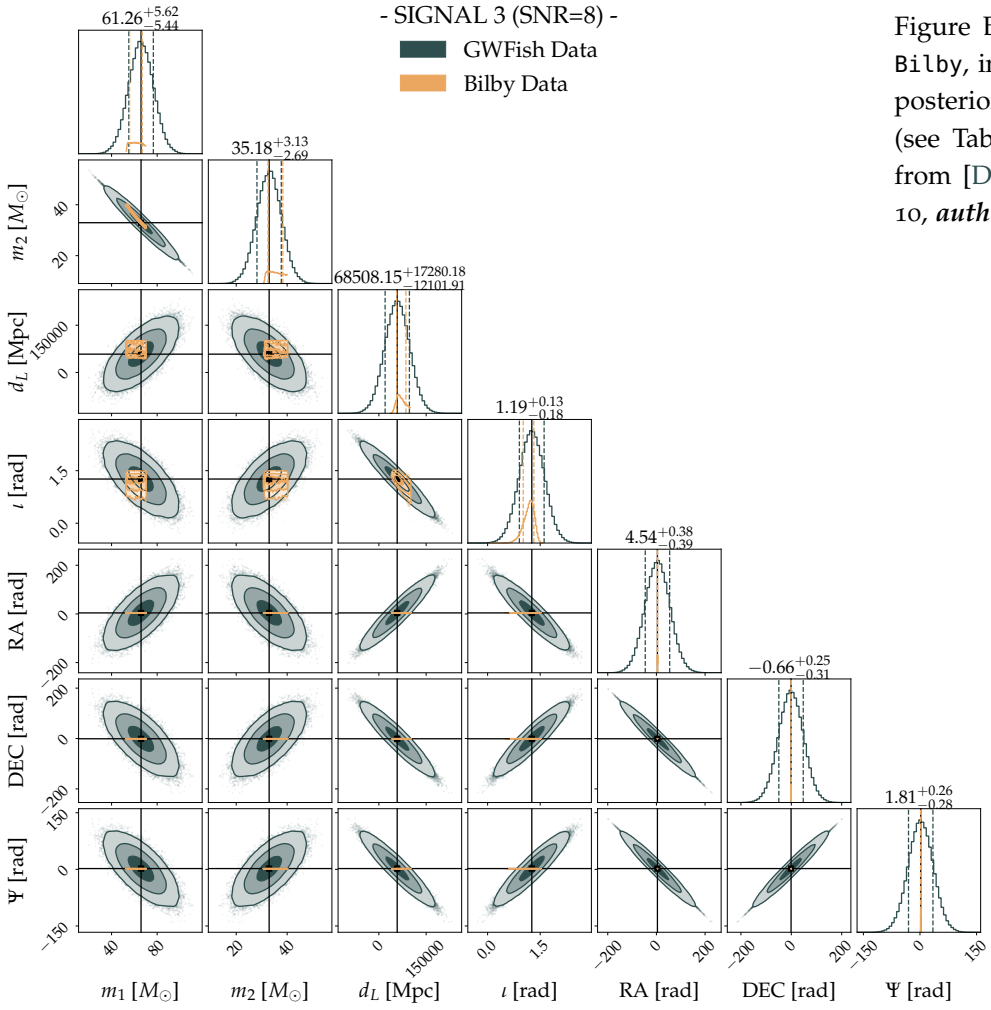

Figure B.5: Corner plot comparing `Bilby`, in *orange*, and `GWFish`, in *teal*, posteriors for Signal 3 at $SNR = 8$ (see Tab. 3.3 and Tab. 3.4). Figure from [Dupletsa et al., 2023] (Figure 10, ***authored by UD***)

B.2 List of GW events from GWTC-3

Table B.1: List of all observed events during the first 3 observing runs by the LVK Collaboration. The runs have been split into 4 parts, highlighted by different shades of blue, and indicating respectively the data-taking subdivision: O1 (3 events), O2 (7 events plus `GW170817`), O3-a (44 events) and O3-b (36 events). For each `EventID` we show if the event is a BBH and, in this case, if it has the analysis with the `IMRPhenomXPHM` waveform approximant. Furthermore, we specify if the official data report the analytic priors used for the analysis. Finally, we show what detectors have seen the event with the SNR of single detectors and of the network (calculated with `GWFish`). The reported SNR value is the median of the values obtained from the analysis over the 30 realizations. The last column signals if the event is included in our analysis (in case not the reason why is specified under the column `Problem`). Table from [Dupletsa et al., 2025] (Table 3, ***authored by UD***)

EventID	BBH	IMRPhenomXPHM	Priors	Network	GWFish SNR detectors → network	Problem	Included
GW150914_095045	✓	✓	✓	[H1, L1]	[19.4, 13.8 → 23.8]	-	✓
GW151012_095443	✓	✓	✓	[H1, L1]	[6.4, 6.0 → 8.7]	-	✓
GW151226_033853	✓	✓	✓	[H1, L1]	[9.5, 7.2 → 11.8]	-	✓
GW170104_101158	✓	✓	✓	[H1, L1]	[8.8, 9.6 → 12.9]	-	✓
GW170608_020116	✓	✓	✗	[H1, L1]	-	no priors	✗
GW170729_185629	✓	✓	✓	[H1, L1]	[5.4, 7.6 → 9.3]	-	✓
GW170809_082821	✓	✓	✓	[H1, L1]	[1.9, 10.2 → 10.5]	-	✓
GW170814_103043	✓	✓	✓	[H1, L1, V1]	[3.4, 13.3, 4.2 → 14.4]	-	✓
GW170818_022509	✓	✓	✓	[H1, L1, V1]	[3.2, 9.2, 4.2 → 10.7]	-	✓
GW170823_131358	✓	✓	✓	[H1, L1]	[6.6, 8.9 → 11.3]	-	✓
GW190403_051519	✓	✓	✓	[H1, L1, V1]	[3.8, 5.1, 1.1 → 6.4]	-	✓
GW190408_181802	✓	✓	✓	[H1, L1, V1]	[9.5, 10.7, 2.6 → 14.6]	-	✓
GW190412_053044	✓	✓	✓	[H1, L1, V1]	[9.9, 15.4, 3.3 → 18.8]	-	✓
GW190413_052954	✓	✓	✓	[H1, L1, V1]	[5.5, 8.8, 1.4 → 10.4]	-	✓
GW190413_134308	✓	✓	✓	[H1, L1, V1]	[4.0, 6.1, 2.1 → 7.7]	-	✓
GW190421_213856	✓	✓	✓	[H1, L1]	[7.5, 6.7 → 10.1]	-	✓
GW190425_081805	✗	-	-	-	-	no BBH	✗
GW190426_190642	✓	✓	✓	[H1, L1, V1]	[2.7, 6.6, 1.4 → 7.3]	-	✓
GW190503_185404	✓	✓	✓	[H1, L1, V1]	[5.7, 7.2, 2.3 → 9.6]	-	✓
GW190512_180714	✓	✓	✓	[H1, L1, V1]	[6.2, 10.1, 1.4 → 12.0]	-	✓
GW190513_205428	✓	✓	✓	[H1, L1, V1]	[7.4, 8.2, 1.8 → 11.3]	-	✓
GW190514_065416	✓	✓	✓	[H1, L1]	[4.5, 5.1 → 6.6]	-	✓
GW190517_055101	✓	✓	✓	[H1, L1, V1]	[4.3, 7.1, 3.4 → 9.2]	-	✓
GW190519_153544	✓	✓	✓	[H1, L1, V1]	[8.4, 12.5, 1.6 → 14.7]	-	✓
GW190521_030229	✓	✓	✓	[H1, L1, V1]	[6.2, 11.6, 1.9 → 13.7]	-	✓
GW190521_074359	✓	✓	✓	[H1, L1]	[11.5, 20.7 → 23.4]	-	✓
GW190527_092055	✓	✓	✓	[H1, L1]	[3.5, 5.2 → 6.8]	-	✓
GW190602_175927	✓	✓	✓	[H1, L1, V1]	[3.0, 9.7, 2.3 → 10.6]	-	✓
GW190620_030421	✓	✓	✓	[L1, V1]	[10.5, 2.3 → 10.7]	-	✓
GW190630_185205	✓	✓	✓	[L1, V1]	[14.4, 5.1 → 15.3]	-	✓
GW190701_203306	✓	✓	✓	[H1, L1, V1]	[4.3, 6.3, 4.3 → 9.0]	-	✓

GW190706_222641	✓	✓	✓	[H1, L1]	[6.3, 7.3 → 9.8]	-	✓
GW190707_093326	✓	✓	✗	[H1, L1]	-	no priors	✗
GW190708_232457	✓	✓	✓	[L1, V1]	[12.5, 2.5 → 12.8]	-	✓
GW190719_215514	✓	✓	✓	[H1, L1]	[4.4, 5.1 → 6.8]	-	✓
GW190720_000836	✓	✓	✗	[H1, L1, V1]	-	no priors	✗
GW190725_174728	✓	✓	✗	[H1, L1, V1]	-	no priors	✗
GW190727_060333	✓	✓	✓	[H1, L1, V1]	[6.8, 8.5, 2.9 → 11.3]	-	✓
GW190728_064510	✓	✓	✗	[H1, L1, V1]	-	no priors	✗
GW190731_140936	✓	✓	✓	[H1, L1]	[4.1, 5.0 → 6.9]	-	✓
GW190803_022701	✓	✓	✓	[H1, L1, V1]	[5.0, 6.0, 1.2 → 7.8]	-	✓
GW190805_211137	✓	✓	✓	[H1, L1, V1]	[3.8, 6.1, < 1 → 7.1]	-	✓
GW190814_211039	✓	✓	✗	[H1, L1, V1]	-	no priors	✗
GW190828_063405	✓	✓	✓	[H1, L1, V1]	[9.5, 11.7, 1.8 → 15.2]	-	✓
GW190828_065509	✓	✓	✓	[H1, L1, V1]	[6.1, 7.0, 1.4 → 9.2]	-	✓
GW190910_112807	✓	✓	✓	[L1, V1]	[13.3, 2.5 → 13.8]	-	✓
GW190915_235702	✓	✓	✓	[H1, L1, V1]	[9.4, 7.5, 2.3 → 12.3]	-	✓
GW190916_200658	✓	✓	✓	[H1, L1, V1]	[4.5, 5.2, 1.1 → 6.9]	-	✓
GW190917_114630	✓	✓	✗	[H1, L1, V1]	-	no priors	✗
GW190924_021846	✓	✓	✗	[H1, L1, V1]	-	no priors	✗
GW190925_232845	✓	✓	✓	[H1, V1]	[6.3, 4.4 → 7.4]	-	✓
GW190926_050336	✓	✓	✓	[H1, L1, V1]	[4.0, 5.0, 1.0 → 6.9]	-	✓
GW190929_012149	✓	✓	✓	[H1, L1, V1]	[5.7, 6.5, < 1 → 8.9]	-	✓
GW190930_133541	✓	✓	✓	[H1, L1]	[3.9, 6.5 → 8.2]	-	✓
GW191103_012549	✓	✓	✓	[H1, L1]	[5.3, 6.0 → 8.0]	-	✓
GW191105_143521	✓	✓	✓	[H1, L1, V1]	[5.2, 7.0, 1.3 → 9.0]	-	✓
GW191109_010717	✓	✓	✓	[H1, L1]	[8.7, 13.1 → 15.6]	-	✓
GW191113_071753	✓	✓	✓	[H1, L1, V1]	[4.1, 5.1, 1.1 → 6.7]	-	✓
GW191126_115259	✓	✓	✓	[H1, L1]	[4.8, 5.8 → 7.5]	-	✓
GW191127_050227	✓	✓	✓	[H1, L1, V1]	[5.9, 6.1, 2.5 → 8.8]	-	✓
GW191129_134029	✓	✓	✓	[H1, L1]	[7.4, 9.7 → 11.9]	-	✓
GW191204_110529	✓	✓	✓	[H1, L1, V1]	[5.3, 6.3 → 8.4]	-	✓
GW191204_171526	✓	✓	✓	[H1, L1]	[9.7, 12.9 → 16.2]	-	✓
GW191215_223052	✓	✓	✓	[H1, L1, V1]	[6.5, 7.9, 1.5 → 10.8]	-	✓
GW191216_213338	✓	✓	✓	[H1, V1]	[16.3, 2.5 → 16.4]	-	✓
GW191219_163120	✗	-	-	-	-	no BBH	✗
GW191222_033537	✓	✓	✓	[H1, L1]	[7.4, 8.7 → 11.4]	-	✓
GW191230_180458	✓	✓	✓	[H1, L1, V1]	[5.5, 6.2, 1.4 → 8.5]	-	✓
GW200105_162426	✗	-	-	-	-	no BBH	✗
GW200112_155838	✓	✓	✓	[L1, V1]	[18.2, 3.4 → 18.6]	-	✓
GW200115_042309	✗	-	-	-	-	no BBH	✗
GW200128_022011	✓	✓	✓	[H1, L1]	[6.7, 7.3 → 9.9]	-	✓
GW200129_065458	✓	✓	✓	[H1, L1, V1]	[13.2, 20.3, 2.9 → 24.7]	-	✓
GW200202_154313	✓	✓	✓	[H1, L1, V1]	[7.7, 8.9, 4.1 → 12.6]	-	✓
GW200208_130117	✓	✓	✓	[H1, L1, V1]	[2.6, 6.9, 4.5 → 8.6]	-	✓
GW200208_222617	✓	✓	✓	[H1, L1, V1]	[4.5, 5.1, 1.2 → 7.0]	-	✓
GW200209_085452	✓	✓	✓	[H1, L1, V1]	[6.3, 5.8, 1.6 → 8.9]	-	✓
GW200210_092254	✓	✓	✓	[H1, L1, V1]	[4.8, 5.9, 1.0 → 7.9]	-	✓
GW200216_220804	✓	✓	✓	[H1, L1, V1]	[5.1, 4.3, 1.6 → 6.9]	-	✓
GW200219_094415	✓	✓	✓	[H1, L1, V1]	[6.2, 7.5, 1.1 → 9.7]	-	✓
GW200220_061928	✓	✓	✓	[H1, L1, V1]	[2.5, 5.2, 1.6 → 5.8]	-	✓
GW200220_124850	✓	✓	✓	[H1, L1]	[5.1, 5.4 → 7.7]	-	✓
GW200224_222234	✓	✓	✓	[H1, L1, V1]	[12.8, 13.3, 4.4 → 19.1]	-	✓
GW200225_060421	✓	✓	✓	[H1, L1]	[8.8, 7.6 → 11.7]	-	✓
GW200302_015811	✓	✓	✓	[H1, V1]	[9.9, 2.5 → 10.1]	-	✓
GW200306_093714	✓	✓	✓	[H1, L1, V1]	[4.8, 4.9, 1.4 → 7.2]	-	✓
GW200308_173609	✓	✓	✓	[H1, L1, V1]	[2.8, 3.5, 1.2 → 4.8]	-	✓
GW200311_115853	✓	✓	✓	[H1, L1, V1]	[10.3, 9.3, 5.6 → 15.0]	-	✓

GW200316_215756	✓	✓	✓	[H1, L1, V1]	$[5.4, 7.3, 2.5 \to 9.4]$	-	✓
GW200322_091133	✓	✓	✓	[H1, L1, V1]	$[2.5, 2.1, < 1 \to 3.6]$	-	✓

B.3 Prior selection in GW analysis

B.3.1 `Uniform Prior`: the uninformative choice

Most of the parameters characterizing a GW event (see Tab. 3.7) have an uninformative uniform prior, meaning that given a physical range of the parameter, any value in the interval is equally probable. The probability density for a uniform distribution is given by:

$$\pi(\theta) = \frac{1}{\theta_{\max} - \theta_{\min}} \tag{B.1}$$

where $[\theta_{\min}, \theta_{\max}]$ is the range of the parameter θ. The probability density is zero outside this interval, meaning values out of range are excluded from consideration. Choosing this prior implies that no prior knowledge favours one value over another within the interval.

$\mathcal{M}_c$ and q: `Uniform in component masses prior` LVK analyses assume a uniform in component masses prior, meaning that the joint probability on m_1 and m_2, $\pi(m_1, m_2)$, is constant. Since we are getting likelihood samples in $\mathcal{M}_{\text{chirp}}$ and q, it is necessary to reweight these samples by the determinant of the Jacobian transformation to component masses. This ensures that the probability remains uniform in the m_1-m_2 plane:

$$\pi(\mathcal{M}_{\text{chirp}}, q) = \pi(m_1, m_2)|J|, \tag{B.2}$$

where the following transformation matrix gives J, the Jacobian:

$$J = \begin{pmatrix} \frac{\partial m_1}{\partial \mathcal{M}_{\text{chirp}}} & \frac{\partial m_1}{\partial q} \\ \frac{\partial m_2}{\partial \mathcal{M}_{\text{chirp}}} & \frac{\partial m_2}{\partial q} \end{pmatrix}. \tag{B.3}$$

The determinant of the Jacobian, J, is:

$$|J| = \mathcal{M}_{\text{chirp}} q^{-6/5} (1+q)^{2/5} \tag{B.4}$$

given that:

$$\begin{cases} m_1 &= \mathcal{M}_{\text{chirp}} q^{-3/5} (1+q)^{1/5} \\ m_2 &= \mathcal{M}_{\text{chirp}} q^{2/5} (1+q)^{1/5} \end{cases} \tag{B.5}$$

Fig. B.6 shows how the distribution on the mass-plane changes if we go from a joint prior that is uniform in $\mathcal{M}$ and q (the *left* plots in both the *upper* and *lower* panels) to a joint prior that is uniform in m_1 and m_2 (the corresponding plots on the *right*).

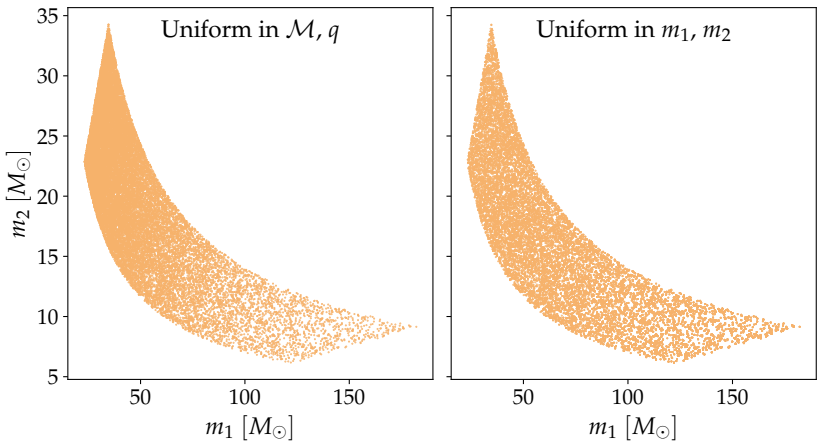

(a) m_1-m_2 plane.

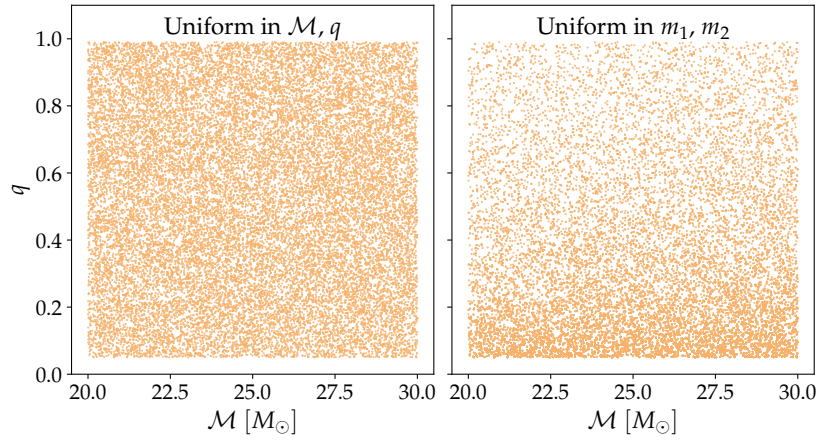

(b) $\mathcal{M}$-q plane.

Figure B.6: The *upper* panel shows the m_1-m_2 plane and, from left to right, highlights how the distribution changes going from a uniform in $\mathcal{M}$ and q prior to a uniform in m_1 and m_2 prior. The same is shown in the *lower* panel, but in the $\mathcal{M}$-q plane

B.3.2 *Angular parameters:* `Uniform on a Sphere` *prior*

While a `Uniform` prior might be the unbiased choice in many contexts, we must consider the spherical geometry when dealing with angular parameters describing positions on a sphere. To ensure a uniform distribution on a sphere, thus isotropy, of certain angular parameters, the right priors are the ones that are uniform in either `Sine` or `Cosine`, depending on the physical range of the angular parameter in consideration.

`RA` and `DEC`: a reference example We choose two well-known parameters to explain how angular priors work: the position in the sky given by `RA` and `DEC` (see Fig. 1.11). The azimuthal angle `RA` ranges in $[0, 2\pi]$ with the zero reference given by the meridian passing through the vernal equinox. The polar angle `DEC` ranges in $[-\pi/2, +\pi/2]$, with zero value at the equator, positive values above and negative below. A uniform

distribution on a sphere implies an equal probability of finding an object for any region on the sphere of equal area. This differs from individually considering a uniform distribution for RA and DEC. The reason is that lines of constant DEC, for example, are circles of different sizes, the ones near the pole smaller than the ones near the equator. A uniform prior in DEC would lead to a higher concentration of points near the poles.

The correct approach is to consider the area element on the sphere:

$$\begin{aligned} dA &= \sin\left(\frac{\pi}{2} - \mathtt{DEC}\right) \mathrm{d}\mathtt{DEC}\mathrm{d}\mathtt{RA} \\ &= \cos(\mathtt{DEC})\mathrm{d}\mathtt{DEC}\mathrm{d}\mathtt{RA} \\ &= \mathrm{d}\sin(\mathtt{DEC})\mathrm{d}\mathtt{RA} \end{aligned} \tag{B.6}$$

where we have accounted for the fact that DEC is not measured starting from the north pole. From Eq. B.6, we can see that if RA is uniformly distributed in $[0, 2\pi]$, for DEC the distribution is uniform in Sine(DEC):

$$\pi(\sin(\mathtt{DEC})) \propto \text{const} \tag{B.7}$$

where the constant can be found by integrating in the DEC range and obtaining const $= 1/2$. We can change variable and directly obtain the prior probability density for declination angle parameter:

$$\begin{aligned} \pi(\mathtt{DEC}) &= \pi(\sin(\mathtt{DEC})) \left| \frac{\mathrm{d}\sin(\mathtt{DEC})}{\mathrm{d}\mathtt{DEC}} \right| \\ &= \frac{1}{2}\cos(\mathtt{DEC}) \quad \text{for} \quad -\frac{\pi}{2} \leq \mathtt{DEC} \leq +\frac{\pi}{2} \end{aligned} \tag{B.8}$$

Angular priors in synthesis In general, azimuthal angles, like RA, follow a uniform distribution in $[0, 2\pi]$. This holds for the phase ϕ, the spin parameters $\mathtt{phi}_{12}$ and $\mathtt{phi}_{JL}$, and the polarization angle Ψ. The prior on the polarization angle Ψ, though, is uniform in $[0, \pi]$. The range is not $[0, 2\pi]$ due to the symmetry of the two GW polarizations, h_+ and $h_\times$. In fact, rotating the polarizations by π does not affect the physical configuration of the system, as the polarization angle enters the signal as $\sin(2\Psi)$ or $\cos(2\Psi)$. Taking the range of the polarization angle to be between $[0, \pi]$ allows to avoid redundancy in parameter space, which is particularly useful in Bayesian analysis.

The dependence on the polarization angle enters the antenna pattern functions:

$$\begin{aligned} F_+(\mathtt{RA}, \mathtt{DEC}, \Psi) &= F_{+,0}(\mathtt{RA}, \mathtt{DEC})\cos(2\Psi) \\ &\quad - F_{\times,0}(\mathtt{RA}, \mathtt{DEC})\sin(2\Psi) \\ F_\times(\mathtt{RA}, \mathtt{DEC}, \Psi) &= F_{+,0}(\mathtt{RA}, \mathtt{DEC})\sin(2\Psi) \\ &\quad + F_{\times,0}(\mathtt{RA}, \mathtt{DEC})\cos(2\Psi) \end{aligned}$$

where the $F_{+,0}(\mathtt{RA}, \mathtt{DEC}), F_{\times,0}(\mathtt{RA}, \mathtt{DEC})$ are the detector's response to the plus and cross polarizations depending only on the sky position of the source.

The parameters θ_{JN}, $\mathtt{tilt}_1$ and $\mathtt{tilt}_2$, instead, follow a zenith-like angular distribution as DEC. All three are uniformly distributed on the sphere in the range $[0, \pi]$. This means their Cosine is uniformly distributed. For example, the prior distribution for the θ_{JN} parameter is given by:

$$\pi(\theta_{JN}) = \frac{1}{2}\sin(\theta_{JN}) \quad \text{for} \quad 0 \leq \theta_{JN} \leq \pi \tag{B.9}$$

which can be obtained in a analogous way as Eq. B.8 starting from $p(\cos(\mathtt{DEC})) \propto \text{const}$.

For a comprehensive visualization of the angles refer to Fig. 1.11 and Fig. 1.10, and to Tab. 1.1.

B.3.3 Luminosity distance

The prior for the luminosity distance parameter varies according to different assumptions about the distribution of sources in the Universe. In the following, we will explore some common choices.

`Power Law` In our comparison with LVK data, we used the `Power Law` prior for the luminosity distance, given by:

$$\pi(d_L) \propto d_L^2 \tag{B.10}$$

This choice implies that the number of GW sources is proportional to the volume, assuming a uniform distribution of sources in space without considering any redshift evolution. Since the volume of space scales with the square of the distance ($\mathrm{d}V = 4\pi d_L^2 \mathrm{d}d_L$), the probability density function is proportional to the square of the source distance. The distance we consider here is the distance we measure, i.e. the luminosity distance.

Choosing this prior assumes that farther events are more likely simply because they cover a larger volume, without accounting for the expansion of the Universe.

`Uniform in Comoving Volume` If we want to account for the expansion of the Universe, then we should choose the uniform in comoving volume prior:

$$\pi(d_L) \propto \frac{\mathrm{d}V_c}{\mathrm{d}d_L} = \frac{\mathrm{d}V_c}{\mathrm{d}z}\frac{\mathrm{d}z}{\mathrm{d}d_L} \tag{B.11}$$

where we have made explicit the redshift dependence for easier calculations (see also Eq. B.15). For the derivative redshift with respect to luminosity distance we compute the inverse, which is easier:

$$\frac{\mathrm{d}d_L}{\mathrm{d}z} = \frac{d_L}{1+z} + \frac{H_0}{c}\frac{1+z}{H(z)} \tag{B.12}$$

where

$$d_L = \frac{H_0}{c}(1+z)\int_0^z \frac{\mathrm{d}z'}{H(z')} \tag{B.13}$$

and

$$H(z) = \sqrt{(1+z)^3\Omega_\mathrm{m} + \Omega_\Lambda} \tag{B.14}$$

with Ω_m and Ω_Λ being the dimensionless matter and dark energy densities in the ΛCDM framework.

Eq. B.11 takes into account the geometry and the expansion of the Universe. A `Uniform in Comoving Volume` prior favors redshifts where larger volumes are available, in accordance with the cosmological principle of a homogeneous and isotropic Universe.

Uniform in Source-Frame Time Furthermore, if we want to assume a constant event rate per unit of time in the source frame, then we have to adjust for the shifting of source frame time:

$$\pi(d_L) \propto \frac{1}{1+z}\frac{\mathrm{d}V_c}{\mathrm{d}d_L} = \frac{1}{1+z}\frac{\mathrm{d}V_c}{\mathrm{d}z}\frac{\mathrm{d}z}{\mathrm{d}d_L} \tag{B.15}$$

The $(1+z)$ factor accounts for the time dilation when passing from source to detector frame:

$$\frac{\mathrm{d}t_{\text{source}}}{\mathrm{d}t_{\text{detector}}} = \frac{1}{1+z} \tag{B.16}$$

This prior ensures a uniform event rate in the source frame.

C. Supplements to Chapter 4

C.1 Gravitational results: supplementary plots

Table C.1: Detectors list used for joint ET and KN analyses and their main characteristics. Table adapted from [Loffredo et al., 2025] (Table B.1, ***authored by UD***)

IFO name	**Length** [km]	**Country**	**Lat** [deg]	**Lon** [deg]	**f_min** [Hz]	**Sensitivity curve**
ET-Δ	10	Italy	$40+31/60$	$9+25/60$	2	ET-cryo-10 km
ET-L1	15	Italy	$40+31/60$	$9+25/60$	2	ET-cryo-15 km
ET-L2	15	Netherlands	$50+43/60$	$5+55/60$	2	ET-cryo-15 km
CE1	40	USA	$46+30/60$	$-119+24/60$	8	CE
CE2	40	Australia	$-25+30/60$	$152+4/60$	8	CE
LHO	4	USA	$46+28/60$	$-119-24/60$	8	A-Plus (O5)
LLO	4	USA	$30+34/60$	$-90-46/60$	8	A-Plus (O5)
Virgo	3	Italy	$43+36/60$	$10+30/60$	8	AdV-Plus (O5)
LIGO-India	4	India	$19+37/60$	$77+2/60$	8	A-Plus (O5)
KAGRA	3	Japan	$36+25/60$	$137+18/60$	8	KAGRA (O5)

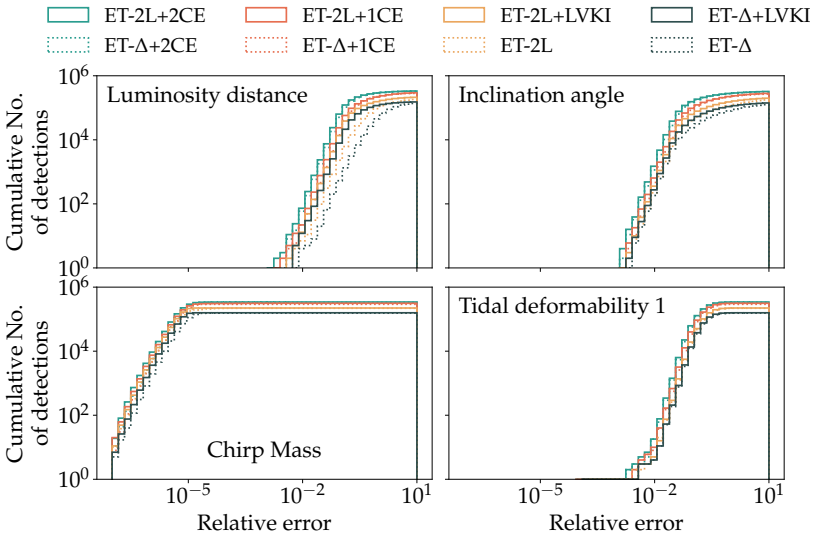

(a) BLh Gaussian, $\alpha = 1.0$

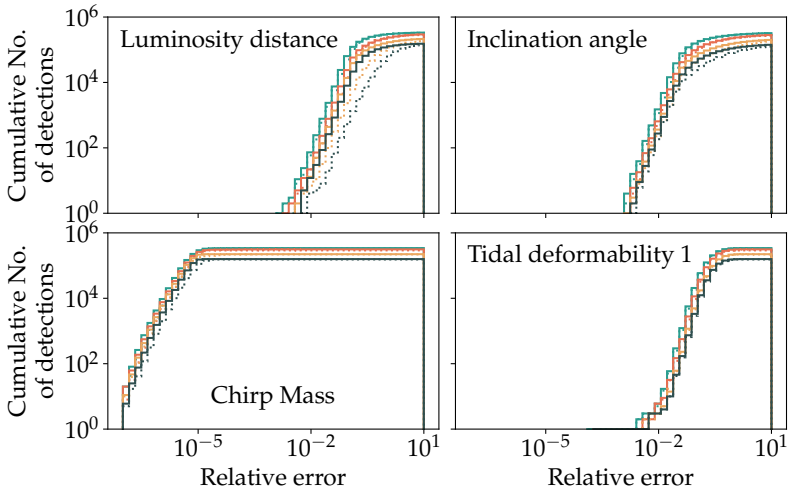

(b) APR4 Gaussian, $\alpha = 1.0$

Figure C.1: PE for a subset of parameters, namely luminosity distance, inclination angle, primary component mass, and tidal deformability of the primary component, for the Gaussian mass distribution of the fiducial population with `BLh` EoS in the *top* panel, and `APR4` EoS in the *bottom* one. We show the relative errors on the parameters on x-axis, and the cumulative number of detections on the y-axis. Different colors indicate different networks. Same color and linestyle schemes as in Fig. 4.9 apply. Figure from [Loffredo et al., 2025] (Figure D5, ***authored by UD***)

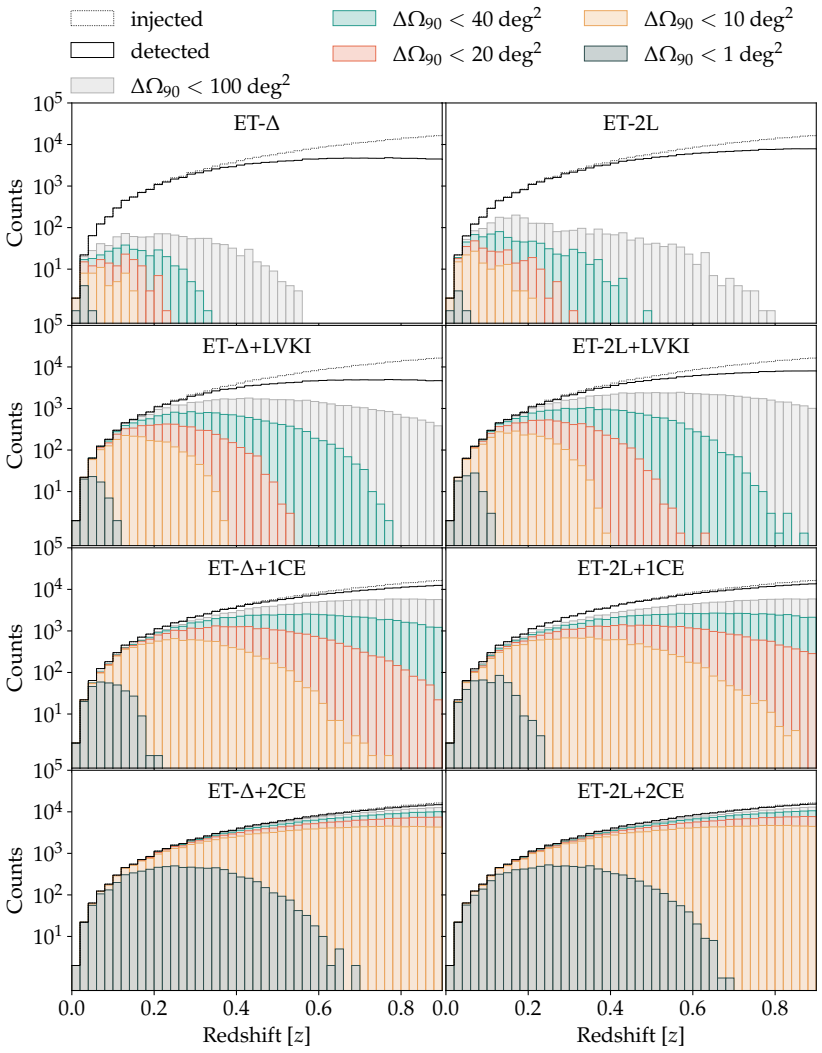

Figure C.2: Number of injected events and events localized better than $100\,\mathrm{deg}^2$, $40\,\mathrm{deg}^2$, $20\,\mathrm{deg}^2$, $10\,\mathrm{deg}^2$, and $1\,\mathrm{deg}^2$ by the different detector networks considered in this work for the fiducial population obtained assuming the `BLh` EoS and Gaussian NS mass distribution. The left plots show ET-Δ, and the right plots ET-2L. Figure adapted from [Lofredo et al., 2025] (Figure D2, ***authored by UD***)

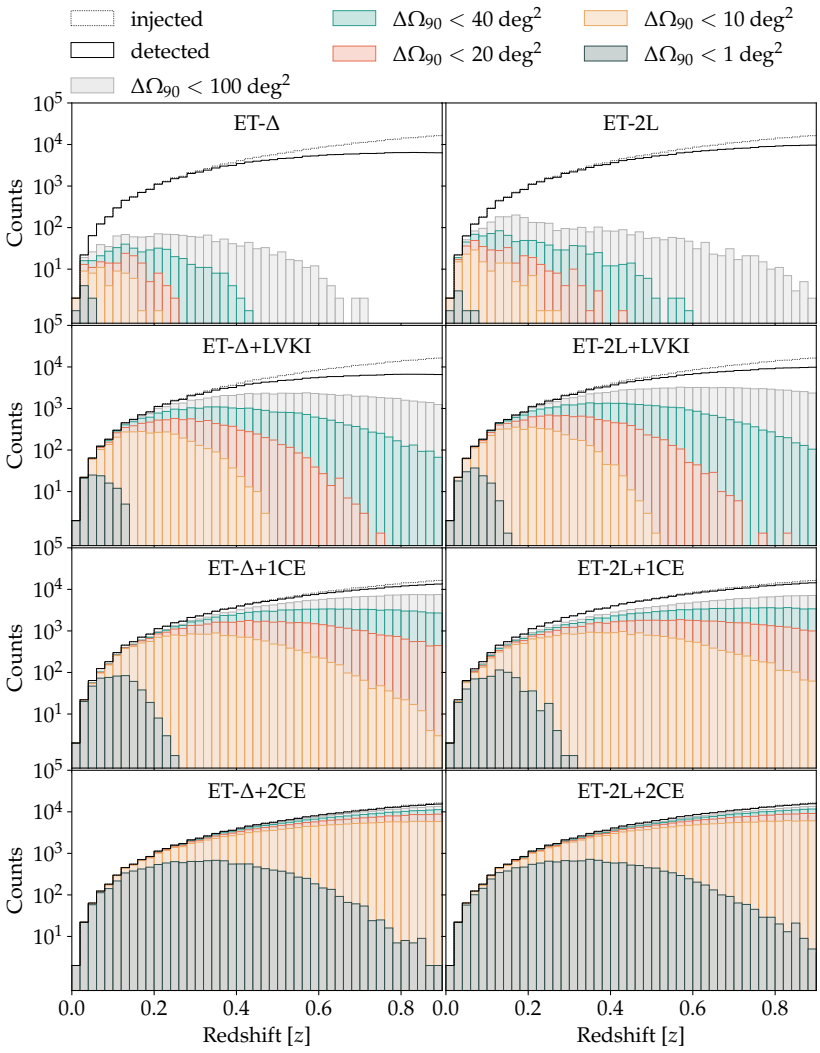

Figure C.3: Number of injected events and events localized better than $100\,\mathrm{deg}^2$, $40\,\mathrm{deg}^2$, $20\,\mathrm{deg}^2$, $10\,\mathrm{deg}^2$, and $1\,\mathrm{deg}^2$ by the different detector networks considered in this work for the fiducial population obtained assuming the `APR4` EoS and uniform NS mass distribution. The left plots show ET-Δ, and the right plots ET-2L. Figure adapted from [Lofredo et al., 2025] (Figure D3, ***authored by UD***)

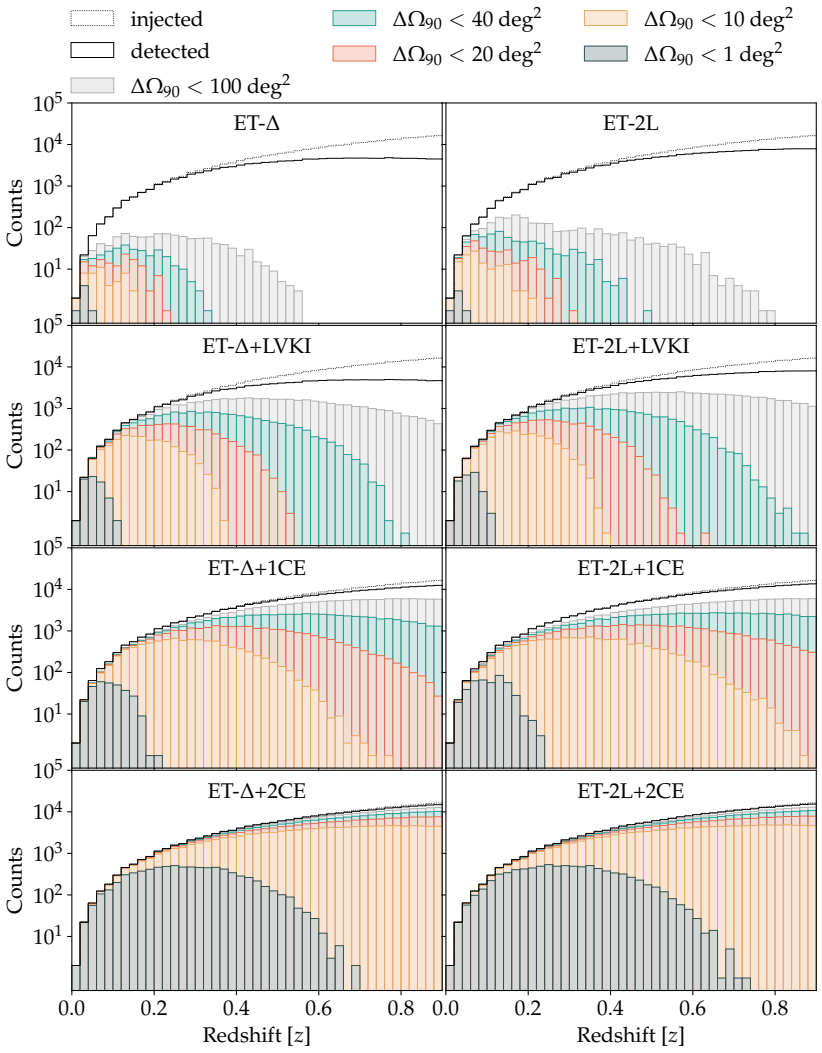

Figure C.4: Number of injected events and events localized better than $100\,\mathrm{deg}^2$, $40\,\mathrm{deg}^2$, $20\,\mathrm{deg}^2$, $10\,\mathrm{deg}^2$, and $1\,\mathrm{deg}^2$ by the different detector networks considered in this work for the fiducial population obtained assuming the `APR4` EoS and Gaussian NS mass distribution. The left plots show ET-Δ, and the right plots ET-2L. Figure adapted from [Lofredo et al., 2025] (Figure D4, ***authored by UD***)

D. Supplements to Chapter 5

D.1 General derivation of the shot noise term

The shot noise term arises when we observe a discrete number of sources that describe an underlying continuous distribution. In general, the more sources we observe, the more accurately we can approximate the continuous field, which in turn reduces the contribution of shot noise. In this section, we derive the shot noise contribution to the angular power spectrum as entered in $C_\ell^{\rm obs} = C_\ell^{\rm true} + C_\ell^{\rm shot}$.

As in the main Chapter 5, we pinpoint dark matter (DM) halos, as our discrete sources. The distribution of the number of halos in the sky fluctuates around a mean value. The number count fluctuation of DM halos can be expanded in spherical harmonics as follows:

$$\delta n(\Omega) = \frac{n(\Omega) - \bar{n}_{\rm sky}}{\bar{n}_{\rm sky}} = \sum_{\ell=0}^{\infty} \sum_{m=-\ell}^{\ell} a_{\ell m} Y_{\ell m}(\Omega), \tag{D.1}$$

where $\delta n(\Omega)$ represents the fluctuations of the halo number, e.g. in a given pixel, $n(\Omega)$ is the observed number of halos in the pixel, and $\bar{n}_{\rm sky}$ is the average number density count[1], given by:

$$\bar{n}_{\rm sky} = \frac{N}{4\pi}. \tag{D.2}$$

[1] Since, numerically, we are dealing with a discretization of the sky area, represented by a certain number of pixels, the quantity that enters the calculations is $N/n_{\rm pix}$, where $n_{\rm pix}$ represents the total number of pixels.

Conversely the harmonic coefficients a_{lm} can be written as:

$$\begin{aligned} a_{\ell m} &= \int_{\rm sky} \delta n(\Omega) Y^*_{\ell m}(\Omega) d\Omega \\ &= \frac{1}{\bar{n}_{\rm sky}} \int_{\rm sky} \left[n(\Omega) - \bar{n}_{\rm sky} \right] Y^*_{\ell m}(\Omega) d\Omega, \end{aligned} \tag{D.3}$$

where Y^*_{lm} represents the complex conjugate of the spherical harmonics, and we used Eq. D.1 to pass from the first to the second line.

We can separate the two terms:

$$a_{\ell m} = \frac{1}{\bar{n}_{\rm sky}} \int_{\rm sky} n(\Omega) Y^*_{\ell m}(\Omega) d\Omega - \frac{1}{\bar{n}_{\rm sky}} \int_{\rm sky} \bar{n}_{\rm sky} Y^*_{\ell m}(\Omega) d\Omega, \tag{D.4}$$

where we can ignore the second term as it just contributes with a constant for $\ell = 0$ (no deviations from the expected average of number

counts) and is zero otherwise, following from the well-known property of spherical harmonics:

$$\int_{\rm sky} Y_{\ell m}(\Omega) d\Omega = \sqrt{4\pi}\delta_{\ell,0}\delta_{m,0}. \tag{D.5}$$

We want to focus on fluctuations instead. Therefore:

$$a_{\ell m} = \frac{1}{\bar{n}_{\rm sky}} \int_{\rm sky} n(\Omega) Y^*_{\ell m}(\Omega) d\Omega \tag{D.6}$$

and we can write the number density of halos as a double (representing the `RA` and `DEC` position in the sky) Dirac delta function sum over the single contributions:

$$n(\Omega) = \sum_i^N \delta_D^2(\Omega - \Omega_i) \tag{D.7}$$

Substituting Eq. (D.7) in Eq. (D.6), we get:

$$a_{\ell m} = \frac{1}{\bar{n}_{\rm sky}} \sum_i^N Y^*_{\ell m}(\Omega_i) \tag{D.8}$$

Our goal is to compute the variance of the $a_{\ell m}$ coefficients:

$$\langle |a_{\ell m}|^2 \rangle = \frac{1}{\bar{n}^2_{\rm sky}} \sum_i^N \langle |Y_{\ell m}(\Omega_i)|^2 \rangle \tag{D.9}$$

Since each halo position is independent of the others and equally probable, we can write:

$$\sum_i^N \langle |Y_{\ell m}(\Omega_i)|^2 \rangle = \frac{N}{4\pi} \tag{D.10}$$

Therefore, given that $\bar{n}_{\rm sky} = N/4\pi$:

$$C_\ell^{\rm shot} = \langle |a_{\ell m}|^2 \rangle = \frac{4\pi}{N} \tag{D.11}$$

which is the expression we provide in Eq. (5.18).

List of Figures

List of Tables

Acronyms

ΛCDM Λ Cold Dark Matter. 9–14, 47, 126, 127, 129, 130, 135

ApJ Astrophysical Journal. 37

ASD Amplitude Spectral Density. 101, 102, 113

BAO Baryonic Acoustic Oscillations. 12, 130, 133

BBH Binary Black Hole. 20–22, 27–29, 33, 38–40, 45, 49–52, 54, 58, 76, 78, 81–84, 89, 90, 97, 99, 100, 125, 126, 130, 140, 146, 162, VI

BBHs Binary Black Holes. 15, 19, 21, 28, 33, 38–40, 57, 58, 77, 78, 81, 84, 125, 130, 135, 141, XIII

BBN Big Bang Nucleosynthesis. 12

BH black hole. 14, 19, 22, 27–29, 31, 39, 45, 49, 59, 110, 145, V

BHs black holes. 14, 19, 20, 28, 29, 31, 33, 39, 47, 49, 54, 58–61, 135, 146, V

BNS Binary Neutron Star. 25, 27–29, 32, 76, 77, 81–83, 85–87, 99–114, 116, 117, 120–129, 146, VI, XII, XIII

BNSs Binary Neutron Stars. 15, 19, 28, 38, 81, 83, 85, 86, 99, 104, 107, 110

CBC compact binary coalescence. 18, 19, 23, 24, 26, 28, 29, 42, 59, 100, 142, 145, XI

CBCs compact binary coalescences. 15, 18, 21, 27, 30, 31, 38, 39, 59, 60, 62, 125, 145–147, V

CE Cosmic Explorer. 15, 22, 29, 66, 71, 72, 77, 85, 110, 113, 114, 116, 117, 129

CMB Cosmic Microwave Background. 6, 9–14, 38, 127, 134

CTA Cherenkov Telescope Array. 86, 102, 107

DE dark energy. 10, 32, 126, 127, 130, 135

DED dark energy domination. 10

DEMNUni Dark Energy and Massive Neutrino Universe. 135, 137, 138, 143, 144

DESI Dark Energy Spectroscopic Instrument. 127

DM dark matter. 9–12, 33, 131, 132, 134–136, 138–142, 144, 175, XIII

ELT Extremely Large Telescope. 102, 110

EM electromagnetic. 15, 27, 38, 99, 101–104, 106–108, 110, 112, 120, 122, 126, 131, 147, VI

EOB Effective-One-Body. 74

EoS Equation of State. 9, 24, 32, 74, 86, 99, 101, 103, 109–122, 127, 135, 147, 170–173, XII, XIII

EoSs Equations of State. 112

ET Einstein Telescope. 15, 22, 29–34, 65, 66, 71, 73, 76–79, 81–86, 94, 97, 99–104, 106–110, 113–117, 119, 120, 122, 125, 126, 129, 130, 135, 141, 146, 147, 169, V, VI, XII

FAR False Alarm Rate. 28, 59

FLRW Friedmann-Lemaitre-Robertson-Walker. 6–8

FoF Friends-of-Friends. 135

FoV field of view. 106, 121

GP Gaussian Process. 126, 127, 130

GR General Relativity. 8, 14, 15, 23

GRB Gamma Ray Burst. 15, 32, 103, 106, 110, 111, 120, 125–130, 147, VI, XIII

GRBs Gamma Ray Bursts. 103, 107, 121, 125–128, 147

GW gravitational wave. 5, 14, 15, 17–25, 27, 29–34, 37, 38, 40–47, 49, 52–55, 57, 62, 65–68, 71–73, 76, 77, 81, 83–90, 100, 102–104, 107–114, 116–118, 120–122, 125, 126, 128–130, 135, 140–147, 149, 154, 155, 162, 164, V, VI, XI–XIII

GWs Gravitational waves. 14–19, 21–23, 38, 44, 53, 103, 125, 126, 130, 135, 139, 141–145, 147, 154

GWs gravitational waves. 37, V

GWTC Gravitational-Wave Transient Catalogue. 27, 40, 59–61, 65, 66, 77, 84, 93, 162, XI, XII

HBI Hierarchical Bayesian Inference. 31, 37, 39–43, 45, 46, 49, 51–53, 61, 141, 142, 144, 145, V, XI

HDI highest density interval. 49, 50

HF High-Frequency. 99–102, XII

HI neutral hydrogen. 33, 125, 126, 130, 131, 135, 140–144, VI, XIII

HR-DEMNUni High-Resolution Dark Energy and Massive Neutrino Universe. 135

IM intensity mapping. 125, 126, 130, 131, 135, 143, XIII

IMBH Intermediate Mass Black Hole. 28, 29, 85, 86

ISB Instrumental Science Board. 101

JCAP Journal of Cosmology and Astroparticle Physics. 125

JWST James Webb Space Telescope. 102

KAGRA Kamioka Gravitational Wave Detector. 15, 27, 65

KDE kernel density estimator. 128

KN kilonova. 15, 32, 99, 101, 103, 107, 109–112, 120–122, 127, 147, 169, VI, XIII

KNe kilonovae. 103, 107, 108, 120, 121, 147

LF Low-Frequency. 99–102, 106–109, XII

LGWA Lunar Gravitational Wave Antenna. 22, 29, 66, 71, 72

LIGO Laser Interferometer Gravitational-wave Observatory. 14, 15, 22, 27, 65, 85, 113, 115, 129

LIGO-India Laser Interferometer Gravitational-wave Observatory India. 15

LISA Laser Interferometer Space Antenna. 22, 29, 66, 71, 72, 77, 85, 86, XII

LSA linear signal approximation. 68–70, XII

LSS large scale structure. 33, 126, 130, 131, 144, 147, VI

LVK LIGO-Virgo-KAGRA. 27, 28, 31, 34, 37, 39, 45, 47, 59–62, 87, 89–94, 96, 104, 109–112, 129, 145, 162, 164, 183, V, VI

LVKI LIGO-Virgo-KAGRA-LIGO India. 71, 113–117, 129

MCMC Markov Chain Monte Carlo. 67, 128

MD matter domination. 9, 10, 12

MDC `Mock Data Challenge`. 31, 37, 39, 40, 44–46, 49, 58, 145, XII

ML machine learning. 127

MLE Maximum Likelihood Estimator. 69, 71

MM multi-messenger. 15, 29–32, 34, 86, 87, 99–103, 107, 109, 120–122, 130, 145–147, V, VI, XIII

NR Numerical Relativity. 74

NS neutron star. 14, 19, 22, 24, 29, 32, 59, 61, 66, 74, 101, 104, 109–112, 116–118, 120, 122, 127, 147, 171–173, VI

NSBH Neutron Star - Black hole. 28, 100, 102, 127

NSBHs Neutron Star - Black holes. 15, 19, 28, 38, 84

NSs neutron stars. 15, 19, 24, 25, 31, 39, 59–61, 103, 104, 111, 146, V

OSB Observational Science Board. 32, 65, 66, 100, 147

PE parameter estimation. 26, 29, 40, 44, 66, 71, 73–83, 97, 99–101, 103, 104, 109, 111, 119, 120, 128, 130, 141, 144, 146, 147, 170, V, VI, XII

PEDE Phenomenological Emergent Dark Energy. 126, 127, 129, 130

PISN pulsational pair instability supernova. 39, 40

PL Power Law. 39, 47–49

PN Post-Newtonian. 23, 73, 74

PSD Power Spectral Density. 22, 72, 76

RD radiation domination. 10

SKA-Mid SKA-Mid. 126, 131, 135

SKAO SKA Observatory. 33, 102, 125, 126, 147

SN supernova. 19, 20, 112

SNe supernovae. 12, 13, 37, 38, 127, 130, V

SNR Signal-to-Noise Ratio. 25, 26, 28, 29, 32, 46, 69–71, 76–84, 88, 91, 93–96, 103, 114, 116, 118, 129, 131, 146, 162, V, XII

SNRs Signal-to-Noise Ratios. 114

TDI Time Delay Interferometry. 72

ToO target-of-opportunity. 121

TT Transverse-Traceless. 16, 17

UV ultra-violet. 103

WST Wide-field Spectroscopic Telescope. 102, 110

XG next-generation. 15, 28, 29, 31, 34, 65–67, 74, 97, 99, 109–111, 113, 114, 116, 117, 120–122, 125, 129, 130, 145–147, V, VI, XII, XIII

Bibliography

Aasi, J. et al. (2015). Advanced LIGO. *Class. Quant. Grav. 32*, 074001.

Abac, A. et al. (2025, 3). The Science of the Einstein Telescope.

Abbott, B. et al. (2019a). Binary Black Hole Population Properties Inferred from the First and Second Observing Runs of Advanced LIGO and Advanced Virgo. *Astrophys. J. Lett. 882*(2), L24.

Abbott, B. P. et al. (2009). LIGO: The Laser interferometer gravitational-wave observatory. *Rept. Prog. Phys. 72*, 076901.

Abbott, B. P. et al. (2016a). Binary Black Hole Mergers in the first Advanced LIGO Observing Run. *Phys. Rev. X 6*(4), 041015. [Erratum: Phys.Rev.X 8, 039903 (2018)].

Abbott, B. P. et al. (2016b). GW150914: First results from the search for binary black hole coalescence with Advanced LIGO. *Phys. Rev. D 93*(12), 122003.

Abbott, B. P. et al. (2017a). A gravitational-wave standard siren measurement of the Hubble constant. *Nature 551*(7678), 85–88.

Abbott, B. P. et al. (2017b). Exploring the Sensitivity of Next Generation Gravitational Wave Detectors. *Class. Quant. Grav. 34*(4), 044001.

Abbott, B. P. et al. (2017c). GW170817: Observation of Gravitational Waves from a Binary Neutron Star Inspiral. *Phys. Rev. Lett. 119*(16), 161101.

Abbott, B. P. et al. (2017d). Multi-messenger Observations of a Binary Neutron Star Merger. *Astrophys. J. Lett. 848*(2), L12.

Abbott, B. P. et al. (2019b). GWTC-1: A Gravitational-Wave Transient Catalog of Compact Binary Mergers Observed by LIGO and Virgo during the First and Second Observing Runs. *Phys. Rev. X 9*(3), 031040.

Abbott, B. P. et al. (2020a). GW190425: Observation of a Compact Binary Coalescence with Total Mass $\sim 3.4 M_\odot$. *Astrophys. J. Lett. 892*(1), L3.

Abbott, B. P. et al. (2020b). Prospects for observing and localizing gravitational-wave transients with Advanced LIGO, Advanced Virgo and KAGRA. *Living Reviews in Relativity 23*(1), 3.

Abbott, R. et al. (2020c). GW190521: A Binary Black Hole Merger with a Total Mass of $150 M_\odot$. *Phys. Rev. Lett. 125*(10), 101102.

Abbott, R. et al. (2020d). GW190814: Gravitational Waves from the Coalescence of a 23 Solar Mass Black Hole with a 2.6 Solar Mass Compact Object. *Astrophys. J. Lett. 896*(2), L44.

Abbott, R. et al. (2021a). GWTC-2: Compact Binary Coalescences Observed by LIGO and Virgo During the First Half of the Third Observing Run. *Phys. Rev. X 11*, 021053.

Abbott, R. et al. (2021b). Population Properties of Compact Objects from the Second LIGO-Virgo Gravitational-Wave Transient Catalog. *Astrophys. J. Lett. 913*(1), L7.

Abbott, R. et al. (2021c, 11). The population of merging compact binaries inferred using gravitational waves through GWTC-3.

Abbott, R. et al. (2023a). Constraints on the Cosmic Expansion History from GWTC–3. *Astrophys. J. 949*(2), 76.

Abbott, R. et al. (2023b). GWTC-3: Compact Binary Coalescences Observed by LIGO and Virgo during the Second Part of the Third Observing Run. *Phys. Rev. X 13*(4), 041039.

Abbott, R. et al. (2024). GWTC-2.1: Deep extended catalog of compact binary coalescences observed by LIGO and Virgo during the first half of the third observing run. *Phys. Rev. D 109*(2), 022001.

Acernese, F. et al. (2015). Advanced Virgo: a second-generation interferometric gravitational wave detector. *Class. Quant. Grav. 32*(2), 024001.

Acharya, B. S. et al. (2013). Introducing the CTA concept. *Astropart. Phys. 43*, 3–18.

Adame, A. G. et al. (2024, 4). DESI 2024 VI: Cosmological Constraints from the Measurements of Baryon Acoustic Oscillations.

Ade, P. A. R. et al. (2014). Planck 2013 results. XVI. Cosmological parameters. *Astron. Astrophys. 571*, A16.

Agarwal, A. et al. (2024, 12). Blinded Mock Data Challenge for Gravitational-Wave Cosmology-I: Assessing the Robustness of Methods Using Binary Black Holes Mass Spectrum.

Aghanim, N. et al. (2020). Planck 2018 results. VI. Cosmological parameters. *Astron. Astrophys. 641*, A6. [Erratum: Astron.Astrophys. 652, C4 (2021)].

Ajith, P. et al. (2025). The Lunar Gravitational-wave Antenna: mission studies and science case. *JCAP 01*, 108.

Akmal, A., V. R. Pandharipande, and D. G. Ravenhall (1998). The Equation of state of nucleon matter and neutron star structure. *Phys. Rev. C 58*, 1804–1828.

Akutsu, T. et al. (2019). KAGRA: 2.5 Generation Interferometric Gravitational Wave Detector. *Nature Astron. 3*(1), 35–40.

Alam, S. et al. (2017). The clustering of galaxies in the completed SDSS-III Baryon Oscillation Spectroscopic Survey: cosmological analysis of the DR12 galaxy sample. *Mon. Not. Roy. Astron. Soc. 470*(3), 2617–2652.

Amaro-Seoane, P. et al. (2017, Feb). Laser Interferometer Space Antenna. *arXiv e-prints*.

Ascenzi, S., G. Oganesyan, M. Branchesi, and R. Ciolfi (2021). Electromagnetic counterparts of compact binary mergers. *J. Plasma Phys. 87*(1), 845870102.

Ashton, G. et al. (2019). BILBY: A user-friendly Bayesian inference library for gravitational-wave astronomy. *Astrophys. J. Suppl. 241*(2), 27.

Ashton, G. and C. Talbot (2021). B ilby-MCMC: an MCMC sampler for gravitational-wave inference. *Mon. Not. Roy. Astron. Soc. 507*(2), 2037–2051.

Aso, Y., Y. Michimura, K. Somiya, M. Ando, O. Miyakawa, T. Sekiguchi, D. Tatsumi, and H. Yamamoto (2013). Interferometer design of the KAGRA gravitational wave detector. *Phys. Rev. D 88*(4), 043007.

Bacon, D. J. et al. (2020). Cosmology with Phase 1 of the Square Kilometre Array: Red Book 2018: Technical specifications and performance forecasts. *Publ. Astron. Soc. Austral. 37*, e007.

Banerjee, B. et al. (2023). Pre-merger alert to detect prompt emission in very-high-energy gamma-rays from binary neutron star mergers: Einstein Telescope and Cherenkov Telescope Array synergy. *Astron. Astrophys. 678*, A126.

Banerjee, S., M. Tanaka, K. Kawaguchi, D. Kato, and G. Gaigalas (2020). Simulations of early kilonova emission from neutron star mergers. *Astrophys. J. 901*(1), 29.

Barbieri, C., O. S. Salafia, M. Colpi, G. Ghirlanda, and A. Perego (2021). Exploring the nature of ambiguous merging systems: GW190425 in low latency. *Astron. Astrophys. 654*, A12.

Barnes, J. and D. Kasen (2013, sep). Effect of a High Opacity on the Light Curves of Radioactively Powered Transients from Compact Object Mergers. *ApJ 775*(1), 18.

Baumann, D. (2022, 7). *Cosmology*. Cambridge University Press.

Baym, G., C. Pethick, and P. Sutherland (1971). The Ground state of matter at high densities: Equation of state and stellar models. *Astrophys. J. 170*, 299–317.

Belczynski, K., T. Bulik, C. L. Fryer, A. Ruiter, F. Valsecchi, J. S. Vink, and J. R. Hurley (2010, April). On the maximum mass of stellar black holes. *The Astrophysical Journal 714*(2), 1217–1226.

Belczynski, K., M. Dominik, T. Bulik, R. O'Shaughnessy, C. Fryer, and D. E. Holz (2010, jun). The Effect of Metallicity on the Detection Prospects for Gravitational Waves. *ApJ Letters 715*(2), L138–L141.

Bera, S., D. Rana, S. More, and S. Bose (2020). Incompleteness Matters Not: Inference of H_0 from Binary Black Hole–Galaxy Cross-correlations. *Astrophys. J. 902*(1), 79.

Bernal, J. L., L. Verde, and A. G. Riess (2016). The trouble with H_0. *JCAP 10*, 019.

Beutler, F., C. Blake, M. Colless, D. H. Jones, L. Staveley-Smith, L. Campbell, Q. Parker, W. Saunders, and F. Watson (2011). The 6dF Galaxy Survey: Baryon Acoustic Oscillations and the Local Hubble Constant. *Mon. Not. Roy. Astron. Soc. 416*, 3017–3032.

Blas, D., J. Lesgourgues, and T. Tram (2011, jul). The cosmic linear anisotropy solving system (class). part ii: Approximation schemes. *Journal of Cosmology and Astroparticle Physics 2011*(07), 034–034.

Blomqvist, M. et al. (2019). Baryon acoustic oscillations from the cross-correlation of Lyα absorption and quasars in eBOSS DR14. *Astron. Astrophys. 629*, A86.

Bombaci, I. and D. Logoteta (2018). Equation of state of dense nuclear matter and neutron star structure from nuclear chiral interactions. *Astron. Astrophys. 609*, A128.

Borhanian, S. (2021). GWBENCH: a novel Fisher information package for gravitational-wave benchmarking. *Class. Quant. Grav. 38*(17), 175014.

Botev, Z. I. (2016, February). The normal law under linear restrictions: Simulation and estimation via minimax tilting. *Journal of the Royal Statistical Society Series B: Statistical Methodology 79*(1), 125–148.

Branchesi, M. et al. (2023). Science with the Einstein Telescope: a comparison of different designs. *JCAP 07*, 068.

Brout, D. et al. (2022). The Pantheon+ Analysis: Cosmological Constraints. *Astrophys. J. 938*(2), 110.

Buonanno, A., B. Iyer, E. Ochsner, Y. Pan, and B. S. Sathyaprakash (2009). Comparison of post-Newtonian templates for compact binary inspiral signals in gravitational-wave detectors. *Phys. Rev. D 80*, 084043.

Burgay, M. et al. (2003, dec). An increased estimate of the merger rate of double neutron stars from observations of a highly relativistic system. *Nature 426*(6966), 531–533.

Calderon, R. et al. (2024, 5). DESI 2024: Reconstructing Dark Energy using Crossing Statistics with DESI DR1 BAO data.

Camilletti, A., L. Chiesa, G. Ricigliano, A. Perego, L. C. Lippold, S. Padamata, S. Bernuzzi, D. Radice, D. Logoteta, and F. M. Guercilena (2022). Numerical relativity simulations of the neutron star merger GW190425: microphysics and mass ratio effects. *Mon. Not. Roy. Astron. Soc. 516*(4), 4760–4781.

Carbone, C., M. Petkova, and K. Dolag (2016). DEMNUni: ISW, Rees-Sciama, and weak-lensing in the presence of massive neutrinos. *JCAP 07*, 034.

Castorina, E., C. Carbone, J. Bel, E. Sefusatti, and K. Dolag (2015). DEMNUni: The clustering of large-scale structures in the presence of massive neutrinos. *JCAP 07*, 043.

Chan, M. L., C. Messenger, I. S. Heng, and M. Hendry (2018). Binary Neutron Star Mergers and Third Generation Detectors: Localization and Early Warning. *Phys. Rev. D 97*(12), 123014.

Chen, H.-Y., S. Vitale, and R. Narayan (2019). Viewing angle of binary neutron star mergers. *Phys. Rev. X 9*(3), 031028.

Chen, Y., A. Bressan, L. Girardi, P. Marigo, X. Kong, and A. Lanza (2015, 07). parsec evolutionary tracks of massive stars up to $350 m_\odot$ at metallicities $0.0001 \leq z \leq 0.04$. *Monthly Notices of the Royal Astronomical Society 452*(1), 1068–1080.

Chernoff, D. F. and L. S. Finn (1993). Gravitational radiation, inspiraling binaries, and cosmology. *Astrophys. J. Lett. 411*, L5–L8.

Christensen, N. and R. Meyer (2022). Parameter estimation with gravitational waves. *Rev. Mod. Phys. 94*(2), 025001.

Clarke, C. J. and V. Bromm (2003). The characteristic stellar mass as a function of redshift. *Monthly Notices of the Royal Astronomical Society 343*(4), 1224–1230.

Clowe, D., M. Bradac, A. H. Gonzalez, M. Markevitch, S. W. Randall, C. Jones, and D. Zaritsky (2006). A direct empirical proof of the existence of dark matter. *Astrophys. J. Lett. 648*, L109–L113.

Codazzo, E., M. Di Giovanni, and J. Harms (2024). Gravitational wave signals from long-lasting binary–single black hole encounters. *Eur. Phys. J. Plus 139*(1), 40.

Codazzo, E., M. Di Giovanni, J. Harms, M. Dall'Amico, and M. Mapelli (2023). Study on the detectability of gravitational radiation from single-binary encounters between black holes in nuclear star clusters: The case of hyperbolic flybys. *Phys. Rev. D 107*(2), 023023.

Cozzumbo, A., U. Dupletsa, R. Calderón, R. Murgia, G. Oganesyan, and M. Branchesi (2025). Model-independent cosmology with joint observations of gravitational waves and γ-ray bursts. *JCAP 05*, 021.

Creighton, J. D. E. and W. G. Anderson (2011). *Gravitational-wave physics and astronomy: An introduction to theory, experiment and data analysis*.

Cruise, M. et al. (2025). The NewAthena mission concept in the context of the next decade of X-ray astronomy. *Nature Astron. 9*(1), 36–44.

Cuoco, E. et al. (2021). Enhancing Gravitational-Wave Science with Machine Learning. *Mach. Learn. Sci. Tech. 2*(1), 011002.

Cuoco, E., M. Cavaglià, I. S. Heng, D. Keitel, and C. Messenger (2024, 12). Applications of machine learning in gravitational wave research with current interferometric detectors.

Cutler, C. (1998). Angular resolution of the LISA gravitational wave detector. *Phys. Rev. D 57*, 7089–7102.

Cutler, C. and E. E. Flanagan (1994). Gravitational waves from merging compact binaries: How accurately can one extract the binary's parameters from the inspiral wave form? *Phys. Rev. D49*, 2658–2697.

Dalal, N., D. E. Holz, S. A. Hughes, and B. Jain (2006). Short grb and binary black hole standard sirens as a probe of dark energy. *Phys. Rev. D 74*, 063006.

De Luca, V., G. Franciolini, P. Pani, and A. Riotto (2021). Bayesian Evidence for Both Astrophysical and Primordial Black Holes: Mapping the GWTC-2 Catalog to Third-Generation Detectors. *JCAP 05*, 003.

de Sainte Agathe, V. et al. (2019). Baryon acoustic oscillations at z = 2.34 from the correlations of Lyα absorption in eBOSS DR14. *Astron. Astrophys. 629*, A85.

Di Valentino, E. (2021). A combined analysis of the H_0 late time direct measurements and the impact on the Dark Energy sector. *Mon. Not. Roy. Astron. Soc. 502*(2), 2065–2073.

Di Valentino, E., O. Mena, S. Pan, L. Visinelli, W. Yang, A. Melchiorri, D. F. Mota, A. G. Riess, and J. Silk (2021). In the realm of the Hubble tension—a review of solutions. *Class. Quant. Grav. 38*(15), 153001.

Dietrich, T., A. Samajdar, S. Khan, N. K. Johnson-McDaniel, R. Dudi, and W. Tichy (2019). Improving the NRTidal model for binary neutron star systems. *Phys. Rev. D 100*, 044003.

Dodelson, S. and F. Schmidt (2020). *Modern Cosmology*. London: Academic Press.

Dopcke, G., S. C. Glover, P. C. Clark, and R. S. Klessen (2013). On the initial mass function of low-metallicity stars: the importance of dust cooling. *The Astrophysical Journal 766*(2), 103.

Douchin, F. and P. Haensel (2001). A unified equation of state of dense matter and neutron star structure. *Astron. Astrophys. 380*, 151.

Droz, S., D. J. Knapp, E. Poisson, and B. J. Owen (1999). Gravitational waves from inspiraling compact binaries: Validity of the stationary phase approximation to the Fourier transform. *Phys. Rev. D 59*, 124016.

Dudi, R., A. Adhikari, B. Brügmann, T. Dietrich, K. Hayashi, K. Kawaguchi, K. Kiuchi, K. Kyutoku, M. Shibata, and W. Tichy (2022). Investigating GW190425 with numerical-relativity simulations. *Phys. Rev. D 106*(8), 084039.

Dupletsa, U. et al. (n.d.). Mapping the Universe's Expansion with Gravitational Waves and Neutral Hydrogen. Unpublished manuscript.

Dupletsa, U., J. Harms, B. Banerjee, M. Branchesi, B. Goncharov, A. Maselli, A. C. S. Oliveira, S. Ronchini, and J. Tissino (2023). gwfish: A simulation software to evaluate parameter-estimation capabilities of gravitational-wave detector networks. *Astron. Comput. 42*, 100671.

Dupletsa, U., J. Harms, K. K. Y. Ng, J. Tissino, F. Santoliquido, and A. Cozzumbo (2025). Validating prior-informed Fisher-matrix analyses against GWTC data. *Phys. Rev. D 111*(2), 024036.

Dupletsa, U., F. Santoliquido, M. Branchesi, and E. Loffredo (2024, sep). Parameter estimation catalogs for binary neutron star mergers detected with next-generation gravitational wave detectors .

Eichler, D., M. Livio, T. Piran, and D. N. Schramm (1989). Nucleosynthesis, Neutrino Bursts and Gamma-Rays from Coalescing Neutron Stars. *Nature 340*, 126–128.

Einstein, A. (1916). The foundation of the general theory of relativity. *Annalen Phys. 49*(7), 769–822.

Essick, R., S. Vitale, and M. Evans (2017). Frequency-dependent responses in third generation gravitational-wave detectors. *Phys. Rev. D 96*(8), 084004.

Evans, M. et al. (2021, 9). A Horizon Study for Cosmic Explorer: Science, Observatories, and Community.

Evans, M. et al. (2023, 6). Cosmic Explorer: A Submission to the NSF MPSAC ngGW Subcommittee.

Ezquiaga, J. M. and D. E. Holz (2022, 2). Spectral sirens: cosmology from the full mass distribution of compact binaries.

Farah, A. M., T. A. Callister, J. M. Ezquiaga, M. Zevin, and D. E. Holz (2025). No Need to Know: Toward Astrophysics-free Gravitational-wave Cosmology. *Astrophys. J. 978*(2), 153.

Farah, A. M., M. Fishbach, R. Essick, D. E. Holz, and S. Galaudage (2022). Bridging the Gap: Categorizing Gravitational-wave Events at the Transition between Neutron Stars and Black Holes. *Astrophys. J. 931*(2), 108.

Farmer, R., M. Renzo, S. de Mink, P. Marchant, and S. Justham (2019). Mind the gap: the location of the lower edge of the pair-instability supernova black hole mass gap. *The Astrophysical Journal 887*(1), 53.

Farr, W. M. (2019, may). Accuracy requirements for empirically measured selection functions. *Research Notes of the AAS 3*(5), 66.

Farr, W. M., M. Fishbach, J. Ye, and D. Holz (2019). A Future Percent-Level Measurement of the Hubble Expansion at Redshift 0.8 With Advanced LIGO. *Astrophys. J. Lett. 883*(2), L42.

Ferri, J. a., I. L. Tashiro, L. R. Abramo, I. Matos, M. Quartin, and R. Sturani (2024, 11). A robust cosmic standard ruler from the cross-correlations of galaxies and dark sirens.

Fishbach, M. et al. (2019). A Standard Siren Measurement of the Hubble Constant from GW170817 without the Electromagnetic Counterpart. *Astrophys. J. Lett. 871*(1), L13.

Fishbach, M., Z. Doctor, T. Callister, B. Edelman, J. Ye, R. Essick, W. M. Farr, B. Farr, and D. E. Holz (2021). When Are LIGO/Virgo's Big Black Hole Mergers? *Astrophys. J. 912*(2), 98.

Fishbach, M., R. Essick, and D. E. Holz (2020). Does Matter Matter? Using the mass distribution to distinguish neutron stars and black holes. *Astrophys. J. Lett. 899*, L8.

Fishbach, M. and D. E. Holz (2017). Where Are LIGO's Big Black Holes? *Astrophys. J. Lett. 851*(2), L25.

Fisher, R. A. (1920, 06). A mathematical examination of the methods of determining the accuracy of observation by the mean error, and by the mean square error. *Monthly Notices of the Royal Astronomical Society 80*(8), 758–770.

Freiburghaus, C., J.-F. Rembges, T. Rauscher, E. Kolbe, F.-K. Thielemann, K.-L. Kratz, B. Pfeiffer, and J. J. Cowan (1999, may). The astrophysical r-process: A comparison of calculations following adiabatic expansion with classical calculations based on neutron densities and temperatures. *The Astrophysical Journal 516*(1), 381.

Friedman, A. (1922). On the Curvature of space. *Z. Phys. 10*, 377–386.

Friedmann, A. (1924). On the Possibility of a world with constant negative curvature of space. *Z. Phys. 21*, 326–332.

Fritschel, P., K. Kuns, J. Driggers, A. Effler, B. Lantz, D., Ottaway, S. Ballmer, K. Dooley, R. Adhikari, M. Evans, B. Farr, G. Gonzalez, P. Schmidt, and S. Raja (2022). Report from the lsc post-o5 study group. *Tech. Rep. T2200287 (LIGO).*

Fryer, C. L., K. Belczynski, G. Wiktorowicz, M. Dominik, V. Kalogera, and D. E. Holz (2012, March). Compact remnant mass function: Dependence on the explosion mechanism and metallicity. *The Astrophysical Journal 749*(1), 91.

Gair, J. R. et al. (2023). The Hitchhiker's Guide to the Galaxy Catalog Approach for Dark Siren Gravitational-wave Cosmology. *Astron. J. 166*(1), 22.

Gamba, R., M. Breschi, S. Bernuzzi, M. Agathos, and A. Nagar (2021). Waveform systematics in the gravitational-wave inference of tidal parameters and equation of state from binary neutron star signals. *Phys. Rev. D 103*(12), 124015.

Gardner, J. P. et al. (2006). The James Webb Space Telescope. *Space Sci. Rev. 123*, 485.

Gehrels, N. et al. (2004). The Swift Gamma-Ray Burst Mission. *Astrophys. J. 611*, 1005–1020. [Erratum: Astrophys.J. 621, 558 (2005)].

Giacobbo, N. and M. Mapelli (2018). The progenitors of compact-object binaries: impact of metallicity, common envelope and natal kicks. *Mon. Not. Roy. Astron. Soc. 480*(2), 2011–2030.

Giacobbo, N., M. Mapelli, and M. Spera (2018). Merging black hole binaries: the effects of progenitor's metallicity, mass-loss rate and Eddington factor. *Mon. Not. Roy. Astron. Soc. 474*(3), 2959–2974.

Gilmozzi, R. and J. Spyromilio (2008, July). The 42m European ELT: status. In L. M. Stepp and R. Gilmozzi (Eds.), *Ground-based and Airborne Telescopes II*, Volume 7012 of *Society of Photo-Optical Instrumentation Engineers (SPIE) Conference Series*, pp. 701219.

Górski, K. M., E. Hivon, A. J. Banday, B. D. Wandelt, F. K. Hansen, M. Reinecke, and M. Bartelmann (2005, apr). Healpix: A framework for high-resolution discretization and fast analysis of data distributed on the sphere. *ApJ 622*, 759–771.

Gray, R. et al. (2023). Joint cosmological and gravitational-wave population inference using dark sirens and galaxy catalogues. *JCAP 12*, 023.

Gray, R., I. M. n. Hernandez, H. Qi, A. Sur, P. R. Brady, H.-Y. Chen, W. M. Farr, M. Fishbach, J. R. Gair, A. Ghosh, D. E. Holz, S. Mastrogiovanni, C. Messenger, D. A. Steer, and J. Veitch (2020, Jun). Cosmological inference using gravitational wave standard sirens: A mock data analysis. *Phys. Rev. D 101*, 122001.

Grimm, S. and J. Harms (2020). Multiband gravitational-wave parameter estimation: A study of future detectors. *Phys. Rev. D 102*(2), 022007.

Grossman, D., O. Korobkin, S. Rosswog, and T. Piran (2014, mar). The long-term evolution of neutron star merger remnants - II. Radioactively powered transients. *MNRAS 439*(1), 757–770.

Grote, H., K. Danzmann, K. L. Dooley, R. Schnabel, J. Slutsky, and H. Vahlbruch (2013). First Long-Term Application of Squeezed States of Light in a Gravitational-Wave Observatory. *Phys. Rev. Lett. 110*(18), 181101.

Gupta, I. et al. (2024). Characterizing gravitational wave detector networks: from A$^\sharp$ to cosmic explorer. *Class. Quant. Grav. 41*(24), 245001.

Harms, J., B. J. J. Slagmolen, R. X. Adhikari, M. C. Miller, M. Evans, Y. Chen, H. Müller, and M. Ando (2013). Low-Frequency Terrestrial Gravitational-Wave Detectors. *Phys. Rev. D 88*(12), 122003.

Harris, C. R., K. J. Millman, S. J. van der Walt, R. Gommers, P. Virtanen, D. Cournapeau, E. Wieser, J. Taylor, S. Berg, N. J. Smith, R. Kern, M. Picus, S. Hoyer, M. H. van Kerkwijk, M. Brett, A. Haldane, J. F. del Río, M. Wiebe, P. Peterson, P. Gérard-Marchant, K. Sheppard, T. Reddy, W. Weckesser, H. Abbasi, C. Gohlke, and T. E. Oliphant (2020, September). Array programming with numpy. *Nature 585*(7825), 357–362.

Heger, A., C. L. Fryer, S. E. Woosley, N. Langer, and D. H. Hartmann (2003). How massive single stars end their life. *Astrophys. J. 591*, 288–300.

Hernández-Molinero, B., C. Carbone, R. Jimenez, and C. Peña Garay (2024). Cosmic background neutrinos deflected by gravity: DEMNUni simulation analysis. *JCAP 01*, 006.

Hild, S. et al. (2011). Sensitivity Studies for Third-Generation Gravitational Wave Observatories. *Class. Quant. Grav. 28*, 094013.

Hild, S., S. Chelkowski, and A. Freise (2008, 10). Pushing towards the ET sensitivity using 'conventional' technology.

Holz, D. E. and S. A. Hughes (2005). Using gravitational-wave standard sirens. *ApJ 629*, 15–22.

Hoy, C. and V. Raymond (2021). PESummary: the code agnostic Parameter Estimation Summary page builder. *SoftwareX 15*, 100765.

Hu, J.-P. and F.-Y. Wang (2023). Hubble Tension: The Evidence of New Physics. *Universe 9*(2), 94.

Hubble, E. (1929, mar). A relation between distance and radial velocity among extra-galactic nebulae. *Proceedings of the National Academy of Science 15*(3), 168–173.

Hulse, R. A. and J. H. Taylor (1975). Discovery of a pulsar in a binary system. *Astrophys. J. Lett. 195*, L51–L53.

Husa, S., S. Khan, M. Hannam, M. Pürrer, F. Ohme, X. Jiménez Forteza, and A. Bohé (2016). Frequency-domain gravitational waves from nonprecessing black-hole binaries. I. New numerical waveforms and anatomy of the signal. *Phys. Rev. D 93*(4), 044006.

Iacovelli, F., M. Mancarella, S. Foffa, and M. Maggiore (2022a). Forecasting the Detection Capabilities of Third-generation Gravitational-wave Detectors Using GWFAST. *Astrophys. J. 941*(2), 208.

Iacovelli, F., M. Mancarella, S. Foffa, and M. Maggiore (2022b). GWFAST: A Fisher Information Matrix Python Code for Third-generation Gravitational-wave Detectors. *Astrophys. J. Supp. 263*(1), 2.

Iacovelli, F., M. Mancarella, C. Mondal, A. Puecher, T. Dietrich, F. Gulminelli, M. Maggiore, and M. Oertel (2023). Nuclear physics constraints from binary neutron star mergers in the Einstein Telescope era. *Phys. Rev. D 108*(12), 122006.

Iorio, G. et al. (2022, 11). Compact object mergers: exploring uncertainties from stellar and binary evolution with SEVN.

Isoyama, S., R. Sturani, and H. Nakano (2020, 12). Post-Newtonian templates for gravitational waves from compact binary inspirals.

Ivezić, Z., S. M. Kahn, J. A. Tyson, B. Abel, E. Acosta, R. Allsman, D. Alonso, Y. AlSayyad, S. F. Anderson, J. Andrew, and et al. (2019, March). LSST: From Science Drivers to Reference Design and Anticipated Data Products. *The Astrophysical Journal 873*, 111.

Kalogera, V. et al. (2021, 11). The Next Generation Global Gravitational Wave Observatory: The Science Book.

Kamionkowski, M. and A. G. Riess (2023). The Hubble Tension and Early Dark Energy. *Ann. Rev. Nucl. Part. Sci. 73*, 153–180.

Kapil, V., L. Reali, R. Cotesta, and E. Berti (2024). Systematic bias from waveform modeling for binary black hole populations in next-generation gravitational wave detectors. *Phys. Rev. D 109*(10), 104043.

Karathanasis, C., S. Mukherjee, and S. Mastrogiovanni (2023). Binary black holes population and cosmology in new lights: signature of PISN mass and formation channel in GWTC-3. *Mon. Not. Roy. Astron. Soc. 523*(3), 4539–4555.

Karathanasis, C., B. Revenu, S. Mukherjee, and F. Stachurski (2023). GWSim: Python package for creating mock GW samples for different astrophysical populations and cosmological models of binary black holes. *Astron. Astrophys. 677*, A124. [Erratum: Astron.Astrophys. 682, C1 (2024)].

Karnesis, N. et al. (2024). The Laser Interferometer Space Antenna mission in Greece White Paper. *Int. J. Mod. Phys. D 33*(07n08), 2450027.

Karwal, T. and M. Kamionkowski (2016). Dark energy at early times, the Hubble parameter, and the string axiverse. *Phys. Rev. D 94*(10), 103523.

Kasen, D., N. R. Badnell, and J. Barnes (2013, sep). Opacities and Spectra of the r-process Ejecta from Neutron Star Mergers. *ApJ 774*(1), 25.

Khan, S., S. Husa, M. Hannam, F. Ohme, M. Pürrer, X. Jiménez Forteza, and A. Bohé (2016). Frequency-domain gravitational waves from nonprecessing black-hole binaries. II. A phenomenological model for the advanced detector era. *Phys. Rev. D 93*(4), 044007.

Khan, S., F. Ohme, K. Chatziioannou, and M. Hannam (2020). Including higher order multipoles in gravitational-wave models for precessing binary black holes. *Phys. Rev. D 101*(2), 024056.

Kiziltan, B., A. Kottas, M. De Yoreo, and S. E. Thorsett (2013). The Neutron Star Mass Distribution. *Astrophys. J. 778*, 66.

Knox, L. and M. Millea (2020). Hubble constant hunter's guide. *Phys. Rev. D 101*(4), 043533.

Kouveliotou, C., C. A. Meegan, G. J. Fishman, N. P. Bhat, M. S. Briggs, T. M. Koshut, W. S. Paciesas, and G. N. Pendleton (1993, aug). Identification of two classes of gamma-ray bursts. *ApJ Letters 413*, L101.

Kovetz, E. D. et al. (2017, 9). Line-Intensity Mapping: 2017 Status Report.

Kunert, N., J. Gair, P. T. H. Pang, and T. Dietrich (2024, Aug). Impact of gravitational waveform model systematics on the measurement of the hubble constant. *Phys. Rev. D 110*, 043520.

Kyutoku, K., S. Fujibayashi, K. Hayashi, K. Kawaguchi, K. Kiuchi, M. Shibata, and M. Tanaka (2020). On the Possibility of GW190425 Being a Black Hole–Neutron Star Binary Merger. *Astrophys. J. Lett. 890*(1), L4.

Leavitt, H. S. and E. C. Pickering (1912). Periods of 25 Variable Stars in the Small Magellanic Cloud. *Harvard Obs. Circ. 173*, 1–3.

Lemaitre, G. (1927). A Homogeneous Universe of Constant Mass and Growing Radius Accounting for the Radial Velocity of Extragalactic Nebulae. *Annales Soc. Sci. Bruxelles A 47*, 49–59.

Lesgourgues, J. (2011). The cosmic linear anisotropy solving system (class) i: Overview.

Levan, A. J. et al. (2024). Heavy-element production in a compact object merger observed by JWST. *Nature 626*(8000), 737–741.

Leyde, K., S. R. Green, A. Toubiana, and J. Gair (2024). Gravitational wave populations and cosmology with neural posterior estimation. *Phys. Rev. D 109*(6), 064056.

Leyde, K., S. Mastrogiovanni, D. A. Steer, E. Chassande-Mottin, and C. Karathanasis (2022, 1). Current and future constraints on cosmology and modified gravitational wave friction from binary black holes.

Li, J., C. Liu, Z.-Y. Zhang, H. Tian, X. Fu, J. Li, and Z.-Q. Yan (2023). Stellar initial mass function varies with metallicity and time. *Nature 613*(7944), 460–462.

Li, L.-X. and B. Paczynski (1998). Transient events from neutron star mergers. *Astrophys. J. Lett. 507*, L59.

Li, X. and A. Shafieloo (2019). A Simple Phenomenological Emergent Dark Energy Model can Resolve the Hubble Tension. *Astrophys. J. Lett. 883*(1), L3.

Li, X. and A. Shafieloo (2020). Evidence for Emergent Dark Energy. *Astrophys. J. 902*(1), 58.

Li, Y., I. S. Heng, M. L. Chan, C. Messenger, and X. Fan (2022). Exploring the sky localization and early warning capabilities of third generation gravitational wave detectors in three-detector network configurations. *Phys. Rev. D 105*(4), 043010.

LIGO Scientific Collaboration (2020, December). LALSuite: LIGO Scientific Collaboration Algorithm Library Suite. Astrophysics Source Code Library, record ascl:2012.021.

Lin, T. (2019). Dark matter models and direct detection. *PoS 333*, 009.

Lodha, K. et al. (2024, 5). DESI 2024: Constraints on Physics-Focused Aspects of Dark Energy using DESI DR1 BAO Data.

Loffredo, E. et al. (2025). Prospects for optical detections from binary neutron star mergers with the next-generation multi-messenger observatories. *Astron. Astrophys. 697*, A36.

Logoteta, D., A. Perego, and I. Bombaci (2021). Microscopic equation of state of hot nuclear matter for numerical relativity simulations. *Astron. Astrophys. 646*, A55.

Lorenzo-Medina, A. and T. Dent (2025). A physically modelled selection function for compact binary mergers in the LIGO-Virgo O3 run and beyond. *Class. Quant. Grav. 42*(4), 045008.

MacFadyen, A. and S. E. Woosley (1999). Collapsars: Gamma-ray bursts and explosions in 'failed supernovae'. *Astrophys. J. 524*, 262.

Madau, P. and M. Dickinson (2014). Cosmic Star Formation History. *Ann. Rev. Astron. Astrophys. 52*, 415–486.

Madau, P. and T. Fragos (2017). Radiation Backgrounds at Cosmic Dawn: X-Rays from Compact Binaries. *Astrophys. J. 840*(1), 39.

Magaña Hernandez, I. and A. Ray (2024, 4). Beyond Gaps and Bumps: Spectral Siren Cosmology with Non-Parametric Population Models.

Maggiore, M. (2007). *Gravitational Waves. Vol. 1: Theory and Experiments*. Oxford University Press.

Maggiore, M. (2018, 3). *Gravitational Waves. Vol. 2: Astrophysics and Cosmology*. Oxford University Press.

Maggiore, M. et al. (2020). Science Case for the Einstein Telescope. *JCAP 03*, 050.

Mainieri, V. et al. (2024, 3). The Wide-field Spectroscopic Telescope (WST) Science White Paper.

Mali, U. and R. Essick (2024, 10). Striking a Chord with Spectral Sirens: multiple features in the compact binary population correlate with H_0.

Malmquist, K. G. (1922, March). On some relations in stellar statistics. *Meddelanden fran Lunds Astronomiska Observatorium Serie I 100*, 1–52.

Mandel, I., W. M. Farr, and J. R. Gair (2019). Extracting distribution parameters from multiple uncertain observations with selection biases. *Mon. Not. Roy. Astron. Soc. 486*(1), 1086–1093.

Mapelli, M. (2020). Binary Black Hole Mergers: Formation and Populations. *Front. Astron. Space Sci. 7*, 38.

Mapelli, M. (2021). Formation Channels of Single and Binary Stellar-Mass Black Holes. In C. Bambi, S. Katsanevas, and K. D. Kokkotas (Eds.), *Handbook of Gravitational Wave Astronomy*, pp. 16.

Mapelli, M. and A. Bressan (2013, February). Impact of metallicity on the evolution of young star clusters. *Monthly Notices of the Royal Astronomical Society 430*(4), 3120–3127.

Mapelli, M., N. Giacobbo, E. Ripamonti, and M. Spera (2017). The cosmic merger rate of stellar black hole binaries from the Illustris simulation. *Mon. Not. Roy. Astron. Soc. 472*(2), 2422–2435.

Mapelli, M., E. Ripamonti, L. Zampieri, and M. Colpi (2011, April). Remnants of massive metal-poor stars: Viable engines for ultra-luminous x-ray sources. *Astronomische Nachrichten 332*(4), 414–417.

Mapelli, M., M. Spera, E. Montanari, M. Limongi, A. Chieffi, N. Giacobbo, A. Bressan, and Y. Bouffanais (2020). Impact of the Rotation and Compactness of Progenitors on the Mass of Black Holes. *Astrophys. J. 888*, 76.

Marsat, S. and J. G. Baker (2018, 6). Fourier-domain modulations and delays of gravitational-wave signals.

Mastrogiovanni, S., D. Laghi, R. Gray, G. C. Santoro, A. Ghosh, C. Karathanasis, K. Leyde, D. A. Steer, S. Perries, and G. Pierra (2023). Joint population and cosmological properties inference with gravitational waves standard sirens and galaxy surveys. *Phys. Rev. D 108*(4), 042002.

Mastrogiovanni, S., K. Leyde, C. Karathanasis, E. Chassande-Mottin, D. A. Steer, J. Gair, A. Ghosh, R. Gray, S. Mukherjee, and S. Rinaldi (2021). On the importance of source population models for gravitational-wave cosmology. *Phys. Rev. D 104*(6), 062009.

Mastrogiovanni, S., G. Pierra, S. Perriès, D. Laghi, G. Caneva Santoro, A. Ghosh, R. Gray, C. Karathanasis, and K. Leyde (2024). ICAROGW: A python package for inference of astrophysical population properties of noisy, heterogeneous, and incomplete observations. *Astron. Astrophys. 682*, A167.

Meegan, C., G. Lichti, P. N. Bhat, E. Bissaldi, M. S. Briggs, V. Connaughton, R. Diehl, G. Fishman, J. Greiner, A. S. Hoover, A. J. van der Horst, A. von Kienlin, R. M. Kippen, C. Kouveliotou, S. McBreen, W. S. Paciesas, R. Preece, H. Steinle, M. S. Wallace, R. B. Wilson, and C. Wilson-Hodge (2009, August). Thefermigamma-ray burst monitor. *The Astrophysical Journal 702*(1), 791–804.

Metzger, B. D. (2019, dec). Kilonovae. *Living Reviews in Relativity 23*(1), 1.

Metzger, B. D., G. Martínez-Pinedo, S. Darbha, E. Quataert, A. Arcones, D. Kasen, R. Thomas, P. Nugent, I. V. Panov, and N. T. Zinner (2010, aug). Electromagnetic counterparts of compact object mergers powered by the radioactive decay of r-process nuclei. *MNRAS 406*(4), 2650–2662.

Misner, C. W., K. S. Thorne, and J. A. Wheeler (1973). *Gravitation*. San Francisco: W. H. Freeman.

Mokiem, M., A. de Koter, J. Vink, J. Puls, C. Evans, S. Smartt, P. Crowther, A. Herrero, N. Langer, D. Lennon, et al. (2007). The empirical metallicity dependence of the mass-loss rate of o-and early b-type stars. *Astronomy & Astrophysics 473*(2), 603–614.

Moore, C. J., R. H. Cole, and C. P. L. Berry (2015). Gravitational-wave sensitivity curves. *Class. Quant. Grav. 32*(1), 015014.

Mukherjee, S. (2021, 12). The redshift dependence of black hole mass distribution: Is it reliable for standard sirens cosmology?

Mukherjee, S., G. Lavaux, F. R. Bouchet, J. Jasche, B. D. Wandelt, S. M. Nissanke, F. Leclercq, and K. Hotokezaka (2021). Velocity correction for Hubble constant measurements from standard sirens. *Astron. Astrophys. 646*, A65.

Mukherjee, S. and B. D. Wandelt (2018, 8). Beyond the classical distance-redshift test: cross-correlating redshift-free standard candles and sirens with redshift surveys. *arXiv:1808.06615*.

Mukherjee, S., B. D. Wandelt, S. M. Nissanke, and A. Silvestri (2021). Accurate precision Cosmology with redshift unknown gravitational wave sources. *Phys. Rev. D 103*(4), 043520.

Mukherjee, S., B. D. Wandelt, and J. Silk (2020). Probing the theory of gravity with gravitational lensing of gravitational waves and galaxy surveys. *Mon. Not. Roy. Astron. Soc. 494*(2), 1956–1970.

Müller, M., S. Mukherjee, and G. Ryan (2024, 6). Be careful in multi-messenger inference of the Hubble constant: A path forward for robust inference.

Murguia-Berthier, A., G. Montes, E. Ramirez-Ruiz, F. De Colle, and W. H. Lee (2014). Necessary Conditions for Short Gamma-Ray Burst Production in Binary Neutron Star Mergers. *Astrophys. J. Lett. 788*, L8.

Ng, K. K. Y. et al. (2023). Measuring properties of primordial black hole mergers at cosmological distances: Effect of higher order modes in gravitational waves. *Phys. Rev. D 107*(2), 024041.

Ng, K. K. Y., S. Chen, B. Goncharov, U. Dupletsa, S. Borhanian, M. Branchesi, J. Harms, M. Maggiore, B. S. Sathyaprakash, and S. Vitale (2022). On the Single-event-based Identification of Primordial Black Hole Mergers at Cosmological Distances. *Astrophys. J. Lett. 931*(1), L12.

Nimonkar, H. and S. Mukherjee (2023). Dependence of peculiar velocity on the host properties of the gravitational wave sources and its impact on the measurement of Hubble constant. *Mon. Not. Roy. Astron. Soc. 527*(2), 2152–2164.

Nitz, A. H. and T. Dal Canton (2021). Pre-merger Localization of Compact-binary Mergers with Third-generation Observatories. *Astrophys. J. Lett. 917*(2), L27.

Owen, C. B., C.-J. Haster, S. Perkins, N. J. Cornish, and N. Yunes (2023). Waveform accuracy and systematic uncertainties in current gravitational wave observations. *Phys. Rev. D 108*(4), 044018.

Özel, F. and P. Freire (2016). Masses, Radii, and the Equation of State of Neutron Stars. *Ann. Rev. Astron. Astrophys. 54*, 401–440.

Ozel, F., D. Psaltis, R. Narayan, and A. S. Villarreal (2012). On the Mass Distribution and Birth Masses of Neutron Stars. *Astrophys. J. 757*, 55.

Palmese, A., C. R. Bom, S. Mucesh, and W. G. Hartley (2021, 11). A standard siren measurement of the Hubble constant using gravitational wave events from the first three LIGO/Virgo observing runs and the DESI Legacy Survey.

Palmese, A. and S. Mastrogiovanni (2025, 1). Gravitational Wave Cosmology.

Parida, A., S. Mitra, and S. Jhingan (2016). Component Separation of a Isotropic Gravitational Wave Background. *JCAP 04*, 024.

Parimbelli, G., G. Scelfo, S. K. Giri, A. Schneider, M. Archidiacono, S. Camera, and M. Viel (2021). Mixed dark matter: matter power spectrum and halo mass function. *JCAP 12*(12), 044.

Perlmutter, S. et al. (1999). Measurements of Ω and Λ from 42 High Redshift Supernovae. *Astrophys. J. 517*, 565–586.

Pescalli, A., G. Ghirlanda, R. Salvaterra, G. Ghisellini, S. D. Vergani, F. Nappo, O. S. Salafia, A. Melandri, S. Covino, and D. Götz (2016). The rate and luminosity function of long Gamma Ray Bursts. *Astron. Astrophys. 587*, A40.

Petrov, P., L. P. Singer, M. W. Coughlin, V. Kumar, M. Almualla, S. Anand, M. Bulla, T. Dietrich, F. Foucart, and N. Guessoum (2022). Data-driven Expectations for Electromagnetic Counterpart Searches Based on LIGO/Virgo Public Alerts. *Astrophys. J. 924*(2), 54.

Pierra, G., S. Mastrogiovanni, S. Perriès, and M. Mapelli (2024). Study of systematics on the cosmological inference of the Hubble constant from gravitational wave standard sirens. *Phys. Rev. D 109*(8), 083504.

Poulin, V., T. L. Smith, D. Grin, T. Karwal, and M. Kamionkowski (2018). Cosmological implications of ultralight axionlike fields. *Phys. Rev. D 98*(8), 083525.

Pratten, G. et al. (2021). Computationally efficient models for the dominant and subdominant harmonic modes of precessing binary black holes. *Phys. Rev. D 103*(10), 104056.

Press, W. H., S. A. Teukolsky, W. T. Vetterling, and B. P. Flannery (2007). *Numerical recipes 3rd edition: The art of scientific computing*. Cambridge University Press.

Prialnik, D. (2010). *An introduction to the theory of stellar structure and evolution*. Cambridge University Press.

Punturo, M. et al. (2010). The Einstein Telescope: A third-generation gravitational wave observatory. *Class. Quant. Grav. 27*, 194002.

Pürrer, M. and C.-J. Haster (2020). Gravitational waveform accuracy requirements for future ground-based detectors. *Phys. Rev. Res. 2*(2), 023151.

Raaijmakers, G. et al. (2021). The Challenges Ahead for Multimessenger Analyses of Gravitational Waves and Kilonova: A Case Study on GW190425. *Astrophys. J. 922*(2), 269.

Radice, D., G. Ricigliano, M. Bhattacharya, A. Perego, F. J. Fattoyev, and K. Murase (2024). What if GW190425 did not produce a black hole promptly? *Mon. Not. Roy. Astron. Soc. 528*(4), 5836–5844.

Rastinejad, J. C. et al. (2022). A kilonova following a long-duration gamma-ray burst at 350 Mpc. *Nature 612*(7939), 223–227.

Razzano, M. and E. Cuoco (2018). Image-based deep learning for classification of noise transients in gravitational wave detectors. *Class. Quant. Grav. 35*(9), 095016.

Read, J. S. (2023). Waveform uncertainty quantification and interpretation for gravitational-wave astronomy. *Class. Quant. Grav. 40*(13), 135002.

Reitze, D. et al. (2019). Cosmic Explorer: The U.S. Contribution to Gravitational-Wave Astronomy beyond LIGO. *Bull. Am. Astron. Soc. 51*(7), 035.

Research, E. O. F. N. and OpenAIRE (2013). Zenodo.

Riess, A. G. et al. (1998). Observational evidence from supernovae for an accelerating universe and a cosmological constant. *Astron. J. 116*, 1009–1038.

Riess, A. G. et al. (2021, 12). A Comprehensive Measurement of the Local Value of the Hubble Constant with 1 km/s/Mpc Uncertainty from the Hubble Space Telescope and the SHoES Team.

Riess, A. G., S. Casertano, W. Yuan, L. M. Macri, and D. Scolnic (2019). Large Magellanic Cloud Cepheid Standards Provide a 1% Foundation for the Determination of the Hubble Constant and Stronger Evidence for Physics beyond ΛCDM. *876*(1), 85.

Rodriguez, C. L., B. Farr, W. M. Farr, and I. Mandel (2013). Inadequacies of the Fisher Information Matrix in gravitational-wave parameter estimation. *Phys. Rev. D 88*(8), 084013.

Romero-Shaw, I. M. et al. (2020). Bayesian inference for compact binary coalescences with bilby: validation and application to the first LIGO–Virgo gravitational-wave transient catalogue. *Mon. Not. Roy. Astron. Soc. 499*(3), 3295–3319.

Ronchini, S., M. Branchesi, G. Oganesyan, B. Banerjee, U. Dupletsa, G. Ghirlanda, J. Harms, M. Mapelli, and F. Santoliquido (2022). Perspectives for multimessenger astronomy with the next generation of gravitational-wave detectors and high-energy satellites. *Astron. Astrophys. 665*, A97.

Ross, A. J., L. Samushia, C. Howlett, W. J. Percival, A. Burden, and M. Manera (2015). The clustering of the SDSS DR7 main Galaxy sample – I. A 4 per cent distance measure at $z = 0.15$. *Mon. Not. Roy. Astron. Soc. 449*(1), 835–847.

Roulet, J., S. Olsen, J. Mushkin, T. Islam, T. Venumadhav, B. Zackay, and M. Zaldarriaga (2022). Removing degeneracy and multimodality in gravitational wave source parameters. *Phys. Rev. D 106*(12), 123015.

Rubin, V. C. (1983, jun). The rotation of spiral galaxies. *Science 220*(4604), 1339–1344.

Ryden, B. (1970). *Introduction to cosmology*. Cambridge University Press.

Salvarese, A. and H.-Y. Chen (2024). Mitigating the Binary Viewing Angle Bias for Standard Sirens. *Astrophys. J. Lett. 974*(1), L16.

Santoliquido, F. et al. (2025, 4). Fast and accurate parameter estimation of high-redshift sources with the Einstein Telescope.

Santoliquido, F., U. Dupletsa, J. Tissino, M. Branchesi, F. Iacovelli, G. Iorio, M. Mapelli, D. Gerosa, J. Harms, and M. Pasquato (2024, 4). Classifying binary black holes from Population III stars with the Einstein Telescope: a machine-learning approach.

Santoliquido, F., M. Mapelli, Y. Bouffanais, N. Giacobbo, U. N. Di Carlo, S. Rastello, M. C. Artale, and A. Ballone (2020). The cosmic merger rate density evolution of compact binaries formed in young star clusters and in isolated binaries. *Astrophys. J. 898*(2), 152.

Santoliquido, F., M. Mapelli, N. Giacobbo, Y. Bouffanais, and M. C. Artale (2021). The cosmic merger rate density of compact objects: impact of star formation, metallicity, initial mass function and binary evolution. *Mon. Not. Roy. Astron. Soc. 502*(4), 4877–4889.

Santos, M. G. et al. (2017, 9). MeerKLASS: MeerKAT Large Area Synoptic Survey. In *MeerKAT Science: On the Pathway to the SKA*.

Sathyaprakash, B. et al. (2012). Scientific Objectives of Einstein Telescope. *Class. Quant. Grav. 29*, 124013. Erratum: Class.Quant.Grav. 30, 079501 (2013).

Sathyaprakash, B. S. and B. F. Schutz (2009). Physics, Astrophysics and Cosmology with Gravitational Waves. *Living Rev. Rel. 12*, 2.

Scelfo, G., M. Spinelli, A. Raccanelli, L. Boco, A. Lapi, and M. Viel (2022). Gravitational waves × HI intensity mapping: cosmological and astrophysical applications. *JCAP 01*(01), 004.

Schilling, R. (1997, jun). Angular and frequency response of lisa. *Classical and Quantum Gravity 14*(6), 1513.

Schutz (1986, sep). Determining the hubble constant from gravitational wave observations. *Nature 323*(6086), 310–311.

Schutz, B. F. (1997). Low frequency sources of gravitational waves: A Tutorial. *ESA Spec. Publ. 420*, 229.

Shah, P., P. Lemos, and O. Lahav (2021). A buyer's guide to the Hubble constant. *Astron. Astrophys. Rev. 29*(1), 9.

Smith, R. E., J. A. Peacock, A. Jenkins, S. D. M. White, C. S. Frenk, F. R. Pearce, P. A. Thomas, G. Efstathiou, and H. M. P. Couchmann (2003). Stable clustering, the halo model and nonlinear cosmological power spectra. *Mon. Not. Roy. Astron. Soc. 341*, 1311.

Soares-Santos, M. et al. (2019). First Measurement of the Hubble Constant from a Dark Standard Siren using the Dark Energy Survey Galaxies and the LIGO/Virgo Binary–Black-hole Merger GW170814. *Astrophys. J. Lett. 876*(1), L7.

Somiya, K. (2012). Detector configuration of KAGRA: The Japanese cryogenic gravitational-wave detector. *Class. Quant. Grav. 29*, 124007.

Souradeep, T. (2016). LIGO-India. *Resonance 21*, 225 – 231.

Speagle, J. S. (2020, February). dynesty: a dynamic nested sampling package for estimating bayesian posteriors and evidences. *Monthly Notices of the Royal Astronomical Society 493*(3), 3132–3158.

Spera, M., M. Mapelli, and A. Bressan (2015). The mass spectrum of compact remnants from the parsec stellar evolution tracks.

Spera, M., M. Mapelli, N. Giacobbo, A. A. Trani, A. Bressan, and G. Costa (2019). Merging black hole binaries with the SEVN code. *Mon. Not. Roy. Astron. Soc. 485*(1), 889–907.

Springel, V. (2005). The Cosmological simulation code GADGET-2. *Mon. Not. Roy. Astron. Soc. 364*, 1105–1134.

Talbot, C. and J. Golomb (2023). Growing pains: understanding the impact of likelihood uncertainty on hierarchical Bayesian inference for gravitational-wave astronomy. *Mon. Not. Roy. Astron. Soc. 526*(3), 3495–3503.

Tammann, G. A. and B. Reindl (2000). The luminosity calibration of sne ia: present status. *Mem. Soc. Ast. It. 71*, 539.

Taylor, S. R., J. R. Gair, and I. Mandel (2012). Hubble without the Hubble: Cosmology using advanced gravitational-wave detectors alone. *Phys. Rev. D 85*, 023535.

Thrane, E. and C. Talbot (2019). An introduction to bayesian inference in gravitational-wave astronomy: Parameter estimation, model selection, and hierarchical models. *Publications of the Astronomical Society of Australia 36*.

Troja, E. et al. (2022). A nearby long gamma-ray burst from a merger of compact objects. *Nature 612*(7939), 228–231.

Turski, C., M. Bilicki, G. Dálya, R. Gray, and A. Ghosh (2023). Impact of modelling galaxy redshift uncertainties on the gravitational-wave dark standard siren measurement of the Hubble constant. *Mon. Not. Roy. Astron. Soc. 526*(4), 6224–6233.

Usman, S. A., J. C. Mills, and S. Fairhurst (2019). Constraining the Inclinations of Binary Mergers from Gravitational-wave Observations. *Astrophys. J. 877*(2), 82.

Vallisneri, M. (2008). Use and abuse of the Fisher information matrix in the assessment of gravitational-wave parameter-estimation prospects. *Phys. Rev. D 77*, 042001.

Vallisneri, M. (2011). Beyond Fisher: exact sampling distributions of the maximum-likelihood estimator in gravitational-wave parameter estimation. *Phys. Rev. Lett. 107*, 191104.

Van Den Broeck, C. and A. S. Sengupta (2007). Binary black hole spectroscopy. *Class. Quant. Grav. 24*, 1089–1114.

van Loon, J. T. (2005). On the metallicity dependence of the winds from red supergiants and asymptotic giant branch stars. *arXiv preprint astro-ph/0512326*.

Verde, L., T. Treu, and A. Riess (2019, 7). In *Tensions between the Early and the Late Universe*.

Vink, J. S., A. de Koter, and H. J. G. L. M. Lamers (2001). Mass-loss predictions for o and b stars as a function of metallicity. *Astron. Astrophys. 369*, 574–588.

Vitale, S., D. Gerosa, W. M. Farr, and S. R. Taylor (2020, 7). Inferring the properties of a population of compact binaries in presence of selection effects.

Wang, J. et al. (2021). H i intensity mapping with MeerKAT: calibration pipeline for multidish autocorrelation observations. *Mon. Not. Roy. Astron. Soc. 505*(3), 3698–3721.

Weltman, A. e. a. (2020, January). Fundamental physics with the Square Kilometre Array. *PASA 37*, e002.

Wen, L. and Y. Chen (2010). Geometrical Expression for the Angular Resolution of a Network of Gravitational-Wave Detectors. *Phys. Rev. D 81*, 082001.

Woosley, S. E. (1993, mar). Gamma-ray bursts from stellar mass accretion disks around black holes. *ApJ 405*, 273.

Zonca, A., L. Singer, D. Lenz, M. Reinecke, C. Rosset, E. Hivon, and K. Gorski (2019, March). healpy: equal area pixelization and spherical harmonics transforms for data on the sphere in python. *Journal of Open Source Software 4*(35), 1298.

Zwicky, F. (1933). Die Rotverschiebung von extragalaktischen Nebeln. *Helv. Phys. Acta 6*, 110–127.